12-12-2012 12:00 AM

Parametric Study on a Novel Waste Heat Recovery System

Ghaleb Rustom Abdul Sater
The University of Western Ontario

Supervisor
Dr. Kamran Siddiqui
The University of Western Ontario

Graduate Program in Mechanical and Materials Engineering
A thesis submitted in partial fulfillment of the requirements for the degree in Master of Engineering Science

Parametric Study on a Novel Waste Heat Recovery System

(Thesis format: Monograph)

by

Ghaleb R. A. Sater

Graduate Program in Engineering

Department of Mechanical and Materials Engineering

A thesis submitted in partial fulfillment
of the requirements for the degree of
Master of Engineering Science

School of Graduate and Postdoctoral Studies
The University of Western Ontario
London, Ontario, Canada

THE UNIVERSITY OF WESTERN ONTARIO
SCHOOL OF GRADUATE AND POSTDOCTORAL STUDIES

CERTIFICATE OF EXAMINATION

Supervisor	Examiners
_____	_____
Dr. Kamran Siddiqui	Dr. Chao Zhang
	_____
Supervisory Committee	Dr. Jun Yang
_____	_____
Dr. Chao Zhang	Dr. Rajiv Varma

The thesis by

Ghaleb Rustom Abdul Sater

entitled:

Parametric Study on a Novel Waste Heat Recovery System

is accepted in partial fulfillment
of the requirements for the degree of

Master of Engineering Science

Date_____ _____
Chair of the Thesis Examination Board

ABSTRACT

The present thesis is based on an industry-sponsor project involving a novel waste heat-to-electricity conversion system. This proprietary system utilizes thermal energy from a low temperature heat sources to produce torque that drives an electric generator to produce electricity. The system needs to be studied through scientific research to help with optimizing the product development, component design, and overall system performance. The main objectives of this study are to develop simulation tools (numerical model) that will allow to simulate the thermo-fluid processes in various system components and to use this numerical model to study the heat transfer and phase-change processes along with the work interactions.

In the first part of this study, a novel numerical model was developed using the commercial CFD software Fluent. The novelty of this model was its capability to simultaneously simulate the phase-change and moving boundary processes. To the best of our knowledge, this is the first time such integrated model has been developed. The model coupled the Mixture model and the Dynamic Mesh model via developed user-defined functions. However, due to the limitations of the CFD software, the investigations were restricted to the fundamental heat transfer and phase-change processes in the lower vessel and the associated heat exchanger coil which undergoes the boiling process, along with the piston movement in the vessel.

The heat exchanger coil is one of the key components of the system where the primary phase change process takes place and its design has a direct impact on the overall system performance. Thus, the main focus on the second part of this study was on a detailed investigation of the phase-change process in the heat exchanger coil and its design improvement as well as the type of the working fluid. The investigation of the working fluid involved four volatile substances: methanol, ethanol, pentane and butane. Due to the low boiling point and low latent heat pentane was recommended as the best substance among the four. Its low boiling point also allows the system to extract heat at lower waste heat temperatures.

The study of the heat exchange and phase-change processes in the heat exchanger and the vessel involved a detailed investigation of these processes, which include the spatio-temporal variations of the flow patterns and the mixture quality. Various heat exchanger geometries and configurations were considered. A common feature observed in all these configurations was the presence of a cyclic process inside the heat exchanger tube where the low quality mixture (heavy fluid) near the bottom of the vessel enters from one end of the heat exchanger and the high quality mixture (light fluid) escapes in the form of jet into the vessel from the other end of the tube. It was found that the speed of the jet increased with an increase in the surface area of the heat exchanger coil. The impact of heat exchanger geometry and configuration on the flow patterns and the mixture quality as well as the piston movement is presented and discussed in detail. These results will be utilized by Dyverga to improve the heat exchanger design.

The novel model developed in this study will serve as a valuable tool for Dyverga to further study various thermo-fluid processes in all other system components and for the system optimization.

Keywords: Waste heat, boiling, Isobaric expansion, quality, volume fraction, piston movement, CFD, heat exchanger

Acknowledgments

I would like to express my gratitude to Professor Kamran Siddiqui for being an outstanding advisor and an excellent professor. His guidance and continuous encouragement have made this work successful, and for that I owe him my deepest appreciation.

I would also like to take the opportunity and extend my sincere appreciation to Dyverga, NSERC and Mitacs for their support and granting me this life time opportunity.

I am extremely grateful to my colleagues and friends for the continuous support and wishes.

To my soul mate, Faten your non-stopping love, sincerity and beautiful words were a great leading force for my determination and hope; I love you.

To my all-time supporters my mom and brother, words can't simply express my gratitude and love to all of you. I shall be in debt to you for the rest of my life.

To my role model; throughout my life your values and wisdom have been the back bone of my achievements. I dedicate all my work to your memory; love you father.

Table of Contents

List of Tables

List of Figure

CHAPTER 1: INTRODUCTION

According to U.S. Energy Information Administration's (EIA) latest study; the global energy demand will continue to grow over the next two decades as shown in Figure 1.1 [EIA 2010]. This study predicts that the global energy demand will increase by almost 50% from its 2007 level to reach around 225 Billion MW in 2035. To fulfill this demand, different energy resources will be utilized. Figure 1.2 shows a projection of the contribution of the main energy resources to meet the total global energy demand. It can be noticed that the fossil fuels (coal, oil and gas) will continue to be the main sources of energy accounting for more than 50% of the total global energy supply [EIA 2010]. This heavy dependency on fossil fuels to meet energy needs has high environmental consequences since burning fossil fuels produces greenhouse gases such as carbon dioxide, nitric oxide, etc. At the expected rate of fossil fuel consumption by 2030, the global emission of carbon dioxide gas will increase by 39% to hit 40.4B Mt/year [EIA 2010]. Consequently, it will be necessary to re-evaluate the way in which energy is produced to reduce fossil fuel burning impacts on the environment. However, this may not take place until less expensive, easily implemented, and equally reliable alternatives become available. Therefore, to avoid severe consequences of utilizing fossil fuels, one strategy would be to reduce their consumption.

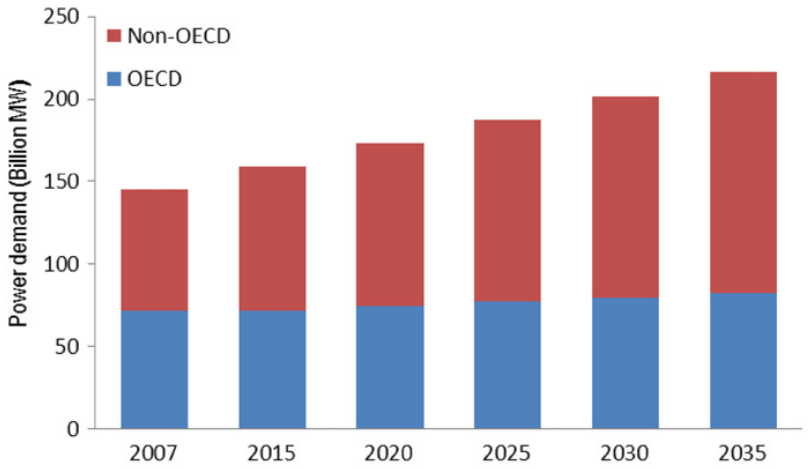

Figure 1.1 Projection of global energy consumption in Billion MW [EIA 2010]

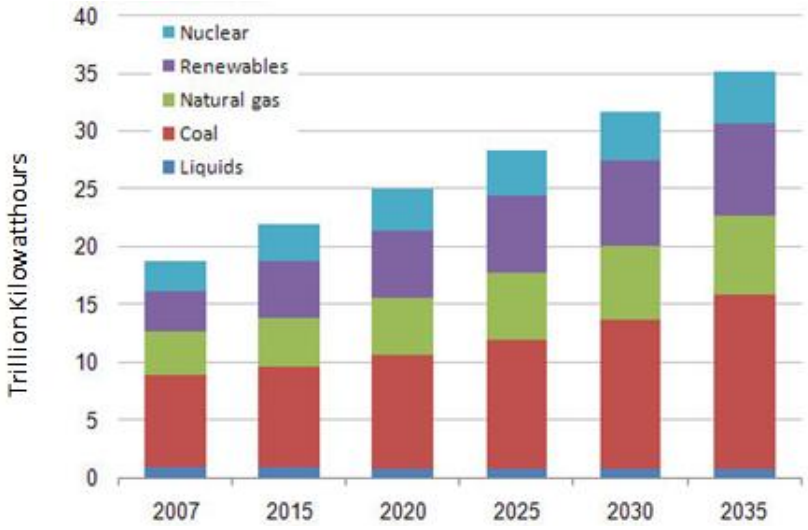

Figure 1.2 Predicted energy sources in Kilowatthours [EIA 2010]

To understand why fossil fuels are causing this great damage to the environment one should understand the process of how this fuel is being converted into useful energy. Most of existing engineering conversion systems that use fossil fuel has low thermal efficiency and typically more than 50% of the energy utilized by these systems is rejected to the environment as waste heat [Cengel and Boles 2008]. Capturing useful energy from waste heat is possible through energy recovery units. Coupling these units with the original conversion system will improve its overall thermal efficiency; this translates into lower operational cost on one hand and most importantly reduces the system's environmental impacts. Furthermore, this option can be applied easily and at low cost since energy is being recovered and used rather than being released to the environment. Currently, such systems are in use in many engineering applications and more studies are taking place to find various methods to recover the wasted energy.

1.2 Waste heat potential

Due to the rapid growth in industry, and the rise in the standard of living, the amount of wasted energy is expected to soar over the coming years. In 2011, the U.S. Department of Energy estimated that the wasted energy in the industrial sector alone was around 7,400 PJ/year [Vatanakul 2011]; this exceeds the combined power generation from all of the current

renewable energy systems [Zhang 2012]. Similarly, Natural Resources Canada estimates that 25% of the 2,300 PJ/year of the available waste heat in Canada could be recovered using existing technology [Bedard 2009] which in return represents a reduction of 27B Mt/year in greenhouse gases. Therefore, recovering this energy through recovery systems will have a noticeable impact in reducing greenhouse emissions to the environmental.

In processes where combustion occurs, efficiency determines the amount of wasted energy which is usually released through an exhaust system to the environment. Typically, the low efficiency is due to incomplete combustion or friction losses as in the case of piston engines. Figure 1.3 displays sources of energy losses that directly reduce the efficiency of a system. Flue losses have the highest share and are the easiest to recover and reuse [DOE 2008].

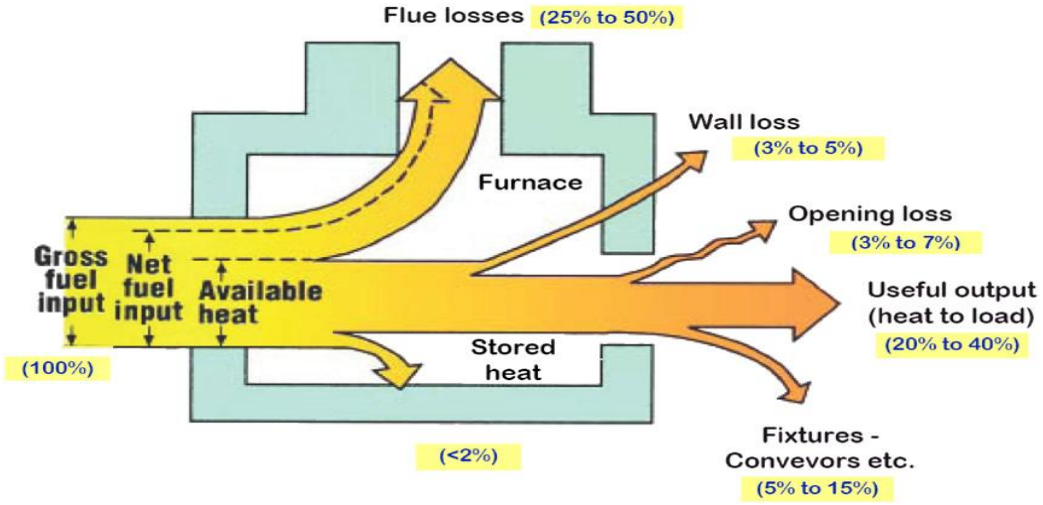

Figure 1.3 Energy losses in combustion process [DOE 2008]

In current industrial fields, efficiency varies for different energy conversion systems. Table 1.1 shows a list of primary heat engines and their corresponding theoretical thermal efficiencies. As we can see in most of the power producing systems, more than 50% of the energy is wasted as heat.

Table 1.1: Maximum efficiency of selected energy conversion systems [Wilbur 1985]

Energy Conversion System	Efficiency %
Steam turbine	50
Gas turbine	30
Gasoline piston engines	25

To help, evaluate a realistic recovery potential, the waste heat is characterized based on the temperature of the exhausted gases and can be classified into three different grades: high, medium and low. Table 1.2 shows the temperature range for the three grades. Also, in this table the relative quantity of each grade to the total wasted heat is presented. It can be noticed that low grade heat has the highest share of around 60%. According to the United States Energy department, although low grade waste heat is still the least thermal energy carrier but with the given quantities it has the highest work potential. In 2008 it was estimated to be around 10,000 MW, 30% higher than that of medium quality and 300% higher than the high grade heat.

Table 1.2 Wasted energy, different grades with their corresponding temperature ranges, quantity in percent [BSC 2008] and work potential for USA [DOE 2008]

Grade	Temperature (^{0}C)	Exhausted Quantity in %	Work Potential (MW)
High	≥650	10%	~3,000
Medium	230-650	30%	~7,200
Low	≤230	60%	~10,000

1.3 Common heat recovery devices

This section will cover different systems commonly used to recover waste heat. These systems vary in applications and some can recover different grades of waste heat while others are only feasible to recover one type.

1.3.1 Recuperators

A recuperator is a heat exchanger that transfers heat from a waste heat source at higher temperature to a fluid at lower temperature. Recuperators are widely used in industry where high grade waste heat is available such as, melting furnaces, annealing ovens, furnace burners etc. In such applications, the exhausted gases can be higher than 1000 ^{o}C [DOE 2008]. It has been shown that the fuel consumption can be reduced by about 25% by using the preheated air (using waste heat) [Hasegawa 2000].

1.3.2 Rotary regenerator

A rotary regenerator is a common air-to-air heat recovery system that consists of a porous disk fabricated with material with high heat capacity. This disk rotates very slowly (at 3 to 5 rpm) about its axis between two side-by-side ducts; one is a hot gas duct and the other is a cold gas duct as shown in Figure 1.4. The primary use of a rotary regenerator is to recover low-to-mid grade waste heat and is primarily used with building HVAC systems.

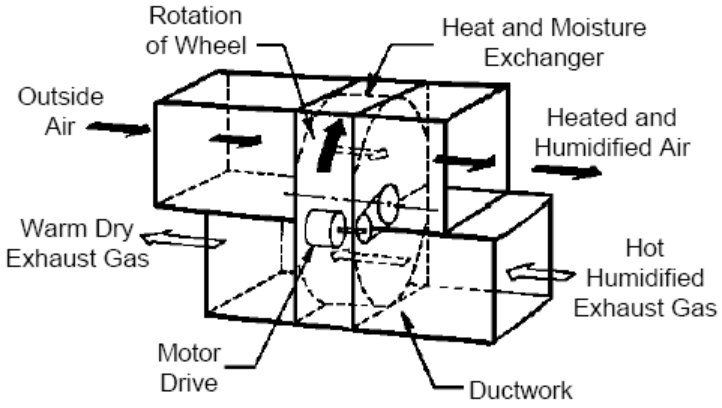

Figure 1.4 Typical heat wheel configuration [UNEP 2006]

1.3.3 Organic Rankin cycle

Most of the available heat recovery systems use the extracted thermal energy for heating purposes. However, in limited applications, this low-to-medium grade heat is converted into mechanical work to generate electricity. An example of this type of system is an Organic Rankine Cylce (ORC) shown in Figure 1.5. The cycle operates using fluids that have low boiling

points such as propane, haloalkanes (e.g. “freons”), iso-pentane etc. and when the fluids evaporate inside the evaporator their vapors expand inside a turbine causing mechanical shaft work, which then drives a generator to produce electricity. Since the cycle functions at lower temperatures, the overall efficiency is low and in the range 10-20% [DOE 2008].

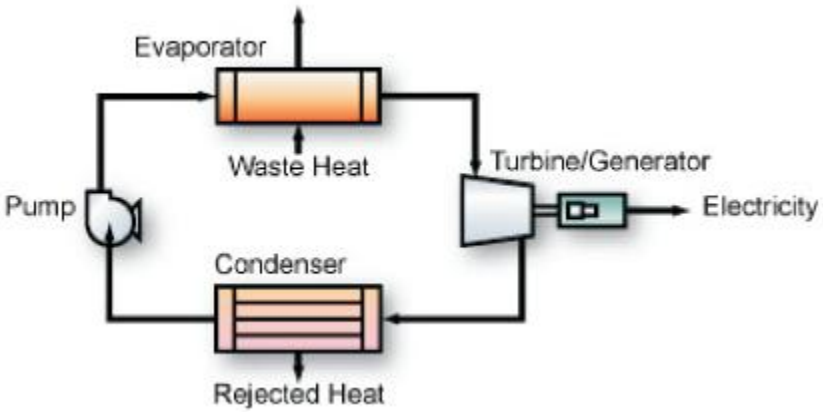

Figure 1.5 Schematic of an Organic Rankine Cycle [DOE 2008]

1.4 SmarTorQ by Dyverga

Dyverga Energy Corporation, a company based in Kitchener-Waterloo has developed a new innovative design that converts the energy from low grade heat (less than 80 ^{o}C) into a shaft work that drives a generator to produce electricity [Godwin 2011]. A conceptual design of this novel system referred to as “SmarTorQ” is shown in Figure 1.6. As can be seen in the figure, the main components of the system are a series of coupled vessels mounted on a hexagonal wheel. The wheel is attached to an electric generator which converts the mechanical rotational energy into electrical energy. The rotation potential of this wheel is simply the resultant of the process that occurs inside the coupled vessel pairs (shown on the vertical pair in Figure 1.6). Each coupled vessel has heat exchangers attached to its end as shown in Figure 1.6. The vessels are connected via a flexible conduit with an insulated membrane within each vessel. Heat exchanger coil of each vessel contains small amount of low boiling point volatile fluid which rapidly undergoes the phase change when subjected to a heat source. Each coupled vessel pair also has a working mass consists of high density liquid which is transferred through the conduit; see Figure 1.7.

When the bottom vessel is in the proximity to the bottom most position, it comes into contact with the heat source (< 80 ^{o}C) causing the volatile fluid inside the heat exchanger coil to change phase (boil) instantly resulting in a rapid pressure increase inside the lower vessel in the coupled pair. At the same time, the top vessel in the pair is undergoing cooling by the surrounding air resulting in the condensation of the volatile fluid and hence a pressure decrease. This pressure differential between the lower and upper vessel acts on the membrane in each vessel causing the working mass to be transferred through the conduit from the lower vessel to the top vessel. Typically this transfer occurs in less than one second.

This transfer of working mass from the lower vessel to the upper vessel causes the system to rotate under the action of gravity. After the system starts rotating, the next vessel pair undergoes the same process and the system continues to turn creating a continuous torque that rotates the electric generator and thus producing electricity.

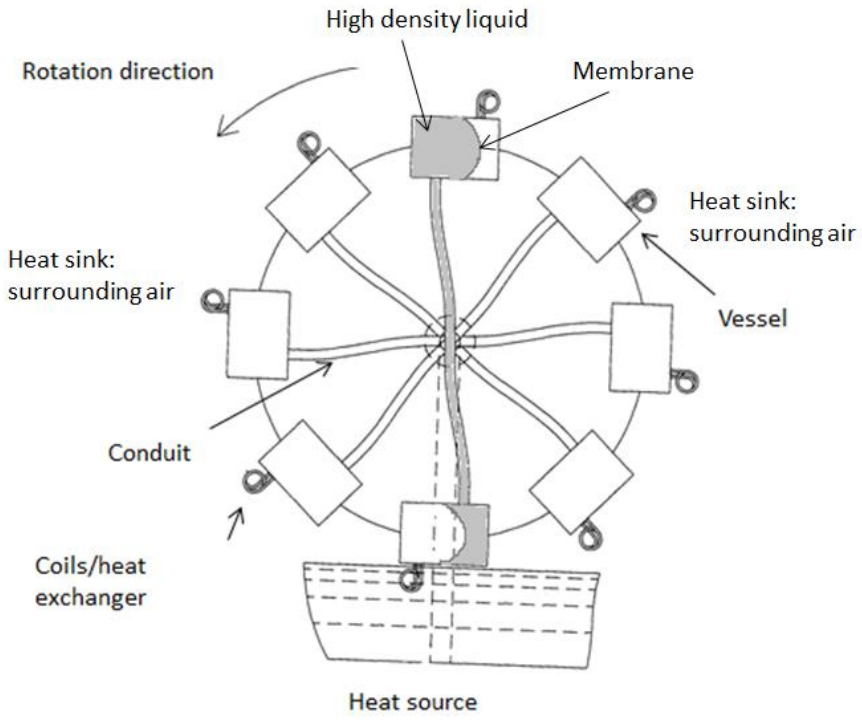

Figure 1.6 Schematic of SmartorQ [Godwin 2011]

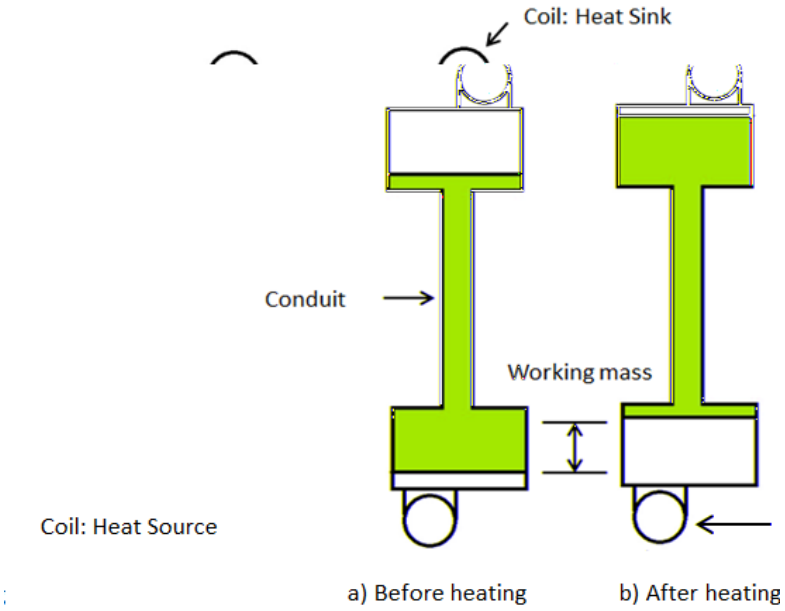

Figure 1.7 Schematic of one coupled vessel with working mass in the middle

SmartorQ concept is similar to a Minto engine which is defined as a liquid piston heat engine that operates on a small temperature gradient [He 2011]. A schematic of a Minto engine is shown in Figure 1.8. As we can see, the main difference between the SmartorQ and the Minto engine is the absence of the working mass between the vessels in the Minto engine. That is, the rotation of the Minto engine depends solely on the mass of the low boiling liquid (working fluid) in each vessel. According to He (2011), a Minto engine operating between 37 ^{o}C and 39 ^{o}C with 14 pairs of the coupled vessel filled with 3.42 m^{3} of propane in each vessel pair with a 12 m long connecting tube between each vessel pair produces 2.4 KW of output power. He (2011) reported the maximum efficiency of Minto engine is 2.5% when propane was used as the working fluid. It is expected that the addition of the working mass in the SmartorQ will increase the torque potential to rotate the system compared to the Minto engine. In addition, the large surface area coils used in the SmartorQ to hold the working fluid will certainly reduce the time required by the working fluid to change phase compared to that in the Minto engine. Thus, it is expected that the power output of SmartorQ will be greater than that of the Minto engine and hence the efficiency.

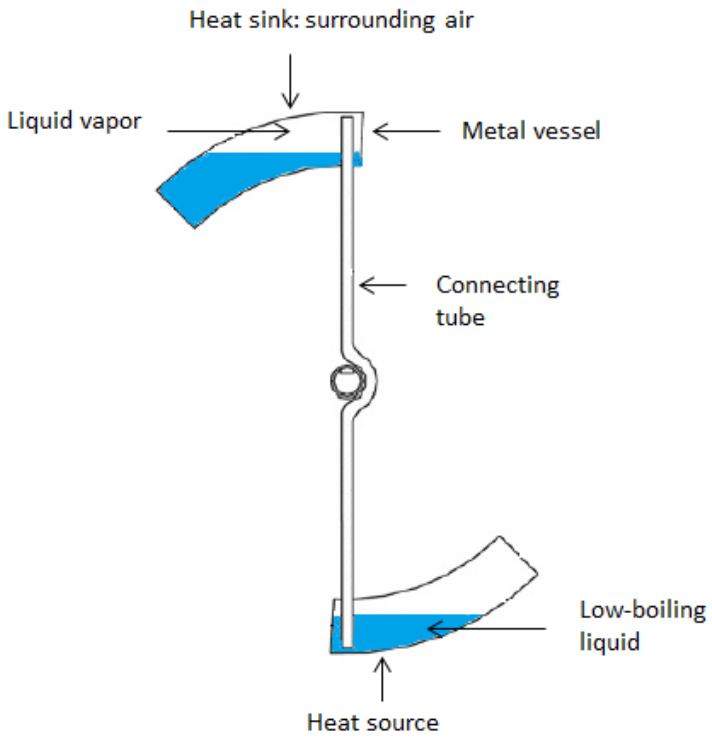

Figure 1.8 Schematic of an original Minto engine [He 2011]

1.5 Literature review

To better understand the concepts behind Dyverga's system, it was decided to build a numerical model using Fluent 13 CFD package where numerical simulations can be created to mimic the phenomena found in the proposed system. Two phase flow problems, fluid dynamics and heat transfer fundamentals are governed by partial differential equations (PDE) which represent the conservation laws for mass, moment, and energy, while CFD is the art of replacing such PDE systems by a set of algebraic equations that can be solved using computers [Kuzmin 2005]. It is considered as a virtual laboratory where numerical experiments can be prepared and provide qualitative and quantitative data that can be analyzed to predict the behavior of a numerical model under certain conditions.

Inside SmarTorQ, three different processes are occurring simultaneously: boiling and condensation occurring in different buckets and a boundary in between moving according to pressure difference. The purpose of this study was to develop a numerical model that can

simulate the thermo-fluid processes found in Dyverga's system and perform a parametric study. The selected CFD package Fluent 13 has the capability to simulate phase change problems such as boiling and condensation and can also simulate problems with moving boundaries. These problems have been reported widely in the literature. However, simulating a phase change process simultaneously with moving boundary is a unique and challenging problem and to the best of our knowledge, has not been reported in the literature. For this reason the literature review is divided into two sections. One presents previous research work that has been done to simulate phase change problems focusing on models and techniques used. The second section covers studies in which dynamic mesh was used to simulate moving objects focusing on mesh types and techniques used.

1.5.1 Phase change literature review

Fluent offers three different models that can simulate phase change problems: Volume of Fluid (VOF), mixture model and Eulerian model. Different studies have used these models to simulate phase change in different applications. According to Dong et al. [2012] it is a great challenge to simulate problems with phase changes accurately. They presented a vapor-liquid phase change model for the VOF method in Fluent. This model is suitable for two phases in which one of the phases is saturated and the other is unsaturated i.e. super-cooled or overheated and the mass transfer between the two phases was written in a User Defined Function (UDF). For the saturated-phase thermal conductivity and specific heat were assumed to be zero. In this study, 2D film boiling was simulated using a geo-reconstruct scheme for the volume fraction equation, and a third-order MUSCL scheme for momentum and energy equations. Different codes for solving the phase change problems based on the VOF method can be also seen in works of Welch and Wilson [2000], and Guo et al. [2011]. In a different study Lili [2012] used the mixture model in Fluent to simulate flow and boiling heat transfer of two phases in a horizontal tube. The source terms of vapor, liquid and energy using De Schepper correlations were defined in a UDF. The discretization for different equations being solved was kept as default (first order scheme) and convergence criteria was set to 10^{-6} for energy while continuity and momentum was 10^{-3}. In this study Lili et al. [2012] found that the performance of heat transfer increased with the increase in the velocity of liquid flowing inside

the horizontal tube. The mixture model was also used by Kristóf et al. [2008] to study boiling water flow in the horizontal steam generator of the Paks nuclear power plant. In this study, a UDF was used to calculate the slip velocity and phase change models. They used a double precision solver including transient for time formulation; and it was recommended to use a sufficient number of iterations per time step to achieve convergence. Ganguli et al. [2010] used Fluent's built-in phase change (mass transfer) model which is derived from the Hertz Knudsen correlation. This correlation gives the evaporation-condensation flux based on the kinetic theory for a flat interface [Fluent 2010] and is only available with the mixture and Eulerian model. Their study was focused on the on passive decay heat removal systems which are used in the nuclear industry and are subject to pool boiling and thermal stratification. They used The Eulerian model. Furthermore, they recommended using higher order discretization for all equations in a phase change problem since this helps to mitigate the unfavorable effect of artificial diffusion that can occur when using low order up-winding schemes. The solution for their unsteady problem was considered to be fully converged when the sum of residuals was below 10^{-5}. Ganguli et al. [2010] observed that vapor volume fraction due to nucleate boiling is confined to the wall region, and vapor accumulated at the top while the simulation was running, suggesting that mixing is not enhanced due to the formation of vapor. In a study on modeling and simulation of flow boiling heat transfer Krause et al. [2010] used the mixture model in Fluent. A detailed explanation of the phase change model in Fluent was presented, focusing on the phase change mass transfer which is solved by sink and source terms in the continuity equation. The mass transfer coefficient which appears in the sink and source terms was described by krause et al. [2010] to be a reflection of the local evaporation and condensation rate and it combines the influence of unknown factors such as bubble size and nucleation size density. krause et al. [2010] defined the values of this coefficient by iterative sensitivity analysis comparing numerical results with experiments and literature.

1.5.2 Moving boundaries literature review

Using the dynamic mesh option in Fluent to simulate a moving boundary in an application has been found in different reported studies. For instance, Waclawiak and Kalisz [2011] used the dynamic mesh in Fluent to predict deposition of ashes on heater tubes during combustion of

solid fuels in a boiler. In their 2D numerical model, User Defined Functions were used to calculate deposition flux by using mass flow rate of ash particles, area of the surface being hit by the particles and the impact angle. The growth of deposits was calculated by considering the deposition density as a function of time. Hence, the nodes of each face of the tube in their model are shifted as they are hit by ash particles. This movement of vertices of the grid is determined using dynamic mesh and a UDF written in C language. In their model, triangular mesh was used and the authors stressed that these cells should be large in order to avoid the "negative volume error" which will halt the simulation. In a different application Dumont et al. [2004] used the dynamic mesh method to model a heart valve. A 2D model that can simulate mechanical heart valves operating during the ejection phase of the cardiac cycle was introduced. The model was meshed using a triangular mesh Dumont et al. [2004] highlighted one limitation of the dynamic mesh model which is the requirement of at least one cell at the initial stage to cover the gap between the valve leaflet and the wall. In a different study, Asad et al. [2011] investigated the unsteady flow structure and flapping trajectories of a dragon fly using a 3D numerical model in FLUNET. To simulate the wing's kinematics, dynamic mesh model was used. The study highlighted the importance of selecting a mesh method (smoothing, layering or re-meshing) since it will ensure that the grid will match the geometric changes, and will maintain satisfactory characteristics of the original mesh Ye [2003] compared two mesh methods to simulate electrostatic spray-painting with a moving atomizer. In the dynamic zone where the atomizer moves, he used the layering mesh method with a quad surface while re-meshing was used on a triangular mesh. The atomizer is included in a moving box, and tetrahedral elements were used. In the layering option, cells in the dynamic zone were added or deleted adjacent to the moving box and in order to limit the total mesh size, coarse grid was used in the static zone above the dynamic zone. He found that the triangular mesh with the re-meshing option outperformed the layering option with the quad mesh in the dynamic zone. To determine the motion of the atomizer, Ye [2003] converted a predefined motion file of an arm robot that operates the atomizer. In a study on Hypersonic Vehicles, Scott et al. [2009] used Fluent's dynamic mesh to accurately characterize vehicle dynamics for control studies. In their proposed model, they utilized the built-in six degree of freedom (6DOF) model where velocity is

calculated based on user defined equations [Fluent 2010]. The 6DOF solver in Fluent uses the solid body forces and moments in order to compute the translational and angular motion of the center of gravity of the solid body.

1.6 Motivation and objectives

Dyverga has built a simplified proof of concept system to successfully demonstrate the operation and to support understanding for patenting. The system needs to be studied further through scientific research to help in the product development, component design, and evaluating the overall system performance. Some key areas of the design which lack thorough understanding are (i) the heat extraction from low temperature heat source and its effective transfer to the working fluid, (ii) phase-change processes and associated dynamics of the working fluid, and (iii) heat rejection from the working fluid to ambient conditions. The heat exchanger design is a crucial component of the system, where the working fluid undergoes two-way phase change process at different stages. The efficiency of the system depends on the performance of the heat exchangers. Therefore, proper design of heat exchanger is crucial for the system performance and hence its marketability.

Objectives

The main objectives of the proposed research are

1. To develop a numerical model that can simulate phase change processes coupled with a moving boundary.

2. To conduct a parametric study using the developed numerical model to understand the behavior of the working fluid inside the heat exchanger and use this knowledge to improve heat exchanger design.

This research work was conducted in collaboration with Dyverga. The project posed challenges from the modeling aspect as the simultaneous modeling of the phase change process and the boundary movement which is essential to simulate Dyverga's system, has not been previously reported. Note that the novel integrated model (phase change + moving boundary) developed

in this research work will also serve as a tool by Dyverga in the future to study other parameters and to conduct the overall system optimization which is beyond the scope of the present study.

1.7 Thesis layout

Chapter 1 provides the introduction, literature review, motivation and objective of this research work. Chapter 2 describes the numerical modeling of the proposed model along with the corresponding mathematical equations. The validation of numerical models and their grid independence tests are also presented in this chapter. Moreover, Chapter 2 includes efforts to model the complete process found in Dyverga's system. The detailed parametric study and analysis of its results are presented in Chapter 3. The main conclusions of this research along with future recommendations are summarized in Chapter 4.

CHAPTER 2: NUMERICAL MODELLING

This chapter describes the numerical modeling. At the beginning, a brief description of the problem is presented, which is followed by the explanation of the available numerical models. The corresponding mathematical equations of the selected models are then introduced. In the final section of this chapter, mesh and time dependency tests are presented along with the model validation. At the end of this chapter an outlook on the strategies developed to model the full process along with obstacles and difficulties encountered during the model development are presented.

2.1 Modeling process

As discussed in Chapter 1, in Dyverga's system, two main phenomena i.e. boiling and condensation occur simultaneously in two opposite heat exchangers separated by a medium (see Figure 1.6 in Chapter 1). In the lower section of the system where the heat source is present, the volatile fluid inside the heat exchanger undergoes boiling while condensation occurs in the heat exchanger that is in contact with the heat sink in the upper section of the system. The separating medium moves with the pressure difference accordingly. In Figure 2.1 a simplified schematic is shown where the medium separating the two heat exchangers is represented by a piston. Modeling of even this simplified version of the complete system that involves two processes occurring simultaneously but different phase change processes and the transient motion of the separating medium, whose movement is dependent on the pressure magnitudes associated with the two phase change processes is extremely challenging. Therefore, it was decided to simplify the model. A further discussion on the modeling of the complete system can be found in at the end of this chapter. This simplified model only simulates the boiling phenomenon along with piston movement without considering the condensation process as depicted in Figure 2.2. It should be noted that even after eliminating one phase change process, the modeling still contains several challenging aspects in particular the integration of the phase change and moving boundary processes into one model, which to the best of our knowledge has not been reported in the literature.

This simplified model; shown in Figure 2.2 will simulate the so called isobaric expansion; a well-known thermodynamic process. Isobaric expansion occurs when a domain expands at a constant pressure while being exposed to continuous heat input [Cengel and Boles 2008]. The numerical model is carried out in the commercial CFD software Fluent 13.

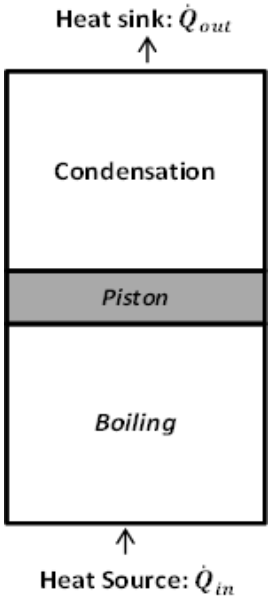

Figure 2.1 A simplified model of Dyverga's system

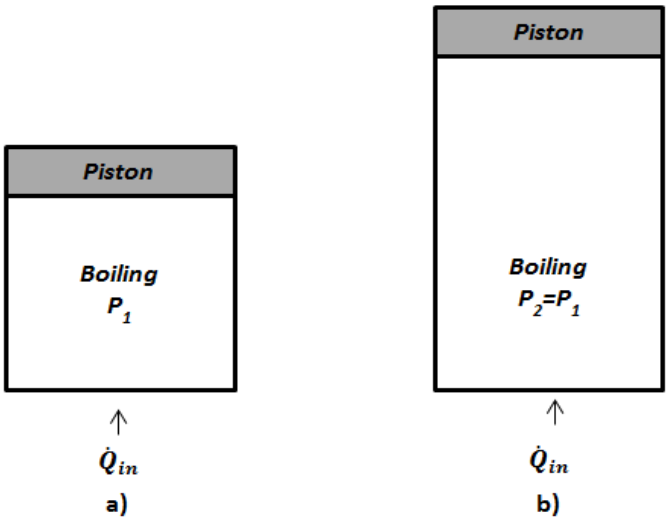

Figure 2.2 Illustration of the Isobaric Expansion process

2.2 Numerical modeling

2.2.1 Phase change models

In the proposed Dyverga's system, phase change is the key process that drives the system. Therefore, it is very important to select a suitable model in order to simulate the phase change phenomenon correctly. In Fluent three Euler-Euler models are available: the volume of fluid model (VOF), the mixture model and the Eulerian model. The first two models solve only one set of Navier stokes equations for the mixture, while the last model solves Navier stokes equations for each phase. These models use the Euler-Euler approach where different phases are treated mathematically as interpenetrating continua and since the volume of a phase cannot be occupied by the other phases, the concept of phasic volume fraction is introduced. These volume fractions are assumed to be continuous functions of space and time and their sum is equal to one.

The VOF model is a surface-tracking technique applied to a fixed mesh; it is designed for two or more immiscible fluids where the position of the interface between these fluids is of interest. In this model, a single set of momentum equations is shared by the domain. Some applications of this model include stratified flows, filling, sloshing and motion of large bubbles in a liquid.

The mixture model is designed for two or more phases. This model solves for the mixture momentum equation and displays relative velocities to describe the dispersed phases. Some applications of this model include particle-laden flows with low mass loading , sedimentation transport and bubbly flows.

The Full multiphase model or Eulerian model is considered to be the most complex of the multiphase models in Fluent, and hence it requires more computational effort and time to solve a given problem since the momentum, continuity and energy equations are solved for each phase. It is a comprehensive model that can be used to solve any problem that involves phase change and has been used widely for granular (fluid-solid) flows and some of its applications include bubble columns, particle suspension and fluidized beds [Fluent 2010].

Fluent user manual suggests the use of either the mixture or Eulerian model for problems where phases mix or separate and the volume fraction of an individual phase exceeds 10%. Intuitively, one can conclude that in boiling problems, the volume fraction of the secondary phase (vapor) will exceed 10% and it will separate from the main phase. In the present problem it is expected that the dispersed-phase (vapor) will not be concentrated in just one portion of the domain, therefore, based on the Fluent theory guide, both the mixture and Eulerian models are suitable for the problem. As the mixture model is less computationally expensive compared to the Eulerian model, the mixture model was used in the present study.

The mixture model solves continuity, momentum and energy equations for the mixture, the volume fraction equation for the secondary phase and its corresponding relative velocity. All equations for the mixture model that are described below are taken from the Fluent user manual [Fluent 2010].

The continuity equation for the mixture is,

$$\frac{\partial}{\partial t}\left(\rho_m\right)+\nabla.\left(\rho_m \overrightarrow{v_m}\right)=S_m \tag{2.1}$$

$\overrightarrow{v_m}$ is the mass-averaged velocity of the mixture, ρ_m is the mixture density and S_m is the mass source term. In the present problem, the liquid and mass sources are balanced thus, S_m is zero ($S_{mass,liquid} = -S_{mass,vapor}$) [Krause 2010] . The mass-averaged velocity of the mixture and mixture density are computed as,

$$\overrightarrow{v_m}=\frac{\sum_{k=1}^{n}\alpha_k\rho_k\overrightarrow{v_k}}{\rho_m} \tag{2.2}$$

$$\rho_m=\sum_{k=1}^{n}\alpha_k\rho_k \tag{2.3}$$

$_k$ is the volume fraction of phase k. The mixture momentum equation is obtained by the summation of the individual momentum equation for each phase and can be written as,

$$\frac{\partial}{\partial t}\left(\rho_m \overrightarrow{v_m}\right)+\nabla.\left(\rho_m \overrightarrow{v_m}\overrightarrow{v_m}\right)=-\nabla p+\nabla.\overline{\overline{\tau}}+\rho_m \vec{g}+\vec{F}+\nabla.\left(\sum_{k=1}^{n}\alpha_k \rho_k \overrightarrow{v_{dr,k}}\overrightarrow{v_{dr,k}}\right) \quad (2.4)$$

In this equation, *n* accounts for the number of phases, p is the static pressure, $\rho_m \vec{g}$ is the gravitational force of the mixture and $\vec{F}$ is the body force. The drift velocity for phase *k*, $\vec{v}_{dr,k}$ is the difference between the phase k velocity and mixture velocity; $\vec{v}_{dr,k}=\vec{v}_k-\vec{v}_m$. The s $\overline{\overline{\tau}}$ in the stress tensor is evaluated as,

$$\overline{\overline{\tau}}=\left(\mu_m(\nabla\overrightarrow{v_m}+\nabla\overrightarrow{v}_m^{T})\right) \quad (2.5)$$

Where μ_m is the mixture viscosity and is calculated in a similar manner as the mixture density in Equation 2.3.

In this proposed numerical model it is expected that pressure and temperature will increase in the domain during the phase change process therefore, the energy equation must also be solved for the mixture model [Fluent 2010]. The energy equation is given as,

$$\frac{\partial}{\partial t}\sum_{k=1}^{n}\left(\alpha_k \rho_k E_k\right)+\nabla.\sum_{k=1}^{n}\left(\alpha_k \overrightarrow{v_k}(\rho_k E_k+p)\right)=\nabla.\left(k_{eff}\nabla T\right)+S_E \quad (2.6)$$

The first term on the right hand side of the equation represents heat transfer due to conduction where, K_{eff} is the effective conductivity. S_E corresponds to any other volumetric heat sources in a boiling problem or heat sink in a condensation problem. Consequently, S_E is equal to the change in latent heat multiplied by the rate mass transfer that appears in Equations 2.11 and 2.12 [Krause 2010]. K_{eff} is computed using the following equation,

$$K_{eff}=\sum\alpha_k\left(k_k+k_t\right) \quad (2.7)$$

Where, k_k is the thermal conductivity of phase *k* and k_t is the turbulent thermal conductivity and is defined according to the turbulence model being used. In the present and for simplicity turbulent was ignored therefore k_t will be equal to zero.

$_k$ that appeared in energy equation is evaluated using the following equation,

$$E_k = h_k - \frac{p}{\rho_k} + \frac{v_k^2}{2} \tag{2.8}$$

Note that for an incompressible phase, E_k is equal to h_k, enthalpy of phase k, however since vapor in the present problem are defined as compressible, the above form of the equation is used.

To determine the volume fraction of the secondary phase i.e. vapor phase (v), the continuity equation for the vapor phase is used to formulate the volume fraction equation.

$$\frac{\partial}{\partial t}\left(\alpha_v \rho_v\right) + \nabla.\left(\alpha_v \rho_v \overrightarrow{v_m}\right) = -\nabla.\left(\alpha_v \rho_v \overrightarrow{v_{dr,v}}\right) + \left(\dot{m}_{l\to v} - \dot{m}_{v\to l}\right) \tag{2.9}$$

Where, $\dot{m}_{l\to v}$ is the rate of mass transfer from the primary phase i.e. liquid phase (l) to the vapor phase (v) while $\dot{m}_{v\to l}$ is the rate of mass transfer from the vapor phase (v) to the liquid phase (l).The rate of mass transfer between the phases also appears in the vapor transport equation,

$$\frac{\partial}{\partial t}\left(\alpha \rho_v\right) + \nabla.\left(\alpha \rho_v \overrightarrow{V_v}\right) = \dot{m}_{l\to v} - \dot{m}_{v\to l} \tag{2.10}$$

Where, α is the vapor volume fraction, ρ_v is the vapor density and $\overrightarrow{V_v}$ is the velocity of the vapor phase. The rate of mass transfer due to boiling and condensation in Kg/m^3-s appears on the right side of the above equations. The rates are evaluated using Equation 2.11 and 2.12 below. In this study only boiling is simulated therefore, $\dot{m}_{l\to v}$ is the only term that will appear in the above equations.

Boiling occurs when $T>T_{Sat}$

$$\dot{m}_{l\to v} = coeff * \alpha_l \rho_l \frac{\left(T - T_{sat}\right)}{T_{sat}} \tag{2.11}$$

When $T<T_{Sat}$

$$\dot{m}_{v\to l} = coeff * \alpha_v \rho_v \frac{\left(T - T_{sat}\right)}{T_{sat}} \tag{2.12}$$

A schematic diagram explaining the process of mass transfer in a phase change problem under a specific heat flux that takes place in Fluent using the mixture model is shown in Figure 2.3.

The coefficients that appear in Equations 2.11 and 2.12 are the inverse of relaxation time (1/s) and are derived using the Hertz Knudsen formula which gives the evaporation-condensation flux based on the kinetic theory for a flat interface. The expression of the coefficient for boiling is given below,

$$coeff = \frac{6}{d}\beta\sqrt{\frac{M}{2\pi R T_{sat}}}L\left(\frac{\rho_l}{\rho_l - \rho_v}\right) \tag{2.13}$$

Where, β is the accommodation coefficient that shows the portion of the vapor molecules going into the liquid surface and adsorbed by this surface, R is the universal gas constant, L is the latent heat (J/kg) and d is the vapor bubble diameter. Since the bubble diameter and accommodation coefficients are not commonly known, Fluent provides an option to tune the "coefficient" parameter in equation 2.13 in order to match experimental or theoretical data. The default value of boiling and condensation coefficients is 0.1, which can be varied to match theoretical or experimental results. The typical working range of the coefficient value is from 10^{-3} to 10 [Punekar 2010].

The relative velocity also referred to as the slip velocity is defined as the velocity of the secondary phase (vapor) relative to the primary phase (liquid) and can be written as,

$$\vec{v}_{lv} = \vec{v}_l - \vec{v}_v \tag{2.14}$$

The mixture model uses an algebraic slip formulation; where the main assumption is to prescribe an algebraic relation for the relative velocity where a local equilibrium between the phases should be reached over a short spatial length scale. According to Mannenen et al. [Fluent 2010], the slip velocity can be evaluated by,

$$\vec{v}_{lv} = \frac{\tau_l(\rho_l - \rho_m)}{f_{drag}\rho_l}\vec{a} \tag{2.15}$$

Where, τ_l is the liquid particle relaxation time and $\vec{a}$ is the vapor particle's acceleration.

Fluent 2010]

$$f_{drag} = \begin{cases} 1+0.15\,Re^{0.687} & Re \le 1000 \\ 0.0183\,Re & Re > 1000 \end{cases} \tag{2.16}$$

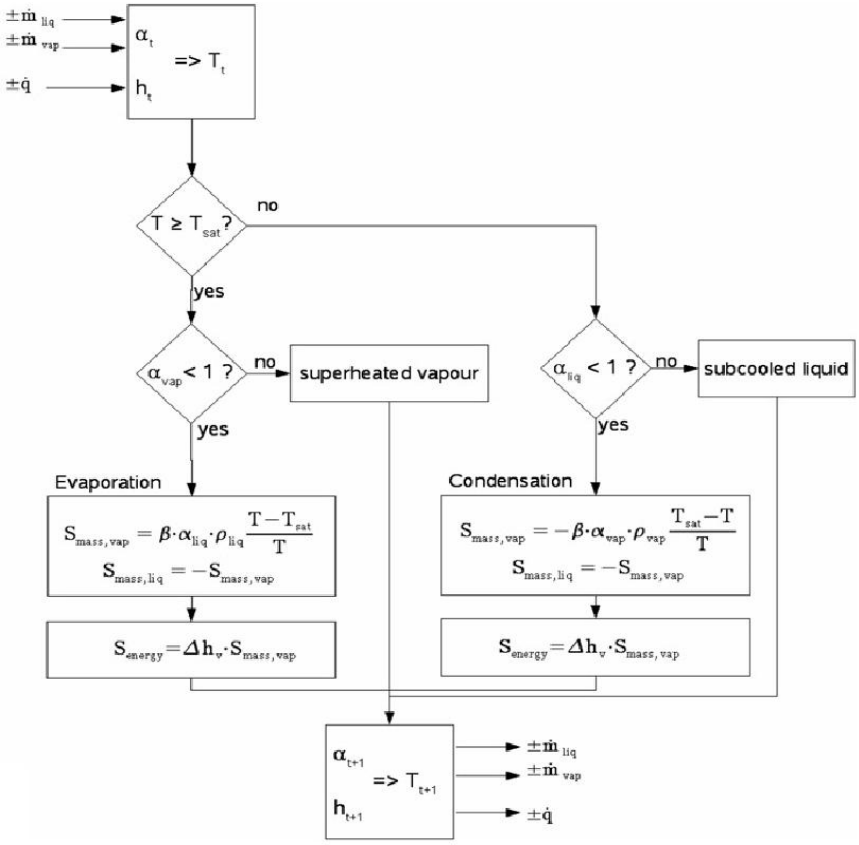

Figure 2.3 The phase change algorithm in Fluent using the mixture model

2.2.2 Dynamic mesh theory:

The dynamic mesh model in ANSYS Fluent is used to model problems where the shape of the domain changes with time due to the motion on the domain boundaries. The update of the

volume mesh is handled automatically by ANSYS Fluent at each time step based on the new positions of the moving boundaries. The motion of a solid object can be prescribed or unprescribed. In the prescribed motion mode, the linear and angular velocities about the center of gravity of a solid body are specified with respect to time. While in the case of unprescribed motion mode, the subsequent motion is determined based on the solution at the current time; for instance the linear and angular velocities are calculated from the force balance on a solid body. The motion of a solid body can be dictated by boundary profiles, user-defined functions (UDFs) or the six degree of freedom solver [Fluent 2010].

In the present model where the piston moves due to the isobaric expansion, the motion of the piston is considered unprescribed. In this case, a User Defined Function (UDF) or a six degree of freedom is to be used. The built-in six degree of freedom option (6DOF) in Fluent uses the object's forces and moments in order to compute the translational and angular motion of the center of gravity of the solid body. In this option, only some properties of the solid object need to be defined. On the other hand, all the equations governing the solid motion need to be defined if the UDF option is used. Note that this option is mostly used for complex motions. In the present isobaric expansion problem, the movement of the piston is linear, thus, the six degree of freedom option is considered which is sufficient to correctly simulate the piston's movement.

The governing equation for the translational motion of the center of gravity is solved in the inertial coordinate system using the following equation:

$$\vec{a}_G = \frac{1}{m}\sum \vec{f}_G \tag{2.17}$$

Where $\vec{a}_G$ is the translational motion of the center of gravity, m is mass and $\vec{f}_G$ is the force vector due to gravity [Fluent 2010]. Since the motion of the piston in the isobaric process is expected to be only translational as mentioned above, the angular motion can be ignored. To specify the mass of the solid object (piston), a UDF is written in the C language by using the DEFINE_SDOF_PROPERTIES macro and its value is passed to the 6DOF function [see Appendix

B]. After the translational acceleration is computed, the rate is derived by numerical integration and the translational velocity is used in the dynamic mesh calculations to update the solid body position.

The piston motion causes the mesh in the domain to deform in order to preserve mesh quality and orthogonality. Thus, the layering option in the dynamic mesh section is utilized as the mesh method. Generally this option adds or removes necessary layers adjacent to the moving boundary. In order to maintain the same size, the cell heights in the mesh option section must be specified to a value equal to the initial mesh size used. Figure 2.4 illustrates the process showing the initial mesh and the preservation of the mesh size while moving the domain boundary with time.

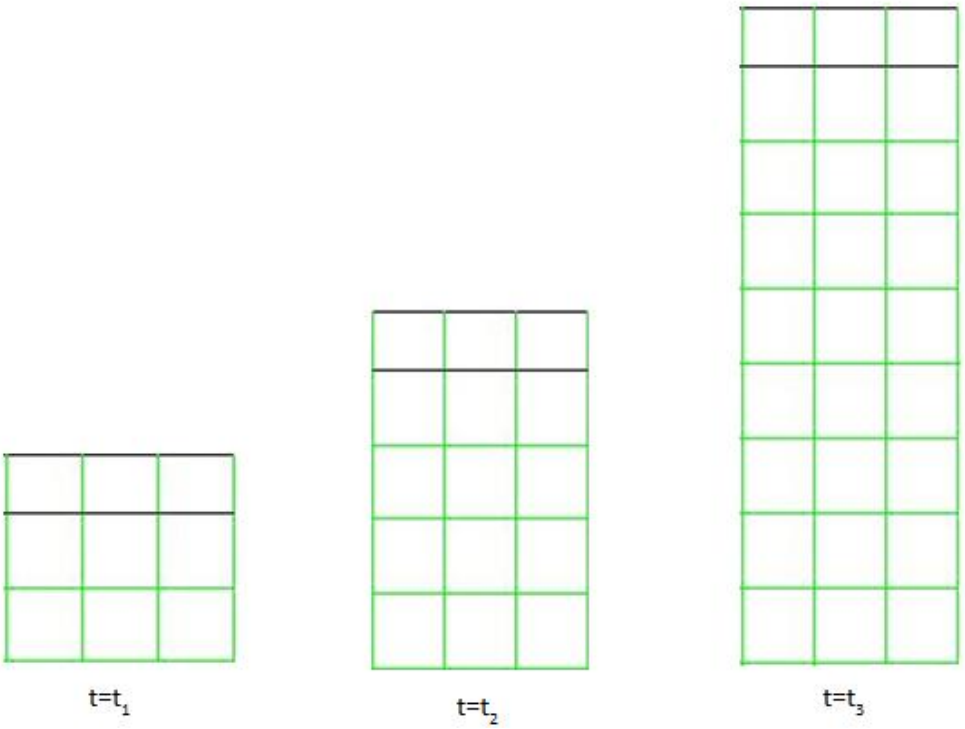

Figure 2.4 Illustration of the dynamic mesh updating process with time

2.2.3 Geometry modeling and boundary conditions

The proposed geometries were generated using ANSYS 13 Design Modular software while ANSYS 13 Mesh Utility software was used to generate their corresponding mesh. Quad mesh was used for all geometries and a 97% orthogonal quality was set as an acceptable criterion.

Walls that are not exposed to any external heating source where defined as adiabatic walls. For non-adiabatic walls where heat is applied, a constant temperature or a constant heat flux (W/m^2) was defined. The side walls were selected in the dynamic mesh zones as deforming walls (see Figure 2.5). The operation pressure was set to atmospheric pressure of 101,325 Pa and gravity was specified to be 9.81 m/s^2.

Since it is expected to see pressure variations in the domain, a code was written using C language that defines a variable saturation temperature using Antoine equation [see Appendix B].

2.2.4 Materials thermophysical properties

In the present study different working fluids were considered in consultation with Dyverga. A list of these materials along with their corresponding thermo-physical properties that were used in this chapter are presented in Table 2.1. In Fluent, liquid was set as the primary phase and vapor as the secondary phase. The vapor was assumed to be the ideal gas. The error associated with this assumption is almost negligible (about 1-2 %) because the pressure relative to the critical pressure and temperature relative to the critical temperature of the fluid is considerably low. In the model setup, to ensure appropriate latent heat removal from the primary phase to the secondary phase, the latent heat should be specified in J/kmol; the molecular weights of liquid and vapor should be the same; and for liquid the standard state enthalpy should be set equal to zero while for vapor it should be equal to the latent heat of vaporization [Punekar 2010].

Table 2.1 Thermophysical properties of materials used for validation [Vargaftik 2005]

		T_{sat} at atmospheric pressure (K)	Density (kg/m^3)	Specific heat (kJ/kg-k)	Conductivity (W/m-k)	Viscosity (kg/m-s)	Molecular Weight (kg/Kg-mol)	vaporization (k/kg)	Standard State Enthalpy (kJ/kgmol)	Coefficient (water/vapor) (N/m)
Methanol	**Liquid**	337.85	751.03	2.630	0.202	3.280e-4	32.04	1120	0	0.019
	Gas		Ideal gas	1.618	0.0018	1.110e-05			3.58e4	
Water	**Liquid**	373.15	958.7	4.182	0.600	1.003e-3	18.01	2256	0	0.058
	Gas		Ideal gas	2.014	0.026	1.340e-05			4.08e4	

2.2.5 Solution parameters

The solver used in the present study was a double precision pressure-based solver with absolute velocity formulation [Fluent 2010]. To control the spatial discretization of the convection terms in the solution equations a Second Order Upwind scheme was used for momentum, energy equations and density parameter. While for the volume fraction equation Second Order Upwind was not available, however, QUICK scheme which is based on weighted average of second-order-upwind was selected. The transient formulation was First Order Implicit**.** Interpolation of pressure was achieved by utilizing the PERSTO scheme. Coupling between pressure and velocity was achieved through COUPLED algorithm. Green-Gauss Node Based was used to evaluate gradients and derivatives (see Fluent user manual for details). Convergence criterion was set as 10^{-4} for the continuity equation, 10^{-3} for the momentum and volume fraction equations, and 10^{-6} for the energy equation. For motion convergence, the residual criterion was set as 10^{-4} in the dynamic mesh analysis. The convergence criterion for each equation was set based on the evaluation of the computational time and results convergence. The results showed that in general, lowering the given convergence criterion by an order of magnitude from the set values, increased the computational time by a factor of four per time step, but did not cause any significant changes in the results.

2.3 Mesh and time dependency tests

For the present numerical problem, grid and time step dependency tests were performed to find the most suitable grid size and time step value at which the numerical results are considered independent of the grid size and time step value. The geometry in Figure 2.5 was used for this purpose. In the mesh dependency test, this geometry was meshed with four different grid sizes. All meshes were of the same type i.e. quad mesh. A summary of different grid sizes used in the test and the corresponding number of elements is presented in Table 2.2. The mesh dependency test was performed first and the optimal grid size obtained from this test was used for the time step dependency test. Four different time step sizes were considered for the time step dependency test, which are listed in Table 2.3. Water was used as the working fluid for both mesh and time-step dependency tests. The problem was initialized at saturation temperature of water (T=373.15 K) assuming zero volume fraction of water vapor.

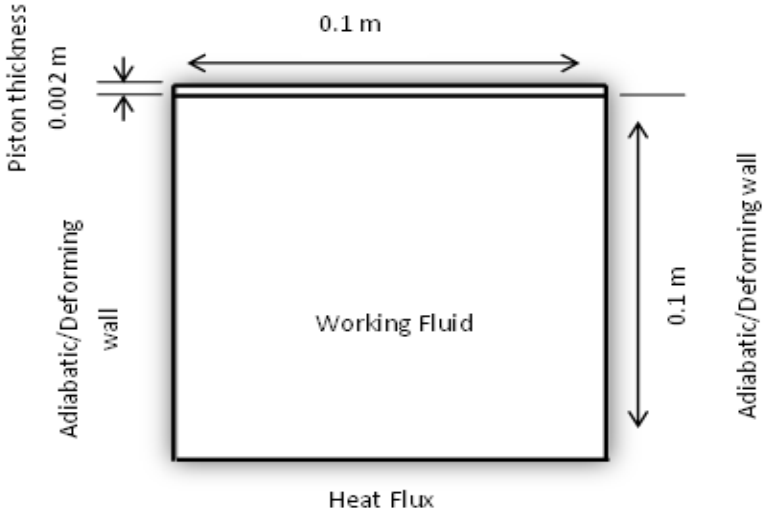

Figure 2.5 Geometry used for mesh and time dependency tests and for model validation

2.3.1 Mesh dependency test

In this test, the dependency criterion was based on the output values of the following parameters: volume fraction of vapor, mass fraction of vapor and piston position. As the problem under consideration is transient in nature, the results are monitored at different times which are, 5, 20 and 40 seconds after the beginning of the process. The mesh dependency test

results for the three parameters are presented in Figures 2.6, 2.7 and 2.8, respectively. In these plots, the parameters do not show a strong dependency on the mesh size in general. It is found that the values between grids 3 and 4 changed by less than 0.5% while between grids 2 and 3 the change in the parameter values ranged from 2% to 5%. One important factor to consider is computational time. It was noticed that as the initial element count doubled the computational time increases up to three times. For instance, it took 3 days to simulate the phase change process coupled with the piston movement using grid 3 while around 10 days to simulate 40 seconds of the two processes using grid 4.

Table 2.2 Grid sizes used in the mesh dependency test

Grid name	Quad element size in (mm)	Initial Element count
Grid-1	2	2500
Grid-2	1.4	4900
Grid-3	1	9900
Grid-4	0.75	17,955

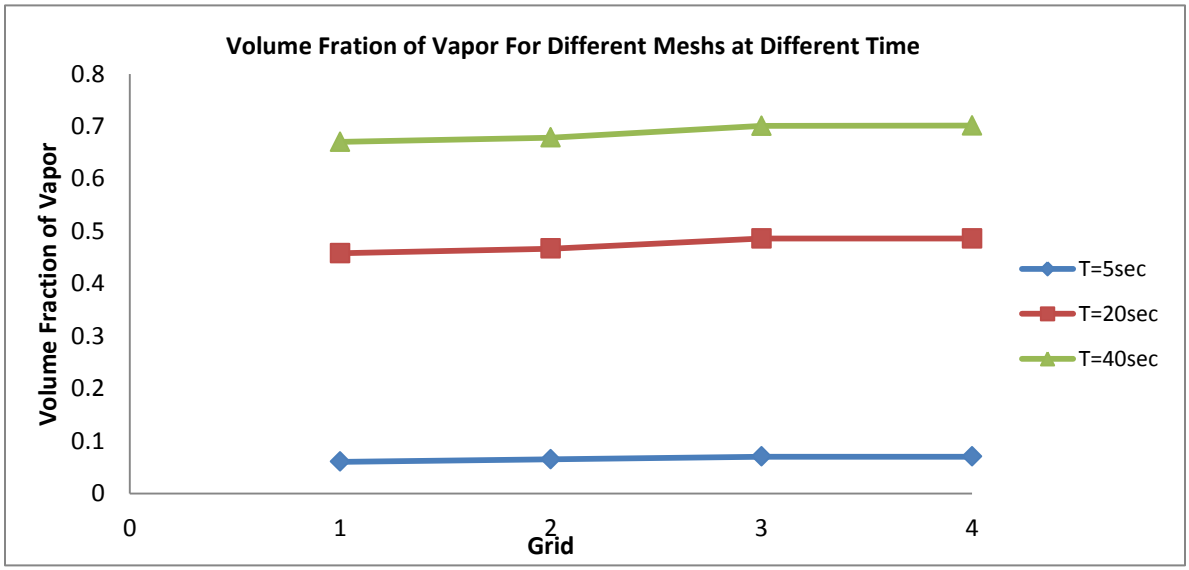

Figure 2.6 Volume fraction of vapor for different grid sizes at different time

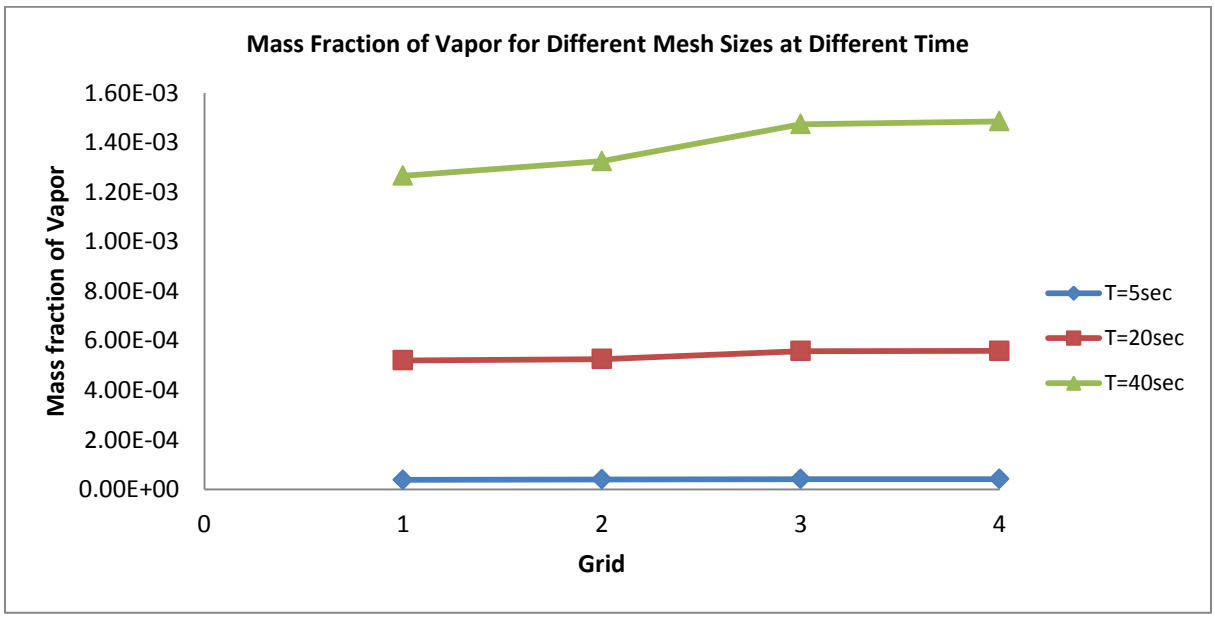

Figure 2.7 Mass fraction of vapor for different grid sizes at different time

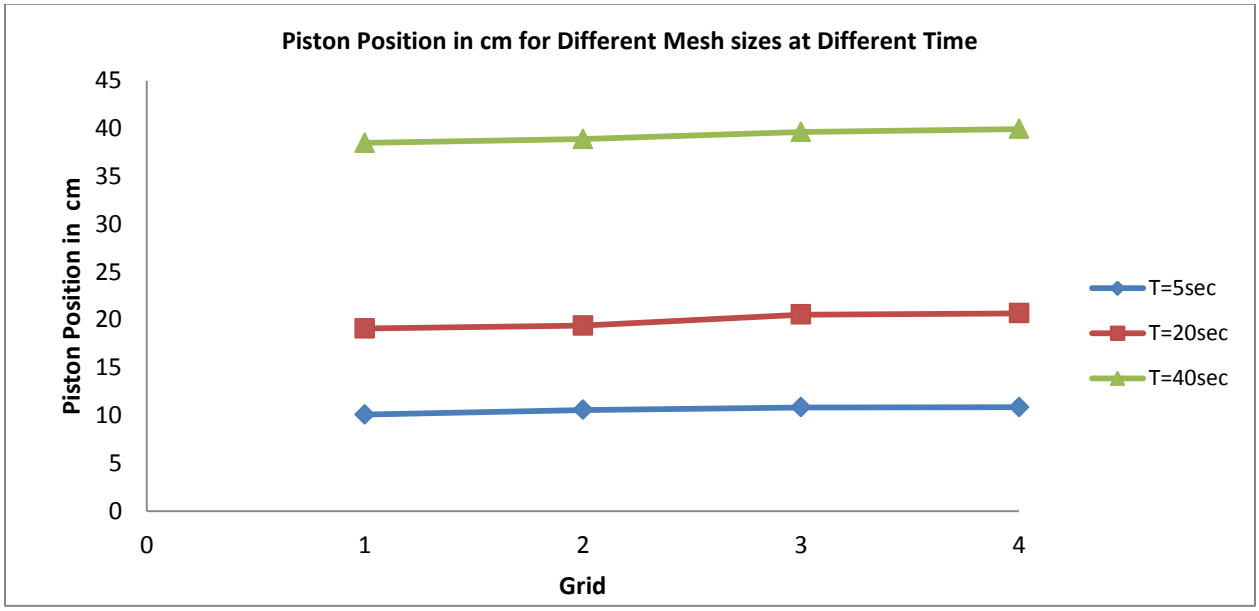

Figure 2.8 Piston position in cm for different grid sizes at different time

2.3.1 Time dependency test

Four time-step values were considered for the time-step dependency test. These values are summarized in Table 2.3. As mentioned above, the selected grid-3 was used for this test. The results obtained from the test for the three different parameters of interest are plotted in

Figures 2.9, 2.10 and 2.11 at time intervals of 5 seconds, 20 seconds and 40 seconds. A gradual convergence was noticed for all parameters as the time step size decreased. The difference in the parameter values between case 3 (time step 0.0025 sec) and case 4 (time step 0.001 sec) is on average, less than 1% while, this difference is above 4% between case 3 and case 2 (time step 0.005 sec). Reducing the time-step size to less than 0.0025 seconds does not significantly improve the results; however, it significantly increases the computational time. Therefore, the time step of 0.0025 seconds was selected to simulate the proposed process.

Table 2.3 Time step values used in for the time-step dependency test

Grid name	Time step value in seconds
Case-1	0.01
Case-2	0.005
Case-3	0.0025
Case-4	0.001

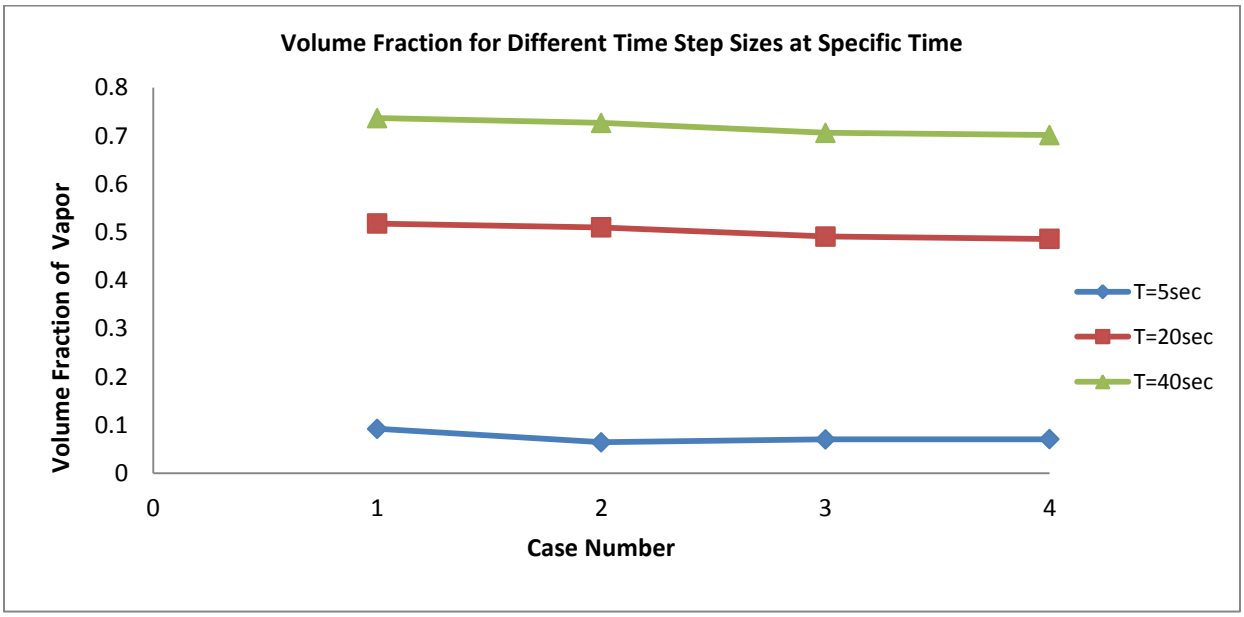

Figure 2.9 Volume fraction of vapor at different time step values

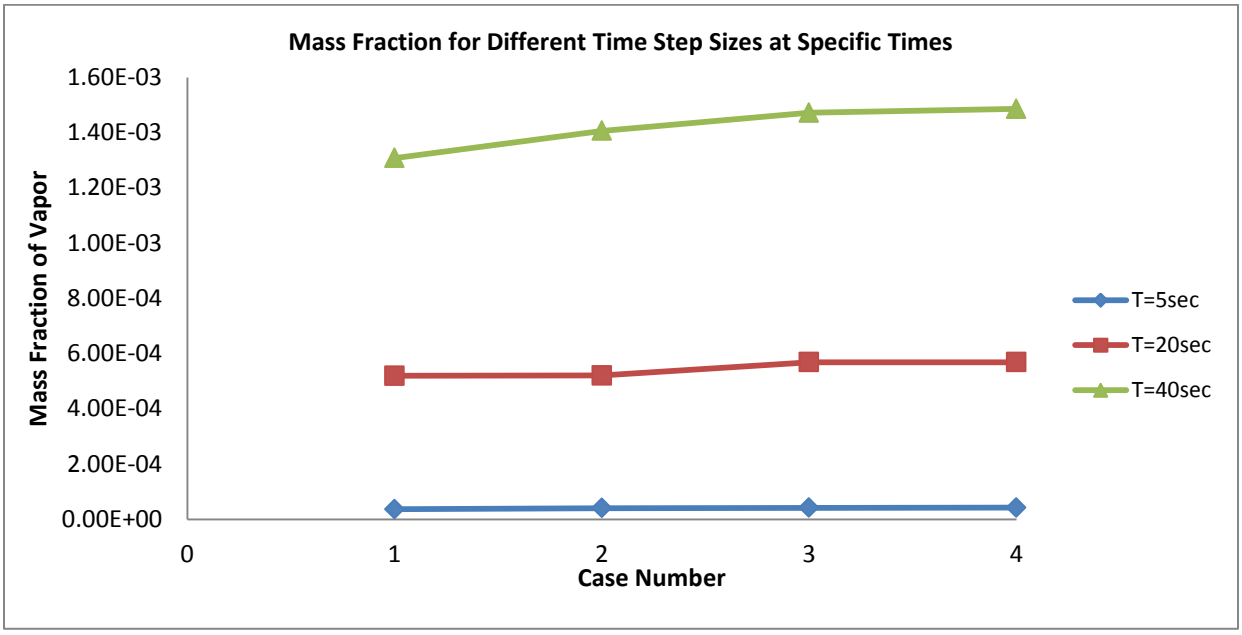

Figure 2.10 Volume fraction of vapor at different time step values

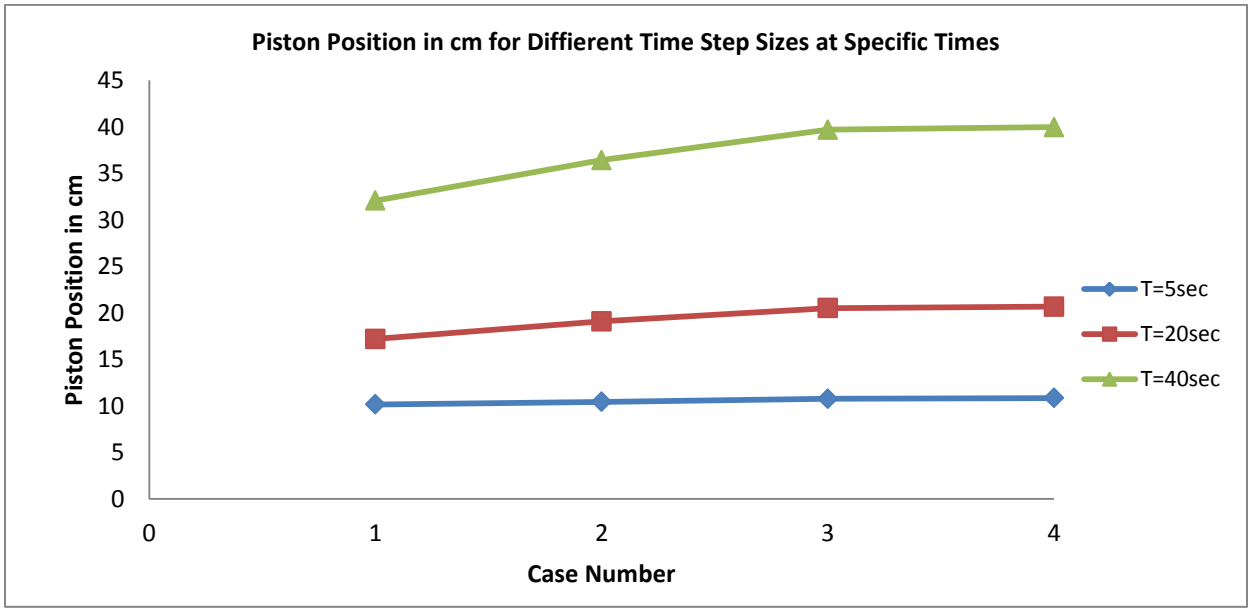

Figure 2.11 Volume fraction of vapor at different time step values

2.4 Model validation

As discussed earlier, the numerical model used in the present study involves the coupled simulation of the phase-change process and the moving boundary. This unique coupled

problem has not been reported in the literature and hence no experimental fluid dynamical data is available for the model validation. However, the fundamental isobaric phase change process, which is under consideration, can be solved analytically for a simple geometry and this theoretical solution can be used for model validation. Thus, this approach is used for the validation of the present model. A simple geometry involving the linear movement of piston is considered as shown in Figure 2.5.

The theoretical analysis considered the domain filled with a mixture of liquid and vapor with an initial vapor volume fraction of 0.98 at the atmospheric pressure [Cengel and Boles 2008]. A constant heat flux of 10,000 W/m^2 was applied for 40 seconds. This heat flux falls in a reasonable range for phase change problems. Using the conservation of energy equation, the parameters of interest at different times were calculated. These parameters are the volume fraction of vapor, mass fraction of vapor and piston position in cm (see Appendix A for the complete analytical solution).

2.4.1 Problem setup and numerical results

For model validation, the mesh of grid-3 obtained from the mesh dependency and a time-step size of 0.0025 seconds from the time-step dependency test were used. The maximum iterations per time step were increased to 300 to allow the solution to converge at every time step. The solution ran for 40 seconds. A heat flux of 10,000 W/m^2 was applied at the bottom wall of the domain. All other walls were specified to be adiabatic and were defined as deforming walls in the dynamic mesh solver.

Initially, water was used as the working fluid and its thermo-physical properties presented in Table 2.1 were imported into Fluent. In this run, the solution was initialized at water saturation temperature (337.15K) and a volume fraction of vapor of 0.98. The value of the boiling coefficient (see Equation 2.11) was kept 0.1 (default value). The simulation results for the volume fraction of vapor, mass fraction of vapor and piston position are shown in Figures 2.12, 2.13 and 2.14, respectively, along with the theoretical values for comparison. The results show an acceptable agreement in the trend but the percentage error was high when compared to the theoretical values. The largest errors are observed for the mass fraction, while the lowest errors

are observed for the volume fraction. For instance, the range of error for volume fraction of vapor was 0.016% to 0.4% while for mass fraction it reached 7.4% to 24.3 % and for the piston position, the error varied from 2.7 % to 21% (see Table 2.4). Plausible sources of these errors could be the lack of information about bubble diameter and the accommodation coefficient that appeared in Equation 2.13. However, as per the guidelines in the Fluent user manual, the error margin between the numerical and theoretical results can be reduced by tuning the value of the boiling coefficient. The percentage error range between the computational and theoretical results for different values of the boiling coefficient is also presented in Table 2.4. As the results show, the percentage error decreased with an increase in the boiling coefficient and hence a higher value of the boiling coefficient could be selected to minimize the error. Note that these error ranges are based on water as the working fluid. Since in the present study different working fluids will be simulated in order to choose the working fluid with the best performance, it was decided to continue validating this problem by using another working fluid i.e. methanol. This will not only confirm the validation process but also help in finding a robust value of the boiling coefficient that can be used for different working fluids.

Similar to water, a theoretical solution was obtained for isobaric expansion and a numerical problem was setup using methanol as the working fluid. The comparisons of numerical and theoretical results are presented in Figures 2.15, 2.16 and 2.17, and the range of errors for methanol simulations is summarized in Table 2.4. The trends are similar to that observed for water, i.e. the error range decreased with an increase in the boiling coefficient. It was observed that an increase in the boiling coefficient above unity causes the solution to diverge for both water and methanol. Although the boiling coefficient of unity provides the lowest error range, but is susceptible to the solution divergence. Hence, the boiling coefficient value of 0.75 was considered for the subsequent simulations, which reduced the average percentage error between the theoretical and numerical results to 0.15%, 12% and 6.5% for volume fraction, mass fraction and piston position, respectively. This percentage error is in an acceptable range thus, confirming the validation of the numerical model.

Table 2.4 Error ranges at different values of the boiling coefficient

		Percentage Error Range		
Material	**Coefficient**	**Volume fraction of vapor**	**Mass fraction of vapor**	**Piston Position**
Water	0.1	0.016 - 0.4	8 - 24.3	3 - 21.5
	0.25	-0.0061 - 0.22	0.5 - 12.6	-6 - 10
	0.5	-0.014 - 0.16	-2 - 10	-5.5 -7.3
	0.75	-0.02 - 0.12	-5.3 - 8	-7 - 5.4
	1	-0.025 - 0.09	-4.5 - 7	-9 - 4
Methanol	0.1	0.1 - 0.45	19 - 30.1	13 - 24
	0.25	0.02 - 0.22	12 - 17	5 - 11
	0.5	0.03 - 0.2	10.7 - 14.5	3 – 9
	0.75	0.02 - 0.15	9 - 12	2 - 6.5
	1	-0.015 - 0.1	7 - 11	-0.22 - 5

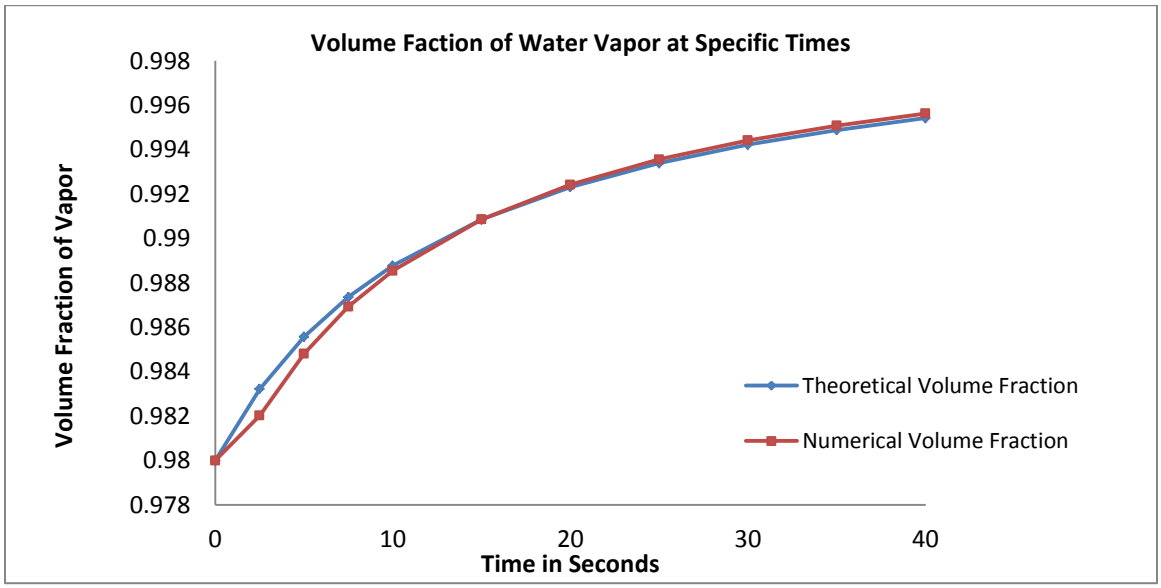

Figure 2.12 Volume fraction of water obtained from numerical and theoretical solutions

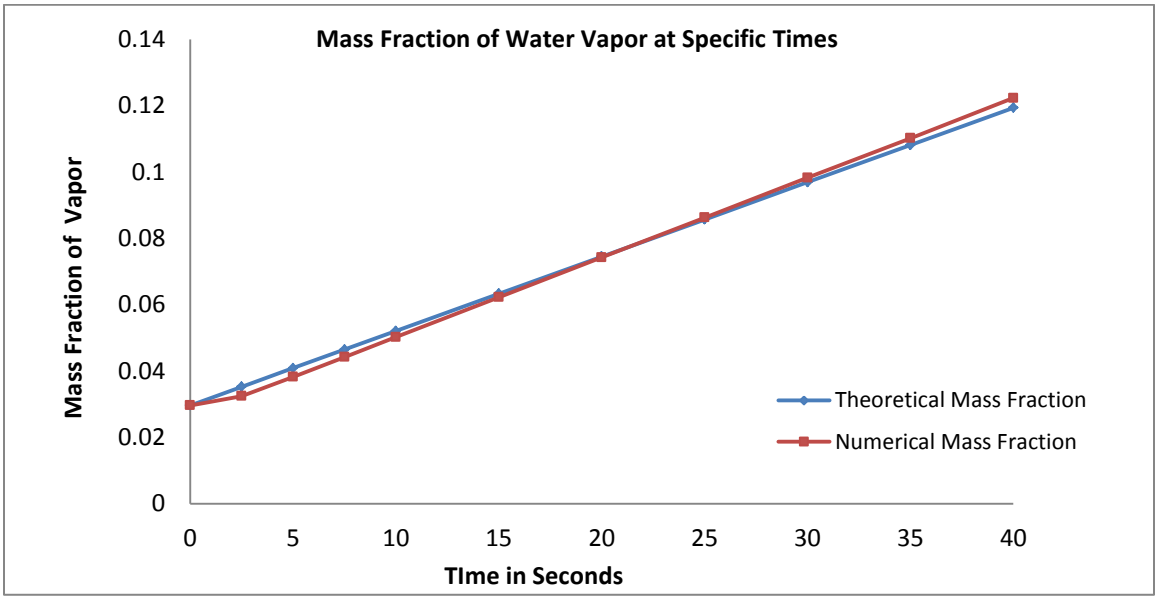

Figure 2.13 Mass fraction of water obtained from numerical and theoretical solutions

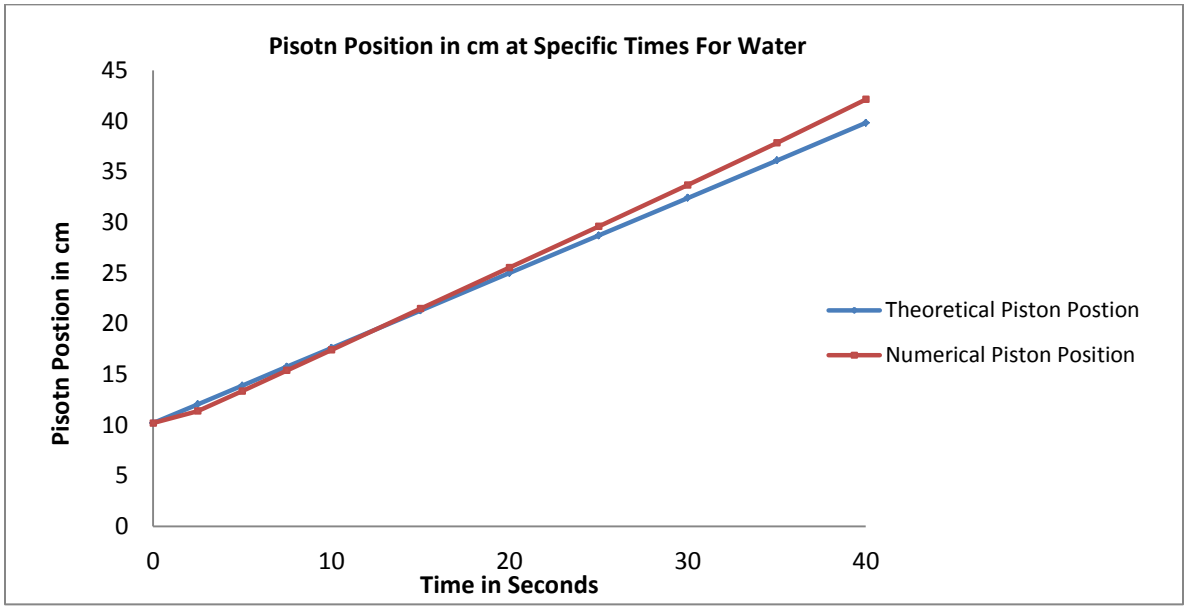

Figure 2.14 Piston position in cm obtained from numerical and theoretical solutions using water as the working fluid

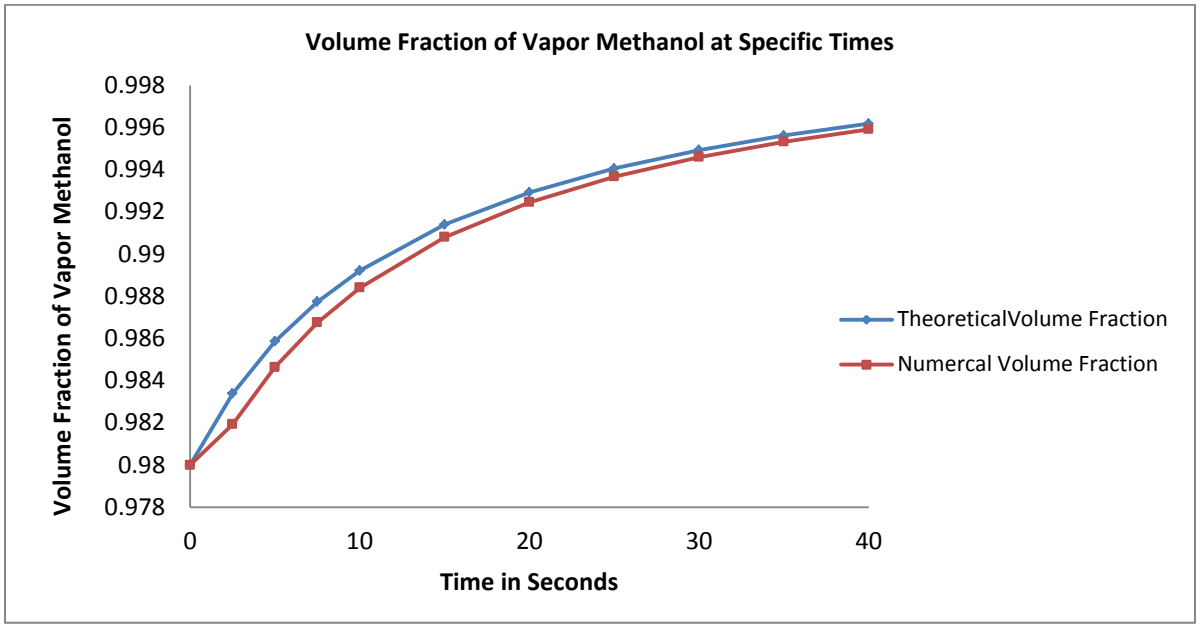

Figure 2.15 Volume fraction of methanol obtained from numerical and theoretical solutions

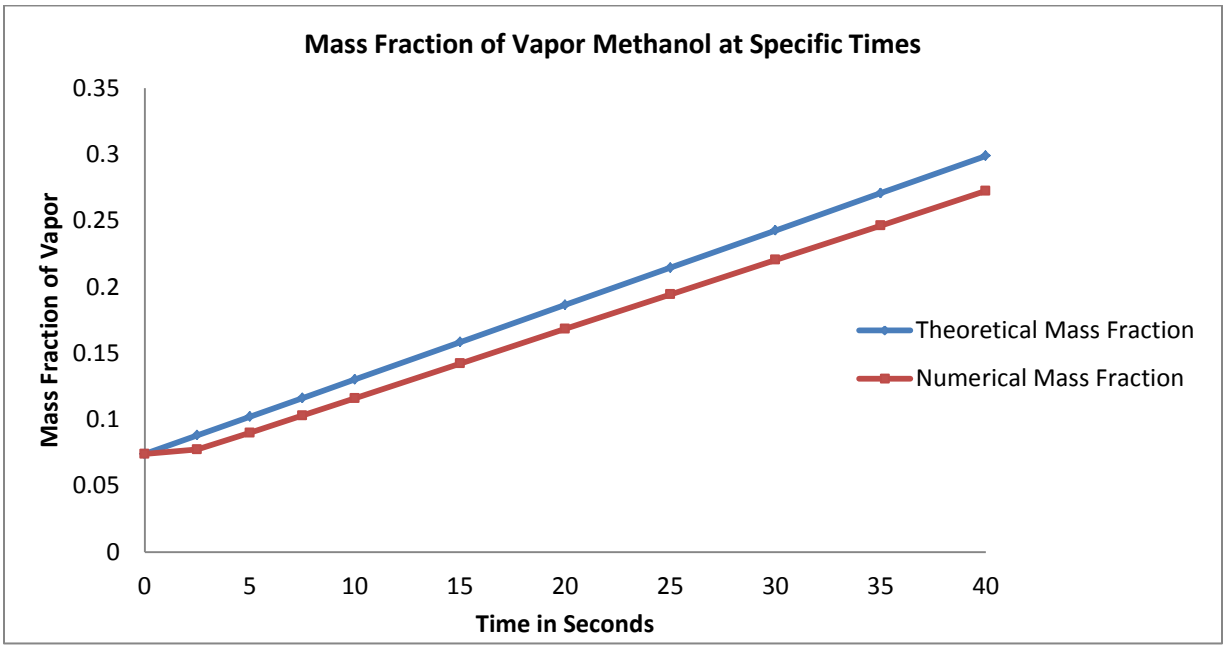

Figure 2.16 Mass fraction of methanol obtained from numerical and theoretical solutions

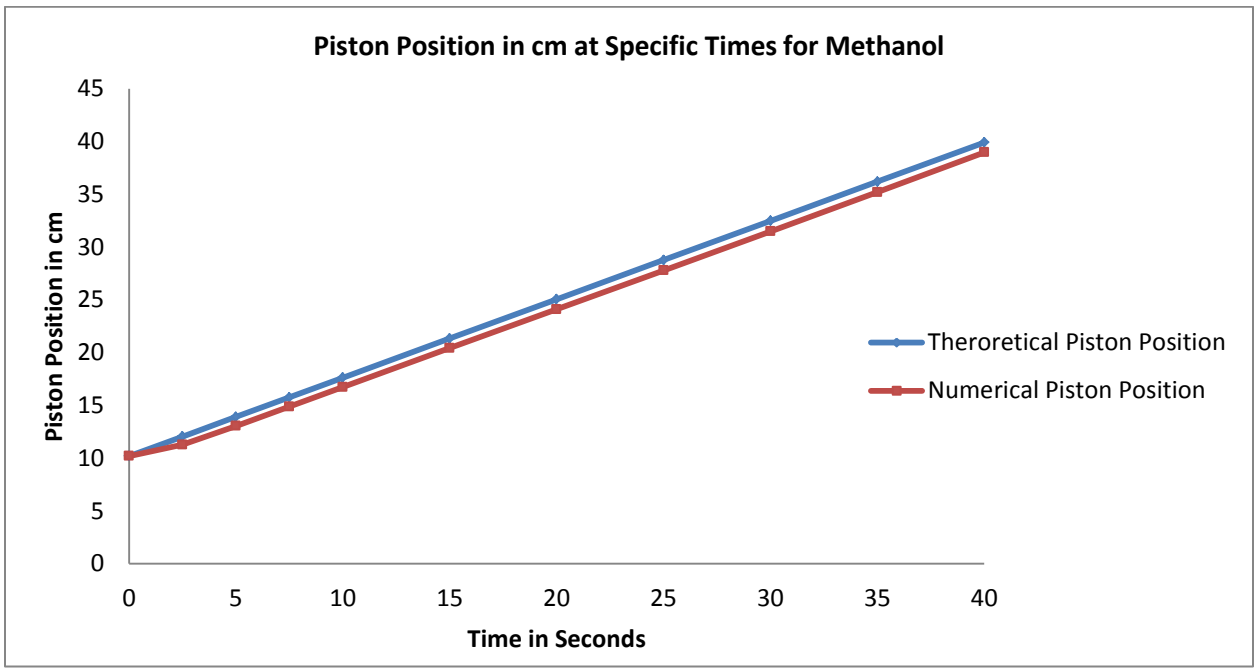

Figure 2.17 Piston position in cm obtained from numerical and theoretical solution using methanol as a working fluid

2.5 Modeling the complete process

Following the validation of the isobaric expansion model presented earlier in this chapter, efforts were made to model the complete process found in the Dyverga system, that is, the simultaneous simulation of the evaporation and condensation processes in the two vessels connected by the moving medium (piston). At first a simplified model as in Figure 2.18a was built and meshed using ANSYS 13 Design Modular and Mesh Utility software. The meshed geometry was imported into Fluent 13 and the problem setup as explained earlier in this chapter was used for this problem. A positive heat flux of 10,000 W/m^2 was applied at the bottom surface of the domain where boiling will occur; while on the top surface of the domain, a negative heat flux of 10,000 W/m^2 (i.e. heat rejection) was applied where condensation will occur (see Figure 2.18b). The entire domain was initialized at atmospheric pressure and saturation temperature of water 373.15 K. To define the upper domain as vapor the patching option was used and in the upper domain cell zone, the volume fraction of vapor was set equal to one. Figure 2.18b shows the volume fraction of vapor in the domain. To dictate the piston

movement, a UDF was written in C language to convert the difference in pressure between the condensation and boiling sections to a force which is then used to calculate the piston's velocity (see Appendix B for the UDF). This velocity is then passed to Fluent and piston moves accordingly.

During simulations, following parameters were monitored: the static pressure on both boiling and condensation sides; the volume fraction of vapor on both sides, and the piston position. The variations of these parameters with time are presented in Figure 2.19. At first when examining the variations of volume fraction of vapor in both domains as seen in Figures 2.19a and 2.19c, one can notice that the volume fraction of vapor is decreasing in the upper domain while it was increasing in the lower domain. Thus, the boiling and condensing processes initiated in the lower and upper domains, respectively. In Figure 2.19e it can be seen that the piston slightly responded to the pressure difference in the domain and moved accordingly. However, the piston movement stopped after 1 second of the simulation time.

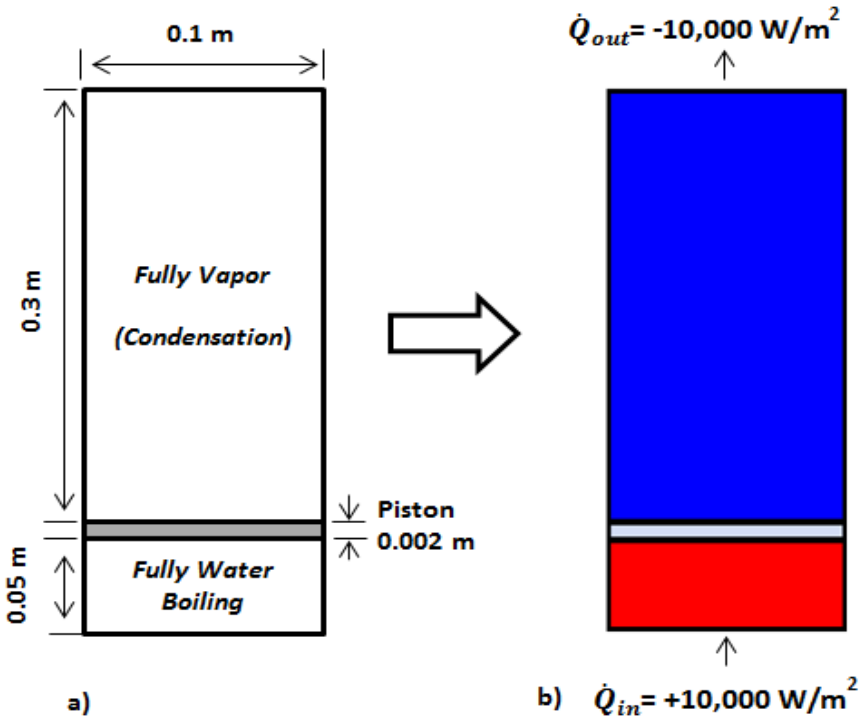

Figure 2.18 Model geometry for simulating boiling process and condensation process in the lower and upper chambers of the domain, separated by a moving piston

In Figure 2.19b, the variation of pressure in the condensation chamber seems to increase throughout the simulation time despite the negative heat flux applied at the top boundary. This pressure has reached 90 kPa after 5 seconds. Similarly, in Figure 2.19d, the pressure in the boiling chamber increased throughout the simulation time reaching 120 kPa. Although there is a pressure difference between the condensing and boiling domains, the piston did not move. When the piston is not moving it is expected that the pressure will build up on the boiling domain and decrease on the condensation domain. However, the pressure was not decreasing in the condensation domain. Other attempts were initiated with expectations to solve this problem. At first the piston was restricted from movement, results of this attempt still showed unreasonable behavior in the pressure on the condensing domain. In this attempt it was noticed that when the condensing domain was initialized at a higher pressure, the pressure in the domain increased to unrealistic values during the simulation. Whereas, when it was initialized at the atmospheric pressure, pressure inside the domain decreased to unrealistic negative values.

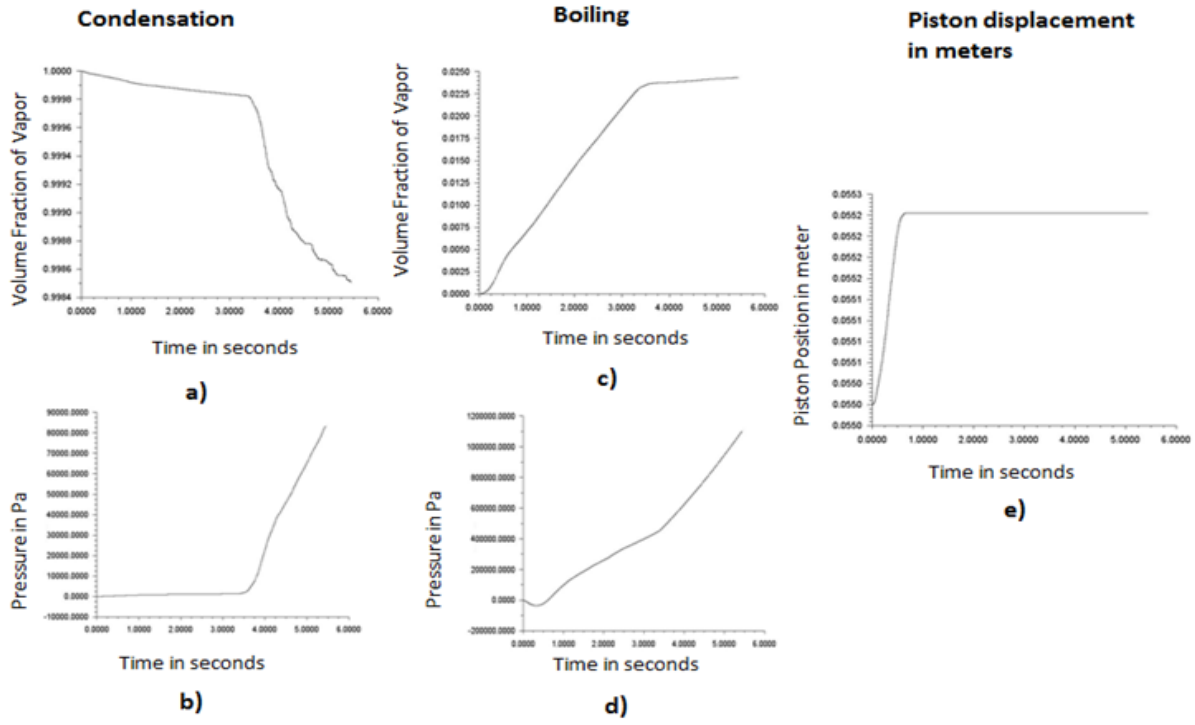

Figure 2.19 Variation of pressure, volume fraction and piston movement as a function of time for the domain in Figure 2.18

To solve this issue Simutech a consultant company in CFD modeling which represents ANSYS technical support in Canada was contacted. After a series of emails, Simutech suggested different approaches to solve this problem. For instance, Simutech suggested defining a mixture of water and water-vapor in the boiling and condensing domains, and speculated that this should stabilize the solution and the results may fall into realistic values. Unfortunately, unrealistic trends in the parameters continued to appear when using this method and other approaches suggested by Simutech, however, no solution was found to resolve this issue.

To ensure that the problem was set up correctly, it was decided to perform three different simulations on the same model. In the first simulation, the condensing domain was defined as a solid zone and boiling was simulated in the bottom domain with the piston movement. Simulation ran smoothly without any non-realistic behavior. Similarly, in the second simulation condensation was simulated in the domain with the piston movement and the boiling domain was defined as solid. Results showed that condensation had occurred in this simulation without any non-realistic behaviors in any of the parameters. In the last simulations, the piston movement was restricted and only boiling and condensation were simulated. The nonrealistic behavior in pressure in the condensing and boiling side had appeared again in this trial. This exercise clearly showed that problems arise when boiling and condensation processes are simulated simultaneously and that there are no issues when a phase change process (boiling or condensation) is coupled with moving boundary. Thus, it was concluded that simulating both boiling and condensation processes simultaneously is beyond Fluent's capabilities and it was decided to simplify the proposed model which can be simulated by Fluent.

2.6 Model Simplification

As mentioned above, due to the limitations of the Fluent software, it was not possible to simulate both boiling and condensation processes that occur simultaneously in the system. Thus, the only possible option was to simulate one process at a time. As the objective of this research is to investigate the fundamental process, it was decided to simulate one process only (i.e. boiling) in the lower vessel and the associated heat exchanger, and to conduct a detailed parametric study to investigate the phase change process in the heat exchanger and its design

improvement during the boiling process. The reason for choosing the boiling process is that it is the process that is responsible for the primary movement of the piston. A similar behavior is expected during the condensation process. Note that the model to simulate the isobaric expansion process during boiling phase has already been validated against theoretical results as shown earlier in this chapter. It is important to emphasize here that the modeling of this so-called simplified model itself is a challenging task due to the integration of the phase change process with the piston movement.

CHAPTER 3: PARAMETRIC STUDY

3.1 Parametric Study

The performance of Dyverga's system is highly dependent on the work done by the volatile working fluid in the lower vessel to push the working mass upward and the response time of the working fluid in the heat exchanger coil to change the phase when subjected to heating. The type of the volatile working fluid and its transient response to the heat, play an important role in regard as well as the design of the heat exchanger coil. This parametric study will focus on the selection of the proper working fluid as well as on the design of the heat exchanger coil to increase the response time as well as the work done on the piston i.e. the performance of the system.

As seen in the model validation section in Chapter 2, the fundamental thermodynamic analysis could provide information about the piston movement and the average mass and volume fractions of the working fluid inside the entire computational domain but it does not provide any information about the detailed phase change process within the computational domain. For example, the thermodynamic analysis could not provide any information about the flow patterns, local mass and volume fractions, boiling regime, etc. This information is very crucial in understanding the behavior of the working fluid and vital for the design improvement of the heat exchanger coil. For example, to improve the design of the heat exchanger coil, the phase change process inside the heat exchanger coil, its relation to the heat exchanger coil geometry has to be studied along with the phase change process in the vessel and the work done by the working fluid on the piston. However, the thermodynamic analysis only provides the mass and volume fraction values averaged over the entire domain that includes the vessel and the heat exchanger coil. It is not possible from the fundamental thermodynamic analysis to extract this information for this coupled geometry in the transient manner. This information can be achieved through CFD simulations. Hence, in the present parametric study it was obtained by simulating the given geometry using the developed numerical model.

The parametric study was divided into two parts. Part I is focused on the working fluid, while Part II is focused on the heat exchanger coil. Different cases were considered in each part and in

each case a parameter in the model was varied then results of this variation are presented and investigated to determine its influence on the process. In simulating these cases, it was assumed that the working fluid is in the mixture phase initially. Since the process under consideration is a transient process, i.e. the phase change process in the vessel never reaches the steady-state; the best way to conduct the parametric study and evaluate the performance of the system is through the transient analysis of the system parameters. Thus, all simulations and the corresponding results presented in this chapter are transient-based. The experimental observation from Dyverga's prototype unit indicated that the time-scale of the process is of the order of few seconds. Therefore, the simulations were conducted to capture the process up to 40 sec.

3.1.1 Part I: working Fluid

The current Dyverga prototype uses methanol as a working fluid. This volatile substance was selected as its boiling point is within the suitable range of the heat source used by Dyverga, and it is also readily available. In this section, other volatile substances in this boiling point range were also investigated to find the best working fluid that would improve system performance as well as the boiling patterns and the boiling regime were studied using simulation results. Four different working fluids were considered which were methanol, ethanol, pentane and butane. These materials and there corresponding thermophysical properties are listed in Table 3.1. The domain geometry is shown in Figure 3.1. Heat flux was set to 10,000 W/m^2 (the rationale for using this heat flux value is already mentioned in Chapter 2). Since the densities of the working fluids vary it was decided to consider two cases. In Case I-A, the initial liquid-to-vapor volume ratio of all working fluids was fixed at 0.02, thus the initial total mass varied in the system. While in Case I-B, the initial total mass of all working fluids was fixed at 0.42 kg/m thus, the initial liquid-to-vapor volume ratio for each of the working fluids varied. The initial values of mass and volume of the four working fluids for both cases are listed in Table 3.2.

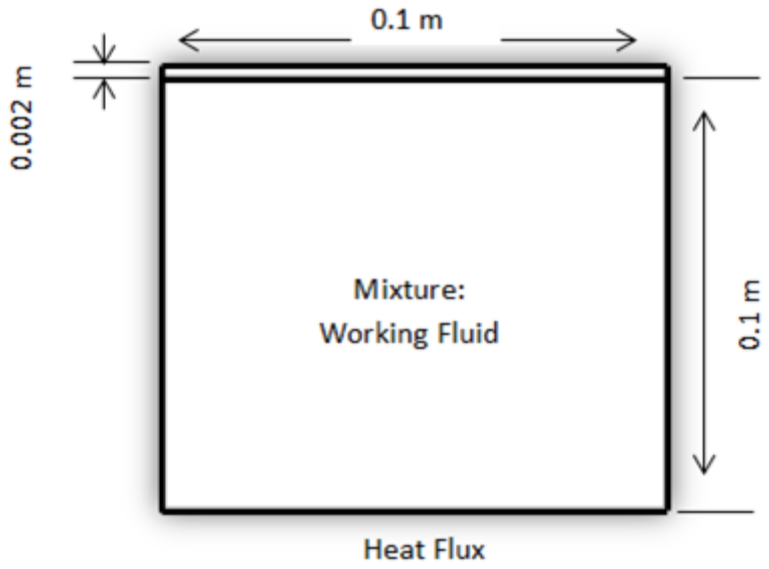

Figure 3.1 Geometry used in Case I

Table 3.1 Thermophysical properties of materials used in this study [Vargaftik 2005]

		T_{sat} at atmospheric pressure (°C)	Density (kg/m^3)	Specific heat (kJ/kg-k)	Thermal Conductivity (W/m-k)	Viscosity (kg/m-s)	Molecular Weight (kg/kg-mol)	Latent heat of vaporization (kJ/kg)	Standard State Enthalpy (kJ/kgmol)	Surface Tension Coefficient (water/vapor) (N/m)
Methanol	**Liquid**	64.7	751.03	2.630	0.202	3.280e-4	32.04	1120	0	0.019
	Gas		Ideal gas	1.618	0.0018	1.110e-05			3.58e4	
Ethanol	**Liquid**	78.3	756.70	3.005	0.169	0.444e-3	46.07	973	0	0.017
	Gas		Ideal gas	1.614	0.020	1.023e-05			4.48e4	
Pentane	**Liquid**	36.07	610.17	2.340	0.112	1.964e-4	72.15	358	0	0.014
	Gas		Ideal gas	1.680	0.015	7.021e-6			2.58e4	
Butane	**Liquid**	0	603	2.340	0.114	2.060e-4	58.12	385	0	0.015
	Gas		Ideal gas	1.670	0.014	7.350e-6			2.23e4	

Table 3.2 Working fluid initial condition for two different cases

Case	Working Fluid	Methanol	Ethanol	Pentane	Butane
I-A	Initial total mass kg/m	0.16	0.17	0.15	0.14
	Liquid-to-vapor volume ratio = 0.02				
I-B	Initial total mass kg/m = 0.42				
	Initial Volume of liquid m^3/m	$5.5x10^{-4}$	$5.2x10^{-4}$	$6.5x10^{-4}$	$6.7x10^{-4}$

Figures 3.2 and 3.3 present the results of Case I-A, where the working fluid has the same initial volume. It can be noticed from these figures that pentane and butane had a similar trends for both parameters. in Figure 3.2 it can be noticed that the rate of evaporation for pentane is slightly higher than that of butane, which resulted in a better quality in the mixture of pentane than that of butane. For instance after 30 seconds, the quality of the mixture was at 65% for pentane while it was 60% for butane. This could be due the lower latent heat of evaporation for pentane (358 kJ/kg) compared to butane (385 kJ/kg). Since the quality of mixture is inversely proportional to the latent heat of evaporation, it is expected to have higher quality at lower latent heat of evaporation (see Equation A.3, Appendix A). Consequently, due to the highest latent heat of evaporation (1120 kJ/kg), methanol has the lowest quality throughout the process, and at 30 seconds it has the quality of 23%. For Butane and Pentane, saturation temperatures are 0^oC and 36^oC, respectively, much lower than that of methanol and ethanol, which are 78.3^oC and $64.7\ ^oC$, respectively. Similarly, the initial liquid densities of pentane and butane are close i.e. 610 and 603 kg/m^3, respectively while methanol and ethanol have higher but closer densities of 751 and 756 kg/m^3, respectively. When densities and saturation temperature are close, the latent heat determines which working fluid will evaporate more.

Therefore, the performance curves formed two distinct groups; one containing pentane and butane and other containing methanol and ethanol.

Although pentane and butane have evaporated at a much higher rate than ethanol and methanol, the piston displacement plotted in Figure 3.3 shows a slight difference in piston displacement. For instance, after 30 seconds, piston was displaced to 36.8 cm for butane and pentane, while the piston displacement was at 33.59 cm with methanol and 30 cm for ethanol. This behavior in displacing the piston could be due to the isobaric phenomenon where the pressure inside the domain is constant throughout the process. The pressure will be equivalent to the pressure caused by the piston's weight on the domain. In this case the gauge pressure was 55 Pa. Since pentane and butane had the higher evaporation rate, pressure builds up in their domains at a much quicker rate than that of methanol and ethanol. This allows the piston to displace earlier for pentane and butane. Now, to explain how the piston position was higher when using methanol though ethanol evaporation was higher one should examine the specific volume of vapor for both working fluids, since it is directly proportional to the volume of the domain (see Equation A.5 in Appendix A). For methanol the specific volume of vapor at its given saturation temperature is 1.79 m^3/kg, 60% higher than that of ethanol. This allowed the domain to expand quicker when using methanol. In Case I-A it is evident that pentane has evaporated the most and has displaced the piston to the highest position.

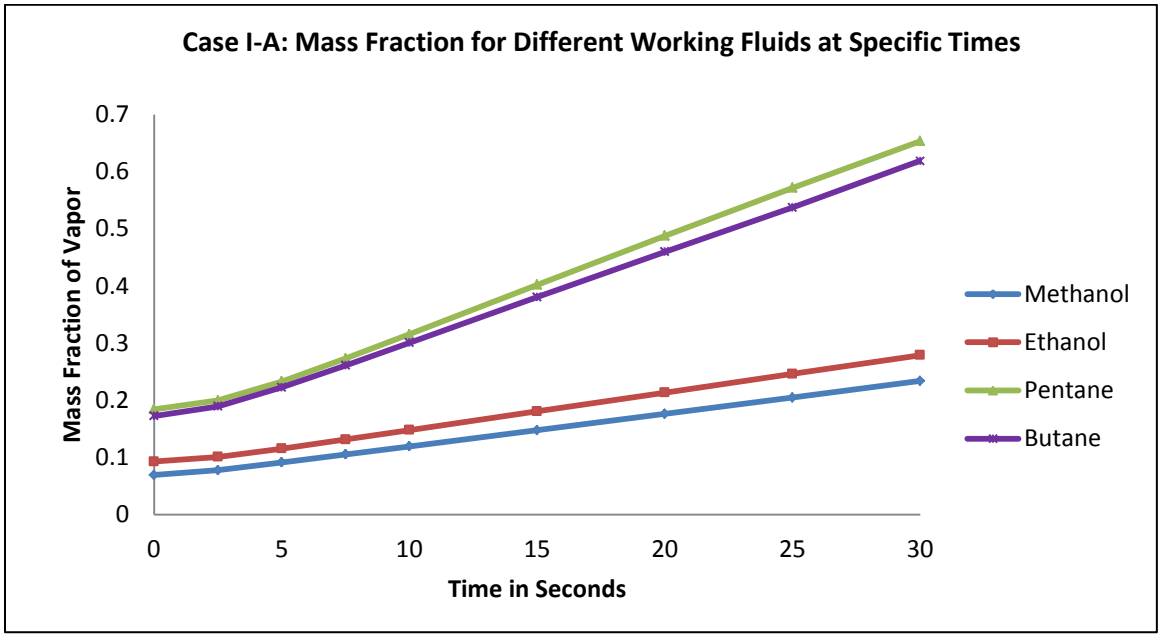

Figure 3.2 Mass fraction of vapor for different working fluid Case-I-A

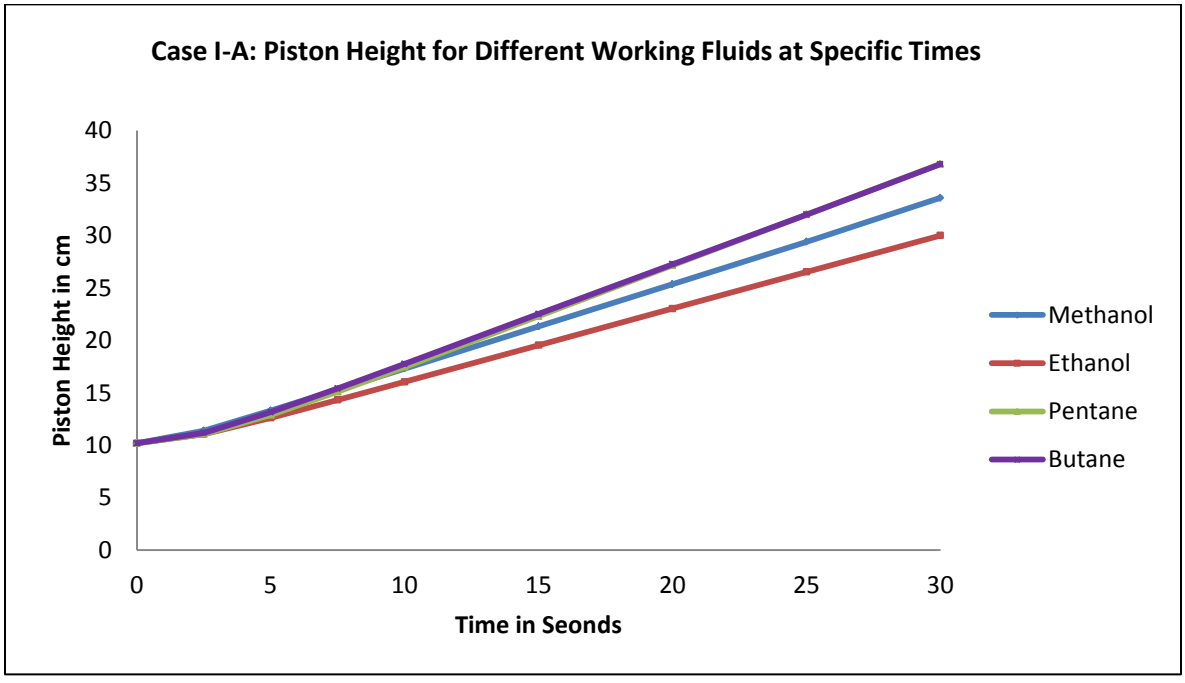

Figure 3.3 Piston position in cm for different working fluid Case-I-A

As mentioned previously, in Case I-B, different working fluids had the equal initial mass, thus the corresponding initial liquid-to-vapor volume ratio for each working fluid was different due

to the difference in densities. Similar to Case I-A, the results for parameters of interest were plotted in Figures 3.4 to 3.6 for different fluids for the first 30 seconds of the process. In Figure 3.4 the volume fraction of vapor for methanol and ethanol was higher initially because of their higher liquid densities. However, after 15 seconds, the volume fraction of vapor for butane and pentane had increased and became closer to that of methanol and ethanol. This can be explained by checking the evaporation rate shown in Figure 3.5. In this figure it is clear that pentane evaporation was the highest among the given working fluids, followed by butane, ethanol and lastly methanol. As for piston position, it was displaced the most for pentane and butane to a distance of 36.7 cm after 30 seconds, while for methanol and ethanol, the piston was displaced by 33.7 cm and 30.1 cm, respectively. Results of this case have shown similar behavior to that of Case I-A.

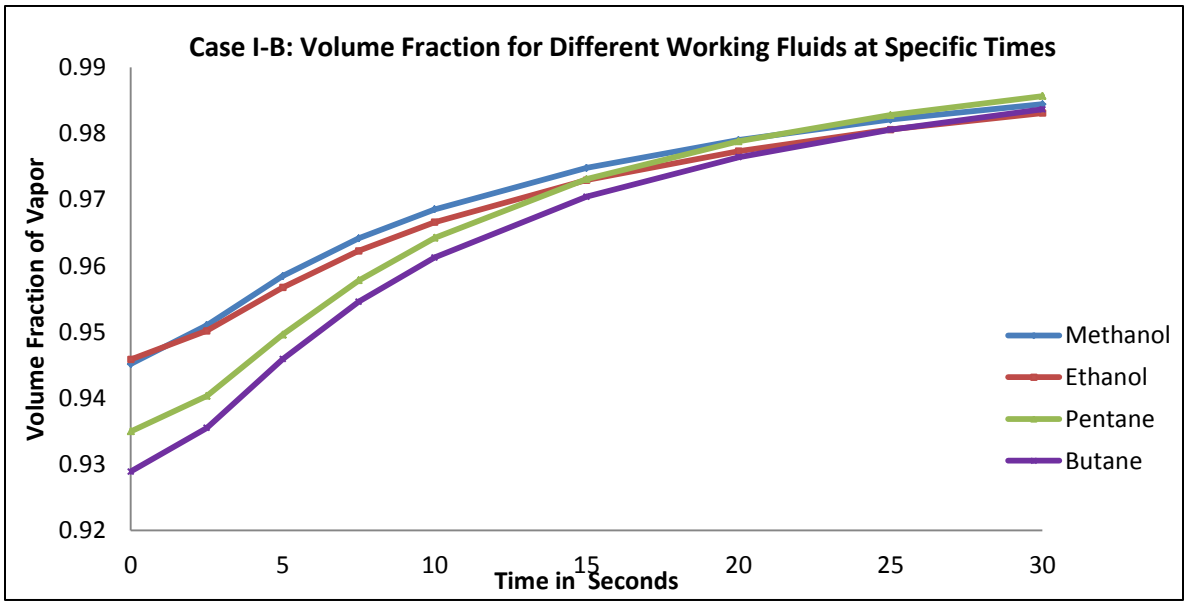

Figure 3.4 Volume fraction of vapor for different working fluid Case I-B

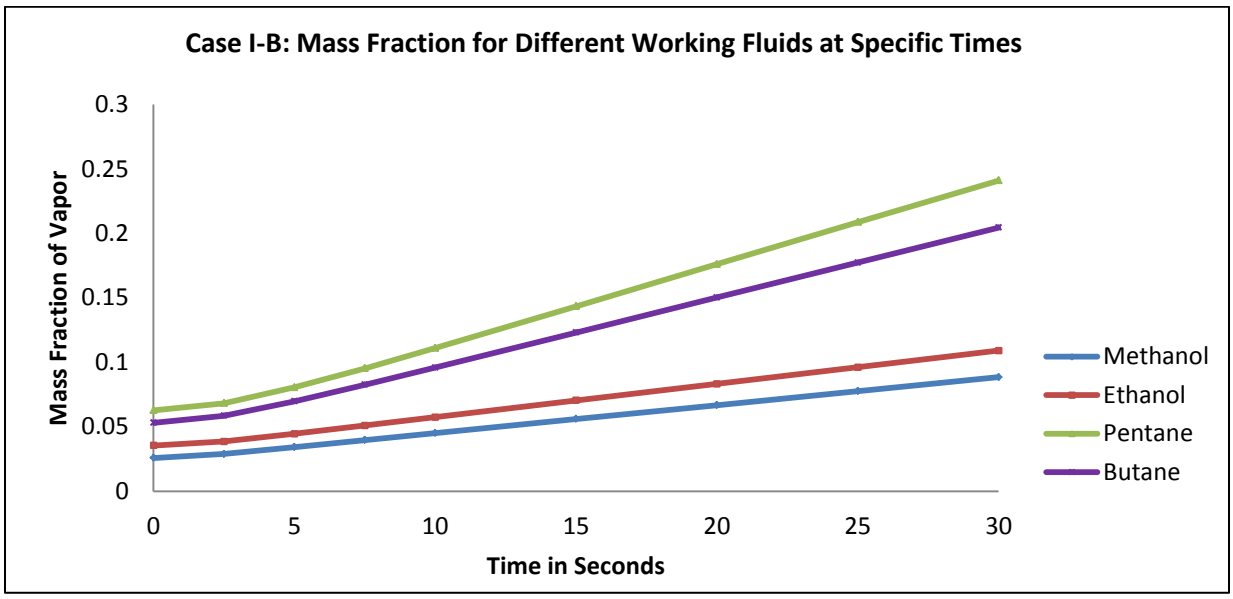

Figure 3.5 Mass fraction of vapor for different working fluid Case I-B

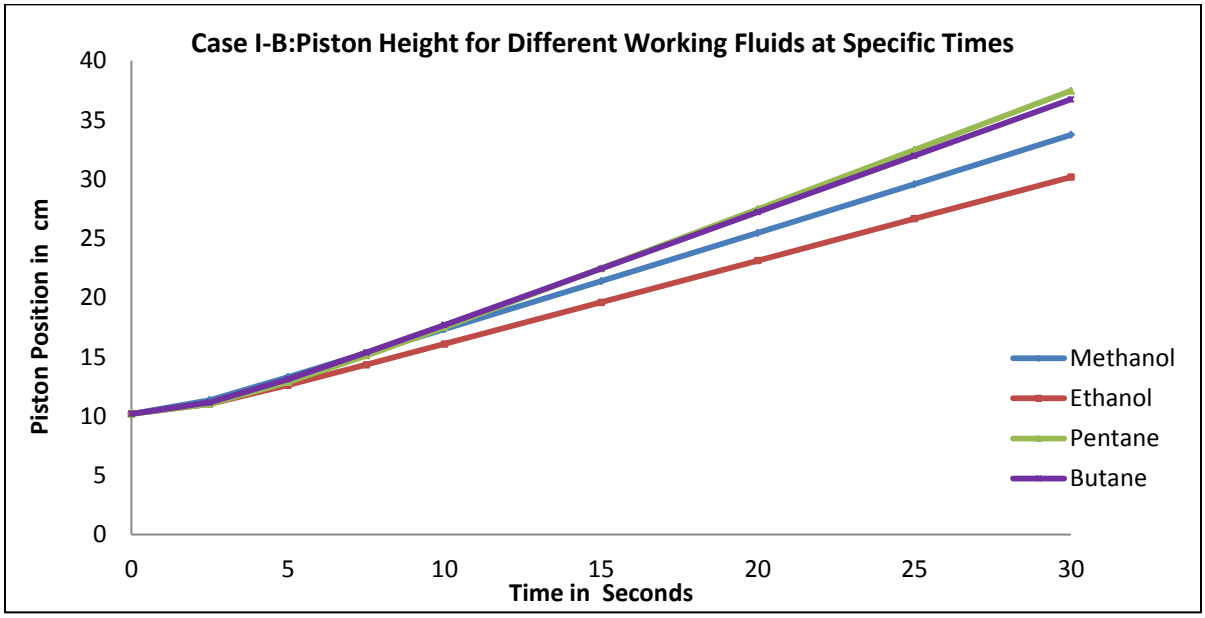

Figure 3.6 Piston position in cm for different working fluid Case I-B

Thus, based on the results from Cases I-A and I-B, it can be concluded that pentane is the best working fluid among the four working fluids considered due to faster evaporation and larger piston work done for the same input heat flux. These features are important in Dyverga's

system and it is expected that if pentane is used, the performance of SmarTorQ will be optimum. Moreover, pentane saturation temperature is lower than that of methanol which is the current working fluid. Thus, when using methanol, temperature of heat source is restricted to be higher than the saturation temperature of methanol which is around 65^{o}C while pentane's saturation temperature is around 36^{o}C, hence the wasted heat temperature can be lower than 65^{o}C. Consequently, lower grade energy can be captured by the system when using a working fluid with a low saturation temperature like pentane.

The simulation results provide data with high spatial and temporal resolution and hence it is used to get a better insight into the phase change process particularly the boiling regime. Conventionally, there are two main boiling regimes nucleated and film boiling. In nucleated boiling bubbles are formed on the heated surface while in film boiling a vapor blanket is formed on the heated surface. In Figure 3.7, contours for the lower section of the domain are shown for pentane at 0.25, 0.5 and 0.75 seconds. The results show that soon after the liquid layer exposed to the heating from the bottom, bubbles started to form within the liquid layer, which indicates that in this range of heat flux, the pentane undergoes nucleate boiling. With an increase in time, the quality of the mixture increased and the adjacent bubbles coalesced and started to grow in size. At 0.75 second the quality of mixture continues to increase and fewer bubbles can be seen. Similar trends are observed for other fluids considered in this study, indicating that these volatile fluids undergo nucleate boiling in this heat flux range.

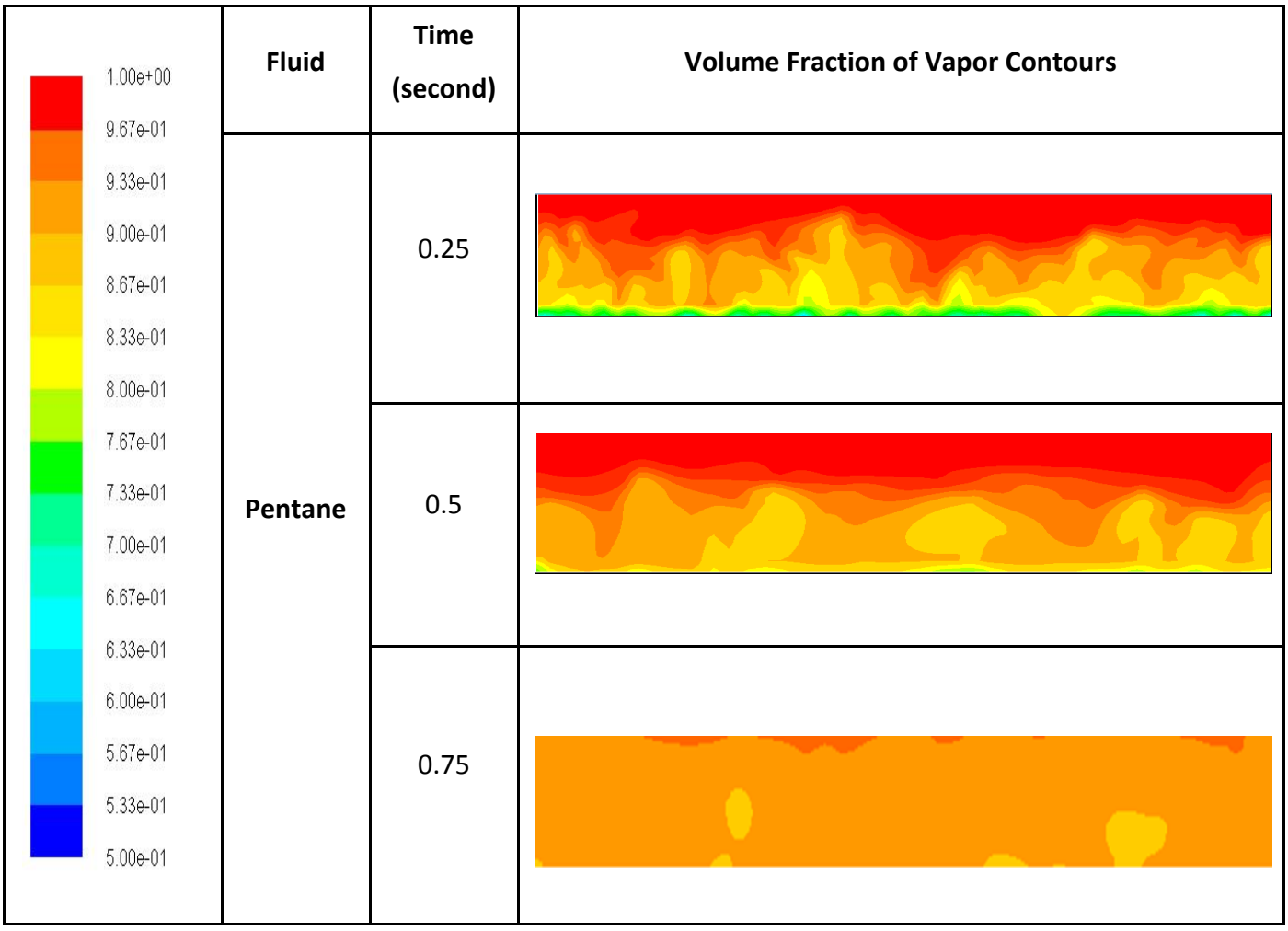

Figure 3.7 Contours of volume fraction of vapor pentane at different times

3.1.2 Part II: Heat exchanger geometry

The heat exchanger used in Dyverga's prototype is made of coils which hold the working fluid and allow heat to be transferred to the working fluid when they are in direct contact with the heat source. As mentioned above in this section of the parametric study, the focus is on investigating the phase change process within the heat exchanger coil and the design improvement of the heat exchanger coil.

3.1.2.1 Case II: U-shaped heat exchanger

Three different geometries with U-shaped tubes were considered, as shown in Figure 3.8. These tubes vary in their hydraulic diameter and the purpose is to resemble the effect of varying the coil's diameter. The lengths of the coils were adjusted to keep the same tube volume. The surface areas of the tubes are 0.13, 0.18, 0.29 m^2/m for Configurations II-A, II-B and II-C, respectively. Based on the results from the preceding section, pentane was considered as the working fluid. Initially, each tube is filled with liquid pentane ($4x10^{-4}$ m^3/m), while the rest of the domain was fully occupied with vapor pentane (same initial liquid-to-vapor volume ratio but unmixed phases), see Figure 3.9. For the purpose of comparison, simulations were also conducted for the reference case of the rectangular geometry (see Figure 3.1), carrying the same liquid-to-vapor volume ratio as of the U-shaped heat exchanger geometries (unmixed phases). A heat flux of 10,000 W/m^2 was applied on the tube wall and 25 seconds of the process was simulated.

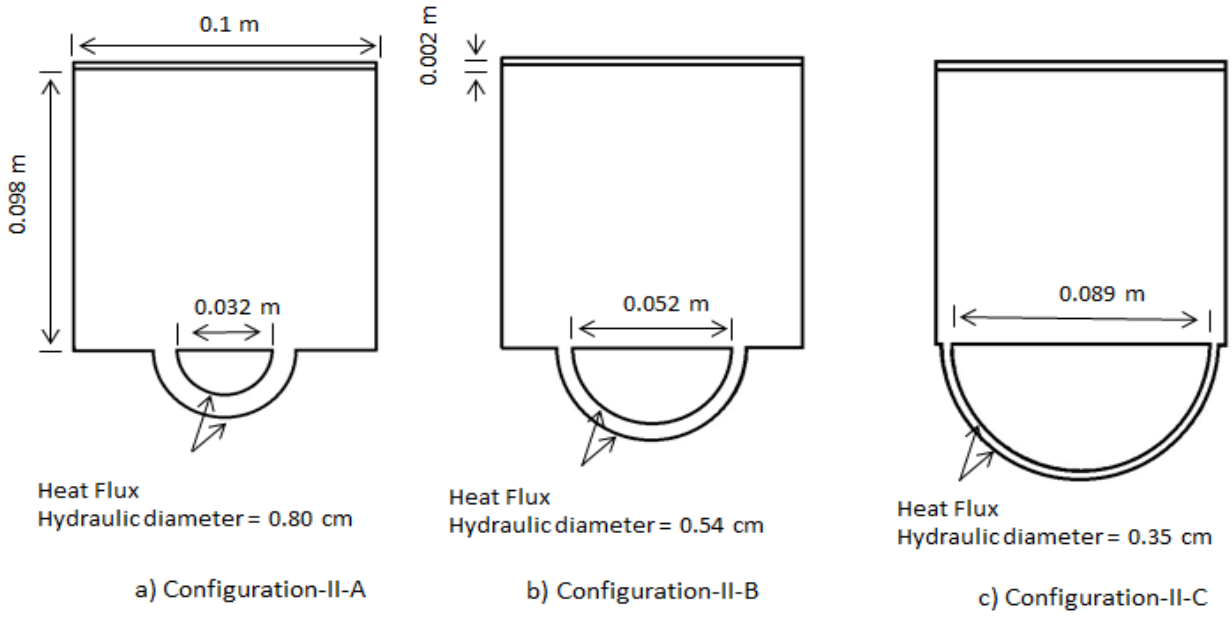

Figure 3.8 U-shape geometries of Case II

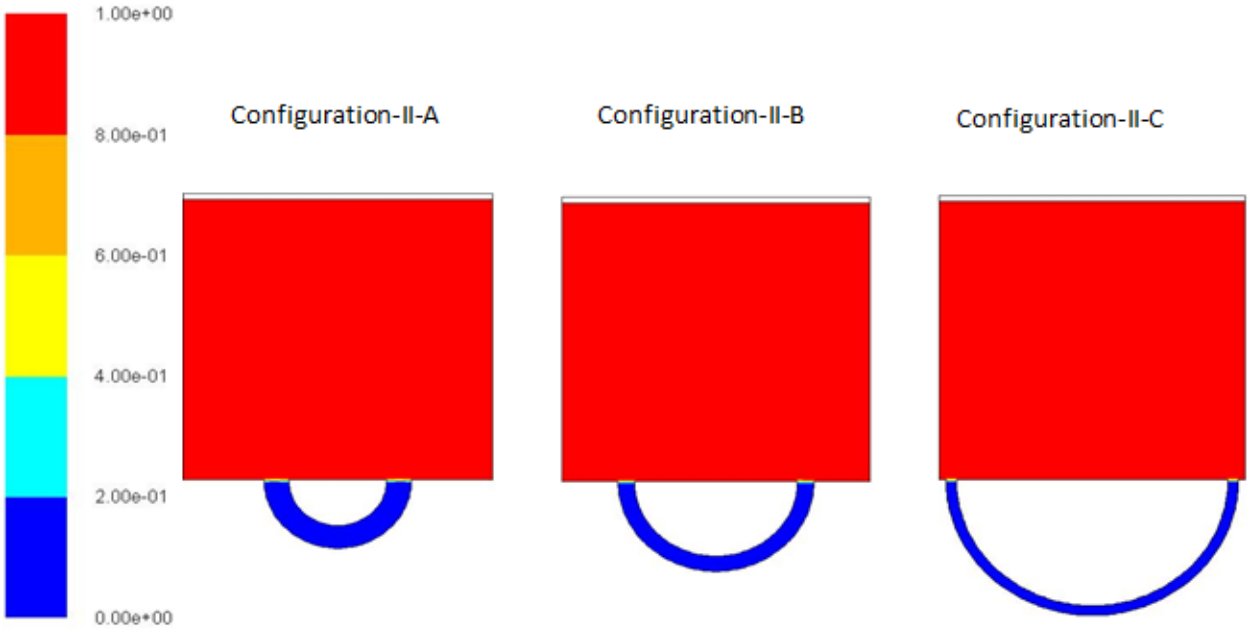

Figure 3.9 Case II: Contours of volume fraction of vapor pentane at t = 0 sec

The contours of the volume fraction of pentane at 0.5, 1, 1.5 and 2 seconds highlighting the phase change process for the different proposed configurations are shown in Figure 3.10. In all three configurations, as the vapors started to form, they ascend due to lower density and the heavier liquid phase was collected at the bottom of the tube. With an increase in time, this liquid phase eventually transformed into the mixture phase however, the mixture formed stably stratified layers within the tube. The comparison of different configurations show that the rate at which the phase change process occurred increased with the surface area of the tube, which is highest for Configuration-II-C, as expected. Note that in these configurations, heat was added only from the tube surface and the vessel surface was insulated. Figure also shows that as the heating process continued, due to the increase in the volume fraction, the mixture started to flow out of the tubes and occupied the bottom section of the vessel by pushing the vapors that occupied this space, upward. A closer look at the tube domain at the initial state of boiling show the presence of bubbles, which indicates that the nucleate boiling regime is present, which is consistent with that observed in the rectangular vessel.

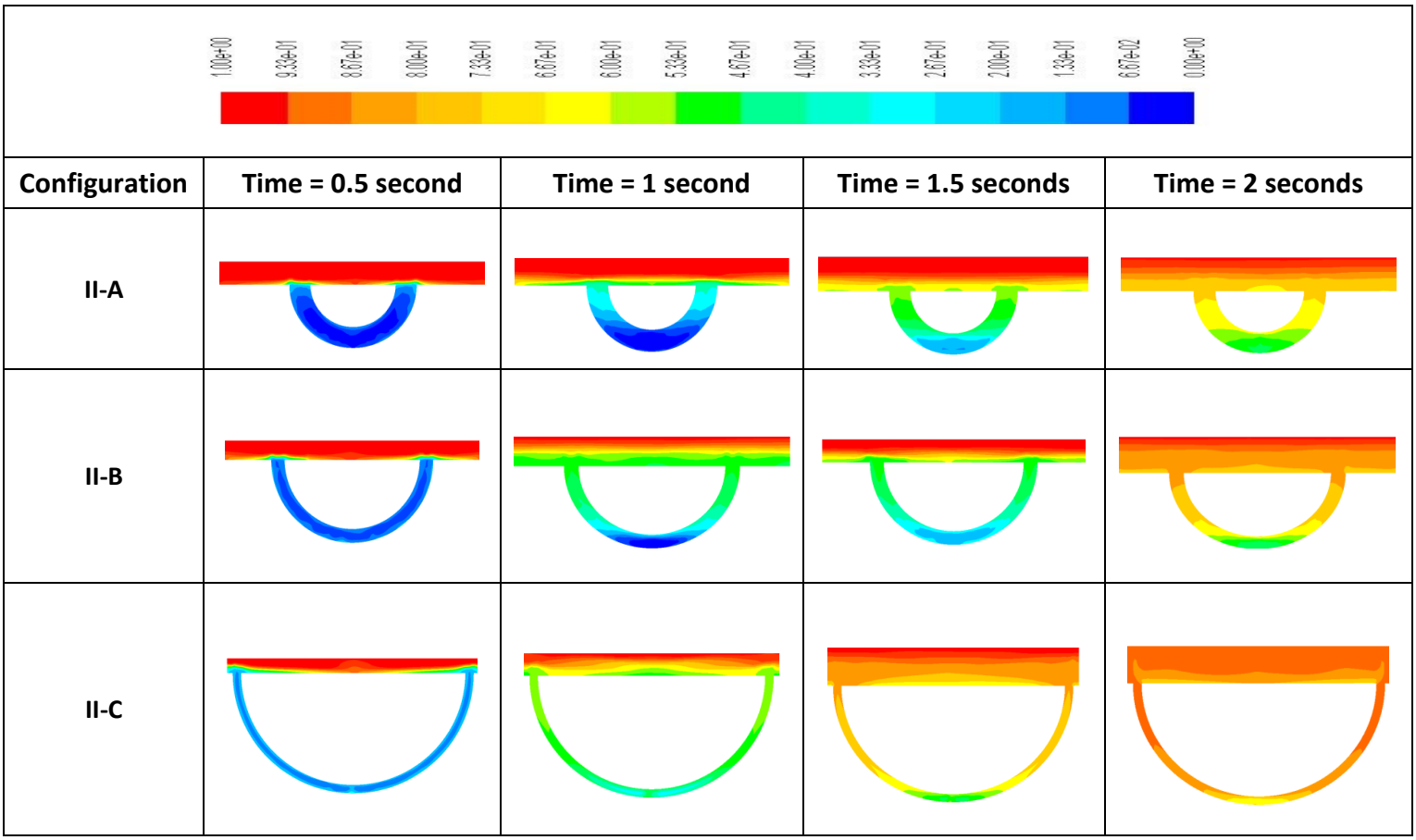

Figure 3.10 Contours of volume fraction pentane for different configuration of Case II

Figure 3.10 only showed the tube region to investigate the phase change process within the tube. However, it is important to see the impact of this phase change process inside the tube, on the overall vessel domain. The contours of the volume fraction of pentane after 5 seconds in the entire flow domain for the three U-shaped configurations are presented in Figure 3.11. The results show that the volume fraction is highest in Configuration-II-C transforming almost the entire liquid in the tube into vapor phase, while the volume fraction decreased with an increase in the tube diameter and a decrease in the surface area. The volume fraction of vapor inside Configuration-II-C, Configuration-II-B and Configuration-II-A tubes at this instant are 0.96, 0.89-0.95 and 0.78-0.89, respectively. In general, the figure also shows a volume fraction of one in the upper section of the domain, indicating that the vapors are gathered in the top section as expected. In this figure it can be seen that the mixture with lowest volume fraction was still

accumulating at the bottom section of the tube for Configuration-II-A as seen before. However, for the other two configurations the mixture with the lowest volume fraction seems to accumulate at the bottom surface of the vessel while the tube contained the mixture with relatively high volume fraction (lower density). Naturally, this should not happen as the heavier fluid always descends due to gravity. The possible cause of the presence of lighter fluid in the tube for Configurations II-B and II-C is their higher pressure which prevents the heavier fluid from above to fall. This will be explained later.

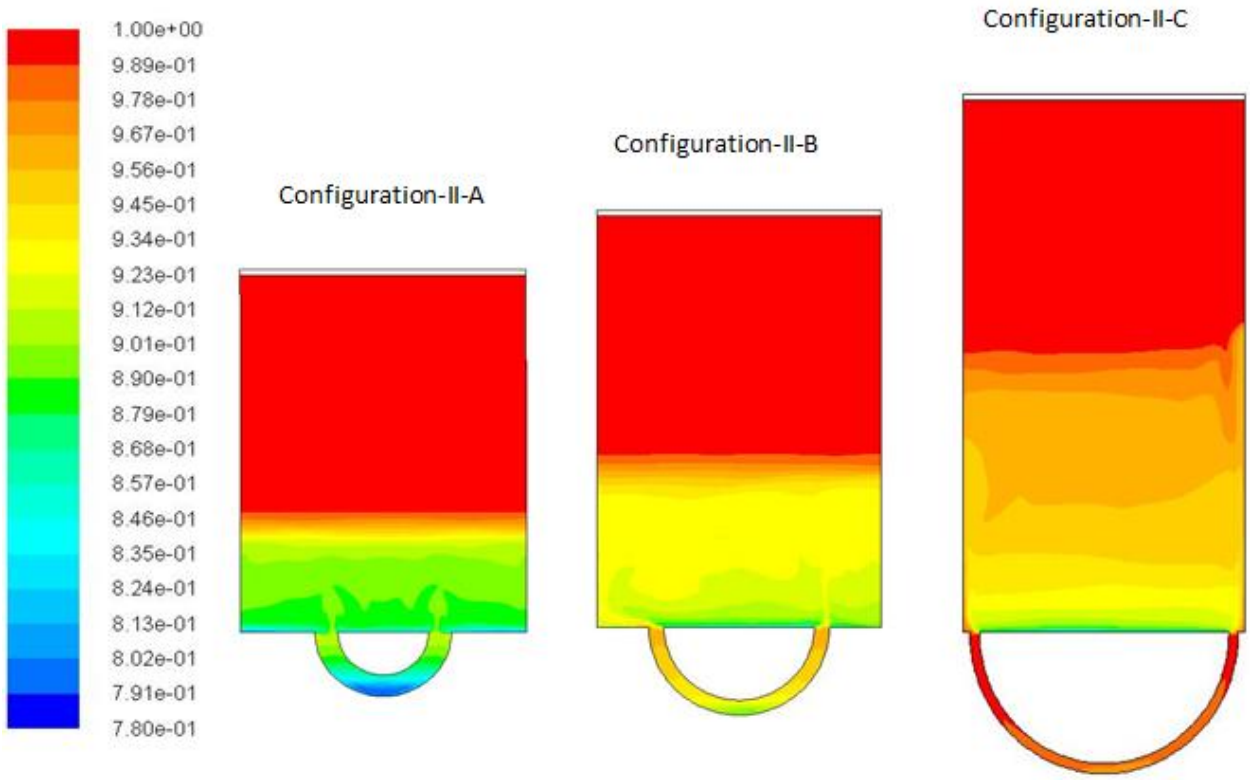

Figure 3.11 Case II: contours of volume fraction of vapor pentane at time = 5 sec

To better understand the flow patterns of the mixture inside these tubes, the velocity contours for Configuration-II-C are plotted in Figures 3.12 and 3.13 at different times. The corresponding velocity vectors at tube ends are also plotted to obtain a better insight. The figures show that higher mixture velocities in the upper sections of the tube compared to the bottom section. This could be due to the rise of low density mixture as discussed earlier. The comparison at different times also show that the overall velocity magnitude of the mixture in the tube

increased with time. The analysis of the velocity vectors show that in the early stages of the phase change process (0.5 to 4 sec), the mixture was coming out of the tube from both ends. However, as the time further progressed, the mixture was coming out of the tube from one end and entering the tube from the other end, which continued for the rest of the process. This trend can be explained as follows:

Initially, the tube was filled was the working fluid in the liquid state. As the heat was added to the tube, the phase change started and the specific volume of the liquid-vapor mixture started to increase. Since the tube has a constant volume, this also caused the pressure to rise. Due to the fluid expansion and rise in its pressure, the mixture started to escape the tube from both ends (symmetric tube). However, as noticed in Figure 3.11 after 4 sec, the high density, low volume fraction fluid started to collect on the bottom surface of the vessel, while the tube contained the low density, high volume fraction fluid. As the time progressed, this high density fluid due to gravity started to enter the tube and hence blocked the escaping of the mixture from that end. As a result, a cyclic process is established. That is, the high density low volume fraction mixture (i.e. one with larger liquid content) from the vessel started to enter the tube from one end. As it flows through the tube, it gained heat and the liquid content started to vaporize and this low density, high volume fraction mixture then escaped from the other end of the tube into the vessel and the cycle continued. The comparison of velocities at the two ends show that when the mixture from the tube was escaping into the vessel from both ends, their velocity magnitudes were similar. However, when the cyclic process was established, the velocity at which the low density high volume fraction mixture was escaping from one end of the tube into the vessel was much higher than the velocity at which the high density, low volume fraction mixture was entering the tube from the other end.

As the tube is symmetric, there should not be any preferred path for the cycle. That is, the high density mixture could enter from the left-side tube and consequently the low density mixture exits from the right-side tube, or vice versa. To understand this behavior, the contours of the mixture pressure inside the tube are plotted in Figure 3.14 at different times. The plot shows that before the cycle started, the pressure distribution was symmetric inside the tube.

However, when the cycle started at 6 sec, the pressure distribution became slightly asymmetric with relatively higher pressure in the right arm of the tube causing the low density mixture to escape from this end.

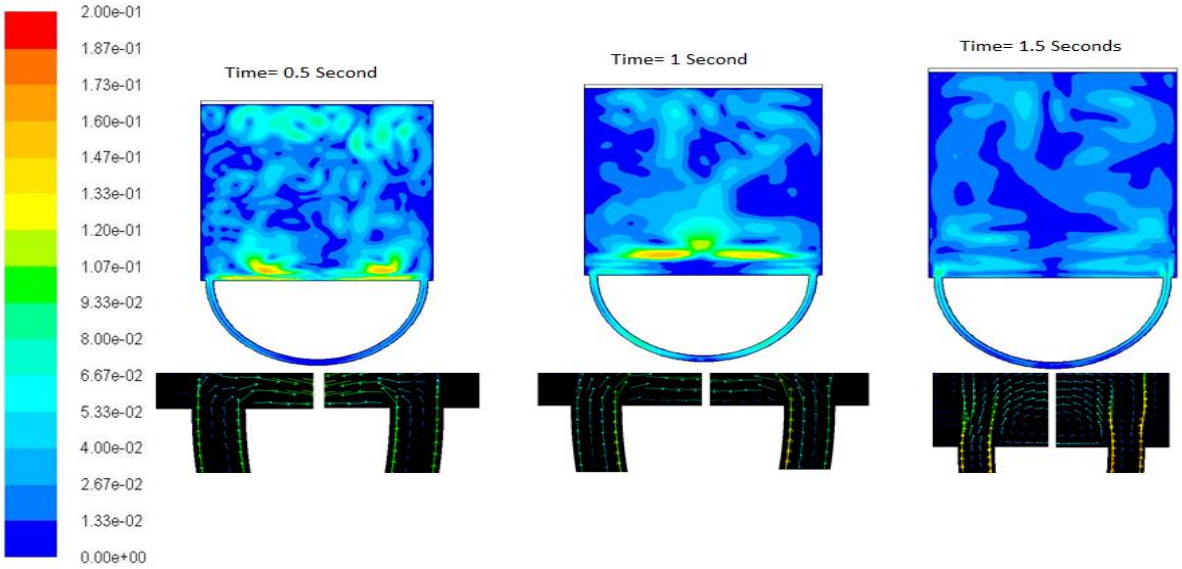

Figure 3.12 Velocity contours of mixture pentane in Configuration-II-C domain at different times

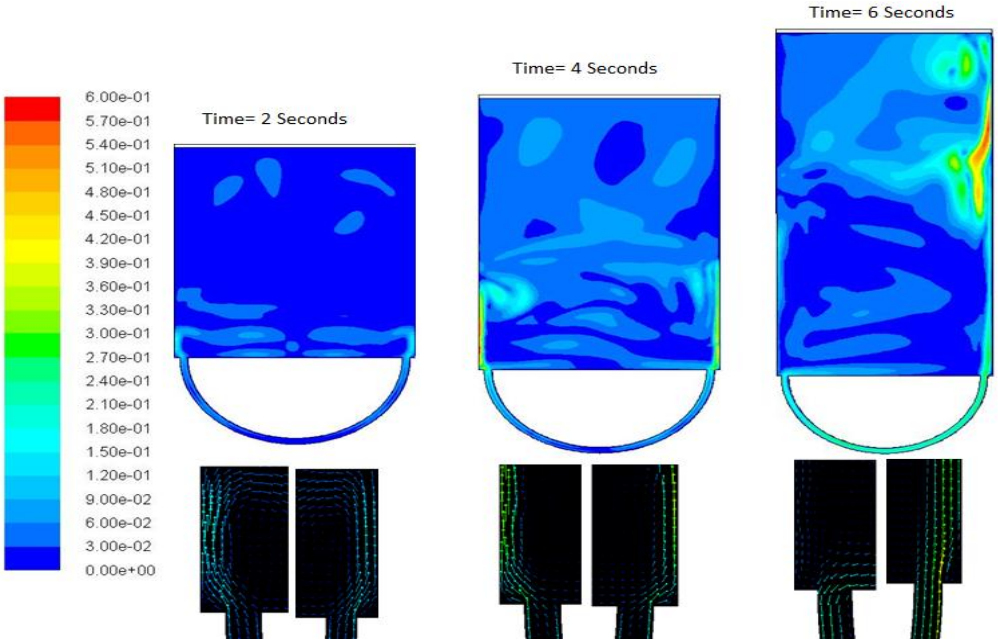

Figure 3.13 Velocity contours of mixture pentane in Configuration-II-C domain at different times

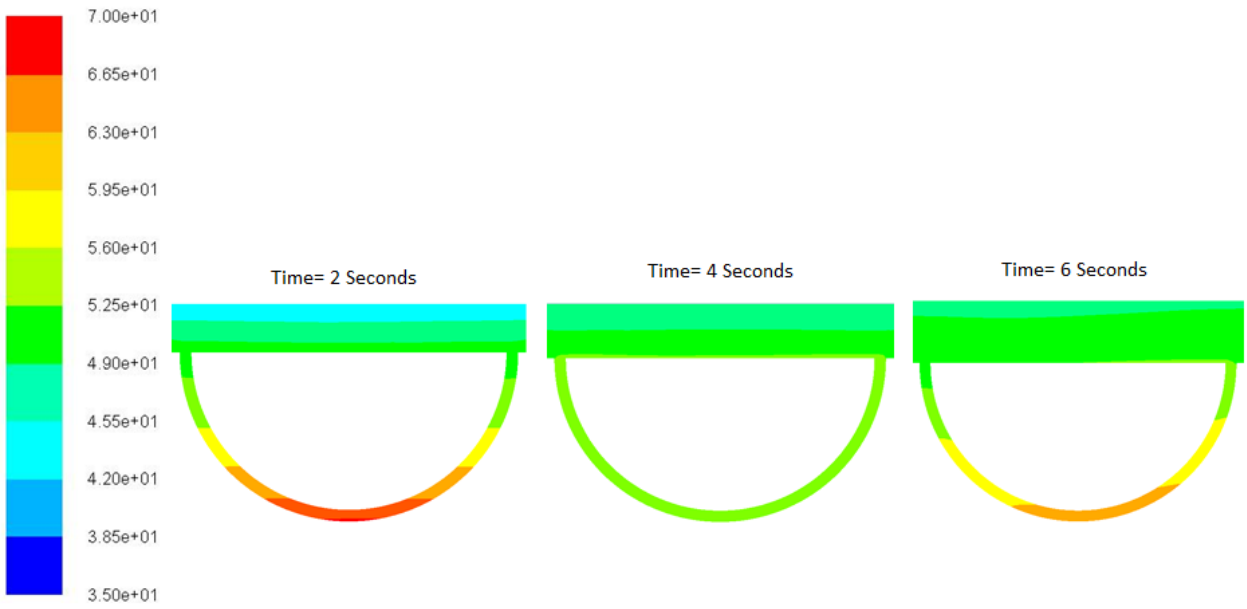

Figure 3.14 Pressure contours of mixture pentane in Configuration-II-C domain at different times

The velocity contours at 10 sec after the beginning of the process for all three configurations are shown in Figure 3.15. The plots show that the cyclic process is present in all configurations. However, the velocity magnitudes at which the mixture was escaping the tube were dependent on the tube configuration. It is observed that the velocity magnitudes of the escaping fluid are highest for the tube with the largest surface area, which decreased with a decrease in the tube surface area, as expected. Note the jet that is formed when the mixture escapes the tube induces secondary flow into the vessel, which in turn effects the pressure distribution as well as the mixing between the two phases inside the vessel. Thus, it is expected to have some influence on the overall system performance.

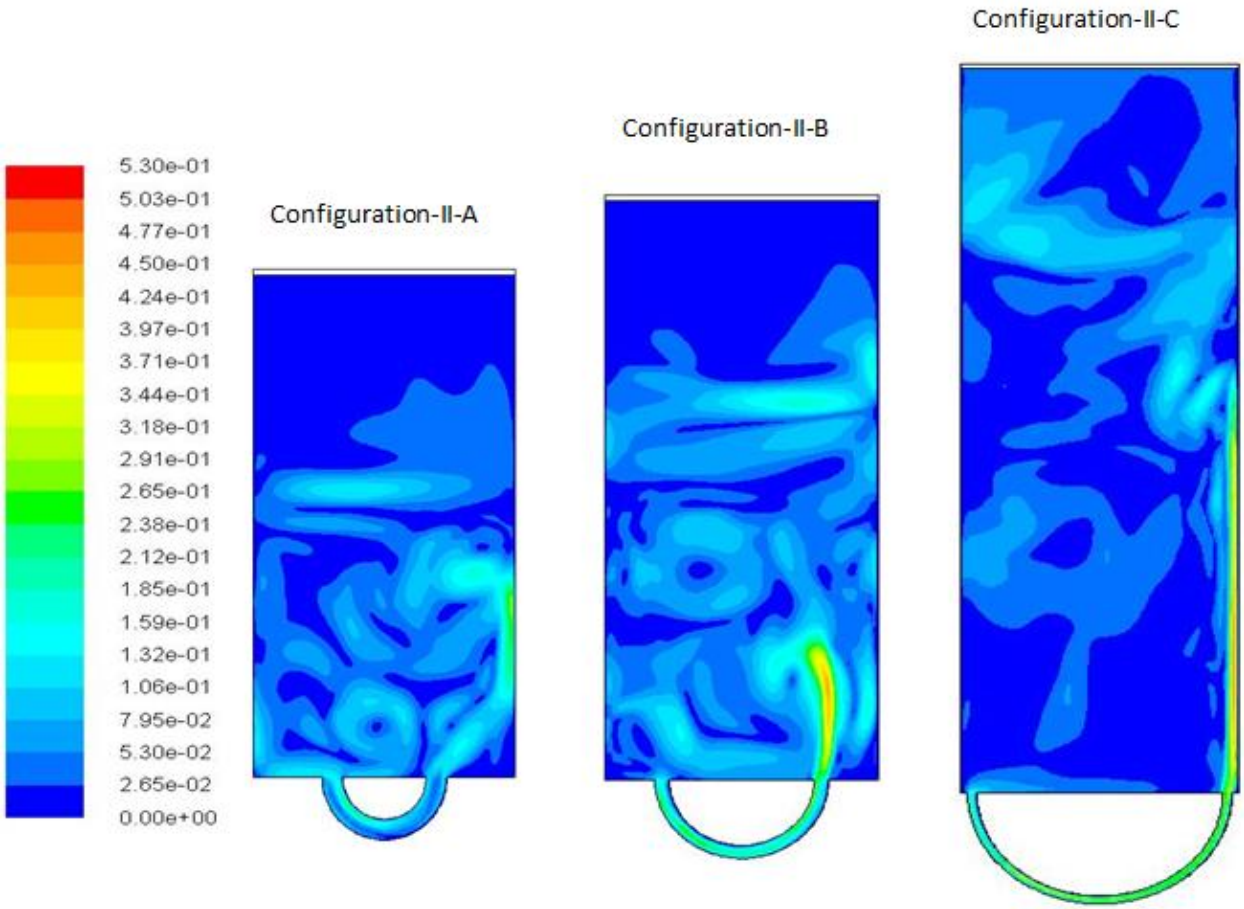

Figure 3.15 Case II: contours of mixture velocity at time = 10 sec

Results for volume fraction of vapor pentane, mass fraction of vapor pentane and piston position are presented in Figures 3.16, 3.17 and 3.18, respectively. In general, it is clear from these figures, that geometry with U-shaped tube of any size has outperformed the rectangular geometry. Results also show that the system performance improved monotonically with a reduction in the tube diameter. For instance, at 25 seconds, the quality of mixture inside the rectangular shape was 22% while Configuration-II-A (d = 0.8 cm) Configuration-II-B (d = 0.54 cm) and Configuration-II-C (d = 0.35 cm), have the mixture quality of 26%, 35% and 48%, respectively. Similarly, the piston velocity was lowest for the rectangular geometry as seen in Figure 3.18 and increased monotonically with the reduction in the tube diameter. A plausible cause for these trends is the heat transfer surface area. The smallest diameter tube has the largest heat transfer surface area, while rectangular geometry has the smallest heat transfer

surface area. Consequently, the working fluid has higher rate of evaporation due to higher heat transfer rate for the larger surface area geometry. Examining Figures 3.16 and 3.18 it can be noticed that at 10 seconds although the domain boundary had expanded up to 31 cm for Configuration-II-C, vapor pentane had occupied 98.7% of that domain while for Configuration-II-B, vapor occupied 98% of a much smaller domain that only expanded to 23 cm and for Configuration-II-A the domain expanded to 20 cm and vapor pentane occupied only 97.6% of it. As for the quality of pentane mixture in the domain, after 10 seconds, its values were 0.25, 0.2 and 0.17, respectively.

Results in this section show that heat exchangers with smaller diameter and larger surface area transfer heat to the working fluid at a much quicker rate than tubes with larger diameter and smaller surface area, as expected. The in depth analysis of the flow pattern showed the cyclic flow pattern inside the tube and the formation of jet by the escaping of the low density, high volume fraction mixture, whose magnitude also increased with an increase in the tube surface area.

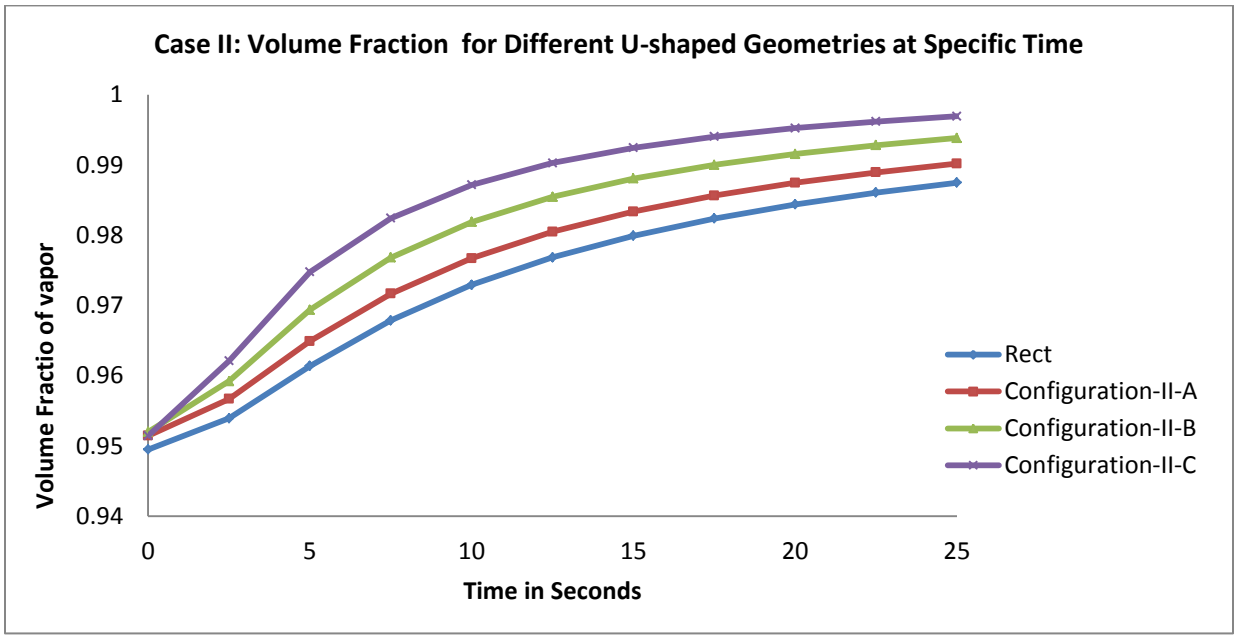

Figure 3.16 Volume fraction of vapor pentane for different configurations of Case II

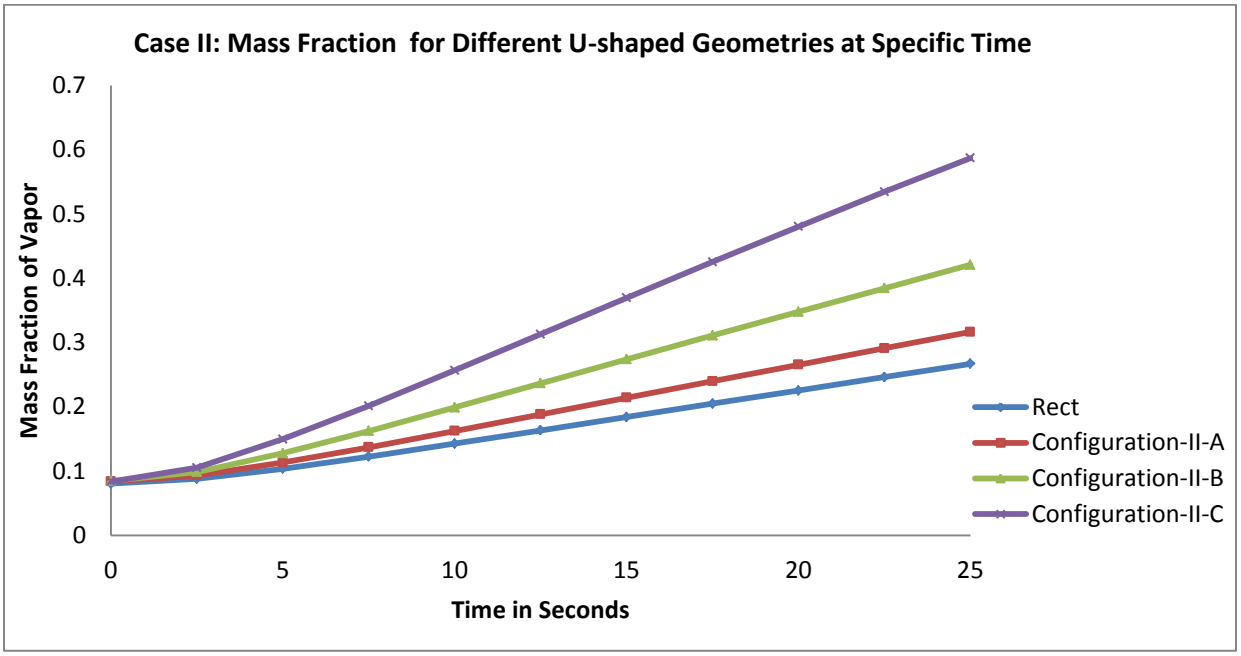

Figure 3.17 Mass fraction of vapor pentane for different configurations of Case II

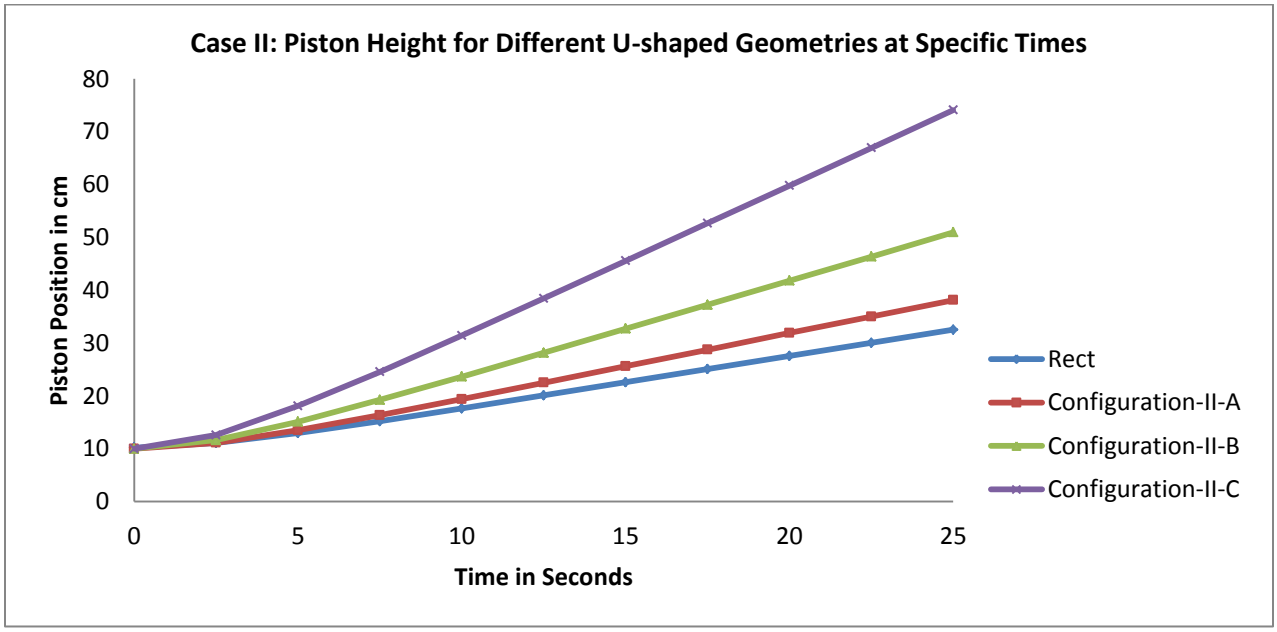

Figure 3.18: Piston Position in cm for different configurations of Case II

3.1.2.2 Case III: heat exchangers with equal surface area

As observed in the previous case, the surface area of the tube has a significant impact on the evaporation process, local velocity magnitudes and the piston movement. In the present case, the objective is to study if the configuration/geometry of the tube has an influence on the process, while the surface area remains the same. Thus, two new geometries were considered using the same diameter tube as for Configuration-II-C, which based on Case II has the best performance among the three configurations tested. These geometries only differ in the tube configuration. The shape and length of these geometries were set in a way that the total surface area for both tube geometries was the same and equal to 0.29 m^2/m. Thus, the total volume of these tubes was $4x10^{-4}$ m^3/m which was also equal to that of Configuration-II-C. As seen in Figure 3.19, the first proposed geometry, Configuration-III-A is made of two tubes circular in shape configured concentrically while the second geometry is made of a continuous tube having a W-shaped tube and was named Configuration-III-B. As in the previous case, initially, the tubes were filled with liquid pentane while the vessel was filled with vapor pentane (see Figure 3.20). Similarly, a heat flux of 10,000 W/m^2 was applied on the entire tube surfaces of the given geometries. The simulations ran for 10 seconds.

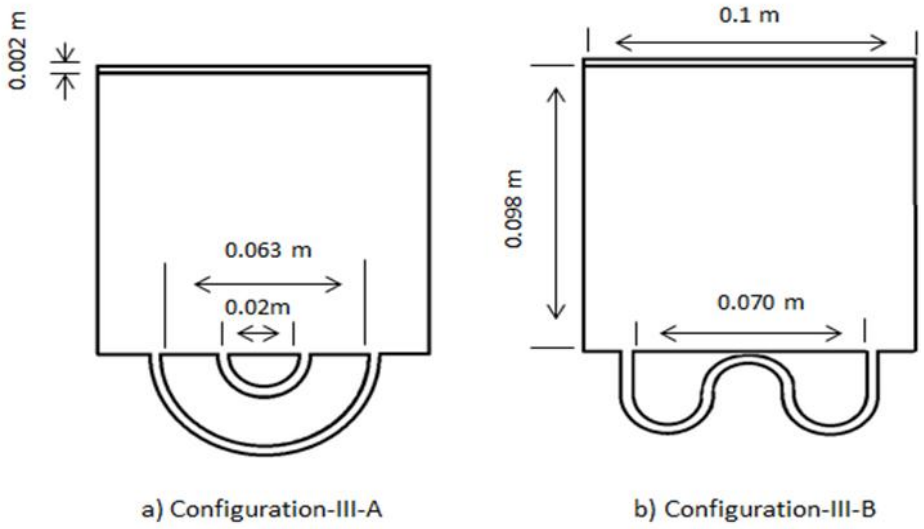

Figure 3.19 Geometries of Case III

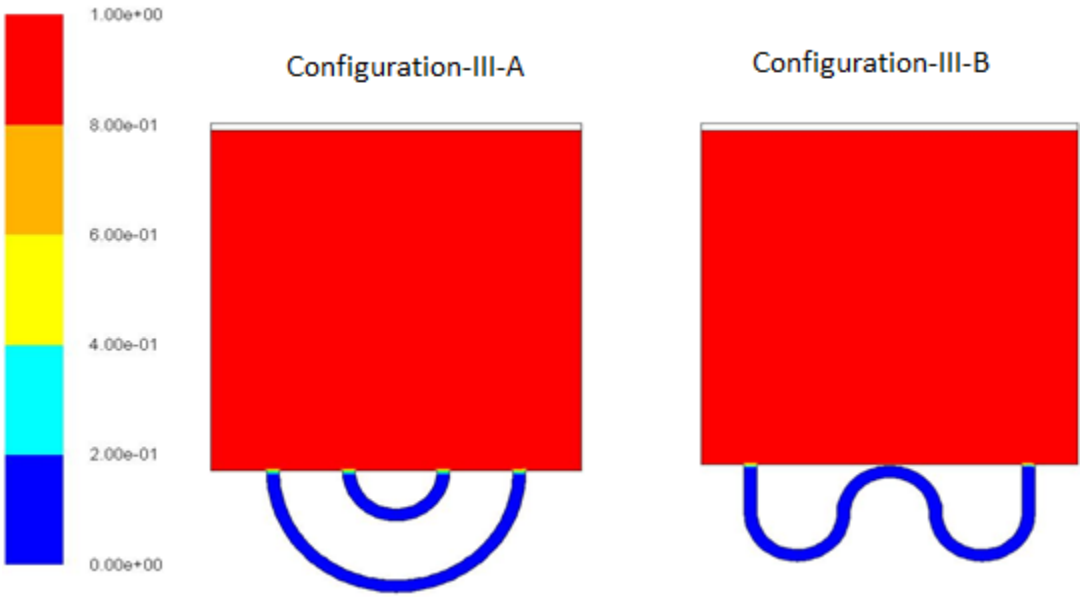

Figure 3.20 Case III contours of volume fraction of vapor pentane at t=0 sec

To investigate the phase change process inside the heat exchanger tubes for these configurations, the volume fraction contours at different times are presented in Figure 3.21. The results of Configuration-II-C are also plotted for comparison, which has the same tube surface area but different tube configuration. Configuration III-A, which has two U-shaped tube of different sizes has similar volume fraction distribution as in Configuration II-C, which is a single U-shaped tube larger in size. That is, as the heat transferred to the fluid, the volume fraction increased and this low density high volume fraction mixture ascend in the tube. Comparison of Configurations II-C and III-A shows that the rates of phase change in a heat exchanger with one tube is relatively faster than that in a heat exchanger with multiple tubes when the total surface area is the same. Configuration III-B however, showed different pattern. Due to its geometry (W-shaped tube), the high volume fraction mixture generated by heating and ascended due to lower density accumulated in the middle section in addition to that in the two arms of the tube. It is also observed that the amount of the high volume fraction mixture accumulated in the middle section is much larger than that accumulated in the tube arms. This accumulated high volume fraction mixture pushed the fluid towards both tube ends resulting in a relatively uniform volume fraction in the tube compared to the other configurations. The

comparison also shows that during this initial stage of the phase change process (0.5—2 sec), the rate of phase change in Configuration-III-B (W-shaped tube) is faster than the other U-shaped configurations. As we discussed in the previous case, at the early stage of phase change inside the heat exchanger tube, the high quality mixture exits the tube from both ends and at a later time, a cyclic process is established in which the high quality mixture exits the tube from one end and low quality mixture from the vessel enters the tube from the other end. We have investigated the time at which this cyclic process started in the heat exchanger geometries considered in this case. It is found that the cyclic process started much earlier for Configuration III-B (approximately 2 sec after the beginning of the phase change process in the heat exchanger tube) compared to Configuration III-A, where the cyclic process started at approximately 4 sec in the smaller tube and at about 6 sec in the larger tube.

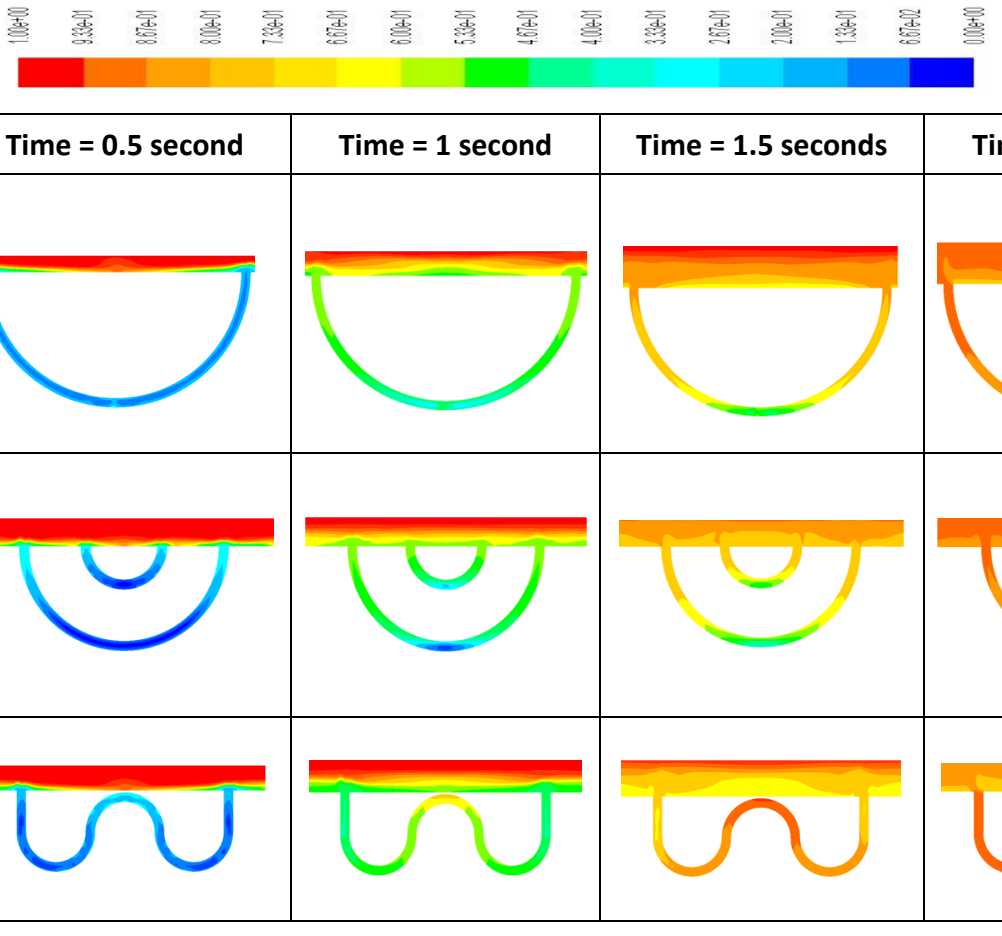

Figure 3.21 Contours of volume fraction pentane for different configuration of Case III

The contours of the volume fraction of pentane after 5 seconds for the proposed geometries in the entire domain are presented in Figure 3.22. The results show that the vapor phase had occupied the upper domain of the three geometries in almost the same proportion; however, some differences are observed in the volume fraction of vapor in the middle and lower sections of the domain and inside the tube. The vapor fraction in the middle section of the domain is slightly higher for Configuration-III-B; however, it is relatively low near the bottom surface of the domain. Configuration-III-A shows a more uniform vapor fraction in the lower section of the domain compared to the other configurations. This effect is investigated through the mixture velocity behavior in the domain and the tubes.

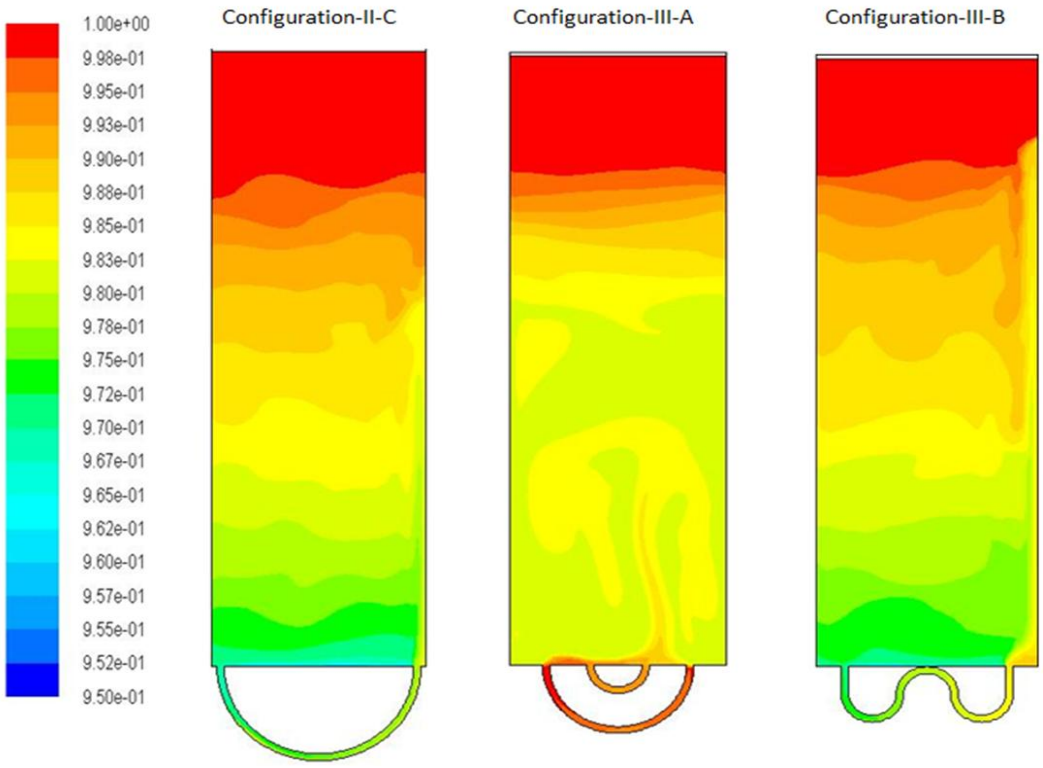

Figure 3.22 Case III: contours of volume fraction of vapor pentane at time = 10 sec

The results in Figure 3.21 show that the W-shaped tube has a faster phase change process and response in the early stage of the process. The results in Figure 3.22 at a later time show almost similar behavior in all configurations in both the heat exchanger tube as well as the vessel. This

indicates that although W-shaped tube performed better in the initial stage of the phase change process but in the longer run, its performance is no better than the other heat exchanger geometries. Similar behavior was observed for the pressure distribution inside the domain for the three configurations (not shown here).

Figure 3.23 shows the contours of mixture velocity for the three configurations at the same time i.e. 10 seconds after the beginning of the process. As the figure shows, for Configuration-III-A a strong mixing zone is observed in the lower section of the domain. This strong mixing is likely the reason for uniform volume fraction in this region. For the other two geometries, the flow was relatively quiescent, which resulted in the variation in the volume fraction in the lower half of the domain. The average velocity in the domain was 0.11 m/s for Configuration-III-A, 0.06 m/s for Configuration-III-B and 0.04 m/sec for Configuration-II-C. Figure also shows the stream of vapor coming out of the tube. As discussed earlier, the vapor exits the tube from one end, which is clearly visible in the figure.

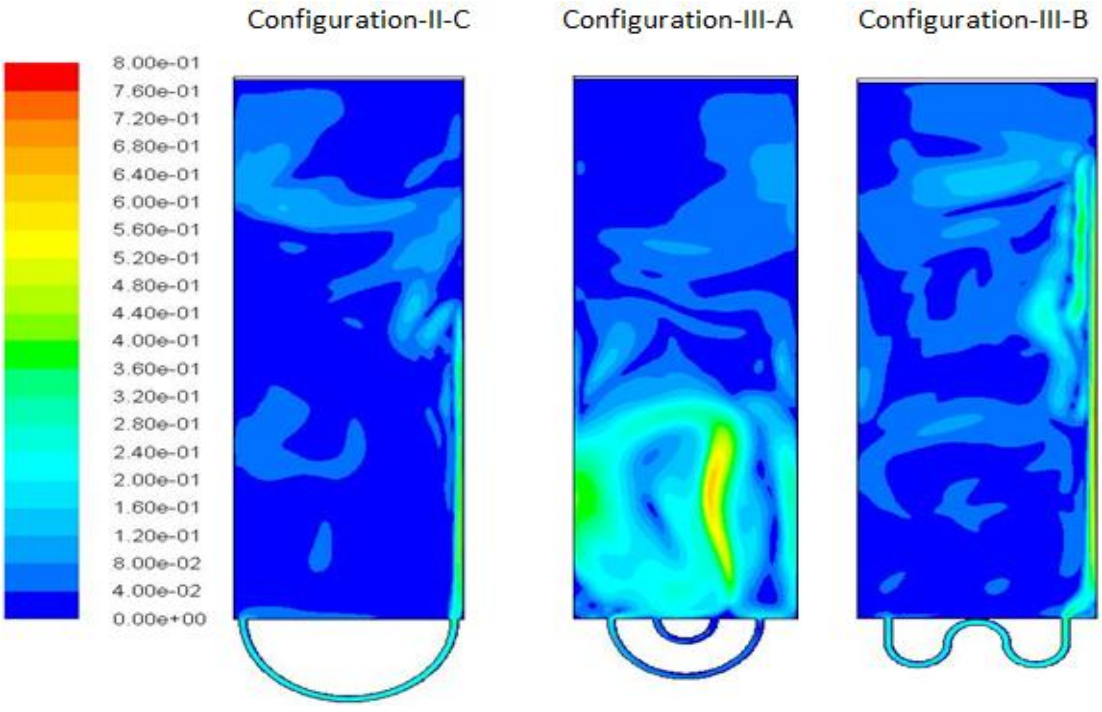

Figure 3.23 Case III: contours of mixture velocity at time = 10 sec

The transient variation of the volume fraction and mass fraction of pentane, and the piston position for the three geometries were compared and as expected from the above results, almost identical behavior of all three parameters is observed in the given three geometries. Thus, it can be concluded that the shape of the heat exchanger tube may has local effect on the process in the early stage, but overall, the process is almost independent of the tube configuration as long as the heat transfer surface area of the tube and the mass of liquid inside the tube are the same.

3.1.2.3 Case IV: increasing mass of the working fluid

The rate of phase change in the heat exchanger tube and its corresponding influence on the pressure and hence the piston movement in the vessel dictates the overall response of the system. Initial testing in Dyverga's prototype showed that quicker the system response, higher the output torque would be. Thus, it is highly desirable to reduce the response time of the system to get a faster movement of the piston. One way of achieving this is by increasing the heat exchanger tube surface area (as discussed in Case II) as well by increasing the mass of working fluid in the heat exchanger tube (larger tube volume). In the present case, the effect of increase in these parameters on the quality and mixing within the heat exchanger tube and vessel, and on the piston movement are studied. For this reason, two new geometries were built using the same diameter tube of 0.35 cm similar to that of Configuration-II-C presented in Case II. As seen, in Figure 3.24 the first proposed geometry, Configuration-IV-A is made of two tubes circular in shape configured concentrically while the second geometry Configuration-IV-B is made of three circular tubes configured similar to that of Configuration-IV-A . In Table 3.3, the initial mass and total surface areas for the three configurations are listed. Note that an increase in the surface area is accompanied by an increase in the initial mass of the working fluid in the heat exchanger tube due to the increase in the volume. The ratio of surface area to mass is almost the same for these configurations. Thus, the impact of larger heat transfer surface area on the rate of phase change is somehow offset by the increase in the mass of the working fluid. A constant heat flux of 10,000 W/m^2 was applied on the tubes. Similar to previous cases, the tubes were initially filled with liquid pentane, while the vessel was initially

filled with vapor pentane (see Figure 3.25). Due to the rapid increase in the vapor volume fraction, the process is simulated for 10 seconds only.

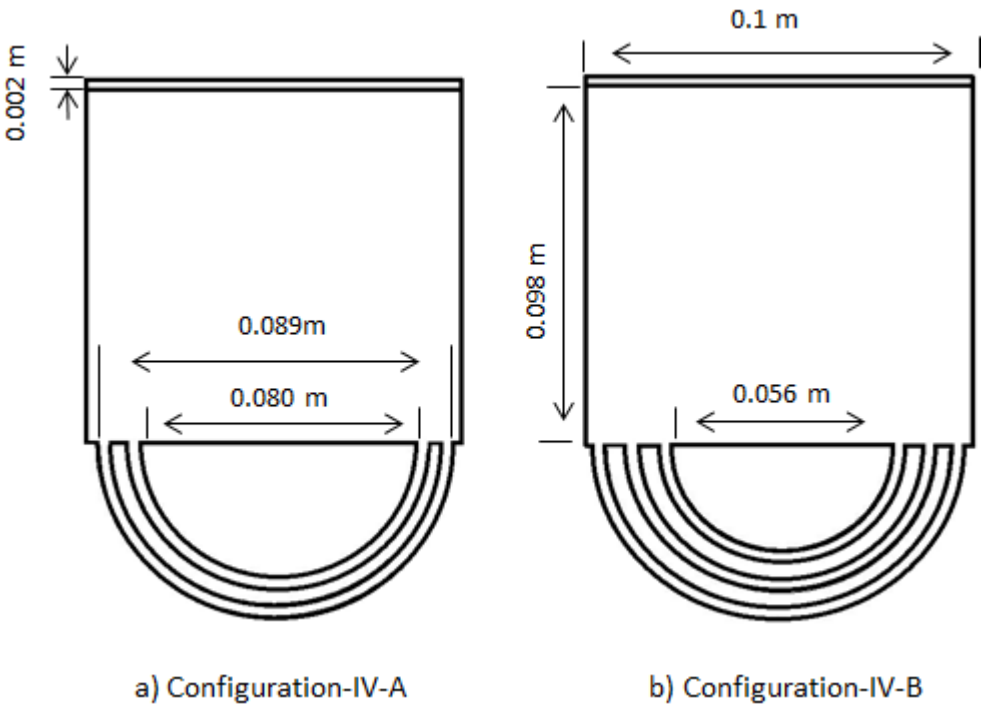

Figure 3.24 Geometries proposed for Case IV

Table 3.3 Case IV: list of mass of pentane in the given geometries

	Mass of liquid pentane in the tubes in kg/m	**Total surface Area of the tubes (m^2/m)**
Configuration-II-C	0.31	0.29
Configuration-IV-A	0.56	0.52
Configuration-IV-B	0.76	0.70

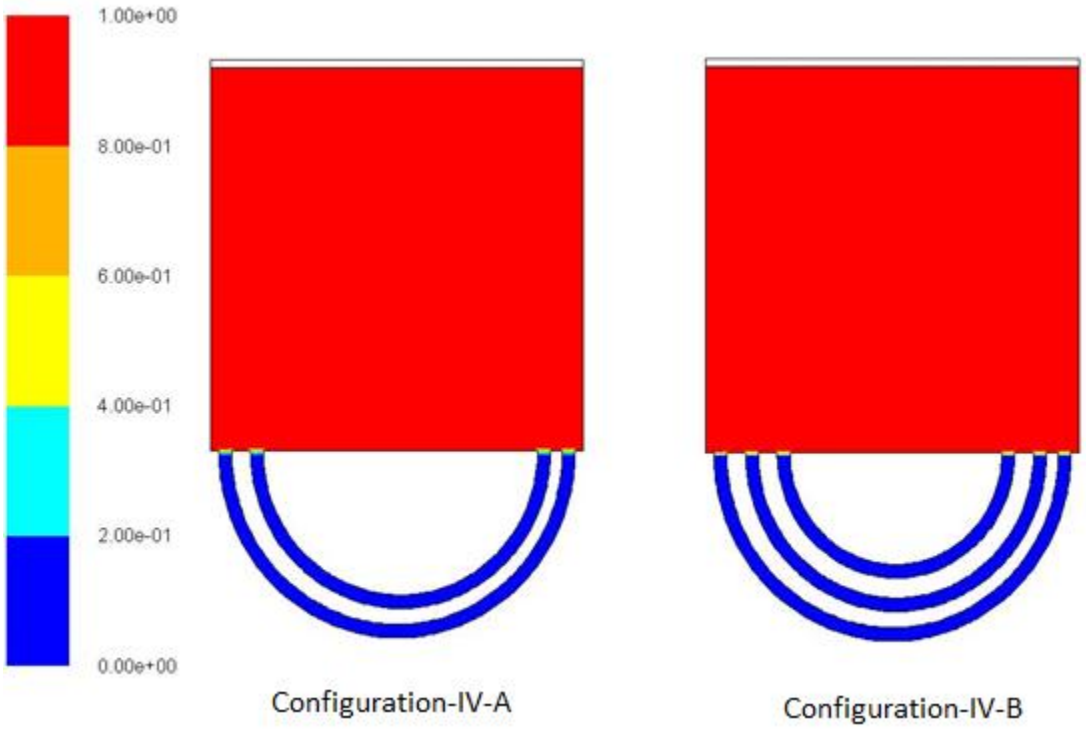

Figure 3.25 Case IV: contours of volume fraction of vapor pentane at t=0 sec

Since all configurations contain similar geometry i.e. U-shaped tubes, the initial phase change process in the tubes was similar, which is already discussed in detail in the earlier section. However, the impact of these configuration on the flow behavior and quality of the mixture and hence the piston movement are discussed here. The velocity contours for the three configurations at different times are presented in Figures 3.26 through 3.28. Results show that although the surface area to mass ratio is same in all three configurations, the velocity magnitudes and hence the mixing effects were varied for each configuration. As can be seen from the plots, the configuration with larger surface area and higher fluid mass produced higher mixture velocities, stronger jet flow from the tube and consequently better mixing in the vessel. It is also observed that the cyclic process started earlier as the tube area and the fluid mass in the tube increased.

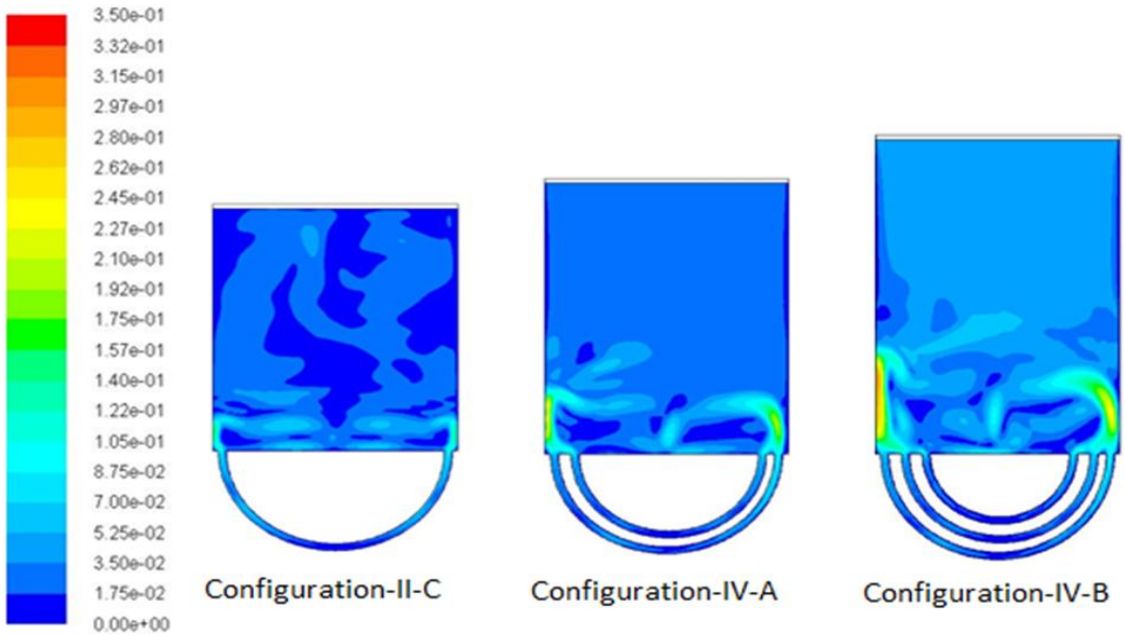

Figure 3.26 Case IV: contours of mixture velocity at time = 2 sec

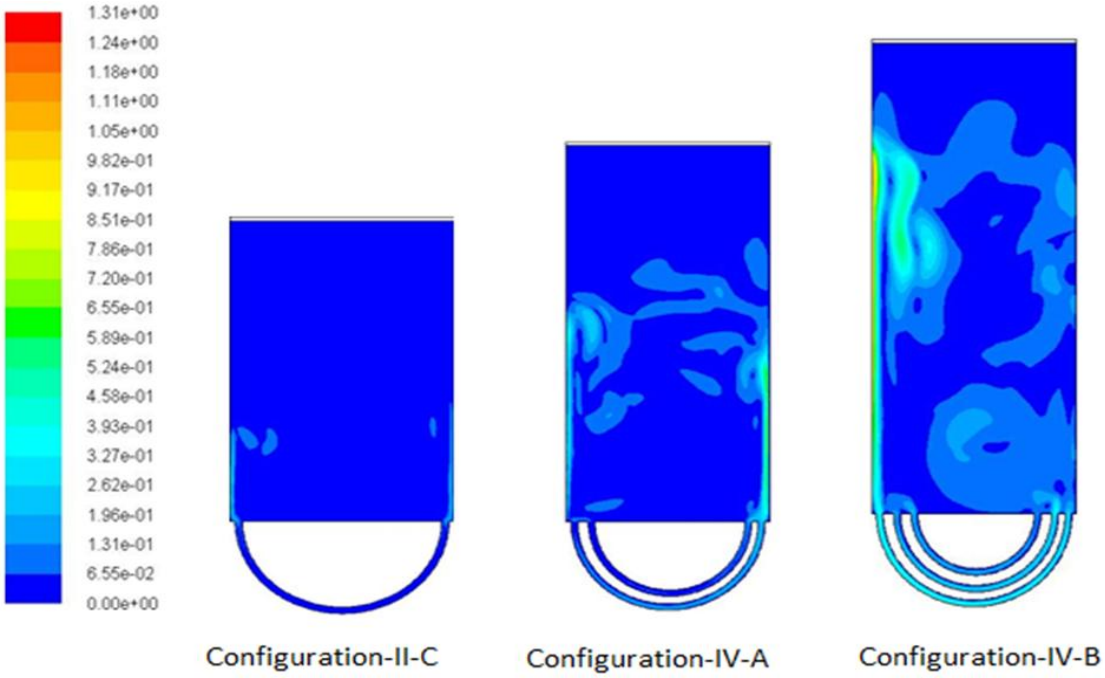

Figure 3.27 Case IV: contours of mixture velocity at time = 4 sec

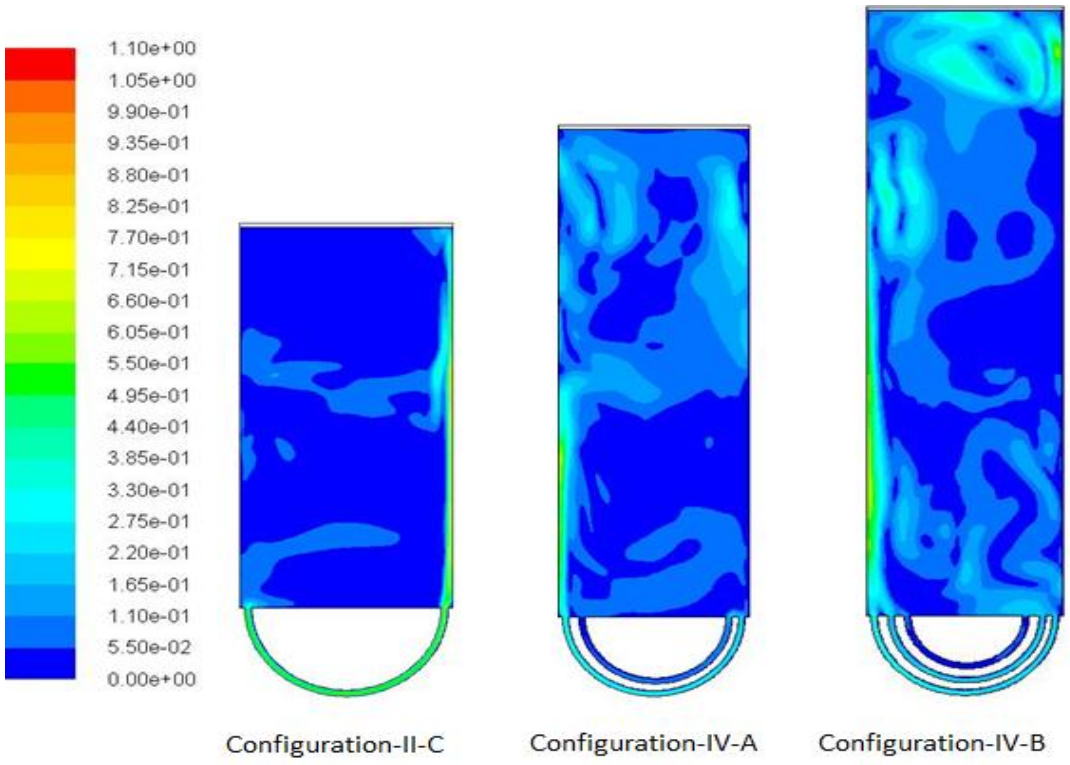

Figure 3.28 Case IV: contours of mixture velocity at time = 6 sec

Results for the transient variation of the volume fraction of pentane are shown in Figure 3.29. As it can be noticed, the volume fraction of vapor increased at different rates. Configuration-IV-B has the fastest rate, while Configuration-II-C has the lowest rate. As a result, although Configuration-II-C has the largest initial volume fraction, due to the lower rate, after 10 seconds the domain of Configuration-IV-B occupied same vapor as that of Configuration-IV-A and Configuration-II-C. The transient piston movement is shown in Figure 3.31. It shows that the velocity of the piston is highest for Configuration-IV-B, then Configuration-IV-A and Configuration-II-C has the slowest piston movement. At 10 seconds, the piston position was at 63.1 cm for Configuration-IV-B while piston was at 54.1 cm and 31.1 cm for Configuration-IV-A and Configuration-II-C, respectively. The mass fraction in Figure 3.30 indicates that the total vapor in the system is the highest for Configuration-IV-B. However, after 10 seconds, the quality of the mixture inside Configuration-II-C domain was the highest at 26% then Configuration-IV-A mixture quality was at 23% and 22% for Configuration-IV-B. This is because Configuration-II-C

has the lowest total mass of working fluid and thus, the mass of vapor in the domain of Configuration-IV-B and Configuration-IV-A is higher than that of Configuration-II-C. Despite the difference in the mass of the working fluid between the cases it can be seen from Figure 3.30 that the rate of evaporation is almost the same. This due to the fact that the surface area to mass ratio is the same for the three configurations as mentioned above.

The results in this section show that although the rate of phase change remained the same, the increase in the surface area and fluid mass increased the piston velocity due to the larger amount of the working fluid as well as better mixing due to the presence of stronger jet and higher velocities. Moreover, these results in this case clearly show that increasing the mass of the working fluid will have a direct impact on the amount of vapor in the system and the piston movement, as expected. Note that the domain did not expand as fast as in the real Dyverga system which has expanded 15 cm in 1 second. This could be due to the reason that the ratio of surface area to mass of working fluid in the Dyverga's system was 2 while, in the present configurations, it was around 0.9.

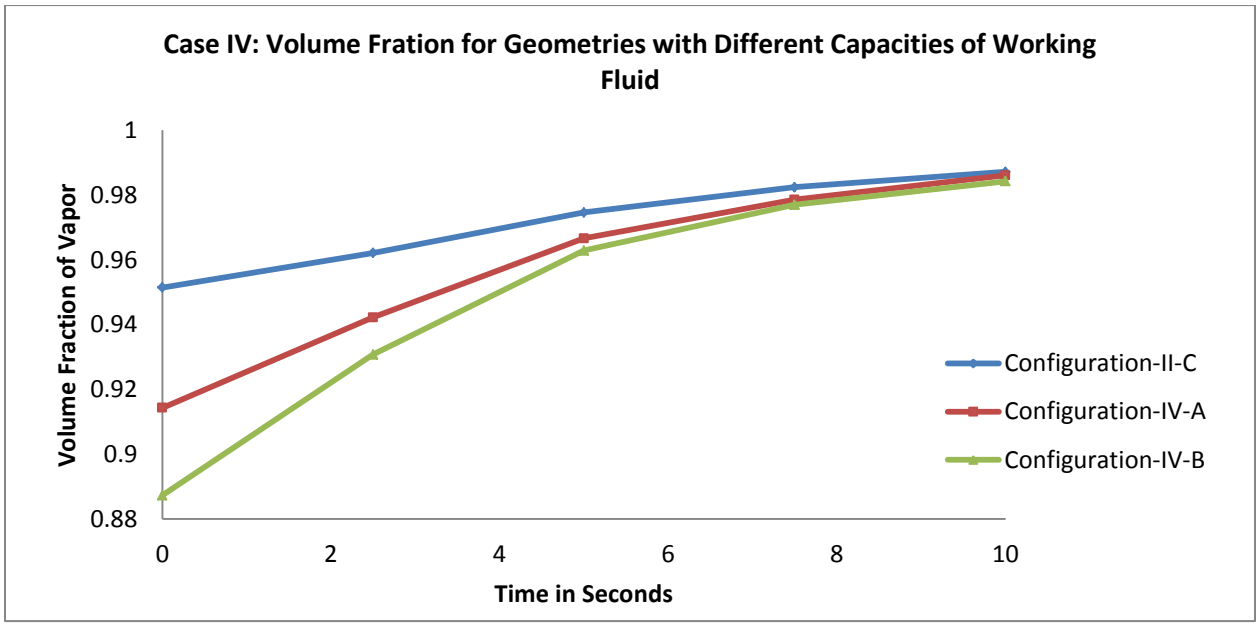

Figure 3.29 Volume fraction of vapor pentane for geometries of Case IV

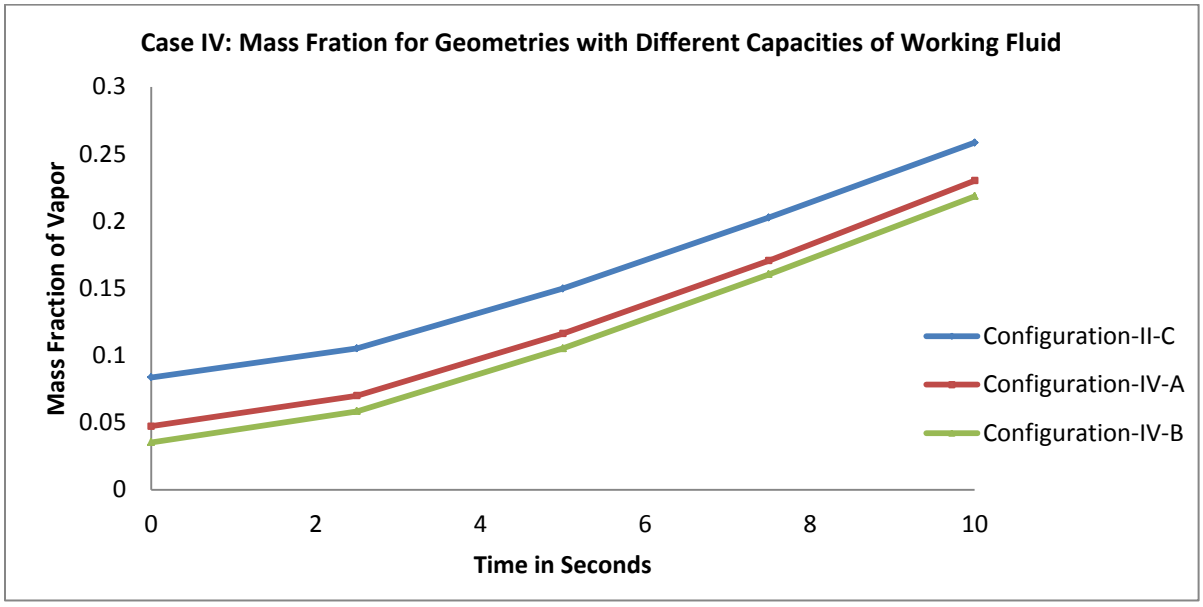

Figure 3.30 Mass fraction of vapor pentane for geometries of Case IV

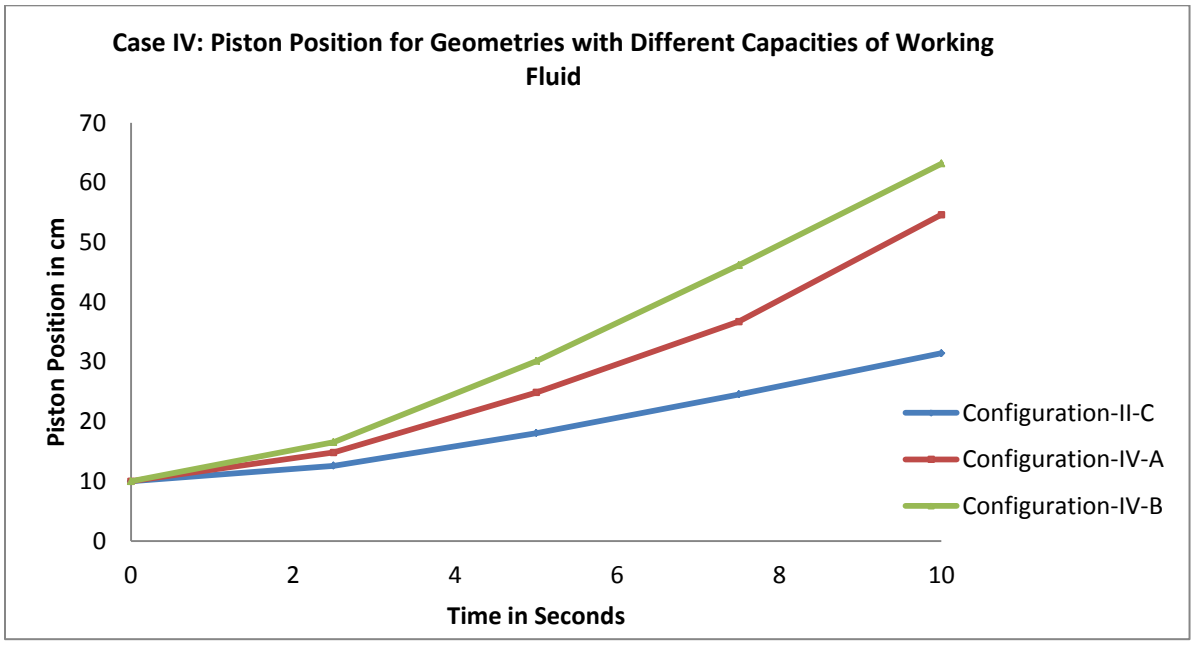

Figure 3.31 Piston position for the different geometries of Case IV

3.1.2.4 Case V: Controlling flow inside the heat exchanger

In most of the previous cases one can note that the vapor mixture exits the tube from one end. This phenomenon was also noticed in Dyverga's prototype. The flow always finds the path of

least flow resistance. Therefore, the preferred tube-end of the vapor to exit is the one where the pressure immediately above the tube-end is relatively lower than that of the other end. If the two tube ends are identical, the vapor mixture pressure above the tube ends decides the preferred path of the vapor to exit the tube. As seen earlier in the velocity contours, the velocity distribution in the domain is relatively random rather than a well-defined pattern, which implies that the pressure variations may occur randomly in the domain. Thus, the flow resistance above the tube outlet may change randomly and hence the vapor may come out from the left end or the right end of the tube. Thus, for the same configuration of the tube outlets, the preferred path of the vapor stream exiting the tube is not controllable.

As the orientation of the domain and the tube with respect to gravity changes continuously due to the rotary motion of the complete system, the tube end from which the vapor stream exits may influence the system performance. Thus, it would be beneficial to control the path of the vapor mixture stream as it exits the tube. This can be achieved by controlling the flow resistance. In this case, a passive approach is used to manipulate the flow resistance such that one end of the tube always provide the least flow resistance and would be used as the preferred vapor stream path. In the present case, this flow resistance manipulation was achieved by reducing the area of one tube end, such that this end acts like a nozzle. Nozzle accelerates the flow and reduces the pressure at the exit. The base geometry with W-shaped (Configuration-III-B) tube of 0.35 cm diameter introduced in Case III (see Figure 3.19b) was used for this study. Two configurations were considered; in one configuration the nozzle was added to the left-end of the tube (Figure 3.32a) while in the other configuration, the nozzle was added to the right-end tube (Figure 3.32b). In both cases the hydraulic diameter at the nozzle was reduced from 0.35 cm to 0.2 cm. Similar to the previous cases, liquid pentane occupied the total volume of the tube while the rest of the domain was occupied by vapor pentane and a constant heat flux of 10,000 W/m^2 was applied on the tube.

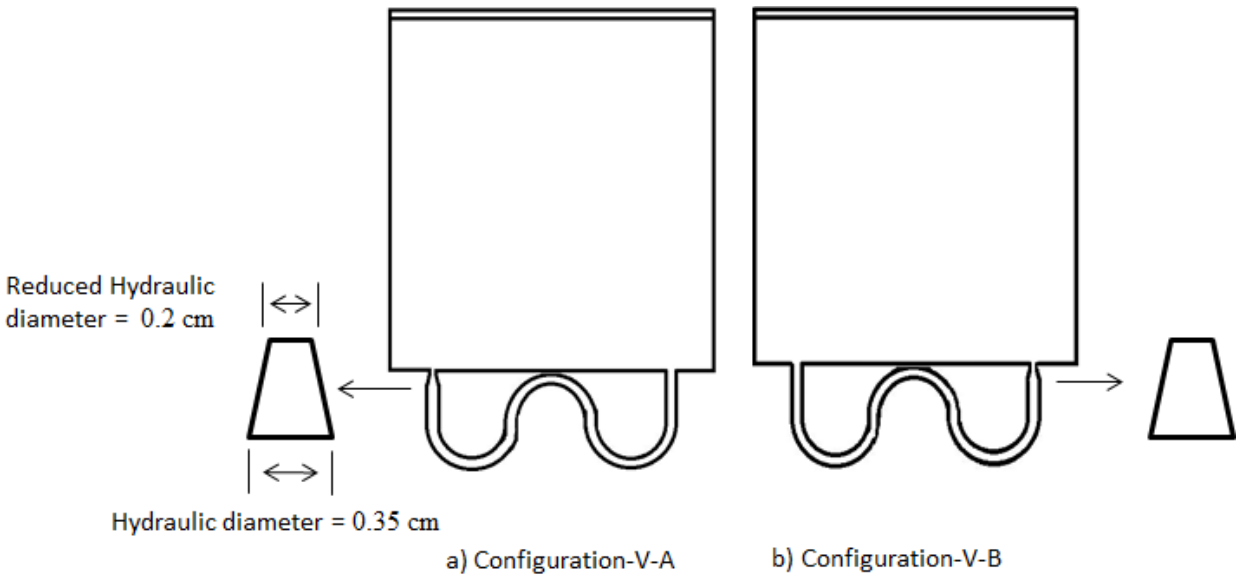

Figure 3.32: Geometries proposed for Case V

To study the impact of this area reduction on the vapor stream, the velocity contours at 1, 3 and 5 seconds after the initiation of the process are plotted in Figures 3.33, 3.34 and 3.35, respectively. Figure 3.33 shows that the flow started to exit from the nozzle end soon after the beginning of the process. After 3 and 5 seconds, there is a clear trend of flow exiting from the nozzle end and the magnitude of vapor stream exiting the tube also increased with time. The maximum velocity at 3 seconds it was 0.52 m/sec while at 5 seconds, it increased to 0.63 m/sec. The process is almost identical for both configurations as expected. Although the nozzle induced higher velocities, but this effect was rather local and did not change the overall velocity magnitude in the domain. In Table 3.4, the domain-averaged velocities for Configuration-V-A, Configuration-V-A are compared with that of Configuration-III-B of Case III and results showed negligible effect on the average velocity of the domain.

Monitoring the transient behavior of the average parameters i.e. volume fraction, mass fraction and piston position showed negligible difference in results between Configurations V-A, V-B and III-B. Hence reducing the cross sectional area of the tube on one end will only control the flow of the vapor stream exiting from a preferred outlet of the tube without influencing the process itself.

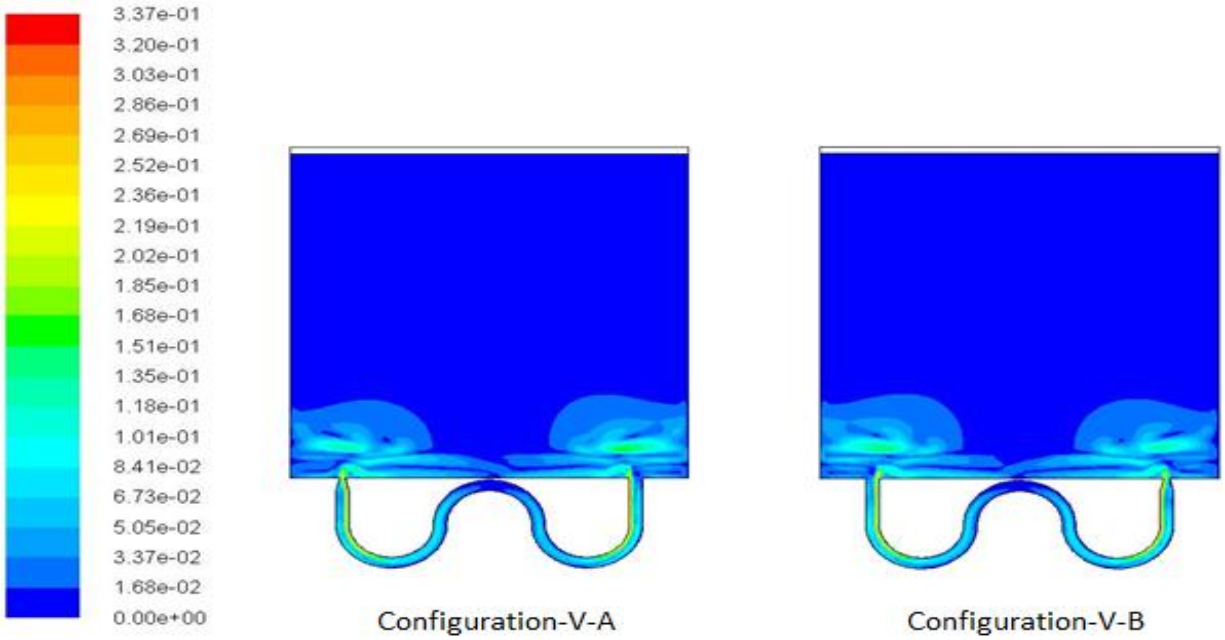

Figure 3.33 Case V: contours of mixture velocity at time = 1 sec

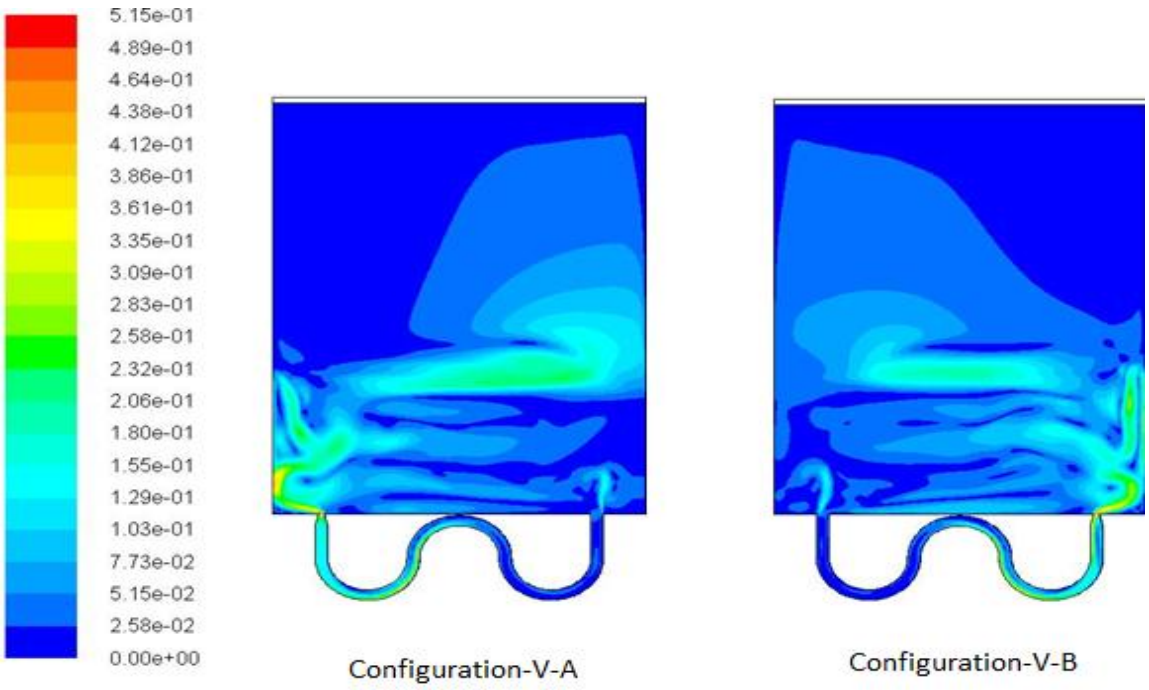

Figure 3.34 Case V: contours of mixture velocity at time = 3 sec

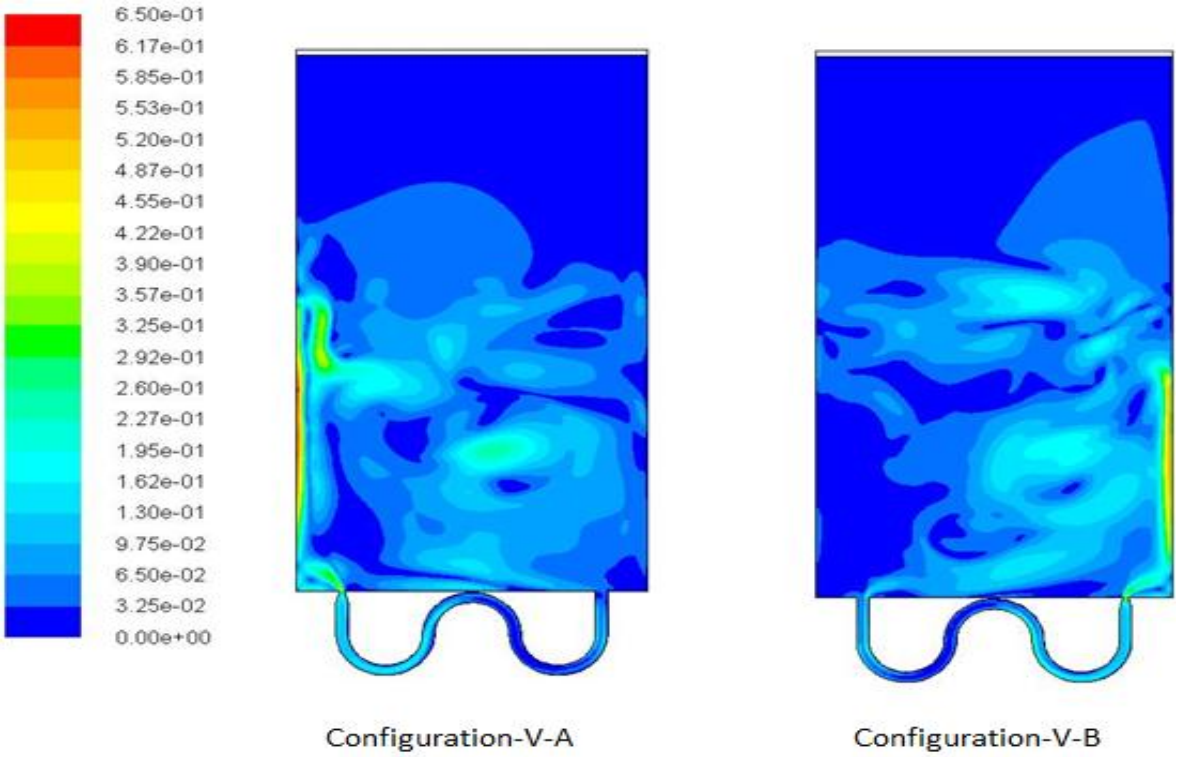

Figure 3.35 Case V: contours of mixture velocity at time = 6 sec

Table 3.4 Case V: volume average velocity for different geometries

Time in seconds	Geometry	Volume average velocity in m/sec
1	Configuration-III-B	0.016
	Configuration-V-A	0.018
	Configuration-V-B	0.018
3	Configuration-III-B	0.045
	Configuration-V-A	0.046
	Configuration-V-B	0.045
5	Configuration-III-B	0.061
	Configuration-V-A	0.061
	Configuration-V-B	0.060

3.1.2.5 Case VI: Partial heating

After the first visit to Dyverga, measurements were taken on SmarTorQ and some adjustments were made in some parameter values to bring them closer to that of the prototype. For example, the volume of vapor was reduced from 0.098 m^3/m to $3x10^{-4}$ m^3/m and the piston mass was set equal to 1.4 kg. Measurements were also taken for the heat exchanger in the system and temperature on the outside surface of this heat exchanger was measured using a wireless thermometer. These measurements were used to estimate the temperature on the inner surface of the coil (see, Appendix A). According to these calculations the temperature of the coil's inner surface is 69 ^oC. This temperature was used as a reference temperature for the subsequent cases.

During Dyverga's visit and while the prototype system is operational, it was noticed that when the heat exchanger reaches the heated water in the tank, the heat exchanger was partially submerged in the tank. Thus its total surfaces area was not utilized to effectively transfer heat to the working fluid. Due to this practical limitation, it is important to study the impact of the partial exposure of the tube surface to the heat source. That is, the heat flux was applied only on the partial surface area of the heat exchanger coil. Note that in previous cases, the uniform heat flux was applied over the entire tube surface which is equivalent to the fully submerged heat exchanger coil. Hence, in the case, the impact of partial submergence of the heat exchanger coil on the system performance is investigated. Three different cases were considered with variable levels of submergence on W-shaped geometry (see Figure 3.36). In Case A, the tube was considered to be fully submerged, while the tube was 75% submerged in Case B and 50% submerged in Case C. The level of submergence is marked by two red arrows in Figure 3.36. The tube wall temperature for the submerged sections for Cases B and C was set to 69 ^oC (same as the one observed in the real prototype) and for the un-submerged sections the tube wall temperature was set as 30 ^oC. In Figure 3.37, the contour of the initial volume fraction of pentane is shown for the given cases.

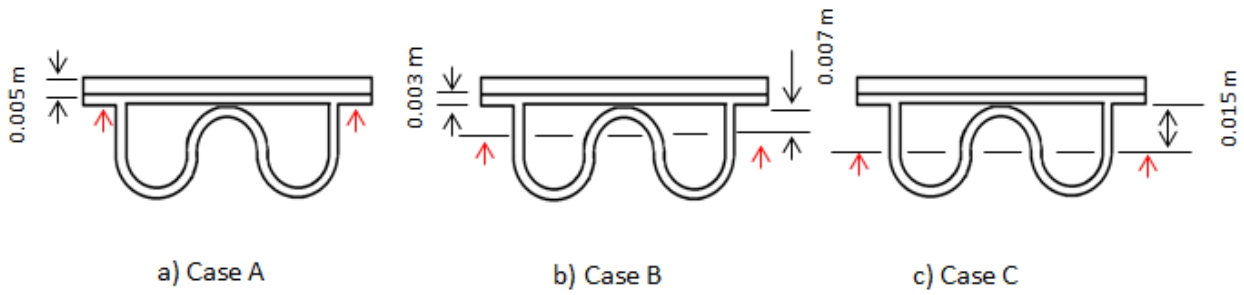

Figure 3.36 W-shaped geometry in different cases of heating level; Case VI

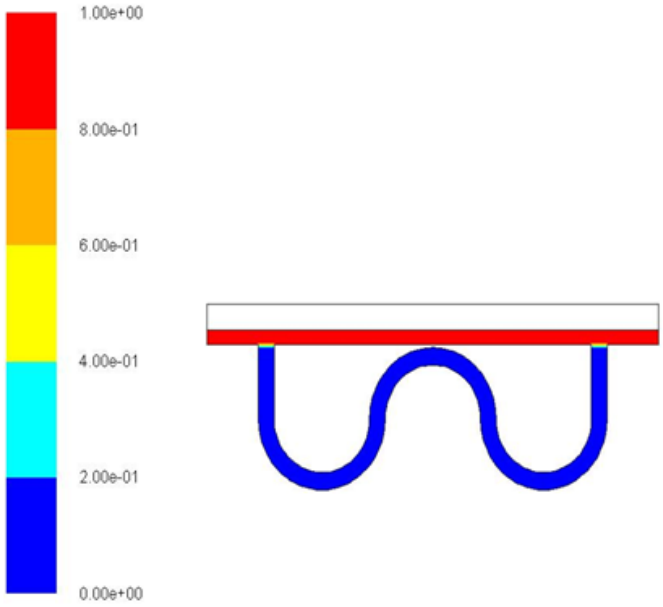

Figure 3.37 Case VI: contours of volume fraction of vapor pentane at time = 0 sec

The contours of the volume fraction of pentane at different times are presented in Figures 3.38 through 3.40. These figures clearly demonstrate the impact of partial submergence on the volume fraction. The plots in Figure 3.38 show that at 0.5 seconds, the volume fraction of vapor inside Case A tube was much higher than that of Cases B and C. Furthermore, it can be noticed from Figure 3.38 that the mixture with higher vapor fraction rises in the middle of the tube as well as at the exits due to the density difference. After 2.5 seconds (Figure 3.39), a high fraction of vapor was accumulating in the tube of Case A and it seems that the domain is more uniform because the vapor mixture appears to exit at a higher rate compared to other cases. Likewise, at 5 seconds (Figure 3.40), Case A volume fraction was substantially higher than the

other two cases not only in the tube but also in the domain. On average, the volume fraction inside the tube after 5 seconds was 0.85 for Case A, 0.80 for Case B and 0.76 for Case C.

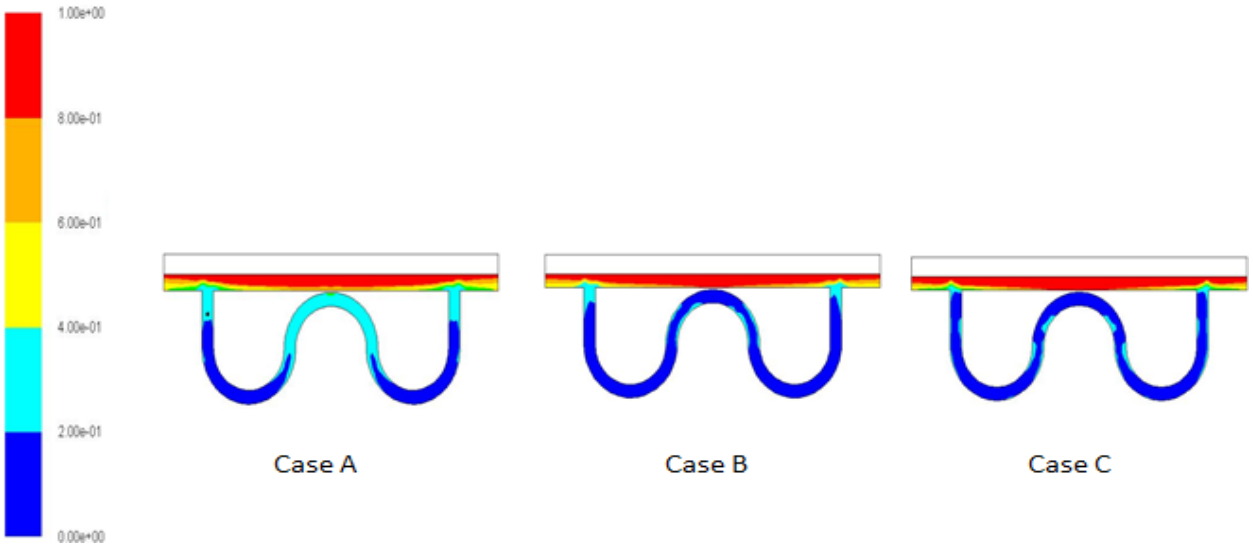

Figure 3.38 Case VI: contours of volume fraction of vapor at time = 0.5 sec

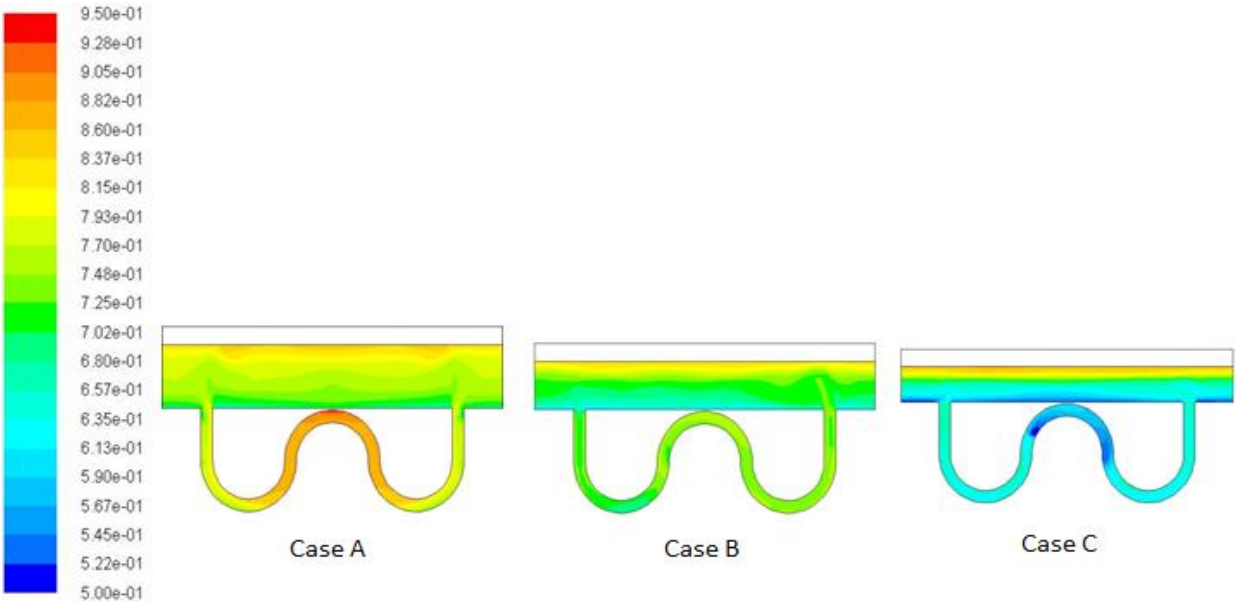

Figure 3.39 Case VI: contours of volume fraction of vapor at time =2.5 sec

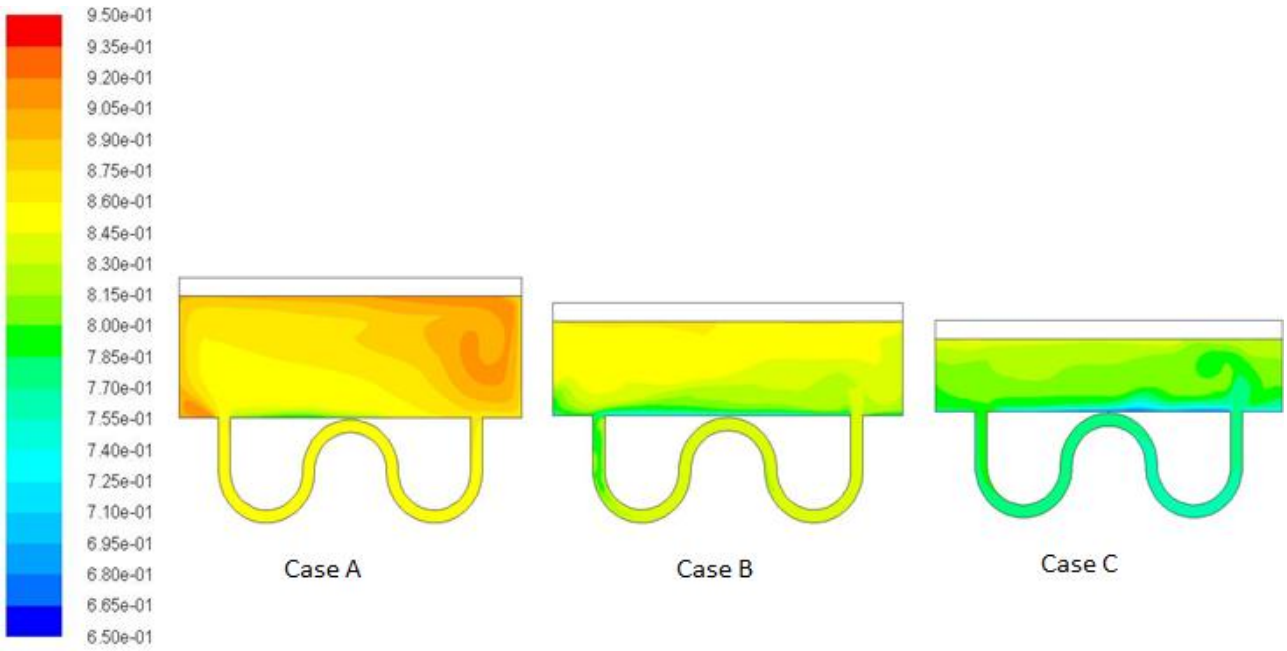

Figure 3.40 Case VI: contours of volume fraction of vapor at time = 5 sec

The results of the average parameters of interest for this case are presented in Figures 3.41 through 3.43. From these results it can be noted the fully submerged W-shaped tube of Case A has outperformed the partial submerged tubes of the other cases. For instance, after 3 seconds of the process time, the volume fraction of vapor pentane was 0.81 for Case A while for Cases B and C it was 0.76 and 0.70, respectively. This implies that more vapors of pentane occupy the domain of case A than the other two cases. Figure 3.43 also shows that the fully submerged tube has higher rate of evaporation, which decreases monotonically with a decrease in the submergence level. Similarly, piston was displaced the most for Case A and after 5 seconds, the piston for this case reaches 3.8 cm corresponding to an expansion of 12 times its initial volume while for Case B, the piston moved 3 cm; 17% lower than that of Case A and for Case C, the piston displaced 2.4 cm; 37% lower than that of Case A.

Although it is expected that higher the submergence level, the better would be the system performance, the focus of this case was to quantify the relative effects on the evaporation rate and the system response. Thus, for the better performance of the system, it is highly recommended to utilize the full area in the Dyverga's heat exchanger as this case highlights.

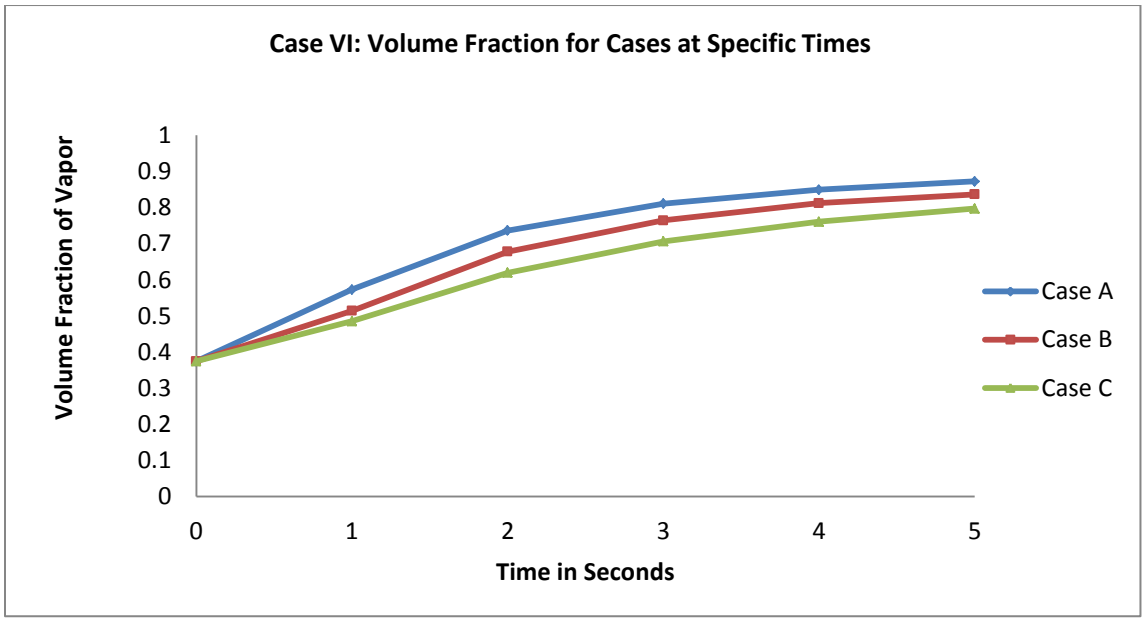

Figure 3.41 Volume fraction of vapor pentane for different heating levels of Case VI

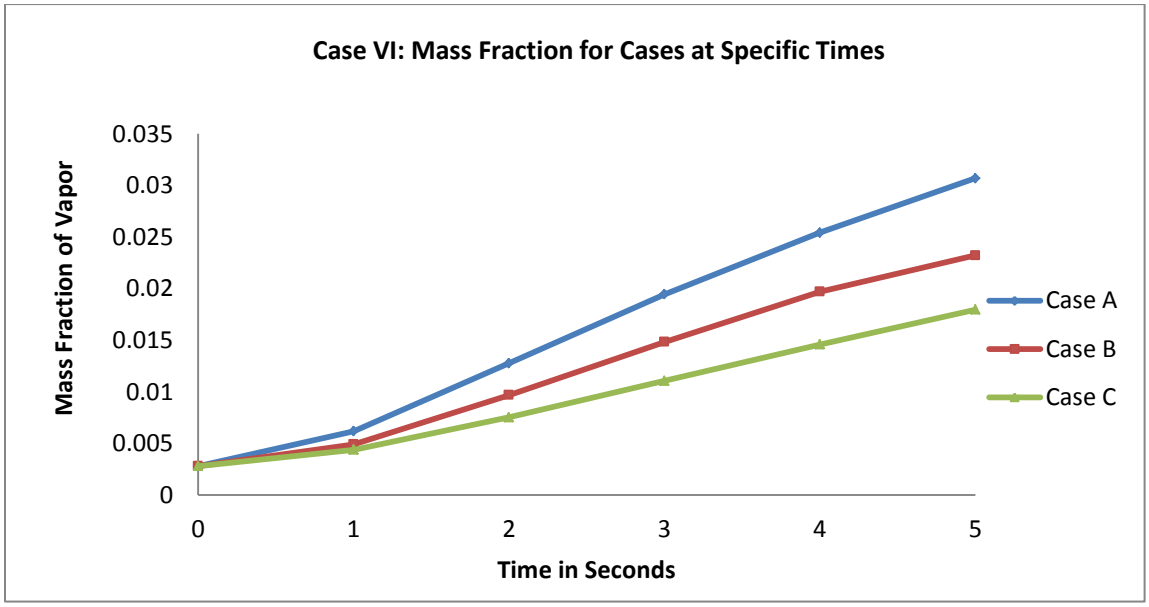

Figure 3.42 Mass fraction Volume fraction of vapor pentane for different heating levels of Case VI

Figure 3.43 Piston position for different heating levels of Case VI

3.1.2.6 Case VII varying wall surface temperature

In the subsequent cases, a new geometry will be used which has three W-shaped tubes; Configuration-VII. These tubes should resemble the three coils heat exchanger used by Dyverga's prototype. The new proposed geometry is shown in Figure 3.44 and its corresponding contour of initial volume fraction of vapor pentane is shown in Figure 3.45. In this case, the objective is to study the change in the system performance when heat source at different temperature is used. An increase in the heat source temperature increases the surface temperature of the tube, thus, impact of the heat source temperature was studied by varying the temperature of the tube surface. By varying the surface temperature and according to studies done on pentane boiling on a flat surface, the boiling regime will change and therefore might affect the performance of the system [Incropera 2006]. Table 3.5 lists different temperatures applied as a boundary condition on the walls of the W-shaped tubes. These

temperatures were selected to be less than 80 ^{o}C and above the saturation temperature of pentane which is 36 ^{o}C. Note that all tubes are considered to be fully submerged.

The contours of volume fraction of vapor pentane are presented in Figure 3.46 at different times for the given cases. A common observation in all these plots is the accumulation of high quality mixture in the upper humps of the tubes. The general patterns of the mixture quality are quite similar for all cases but the quality of the mixture at any particular location in the tube increased with an increase in the temperature.

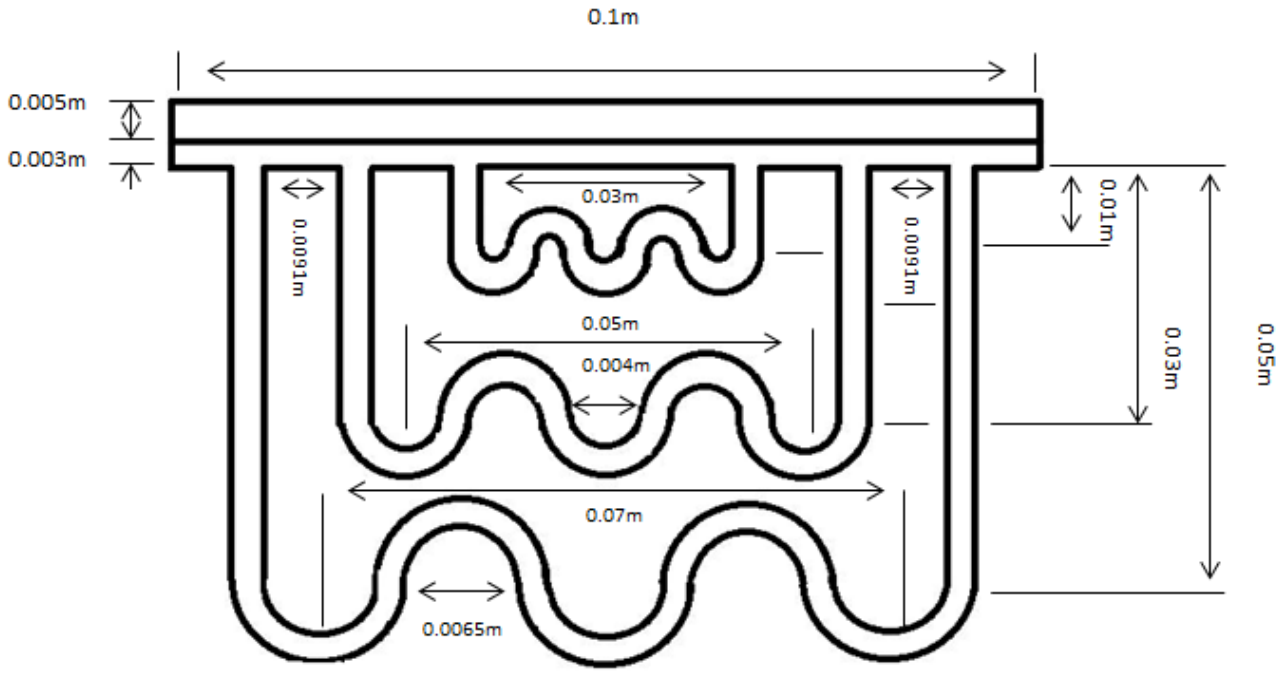

Figure 3.44 Geometry of cases VII and VIII

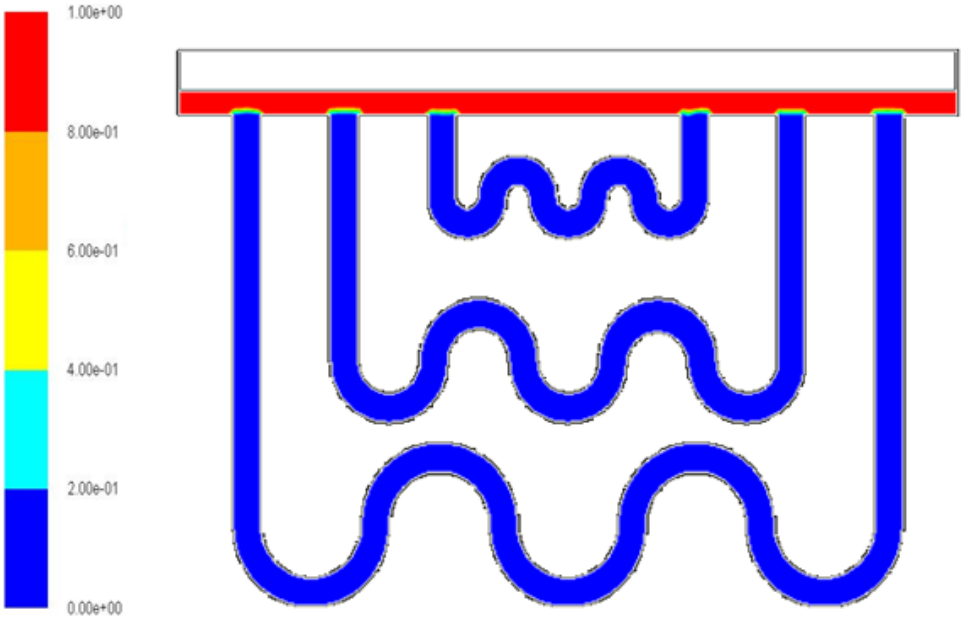

Figure 3.45 Cases VII: contours of volume fraction of vapor pentane at t = 0 sec

Table 3.5 Case VII: list of surface temperatures applied on the walls of Configuration-VII geometry

Cases	Temperature (^{o}C)
case A	45
case B	55
Case C	69
Case D	80

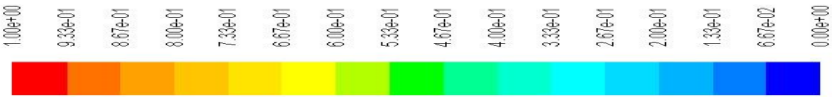

Case	Time = 0.5 second	Time = 1 second	Time = 1.5 seconds	Time = 2 seconds
A				
B				
C				
D				

Figure 3.46 Contours of volume fraction pentane for different configuration of Case VII

The effect of increase in the surface temperature on the parameters of interest is shown in Figures 3.47 through 3.49. As shown in the figures, all parameters of interest that define system

performance increased with an increase in the surface temperature. From Figure 3.47 it can be noticed that the average volume fraction of vapor pentane in the domain increased nonlinearly with time. The trend of this increase was different between these cases; for instance after 1 second, the domains of Cases C and D were occupied by almost 51 % of vapor pentane. While for Case B and A, vapor pentane only occupied 36% and 28% respectively. At 2 seconds, the domain of Case D become the most occupied domain with vapor pentane at 73% while Case C was lower by 6%. Cases B and Case A were still below 60%. The difference in volume fraction of vapor between the cases is due to the difference in the rate of evaporation for every case as seen in Figure 3.48. In this figure, it is clearly evident that the higher the tube surface temperature, higher is the evaporation rate in the system. This also corresponds to a quicker expansion in the domain as seen in Figure 3.49. After 5 seconds, the quality of mixture pentane had reached 3.6% for Case D while for other cases the quality of the mixture was at 2.6 % for Case C, 1.8 % for Case B and 1.1% for Case A. Similar to mass fraction, piston position has increased the most for Case D and it reached 4.8 cm after 2 seconds, this corresponding to a 600% expansion in the domain from its initial volume. As for Case C, piston reached to 3.8 cm and for Cases B and A, it reached to 2.7 cm and 1.7 cm, respectively.

The results from this case show that the system will perform better when the tube surface temperature is the high. Note that the rate of heat transfer to the working fluid inside the heat exchanger tube may be reduced due to the change in the boiling regime with an increase of the surface temperature. According to Stutz et al. [2011], pentane boiling regime is expected to change from nucleated boiling to film boiling when surface temperature is above 70 ^{o}C. In nucleated boiling vapor bubbles are formed at a smaller size on the surface while in film boiling a vapor blanket is formed on the surface creating an insulation region before it detaches as a large vapor bubble. This blanket of vapor causes the heat transfer rate to reduce hence the rate of evaporation was expected to reduce. The presence of film boiling is evident in some plots in Figure 3.46. However, the results from this simulation showed that this shift in the boiling regime does not have any noticeable effect on the overall system performance.

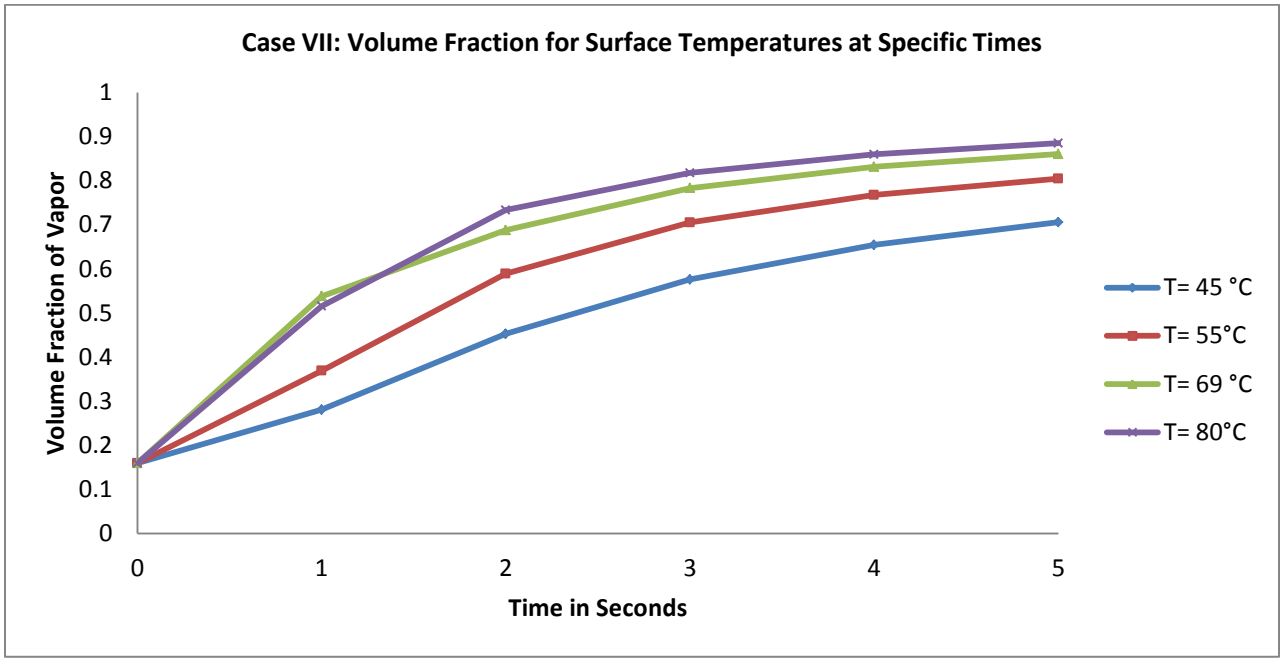

Figure 3.47 Volume fraction of vapor pentane for different surface temperatures for Case VII

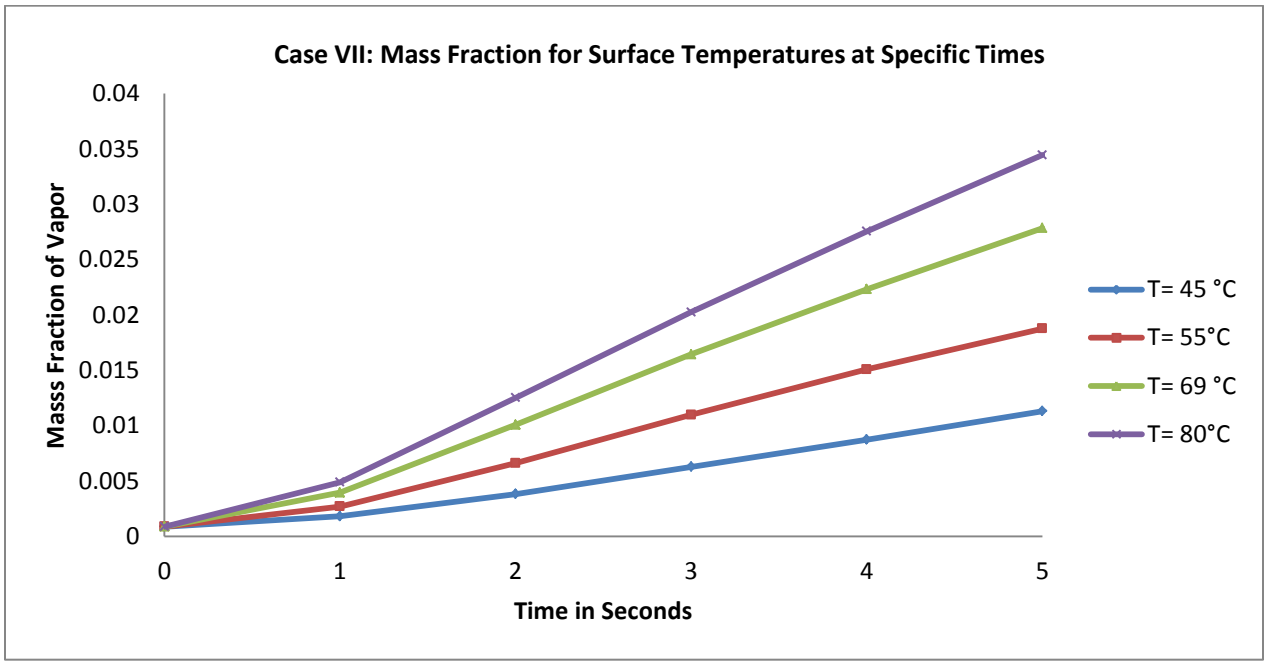

Figure 3.48 Mass fraction of vapor pentane for different surface temperatures for Case VII

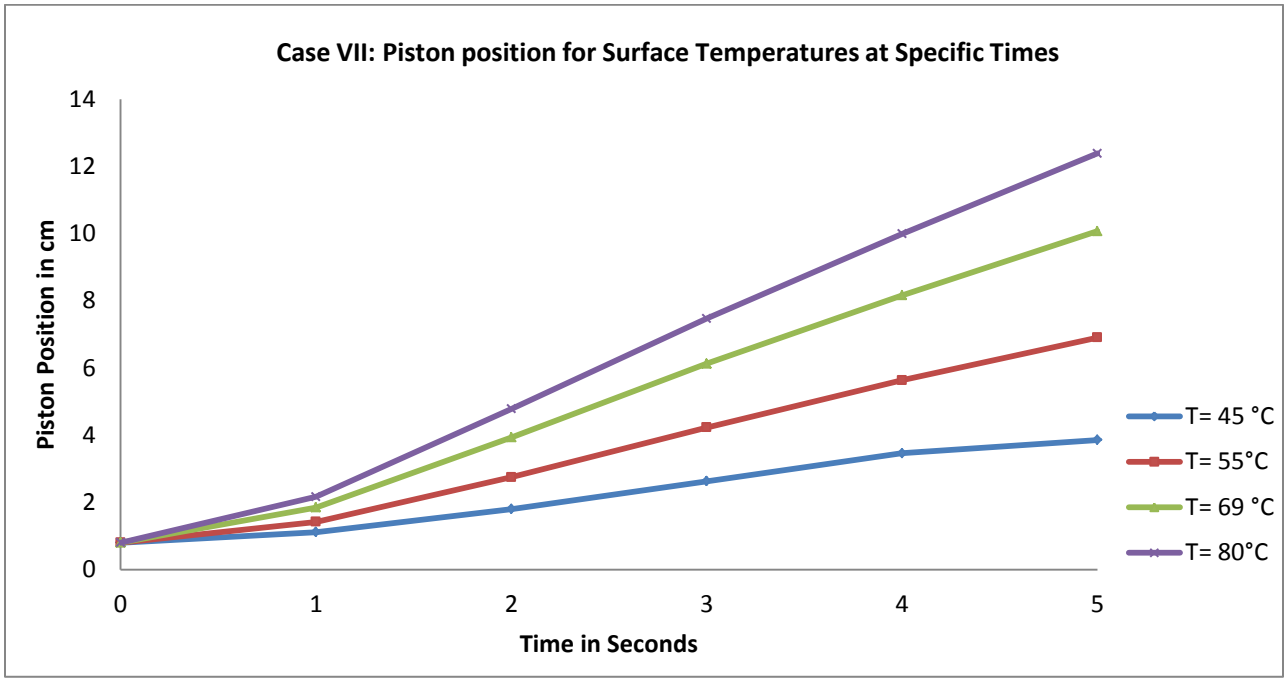

Figure 3.49 Piston position for different surface temperatures of Case VII

3.1.2.7 Case VIII varying orientation of the geometry

As mentioned in Chapter 1, in Dyverga's system, the chamber or domain rotates while undergoing the phase change and expansion/compression. As the domain orientation with respect to gravity changes, it may influence the dynamics of the vapor mixture in the domain and tube since the buoyancy forces due to the density variation acts parallel to gravity. Thus, in this case, the effect of change in the domain orientation with respect of gravity is investigated at different inclination angles. This was achieved by varying the direction of the gravity vector in the numerical model. As seen in Figure 3.50, β is the angle of gravity vector with respect to the x-axis and will be varied to change the domain orientation with respect to gravity. Four different cases were considered having different values of β that varied from the vertical position where β is at 90^{o} to an angle of 65^{o}. These are the angles over which the heat exchanger is expected to be in contact with the heat source. The x and y components of the gravity was modified in the numerical model according to these angles. The tube surface temperature used for this case was 69 ^{o}C and the process was simulated for 5 seconds.

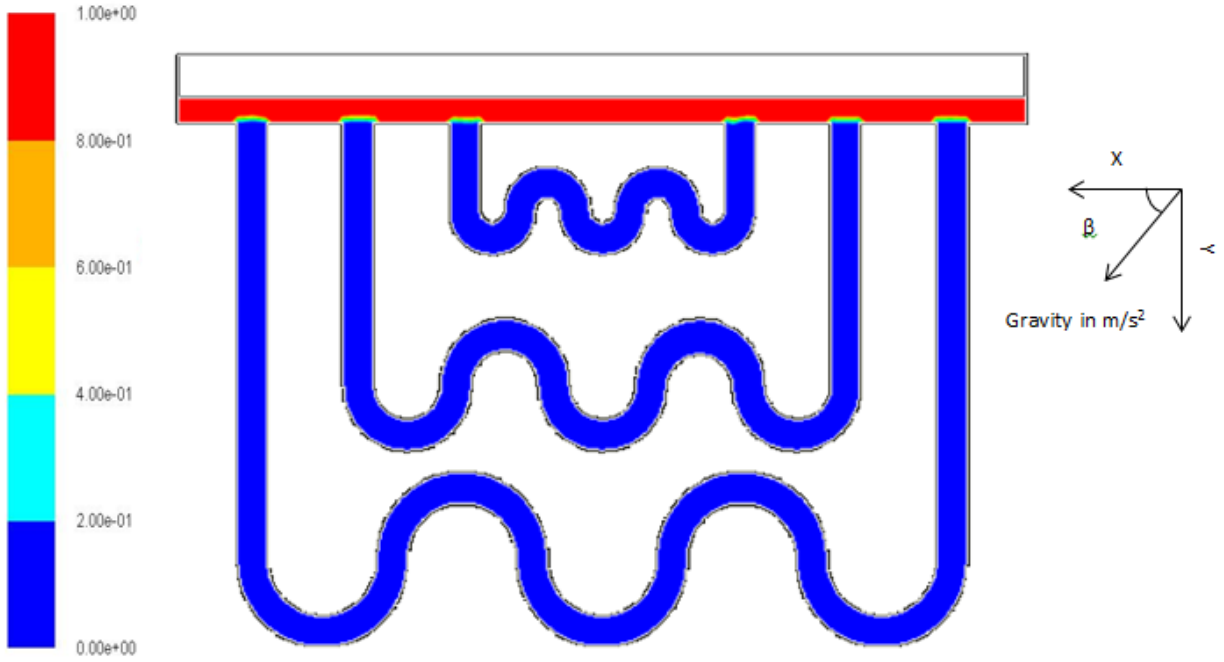

Figure 3.50 Case VIII: contours of volume fraction of vapor showing angle to be varied

Table 3.6 Case VIII: List of angles used for gravity

Cases	Angle β in degrees
Case A	90°
Case B	85°
Case C	75°
Case D	65°

The contours of the volume fraction of vapor pentane are shown in Figures 3.51 and 3.52 at 1 second and 4 seconds, respectively, which illustrates the effect of change in orientation. In Figure 3.51 after 1 second, the volume fraction of the mixture was symmetric with respect to the normal axis in the domain such that the lightest fluid i.e. vapor were evenly collected in the top section of the domain. This is expected as the domain has the vertical orientation. As the inclination angle started to decrease, the light vapor started to gather in the upper right corner, which is the highest section with respect to gravity. In Figure 3.52, the distribution of volume fraction of vapor pentane in each of the domain is shown after 4 seconds, it is clear that the highest volume fraction in each of the domain was still affected by the orientation of the

system. The most uniform distribution seems to be in Case A where the system is in it is vertical position. And the highest volume fraction of vapor was found in the top right corner of geometry of Case C. The effect of domain inclination is also evident in the tubes after 4 seconds.

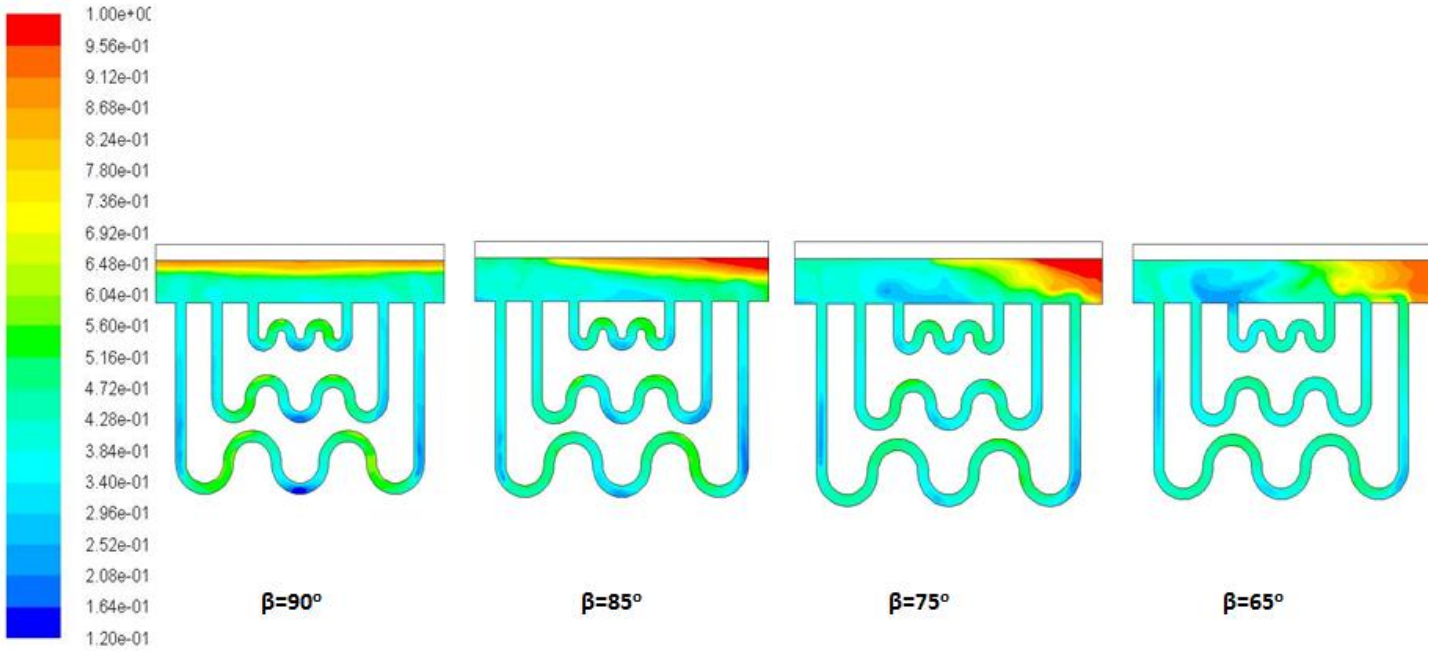

Figure 3.51 Case VIII: contours of volume fraction of vapor at time = 1 sec

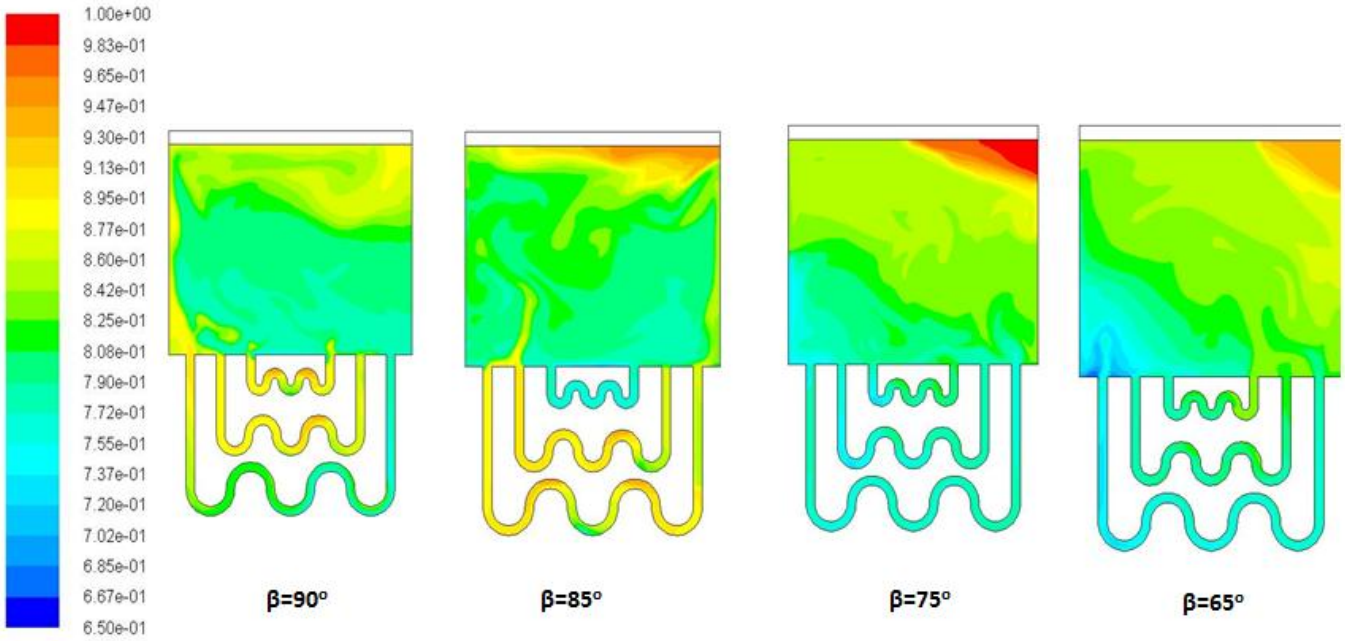

Figure 3.52 Case VIII: contours of volume fraction of vapor at time = 4 sec

The average values of the parameters of interest i.e. volume fraction, mass fraction and piston position are plotted in Figure 3.53 through 3.55. The results show a negligible effect of the orientation of the system on these parameters. This indicates that the orientation of the system does not have any significant effect on the system performance.

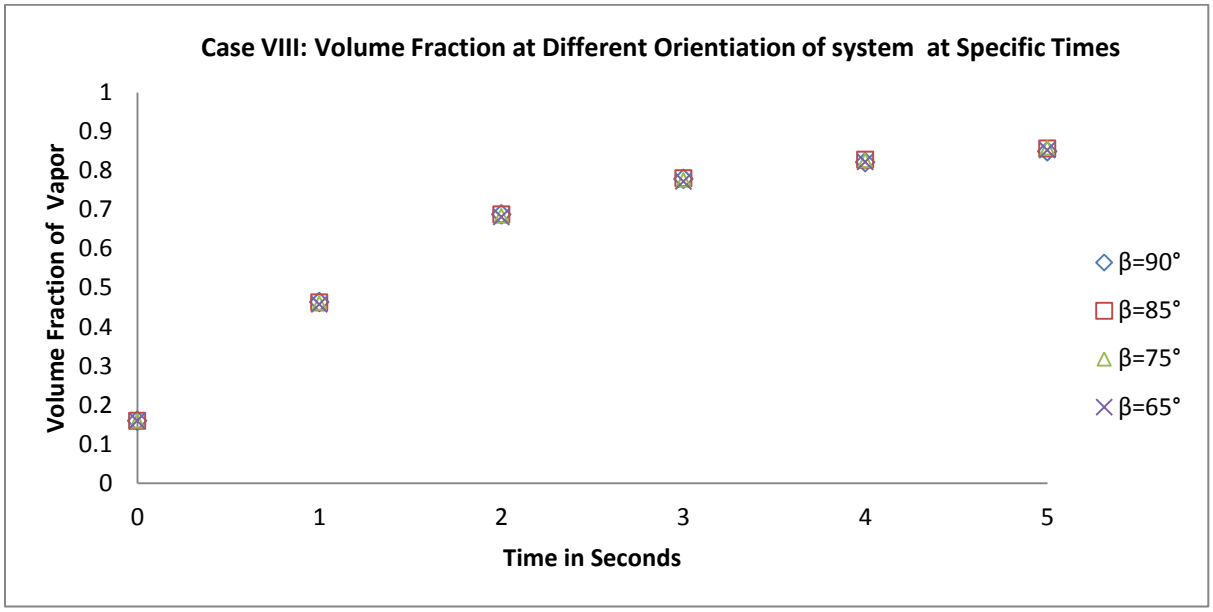

Figure 3.53 Volume fraction of vapor pentane at different orientation for Case VIII

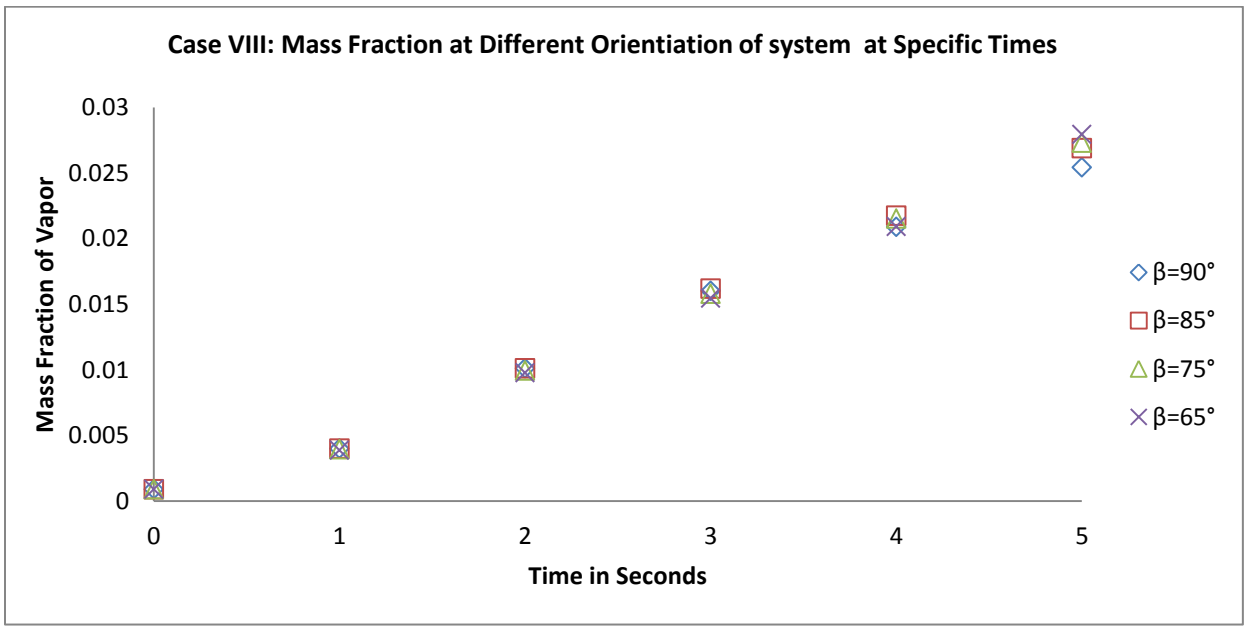

Figure 3.54 Mass fraction of vapor pentane at different orientation for Case VIII

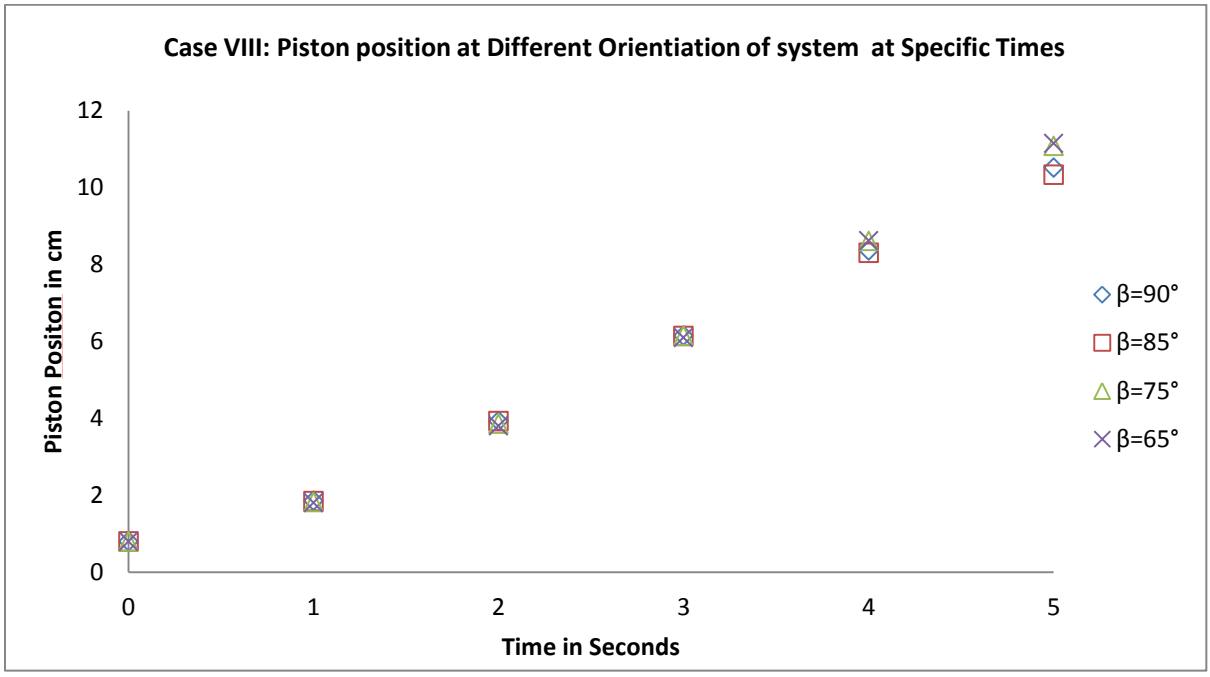

Figure 3.55 Piston position in cm at different orientation for Case VIII

CHAPTER 4: CONCLUSIONS

The present thesis is based on an industry-sponsor project involving a novel waste heat-to-electricity conversion system. The system is developed by an Ontario-based Dyverga Energy Corporation. The proprietary system, named SmartorQ, utilizes thermal energy from a low temperature heat sources to produce torque that drives an electric generator. These low temperature heat sources generally have temperatures below 80 ^{0}C. Dyverga has built a simplified proof of concept system to successfully demonstrate the operation and to support understanding for patenting. The system needs to be studied further through scientific research to help with optimizing the product development, component design, and overall system performance. Some key areas of the design which lack thorough understanding are (i) the heat extraction from low temperature heat source and its effective transfer to the working fluid, (ii) phase-change processes and associated dynamics of the working fluid, and (iii) heat rejection from the working fluid to ambient conditions. The heat exchanger design is a crucial component of the system, where the working fluid undergoes two-way phase change process at different stages. The efficiency of the system depends on the performance of the heat exchanger. Therefore, proper design of heat exchanger is crucial for the system performance and hence its marketability.

The main objectives of this study are to develop simulation tools (numerical model) that will allow to simulate the thermo-fluid processes in various system components and to use this numerical model to study the heat transfer and phase-change processes along with the work interactions.

In the first part of this study, a novel numerical model was developed using the commercial CFD software Fluent. The novelty of this model was its capability to simultaneously simulate the phase-change and moving boundary processes. To the best of our knowledge, this is the first time such integrated model has been developed. The model coupled the Mixture model and the Dynamic Mesh model via developed user-defined functions. Details are presented in Chapter 2. However, due to the limitations of the CFD software, the investigations were restricted to the fundamental heat transfer and phase-change processes in the lower vessel and

the associated heat exchanger coil which undergoes the boiling process, along with the piston movement in the vessel.

The heat exchanger coil is one of the key components of the system where the primary phase change process takes place. The key parameter that regulates the performance of the overall system is the rate of phase-change of the working volatile fluid in the heat exchanger and its influence on the boundary work in the vessel. This rate of phase-change is directly dependent on the heat exchanger design. Similarly, the type of volatile fluid used in the system also influences the system performance as well as dictates the suitability of the waste heat source. Thus, the main focus on the second part of this study was on a detailed investigation of the phase-change process in the heat exchanger coil and its design improvement as well as the type of the working fluid. Chapter 3 presents these results.

In the first part of the parametric study four different working fluids: methanol, ethanol, pentane and butane, which were selected in consultation with Dyverga were compared using the developed numerical model. Two cases were considered, in the first case the working fluids had equal liquid-to-vapor volume ratio while in the second case, the same mass for the working fluids was considered. Results showed that pentane has evaporated the most and had the most work output on the piston among the four working fluids considered. It is expected due to pentane's low boiling point and low latent heat of evaporation. Results also showed that the boiling regime for the four working fluids was the same, i.e. nucleated boiling.

In the second part of the parametric study, the heat exchange and the phase change processes inside the heat exchanger was investigated. In the first case of this part, three U-shaped coil heat exchanger with different coil diameter and heat transfer area were compared. Results showed as expected that the heat exchangers with smaller diameter and larger surface area transfer heat to the working fluid at a much quicker rate. The investigation of the phase change process inside the heat exchanger coil showed the presence of a cyclic process inside the heat exchanger tube where the high density low volume fraction mixture (heavy fluid) near the bottom of the vessel enters from one end of the heat exchanger and the low density high volume fraction mixture (light fluid) escapes in the form of jet into the vessel from the other end of the tube. It was found that the speed of the jet increased with an increase in surface

area of the heat exchanger coil. The cyclic process was noticed to initiate first with configuration with smallest diameter and the largest surface area tube and results of pressure contours showed an asymmetrical distribution of pressure in the coil although the geometry was symmetric.

In the next case, the effect of the configuration of the heat exchanger was investigated while maintaining the same heat transfer surface area and diameter of the coil. Two new configurations were considered, the first had two concentric U-shaped tubes and the second had a single W-shaped tube. Results showed that the local phase change of the working fluid was the fastest for the W-shaped tube however; the average values of volume fraction, mass fraction and work output on the piston were independent of the heat exchanger configuration. In addition, it was noticed that the cyclic process was initiated in the W-shaped heat exchanger much earlier than that in the other configurations.

In the next case, the mass of the working fluid and the surface area of the heat exchanger were increased by increasing the number of U-shaped tubes in the domain. The purpose was to study the effect of increase in these parameters on the quality and mixing within the heat exchanger tube and vessel, and on the piston movement. Results showed that the configuration with larger surface area and higher fluid mass produced higher mixture velocities, stronger jet flow from the tube and consequently better mixing in the vessel. It is also observed that the cyclic process started earlier as the tube area and the fluid mass in the tube increased. Results also showed as expected, that the overall performance and the response time in domain expansion was reduced significantly. In the subsequent case, a novel method to control the cyclic process inside Dyverga system was proposed. The method suggests the use of nozzle shape outlet at the tube end where the mixture is desirable to escape from. The use of this nozzle shape had insignificant effect on the mixture velocity in the vessel and no effects were found on the average parameters of the system.

In next case, the level of submergence of the heat exchanger was studied. Although it is expected that higher the submergence level, the better would be the system performance, the focus of this case was to quantify the relative effects on the evaporation rate and the system

response. Results showed a significant improvement in the local and average evaporation rate inside the heat exchanger and the work output on the piston when the heat exchanger is fully submerged.

In this study it was important to investigate if the boiling regime has any effect on the overall performance of the system. For this reason in the next case the surface temperature was varied and it was expected that pentane boiling regime will change from nucleated to film boiling when surface temperature is above 70 ^{O}C. Due to this transition it was expected that the heat transfer rate might be reduced hence reducing the evaporation rate, however, results showed that increasing the surface temperature increases the evaporation rate and hence system performance.

In the last study, the effect of the orientation of the system on the performance was investigated. For this reason four different angles were considered and results at different orientations showed that mixture with highest quality was found to gather in the highest most area in the vessel as expected. Nevertheless, results also showed that orientation had no significant effect on the average parameters of the system.

4.1 Recommendations for future work

This novel model will be used by Dyverga as the base model and further improvements will be done to simulate thermo-fluid processes is all components of Dyverga's system for better understanding and optimization. Some recommendations for the future work are as follows: Since the findings of this parametric study were related to the boiling and moving boundary covering only a part of the full process occurring in Dyverga's system, it is recommended to simulate the condensation with the moving boundary depicting isobaric contraction. Although, the results for the proposed 2D numerical model can be used to understand the different aspects of the Dyverga system, it was noticed that the time for domain expansion in Dyverga's prototype unit was much less than that seen in the numerical model. For instance, in Dyverga's system, it took less than a second to displace the insulated membrane (piston) to the desired position (~15 cm) while in the proposed numerical model, it took more than 5 seconds for the domain to expand to 15 cm refer to Case IV. The reason behind this slow piston movement is

mainly the heat transfer area to the mass of working fluid ratio which was found to be much lower in the 2D geometries used in this thesis i.e. ~0.9 while in the real system it is 2. Therefore, if time is not a limitation it is recommended to build a 3D geometry that has an equivalent heat transfer area to the mass of working fluid ratio found in the real system. Lastly, if future updates to Fluent software are able to resolve the problems encountered in this thesis when simulating the full model, it is then recommended to run the proposed parametric study on the full model simulating the boiling, condensation processes simultaneously with the boundary movement.

References

Asad, A.R., Ramanathan, A., Kumar, P., Analysis of Unsteady Aerodynamics on Dragonfly Using CFD The 11th Asian International Conference on Fluid Machinery Paper ID AICFM_FM_004, 2011.

BCS Incorporated, Waste Heat Recovery: Technology and Opportunities in United States Industry, USA, 2008.

Bedard, S., Waste Heat to Power Natural Resources Canada, Energy 2009: Lean and Green, Toronto, November, 24 and 25, 2009.

Cengel, A., Boles, M., Thermodynamics: An Engineering Approach, New York, NY: McGraw-Hill, 0-07-2383312-1, 2008.

Dumont, K., Stijnen, J.M.A., Vierendeels, J., Van-de-Vosse F.N. and Verdonck, P.R., Validation of a Fluid–Structure Interaction Model of a Heart Valve using the Dynamic Mesh Method in Fluent, Computer Methods in Biomechanics and Biomedical Engineering, 7:3, 139-146, 2004.

Energy Information Administration report 2010. United States Energy Information Administration, Washington DC, 2010.

Fluent 13 Documentation, Fluent Inc., 2010.

Frendreis, S.G.V, Skujins, T., Cesnik, C.E.S, Six-Degree-of-Freedom Simulation of Hypersonic Vehicles AIAA Atmospheric Flight Mechanics Conference 10, Chicago, Illinois AIAA 2009-5601, 2009.

Galanis, N., Cayer, E., Roy, P., Denis, E.,S., and Désilets, M., Electricity Generation from Low Temperature Sources, Journal of Applied Fluid Mechanics, Vol. 2, No. 2, pp. 55-67, 2009.

Ganguli, A., Sathe, M., Pandit, A., Joshi, J., Vijayan, P., Hydrodynamics and Heat Transfer Characteristics of Passive Decay Heat Removal Systems: CFD Simulations And Experimental Measurements, Chemical Engineering Science 65, 3457–3473, 2010.

Godwin, H., Low Differential Temperature Rotary Engines, Dyverga Energy Corporation, Patent WO 2011-057402 A1. 19 May 2011.

Guo, D.Z., Sun, D.L., Li, Z.Y., Tao, W.Q., Phase Change Heat Transfer Simulation For Boiling Bubbles Arising From a Vapor Film By VOSET Method, Numerical Heat Transfer Part A, 59 857–881, 2011.

Hasegawa, T., Kishimoto S., and Suzukawa, Y, Environmentally Compatible Regenerative Combustion Heating System, 1–8, 2000.

Hasanuzzaman, M., Rahim N.,A., Hosenuzzaman, M., Saidur, R., Energy Savings In The Combustion Based Process Heating In Industrial Sector, Renewable and Sustainable Energy Reviews, 4527-4536, 2012.

He, W., Hou, J., Zhang, Y., Ji, J., Thermodynamic Analysis of Thermal Efficiency and Power of Minto Engine, Energy, 36, 6461-6470, 2011.

Incropera, F. DeWitt, D., Bergman, T., Lavine, A., Fundamentals of Heat and Mass Transfer, sixth edition, NJ, John Wiley and Sons, 07020-5774, 2006.

Krause, F., Schuttenberg, S., and Fritsching, U.,Modeling and Simulation of Flow Boiling Heat Transfer, International Journal of Numerical Methods for Heat and Fluid Flow, Vol. 20 No. 3, pp. 312-331, 2010.

Kristóf, G., Szabó, k.G., Régert, T., Modeling of Boiling Water Flow in the Horizontal Steam Generator of the Paks Nuclear Power Plant, ANSYS Conference and 26th CADFEM Users' Meeting, CFD.HU Ltd., Hungary, 2008.

Kuzmin, D. Introduction to Computational Fluid Dynamics, Institute of Applied Mathematics, University of Dortmund, Germany, 2005.

LiLi, G., Lin, Z., ZhiLei, M., Chen, X., ZhangPing, X., MingZhao, D., The Numerical Simulation of Flow and Boiling Heat Transfer of Two Phases in Horizontal Tube, Chagzhou University, China, 2012.

Liua, J.W., Lee, D.J., Su, A., Boiling of Methanol and HFE-7100 on Heated Surface Covered with a Layer of Mesh, International Journal of Heat and Mass Transfer, 44 241-246, 2001.
[Punekar 2010] Punker, H., Using Evaporation Condensation Model, Fluent, ANSYS Inc. 2010.

Rich,S., Svensson, T., Data Center Energy Efficiency "Outside the box", PTC, 2010.

Stutz, B.,Morceli, C. H. S., Da Silva, M., Cioulachtjian,S., Bonjour, J., Influence of nanoparticle surface coating on pool boiling,Experimental Thermal and Fluid Science 35 1239–1249, 2011.

Sun, D., L., Xu, J.L., Wang, L., Development of a Vapor–Liquid Phase Change Model for Volume-of-Fluid Method in Fluent International Communications in Heat and Mass Transfer 39, 1101–1106, 2012.

Turner, W., and Doty, S., Energy Management Handbook, p. 193, 2006.

U.S Department of Energy (2008), Energy Efficiency and Renewable Energy: Reducing Waste Heat, 2008.

United Nations Environmental Program, Thermal Energy Equipment: Waste Heat Recovery, Energy Efficiency Guide for Industry in Asia, 2006.

Waclawiak, K., and Kalisz, S.,Using Fluent Code to Predict Deposition During Combustion of Solid Fuels; International Conference on Heat Exchanger Fouling and Cleaning, Crete Island, Greece, 2011.

Vatanakul, M.,Cruz, E., and Swanepoel, J.,Energize August, 72, 2011.

Vargaftik, N.B., Tables on the Thermophysical Properties of Liquids and Gases 2nd edition, Hemisphere Publishing Corporation, Washington, USA, 0-470-90310-4, 2005.

Welch, S.W.J., Wilson, J., A volume of Fluid Based Method for Fluid Flows With Phase Change, Journal of Computational Physics 160, 662–682, 2000.

Wilbur, L., C.,Handbook of Energy Systems Engineering-production and Utilization, John Wiley and Sons, 1985.

Ye, Q., Using Dynamic Mesh Models to Simulate Electrostatic Spray-Painting, Institut fur Industrielle Fertigung und Fabrikbetrieb Universitat Stuttgart Nobelstr 12, D-70569 Stuttgart, Germany, 2003.

Zhang, L., Waste Heat Recovery from Metal Industries, JOM, Vol. 64, 2012.

Appendix A: Theoretical Calculations

A.I Theory calculations used for validating the numerical model:

Gets heat transfer in (J/m) using the following equation, where $\dot{q}$ is the heat flux (Watt/sec) applied to the wall All equations using in this appendix where adopted from the following references [Incropera 2006] and [Cengel and Boles 2008]:

$$q_{(t)} = \dot{q} \times Area \times Time \tag{A.1}$$

Using Energy equation, enthalpy of mixture after at time (t) is,

$$h_{(t)} = h_{(t-t_0)} + q_{(t)} \tag{A.2}$$

Quality of mixture at time (t) can be determined by:

$$x_{(t)} = \frac{h_{(t)} - h_{(f)}}{h_{fg}} \tag{A.3}$$

(g) and (f) subscripts refers to saturated vapor and saturated water respectively at the given pressure and temperature.

Specific volume at time (t) can be determined using the equation below:

$$v_{(t)} = v_{(f)} + x_{(t)}(v_{(g)} - v_{(f)}) \tag{A.4}$$

Volume of the domain at time (t) in m^3/m

$$V_{(t)} = v_{(t)} * (Mass) \tag{A.5}$$

Piston Height in meters,

$$H_{(t)} = \frac{V_{(t)}}{Area} \tag{A.6}$$

A.II Surface temperature calculations:

Thermal circuit:

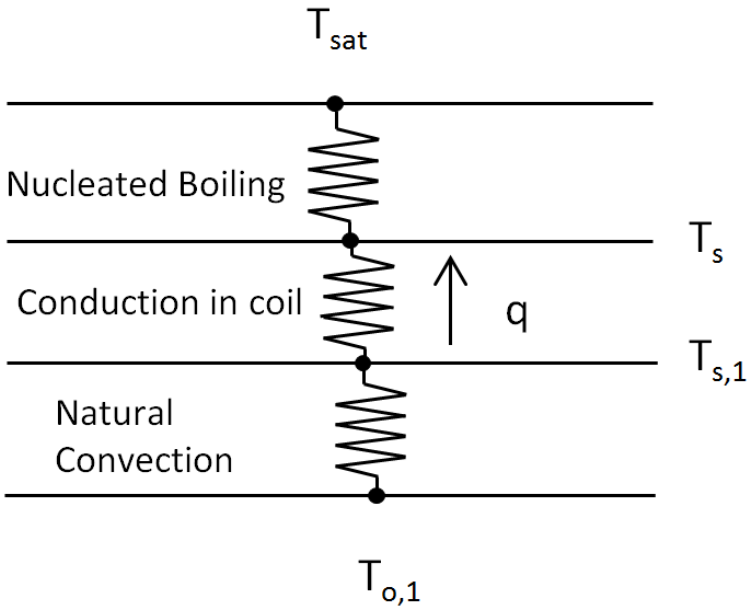

Figure A.1 thermal circuit used to calculate surface temperature T_s

At first methanol was assumed to undergo nucleated boiling in the system, then the correlation of heat transfer rate (Watt/m^2) in the system was estimated. In table A.1 list of parameters used for methanol is presented. All equations using in this appendix where adopted from the following references [Incropera 2006] and [Cengel and Boles 2008].

$$\frac{q}{A} = \mu_L h_{fg} \left[\frac{g(\rho_l - \rho_l)}{\sigma} \right]^{1/2} \left[\frac{C_{pL}(T_s - T_{sat})}{C_{sf} h_{fg} \, \mathrm{Pr}_L^{1.7}} \right]^3 \qquad \text{(A.7)}$$

Table A.1 List of parameters used to solve equation A.7 [Incropera 2006] and [Cengel and Boles 2008]

Viscosity Ns/m2 (μ_L)	3.28E-04
Latent heat J/Kg (h_{fg})	1120530
Density liquid Kg/m3 (ρ_l)	751.03
Density vapor Kg/m3 (ρ_v)	1.43
Gravity m/s2 (g)	9.81
Surface tension N/m (σ)	0.01887
Liquid specific heat J/kg (C_{pL})	2630
Surface-Liquid Combination (Cs,f)	0.00079
Saturation temperature of methanol ^{o}C (T_{sat})	64.7
Surface Temperature (T_s)	69
Prandtl number of liquid (Pr_L)	4.28

Now, Assuming a round coil and using the conduction heat transfer equation temperature $T_{s,1}$ ca be determined:

$$q = \frac{(T_{s,1} - T_s)}{R_{cond}} \tag{A.8}$$

R_{cond} is the thermal resistance of the copper coil and was estimated using cylinder equation and values of r_1, r_2 and L were measured of Diverga's system [Incropera 2006].

$$R_{cond} = \frac{\ln\left(\frac{r_2}{r_1}\right)}{2\pi KL} \tag{A.9}$$

Table A.2 Coil properties and dimensions

Radius, r_2 (m)	0.00635
Radius, r_1 (m)	0.005791
Thermal conductivity of copper (W/mK)	400
Length in m	2.9

After

Calculating $T_{s,1}$, then correlation for long horizontal cylinder was used to find the heat transfer rate (q) calculated using the following equations:

$$NU_D = \left[0.60 + \frac{0.387 Ra_D^{1/6}}{\left(1 + (\frac{0.559}{\Pr})^{9/16}\right)^{8/27}} \right]^2 \quad \text{(A.10)}$$

$$Ra = \frac{L^3 \rho^2 g (T_{o,1} - T_{s,1}) \beta \Pr}{\mu^2} \quad \text{(A.11)}$$

$$Nu = \frac{hL}{K} \quad \text{(A. 12)}$$

$$q = h(T_{o,1} - T_{s,1}) \quad \text{(A.13)}$$

Properties of water at 77 ^{o}C are listed below and using an iterative process surface temperature was found to be 69 ^{o}.

Table A.3 List of Water properties at 77 0C and other parameters used in equations A.10 through A11 [Incropera 2006] and [Cengel and Boles 2008]

Water viscosity Ns/m2 (μ)	0.00034599
Density liquid water Kg/m3 (ρ)	971.21
Gravity m/s2 (g)	9.81
Water Thermal Expansion K^{-1} (β)	0.01367
Water Thermal Expansion W/mK	0.67
Water specific heat J/kg (C_p)	4069.6
Temperature of Water ^{o}C ($T_{o,1}$)	77
Surface Temperature ($T_{s,1}$)	69.3
Prandtl number of water (Pr)	2.1

According to these calculations the temperature difference ($T_S - T_{sat}$) > 5 ^{o}C therefore the first assumption of using nucleated boiling correlation for methanol was correct [Liua 2001].

Appendix B: User Defined Functions

B.I: UDF I-used for full model with condensation and boiling

```
#include "udf.h"
#include "sg_mphase.h"
#include "dynamesh_tools.h"
static real v_prev = 0.0;/*Declaring previous velocity*/
static real force_cond=0.0; /*Declaring Force on piston condensation side */
static real force_boi=0.0; /*Declaring Force on piston boiling side */
static real mass=0.1; /*Declaoiring mass of piston*/

/*Saturation temperature for Pentane as a function of Pressure Using Antoine Equation*/
DEFINE_PROPERTY(saturation_temp,c,t)
{
static real a=6.87632; /* a, b, e are constants to be used in Antoine Equation*/
static real b=1075.780;
static real e=233.205;
real sat_temp, /*Declaring saturation temperature in Kelvin*/
real log_p,
real pressure; /*Declaring Pressure */

pressure= (((((C_P(c,t))/1000)+101.325)*760)/101.325); /* (C_P(c,t); macro to read gauge
pressure from domain in Pa, and convert to mmHg*/
log_p= log10(pressure);

       sat_temp=((b/(a-log_p))-e)+273.15;
       return sat_temp;

Message ("Sat_temp=%f, Pressure=%f",sat_temp , pressure);
}
DEFINE_CG_MOTION(mass_piston,dt,vel,omega,time,dtime)
{
       Thread *t;
       face_t f;
       real volume=0.0;
       real density;
       cell_t c;
       real NV_VEC(A);
       NV_S(vel, =, 0.0);
       NV_S(omega, =, 0.0);
       t=DT_THREAD(dt);
       begin_c_loop_int(c,t)/* Get Volume of the domain using this loop over macro*/
       {
       volume+=C_VOLUME(c,t); /*Adding every cell in the domain to get piston's volume*/

       density=C_R(c,t); /*Macro to call matrials density of piston*/
       }
       end_c_loop_int(c,t)
       vel[1]+= v_prev;/*Passing velocity to Fluent*/
       mass=density*volume; /*Calculates Mass of Piston, to be used in SDOF macro*/

}
```

```
DEFINE_CG_MOTION(Boiling_side,dt,vel,omega,time,dtime)
{
	Thread *t;
	cell_t c;
	face_t f;
	force_total=0.0;
	real NV_VEC(A);
	NV_S(vel, =, 0.0); /*Reset velocities */
	NV_S(omega, =, 0.0);
	if(!Data_Valid_P())
		return;
	t=DT_THREAD(dt); /*Get the thread pointer for which this motion is defined*/
	begin_f_loop(f,t)    /*Compute pressure force on body by looping through all faces
of piston on the boiling side*/
	{
	   F_AREA(A,f,t);
	   force_boi+= (F_P(f,t) * NV_MAG(A));/*Calculation of force on piston-boiling
side*/
	}
	end_f_loop(f,t)

	force_total= force_boi-froce_cond;/*Computing total forces in piston*/

    v_prev =((force_total-mass*9.81)*dtime/mass);/*Using newtons second law to get
piston's velocity*/

	vel[1]+= v_prev;/*Passing velocity to Fluent*/

	Message ("time=%f, y_vel=%f, force_boi=%f\n", time,v_prev, force_boi);
}


DEFINE_CG_MOTION(Cond_side,dt,vel,omega,time,dtime)
{
	Thread *t;
	cell_t c;
	face_t f;
	force_total=0.0;
	real NV_VEC(A);
	NV_S(vel, =, 0.0); /*Reset velocities */
	NV_S(omega, =, 0.0);
	if(!Data_Valid_P())
		return;
	t=DT_THREAD(dt); /*Get the thread pointer for which this motion is defined*/
	begin_f_loop(f,t)    /*Compute pressure force on body by looping through all faces
of piston on the condensation side*/
	{
	   F_AREA(A,f,t);
	   force_cond+= (F_P(f,t) * NV_MAG(A));/*Calculation of force on piston-
condensation side*/
	}
	end_f_loop(f,t)
	vel[1]+= v_prev;/*Passing velocity to Fluent*/
	Message ("time=%f, y_vel=%f, force_boi=%f\n", time,v_prev, force_boi);
}
```

B.II: UDF II-used for simplified model boiling-only

```
#include "udf.h"
#include "sg_mphase.h"
#include "dynamesh_tools.h"
static real mass=0.1; /*Declaring mass of Piston in Kg*/

 /*Saturation temperature for Pentane as a function of Pressure Using Antoine Equation*/
DEFINE_PROPERTY(saturation_temp,c,t)
{
static real a=6.87632; /* a, b, e are constants to be used in Antoine Equation*/
static real b=1075.780;
static real e=233.205;
real sat_temp, /*Declaring saturation temperature in Kelvin*/
real log_p,
real pressure; /*Declaring Pressure */

pressure= (((((C_P(c,t))/1000)+101.325)*760)/101.325); /* (C_P(c,t); macro to read gauge
pressure from domain in Pa, and convert to mmHg*/
log_p= log10(pressure);

       sat_temp=((b/(a-log_p))-e)+273.15;
       return sat_temp;

Message ("Sat_temp=%f, Pressure=%f",sat_temp , pressure);
}

DEFINE_CG_MOTION(mass_piston,dt,vel,omega,time,dtime)
{
       Thread *t;
       face_t f;
       real volume=0.0;
       real density;
       cell_t c;
       real NV_VEC(A);
       NV_S(vel, =, 0.0);
       NV_S(omega, =, 0.0);
       t=DT_THREAD(dt); /*get the thread pointer for which this motion is defined*/
       begin_c_loop_int(c,t)/* Get Volume of the domain using this loop over macro*/
       {
       volume+=C_VOLUME(c,t); /*Adding every cell in the domain to get piston's volume*/

       density=C_R(c,t); /*macro to call matrials density of piston*/
       }
       end_c_loop_int(c,t)

       mass=density*volume; /*Calculates Mass of Piston, to be used in SDOF macro*/

}
DEFINE_SDOF_PROPERTIES(definemass, prop, dt, time, dtime)
{

    prop[SDOF_MASS] = mass; /*Mass of piston*/

}
```

Appendix C: Mesh and time dependency for the different geometries

Mesh and time dependency of Configuration-II-A

Table C.1 Grid sizes used in the mesh dependency test for Configuration-II-A

	Grid 1	Grid 2	Grid 3	Grid 4
Element size in mm	**2**	**1.4**	**1**	**0.75**
Element initial counts	**2,880**	**5,958**	**10,771**	**23,100**

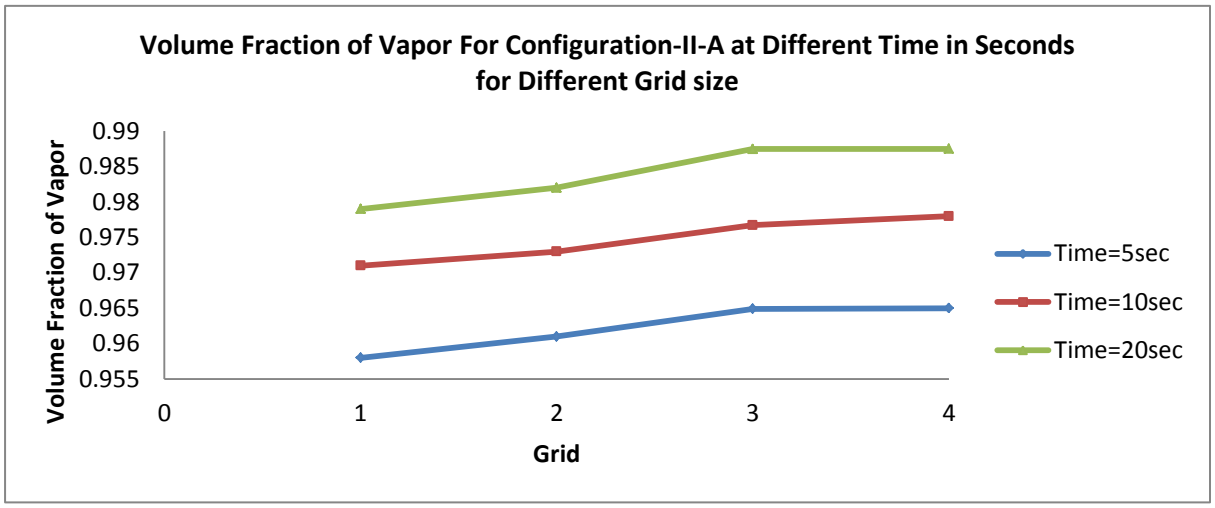

Figure C.1 Volume fraction of vapor at different grids size for Configuration-II-A

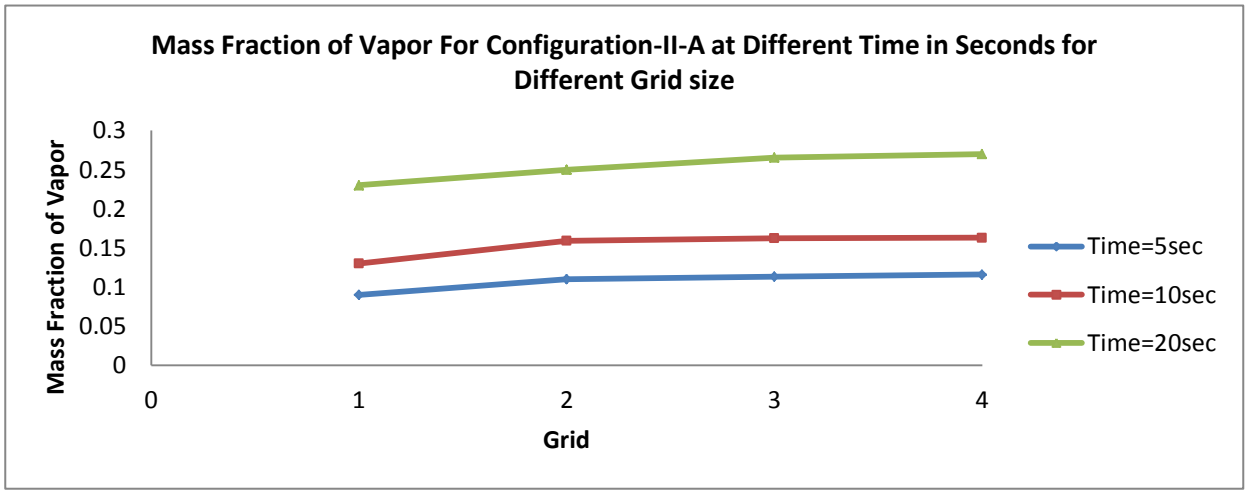

Figure C.2 Mass fraction of vapor at different grids size for Configuration-II-A

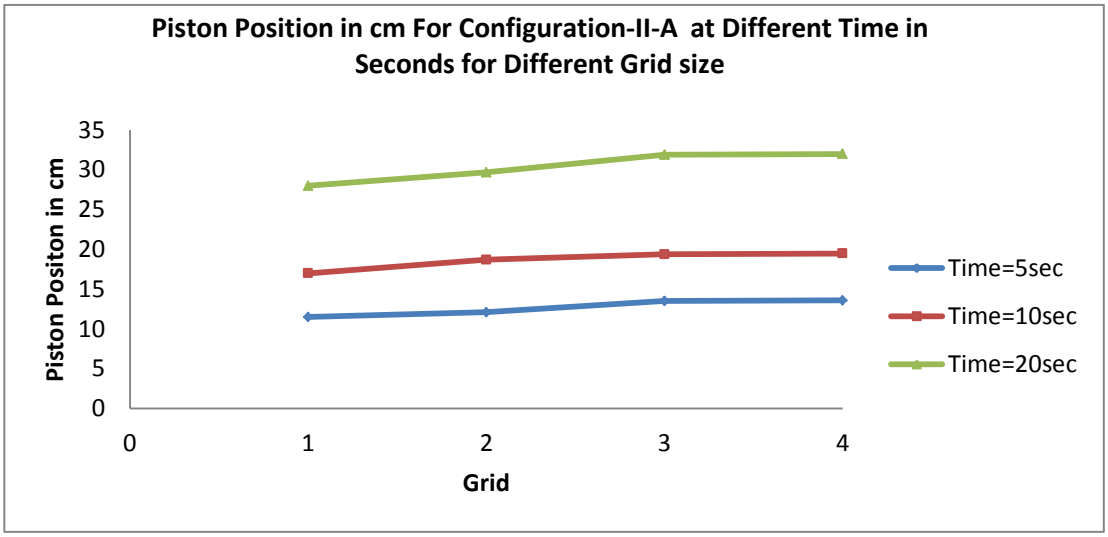

Figure C.3 Piston position at different grids size for Configuration-II-A

Table C.2 Time step values used for the time-step dependency test for Configuration-II-A

Case1	Case 2	Case 3	Case 4
0.01	**0.005**	**0.0025**	**0.001**

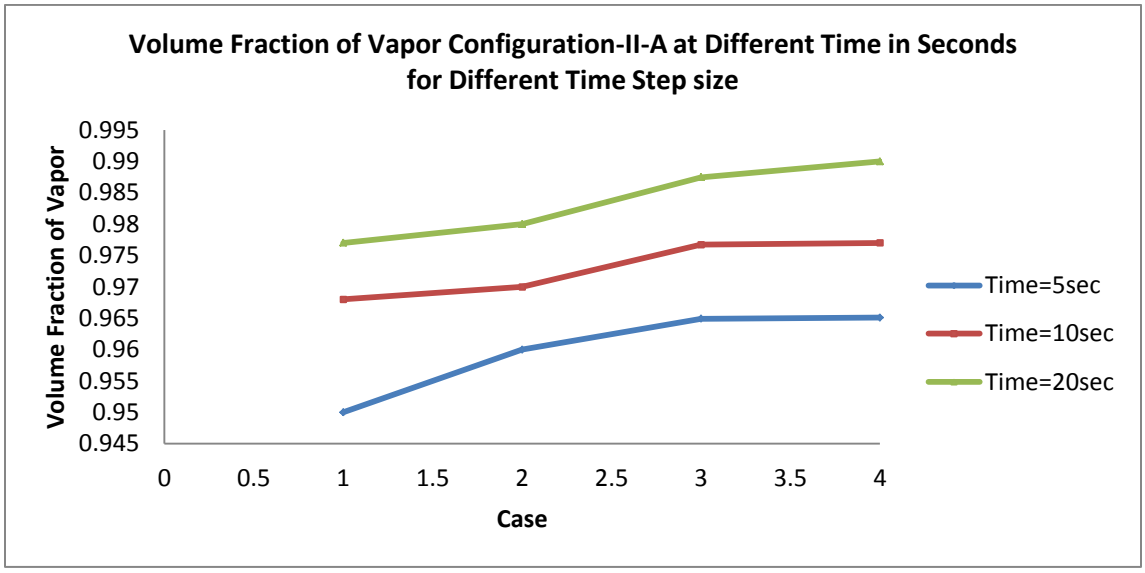

Figure C.4 Volume fraction of vapor at different time step size for Configuration-II-A

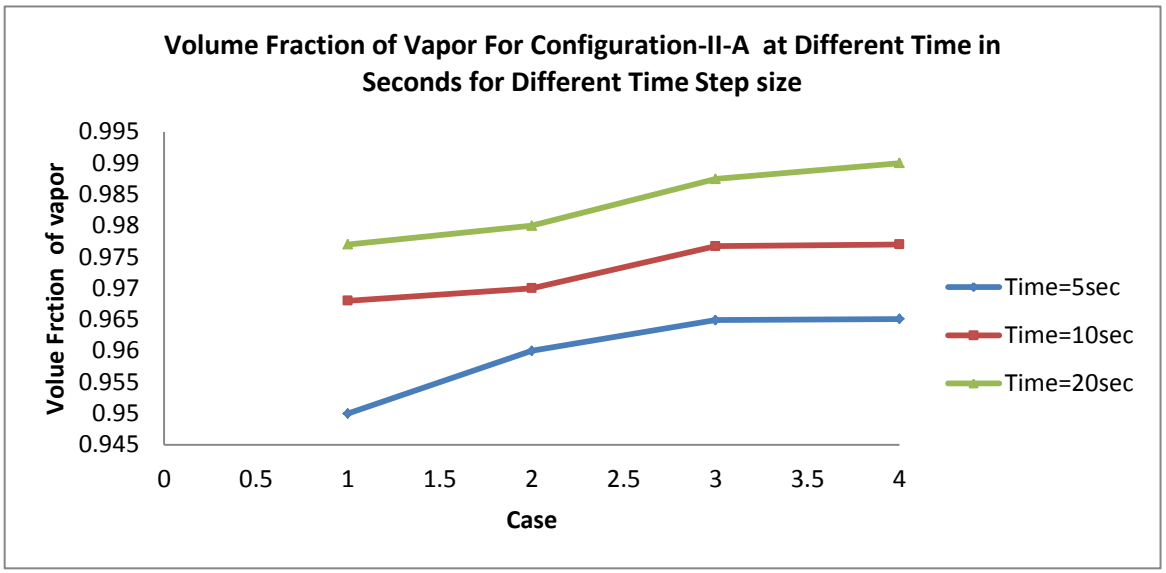

Figure C.5 Mass fraction of vapor at different time step size for Configuration-II-A

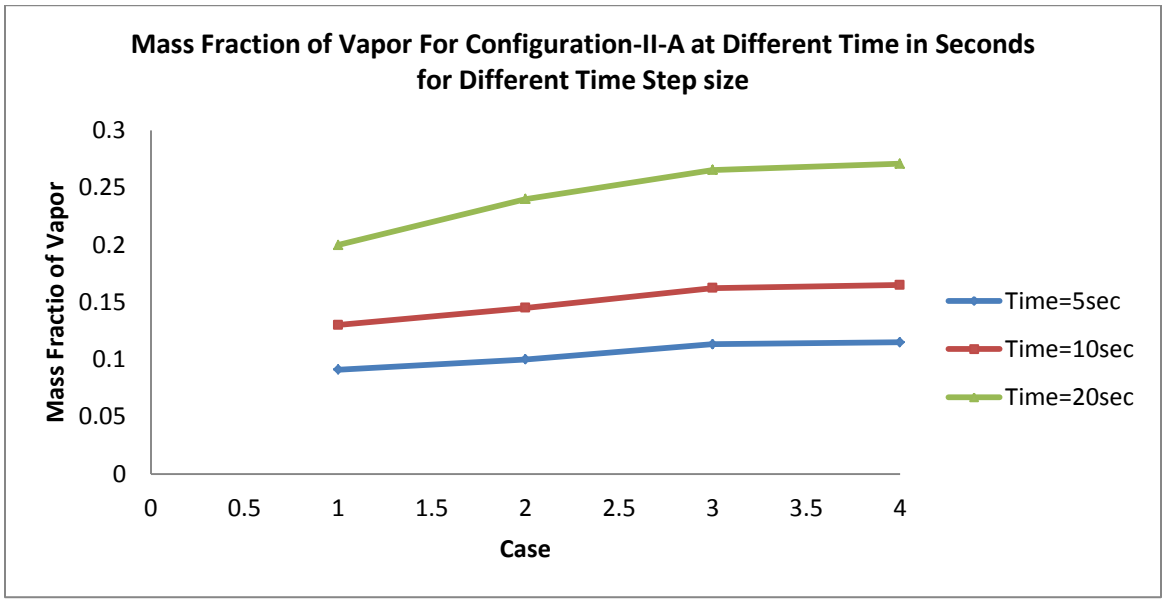

Figure C.6 Mass fraction of vapor at different time step size for Configuration-II-A

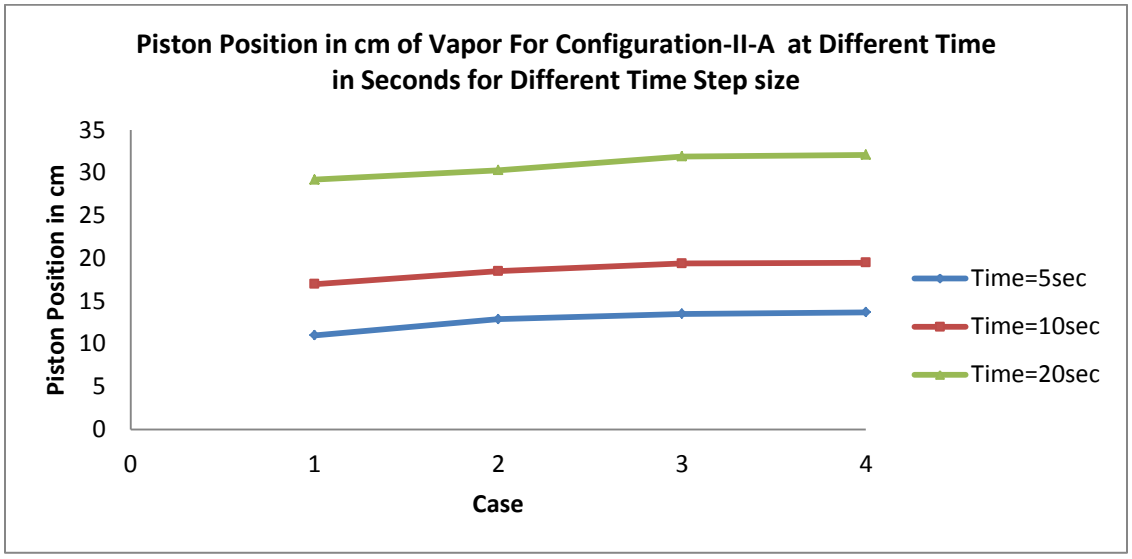

Figure C.7 Piston position at different time step size for Configuration-II-A

Mesh and time dependency of Configuration-II-B:

Table C.3 Grid sizes used in the mesh dependency test for Configuration-II-B

	Grid 1	Grid 2	Grid 3	Grid 4
Element size in mm	**2**	**1.4**	**1**	**0.75**
Element initial counts	**2,698**	**5,858**	**10,869**	**21,592**

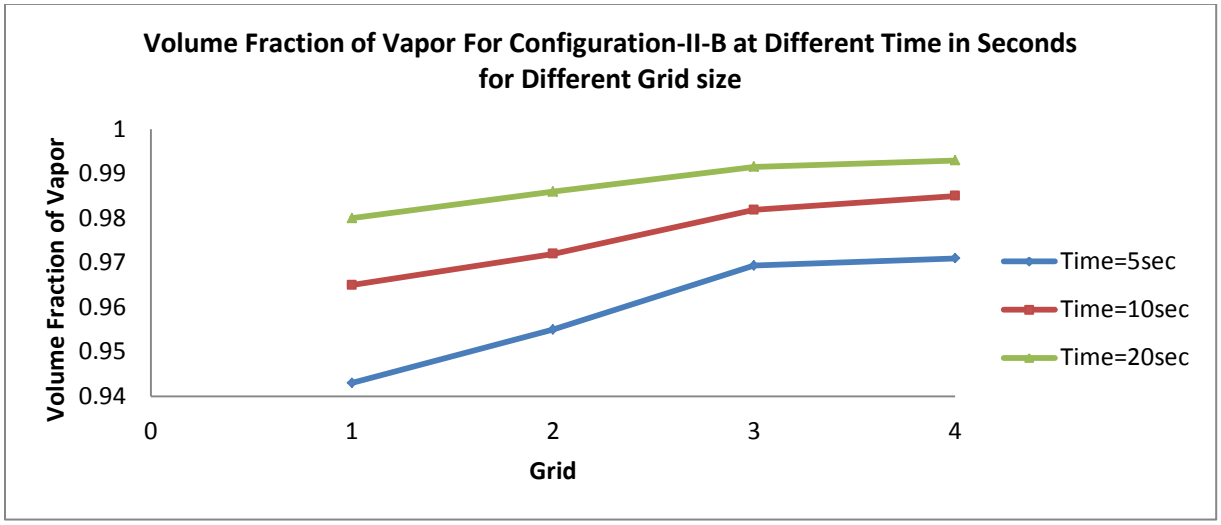

Figure C.8 Volume fraction of vapor at different grids size for Configuration-II-B

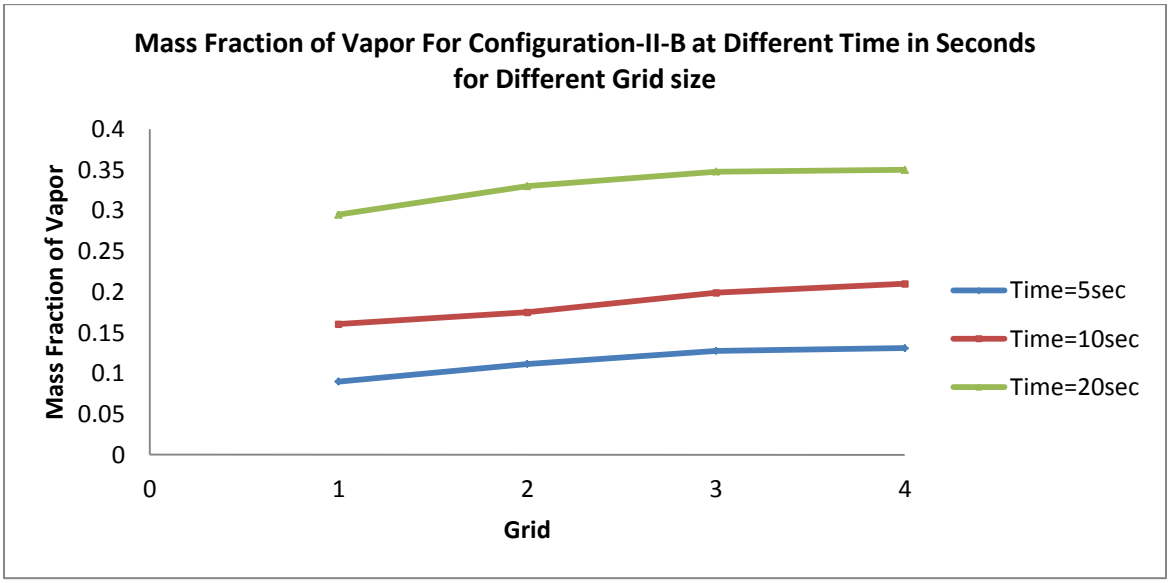

Figure C.9 Mass fraction of vapor at different grids size for Configuration-II-B

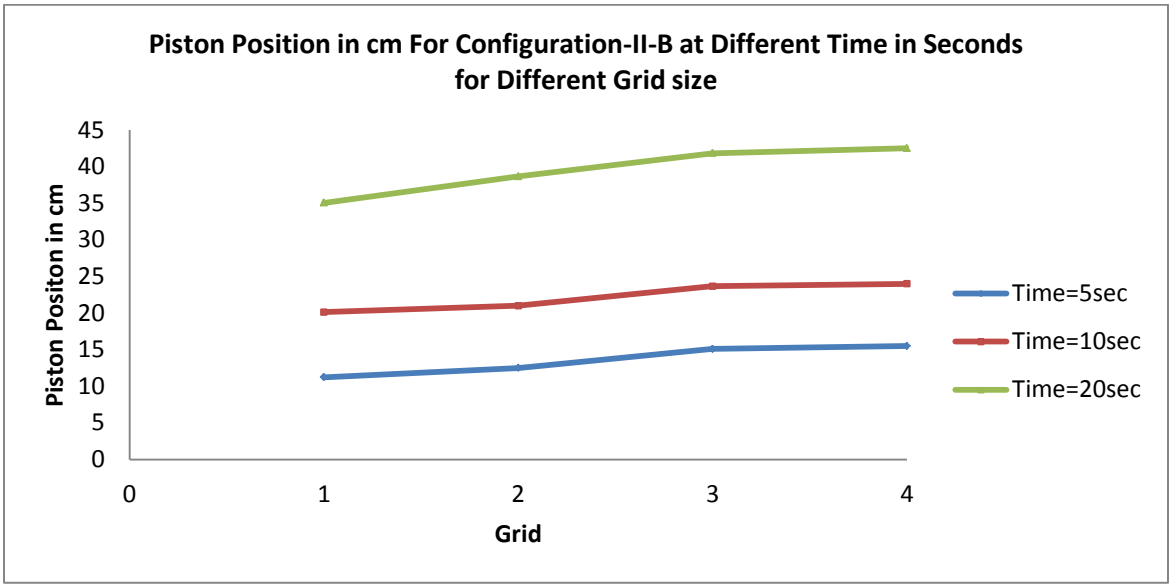

Figure C.10 Piston position at different grids size for Configuration-II-B

Table C.4 Time step values used for the time-step dependency test for Configuration-II-B

Case1	Case 2	Case 3	Case 4
0.01	0.005	0.0025	0.001

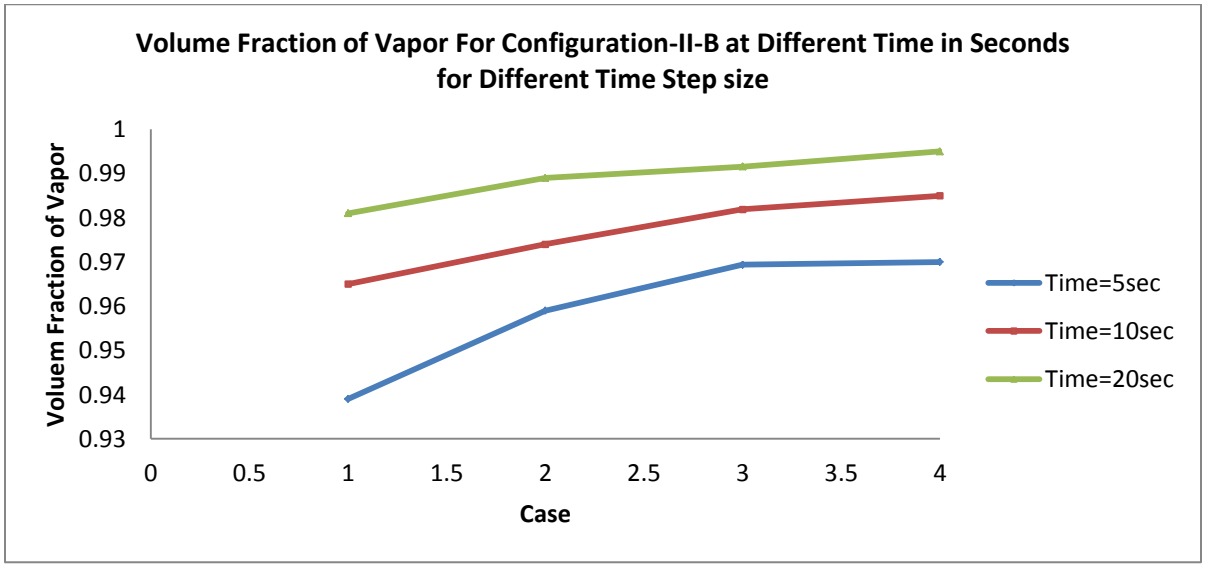

Figure C.11 Volume fraction of vapor at different time step size for Configuration-II-B

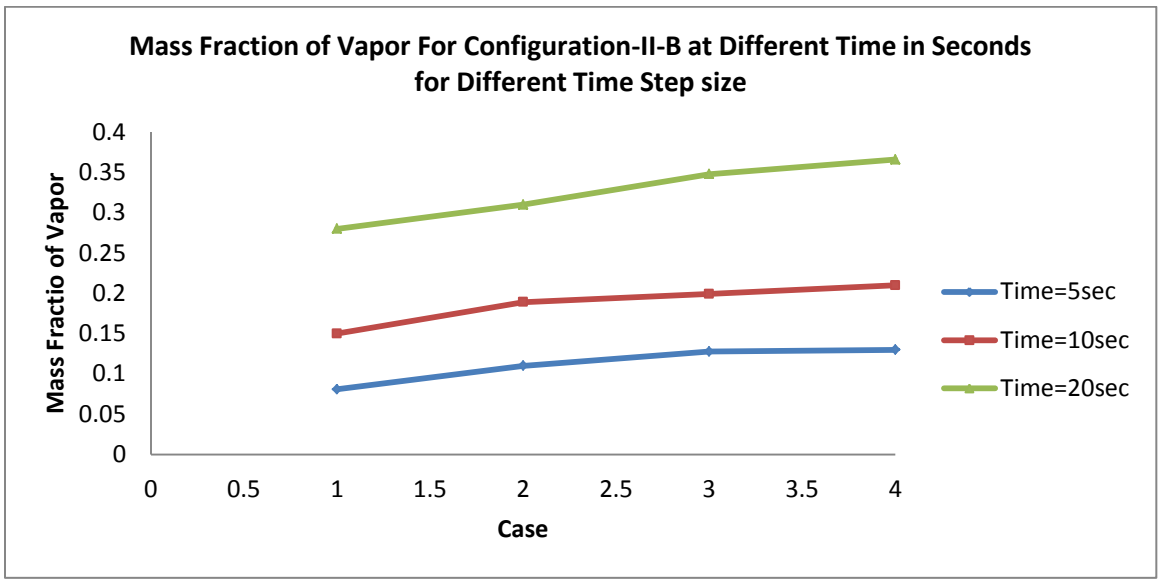

Figure C.12 Mass fraction of vapor at different time step size for Configuration-II-B

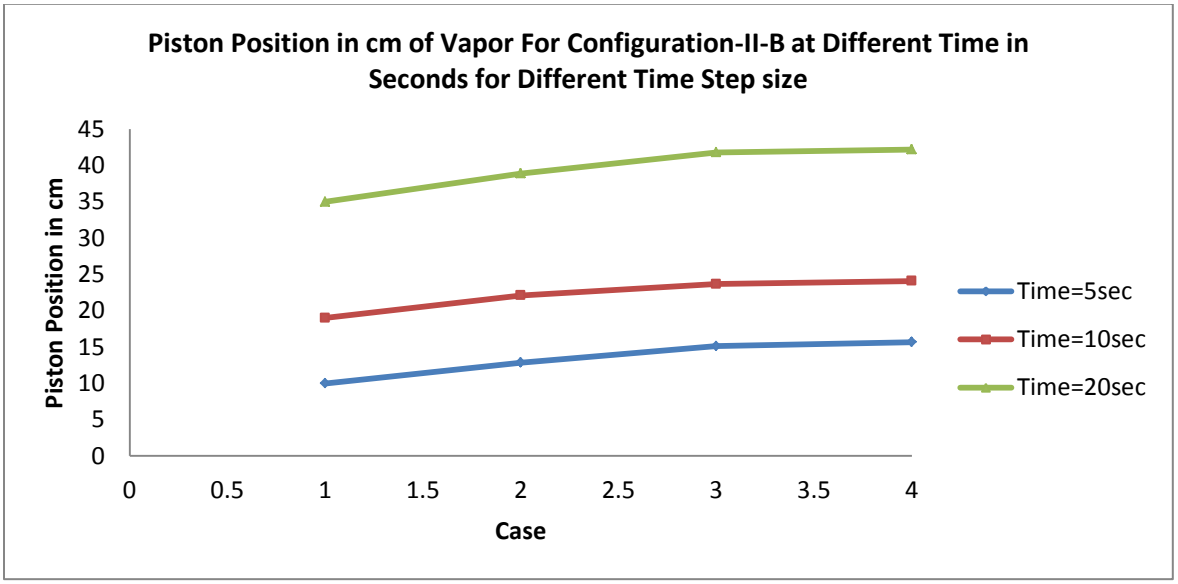

Figure C.13 Piston position at different time step size for Configuration-II-B

Mesh and time dependency of Configuration-II-C

Table C.5 Grid sizes used in the mesh dependency test for Configuration-II-C

	Grid 1	Grid 2	Grid 3	Grid 4
Element size in mm	**2**	**1.4**	**1**	**0.75**
Element initial counts	**2,880**	**5,989**	**10,771**	**23,100**

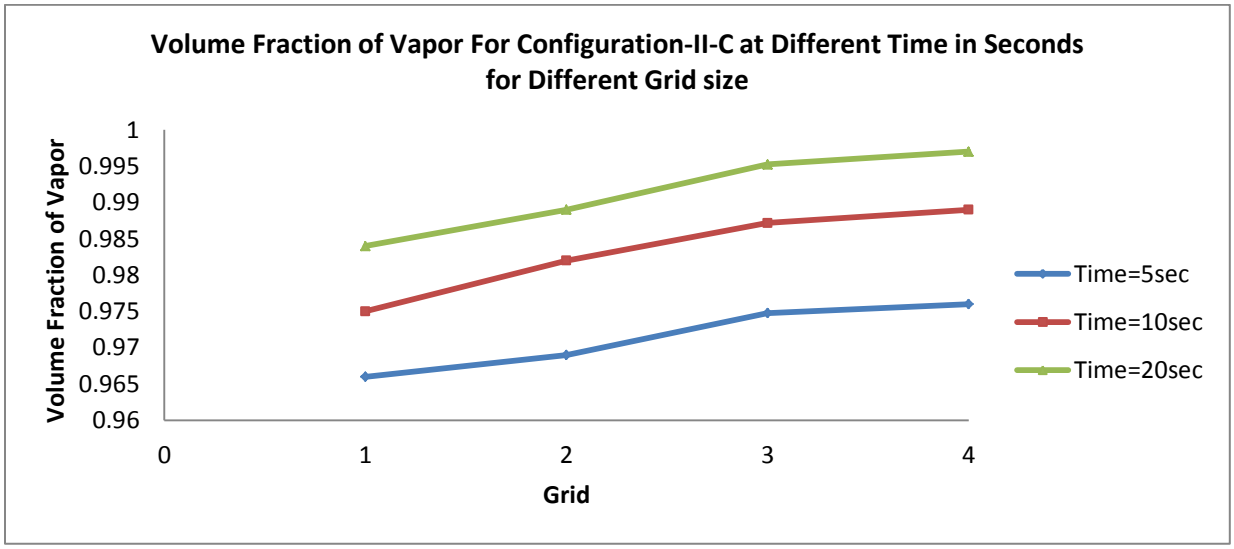

Figure C.14 Volume fraction of vapor at different grids size for Configuration-II-C

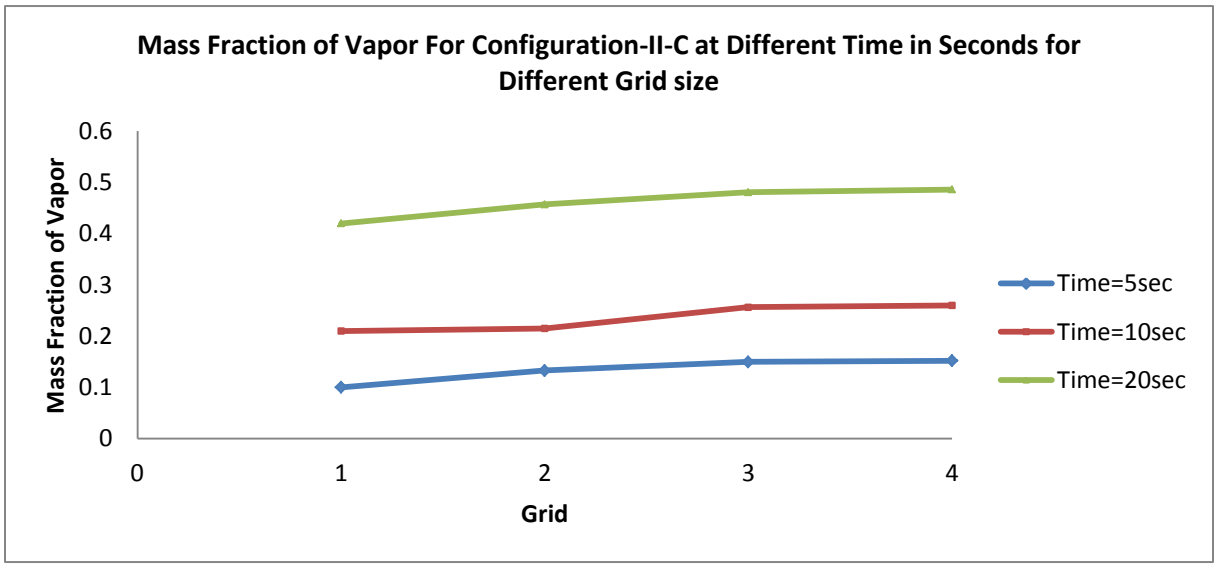

Figure C.15 Mass fraction of vapor at different grids size for Configuration-II-C

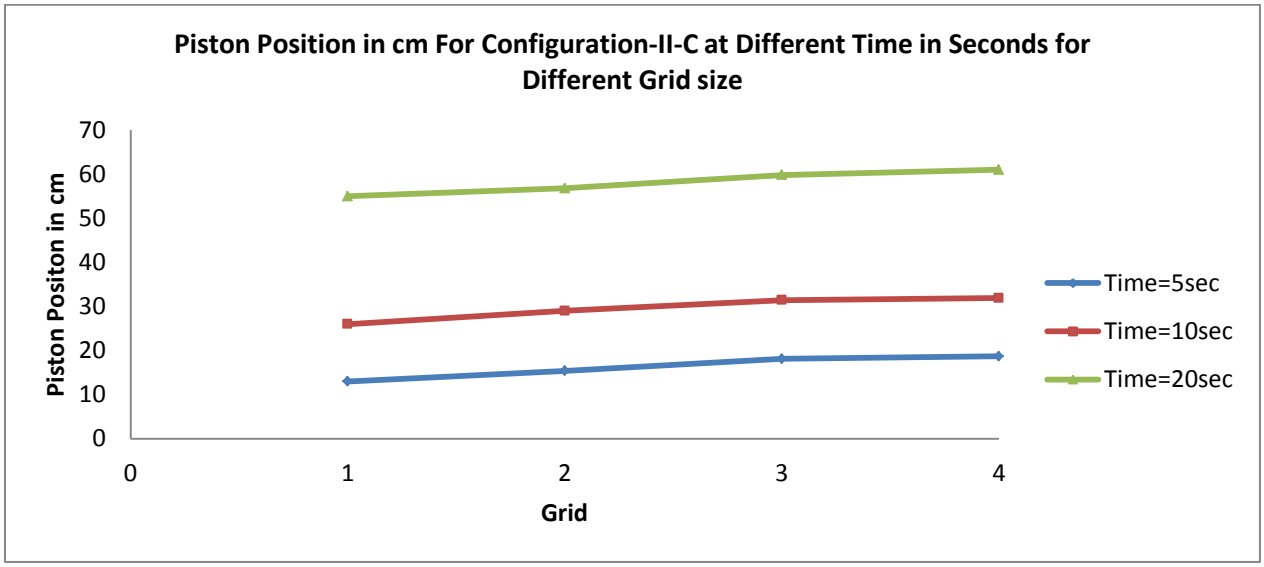

Figure C.16 Piston position at different grids size for Configuration-II-C

Table C.6 Time step values used for the time-step dependency test for Configuration-II-C

Case1	Case 2	Case 3	Case 4
0.01	0.005	0.0025	0.001

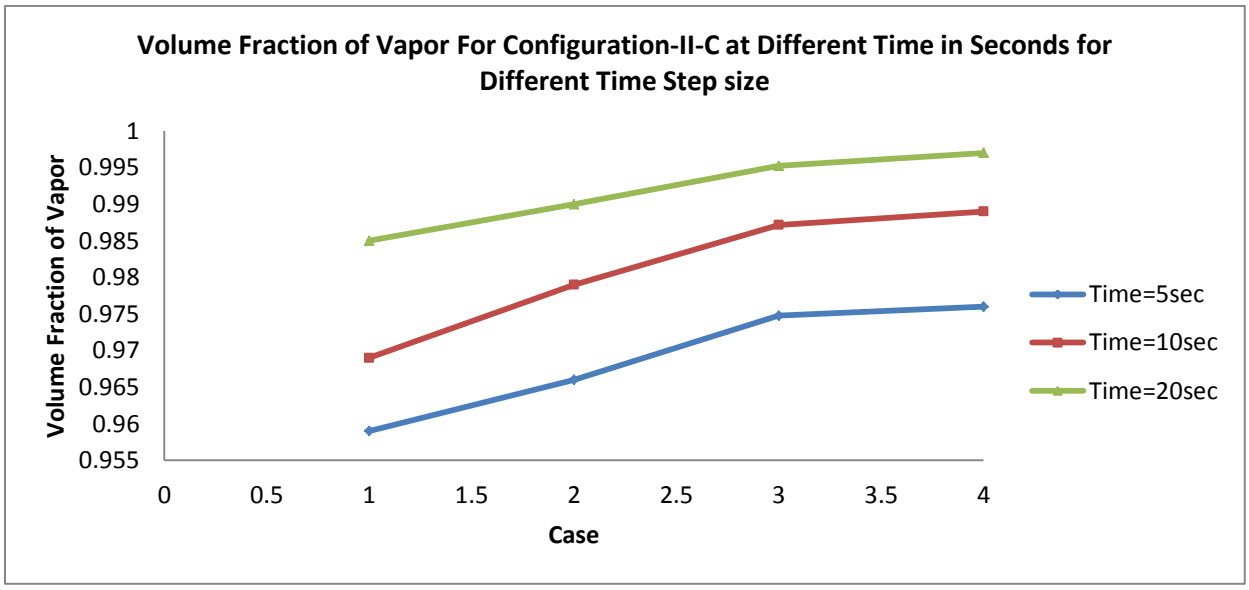

Figure C.17 Volume fraction of vapor at different time step size for Configuration-II-C

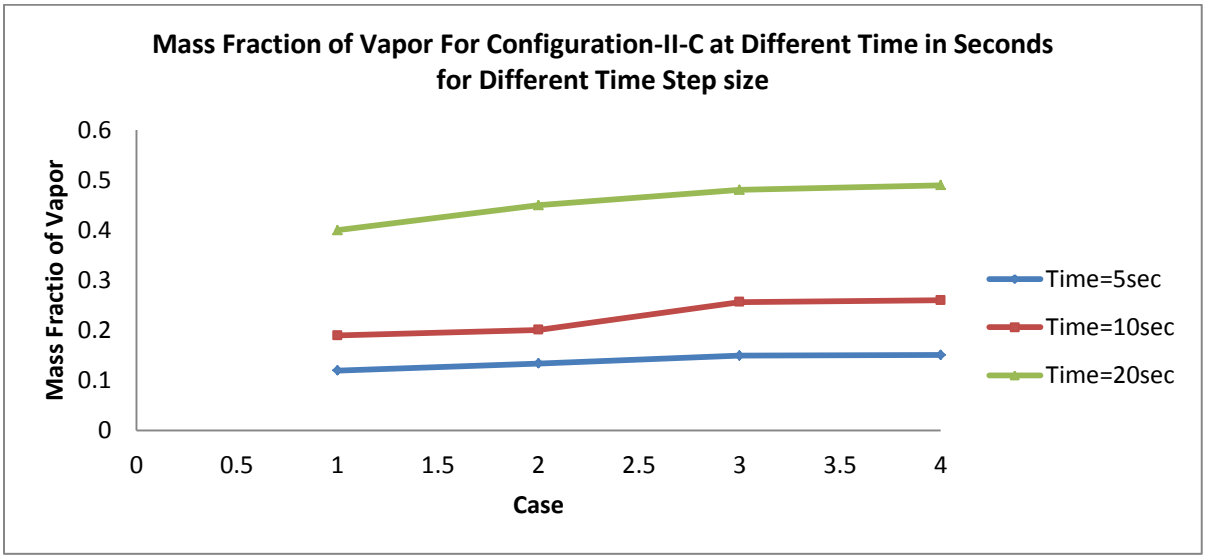

Figure C.18 Mass fraction of vapor at different time step size for Configuration-II-C

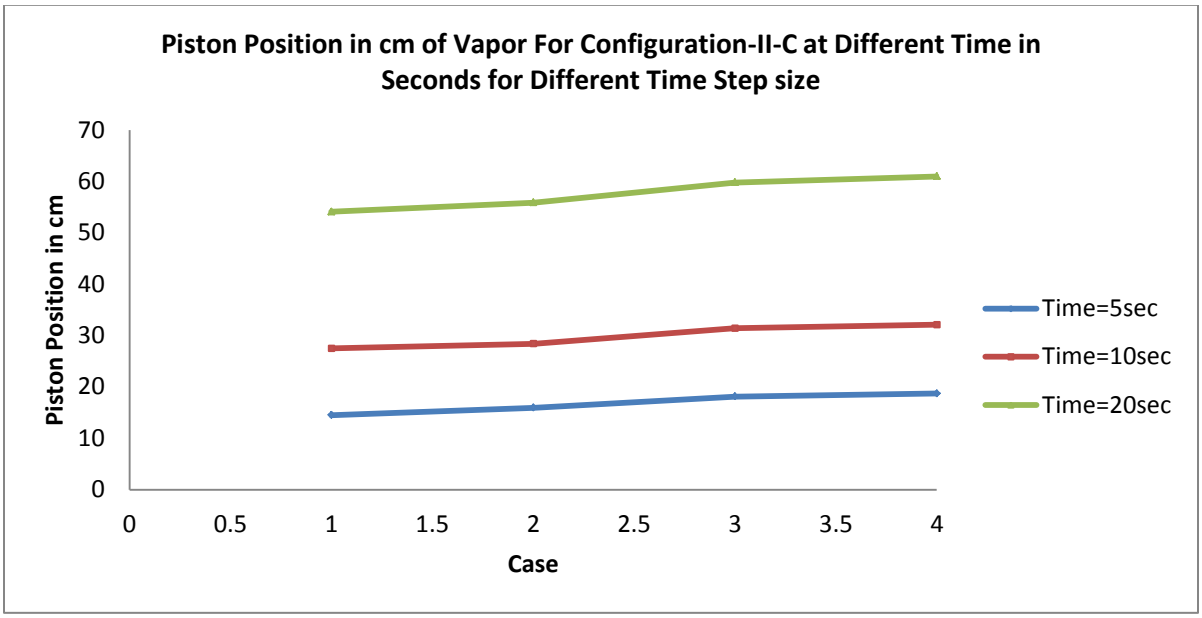

Figure C.19 Piston position at different time step size for Configuration-II-C

Mesh and time dependency of Configuration-III-A

Table C.7 Grid sizes used in the mesh dependency test for Configuration-III-A

	Grid 1	Grid 2	Grid 3	Grid 4
Element size in mm	**2**	**1.4**	**1**	**0.75**
Element initial counts	**2,945**	**6,050**	**10,880**	**23,154**

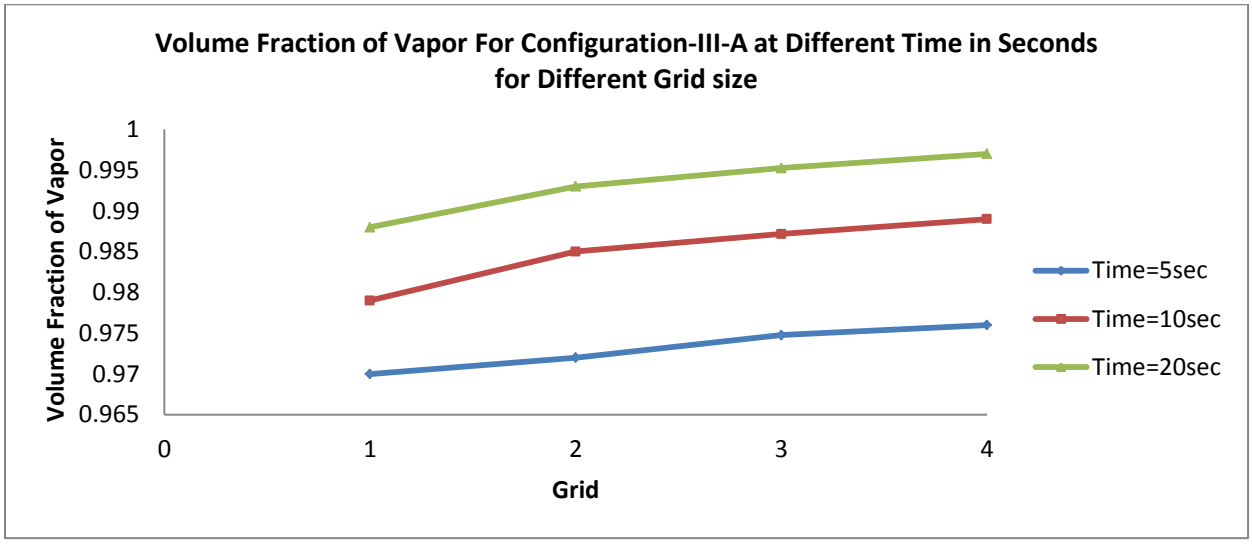

Figure C.20 Volume fraction of vapor at different grids size for Configuration-III-A

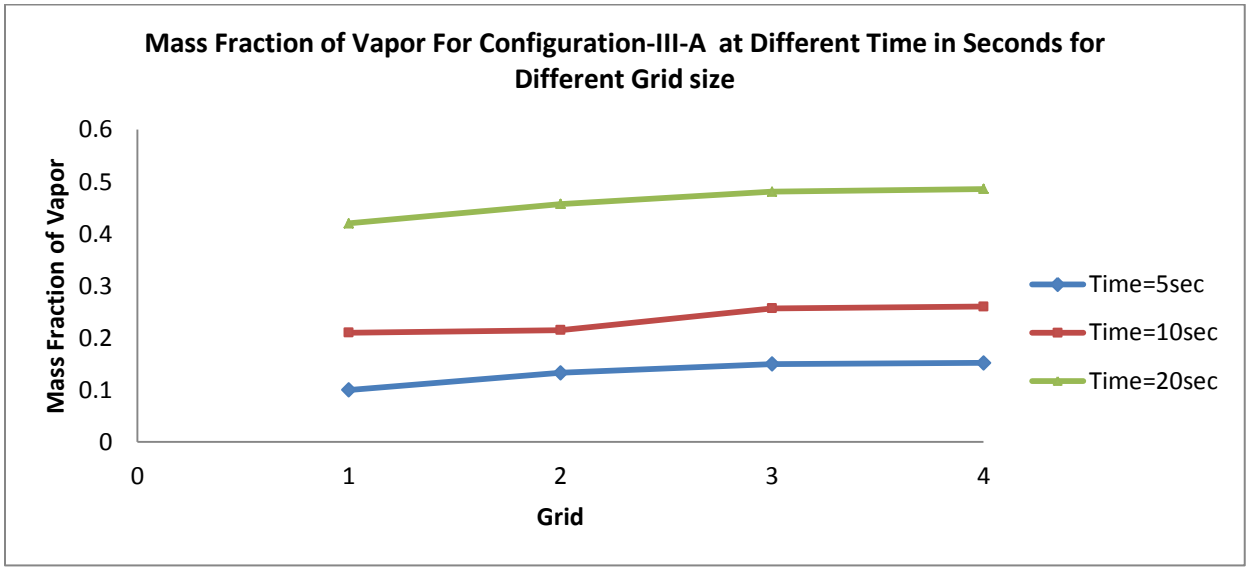

Figure C.21 Mass fraction of vapor at different grids size for Configuration-III-A

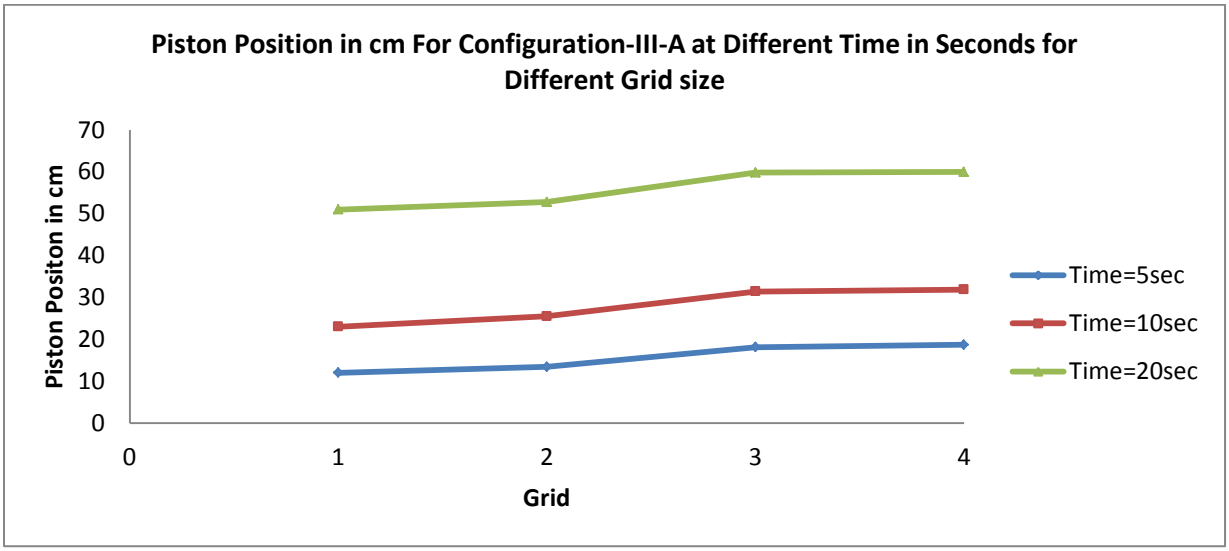

Figure C.22 Piston position at different grids size for Configuration-III-A

Table C.8 Time step values used for the time-step dependency test for Configuration-III-A

Case1	Case 2	Case 3	Case 4
0.01	0.005	0.0025	0.001

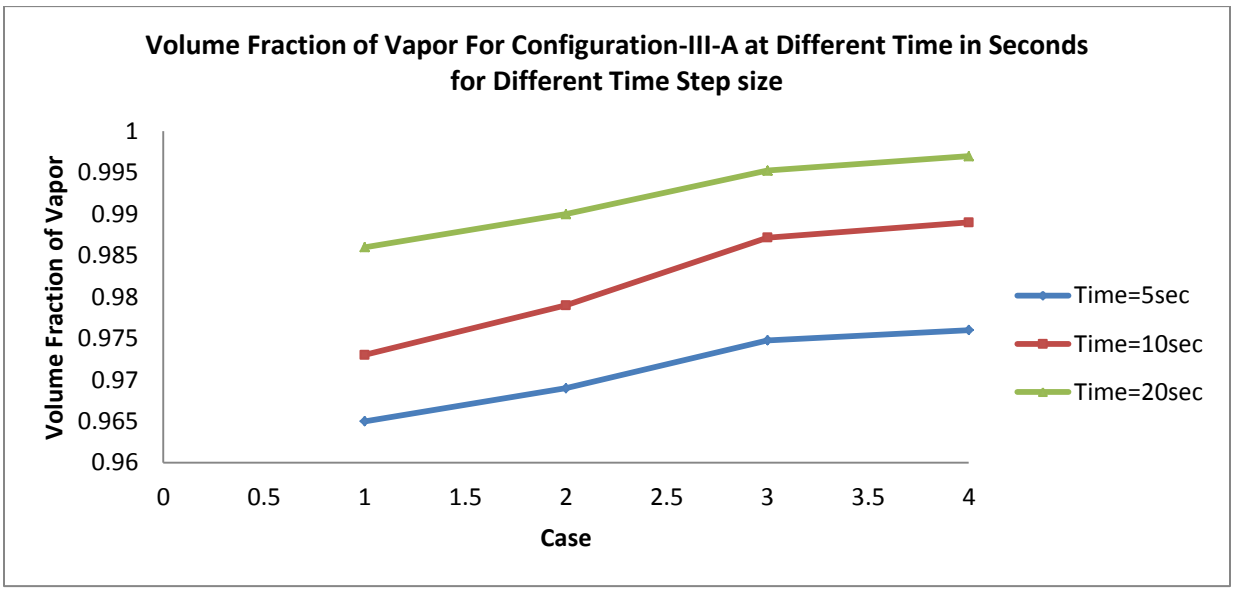

Figure C.23 Volume fraction of vapor at different time step size for Configuration-III-A

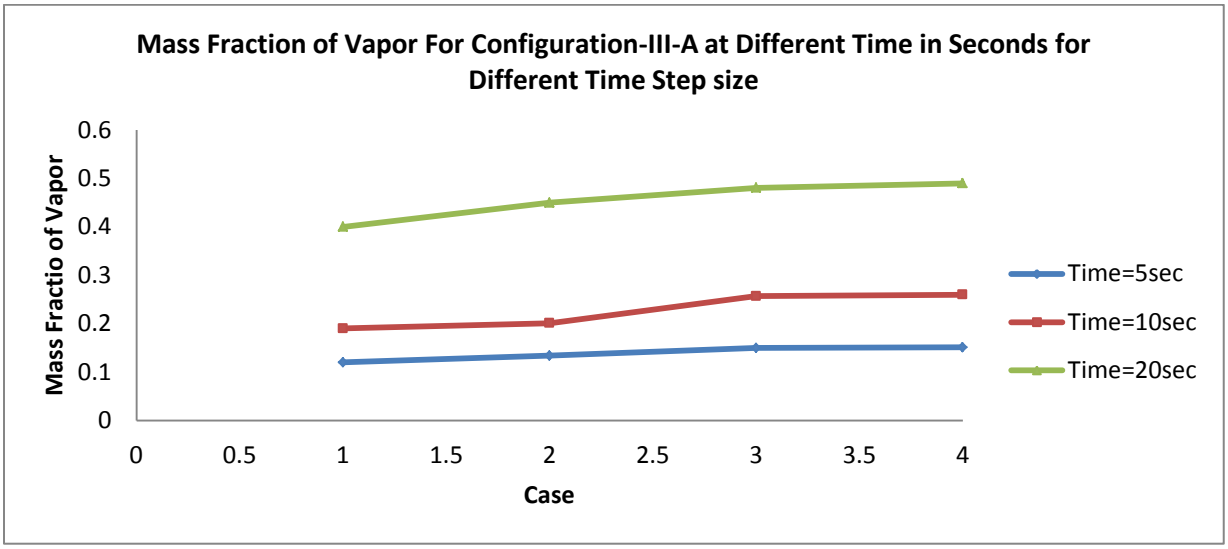

Figure C.24 Mass fraction of vapor at different time step size for Configuration-III-A

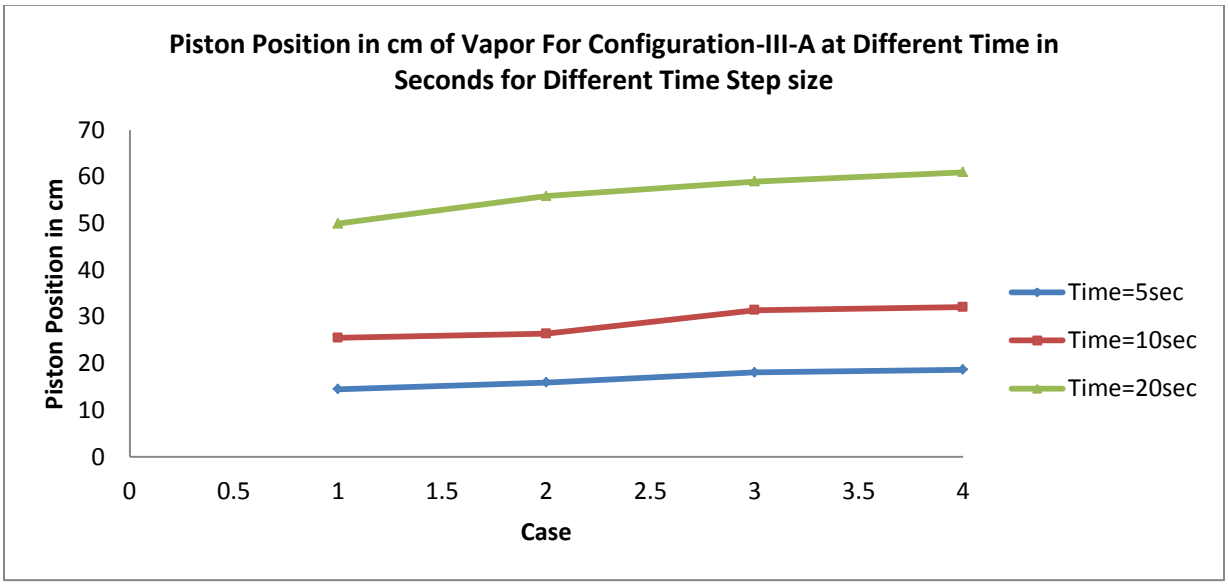

Figure C.25 Piston Position at different time step size for Configuration-III-A

Mesh and time dependency of Configuration-III-B

Table C.9 Grid sizes used in the mesh dependency test for Configuration-III-B

	Grid 1	Grid 2	Grid 3	Grid 4
Element size in mm	**2**	**1.4**	**1**	**0.75**
Element initial counts	**3,200**	**6,120**	**10,550**	**22,054**

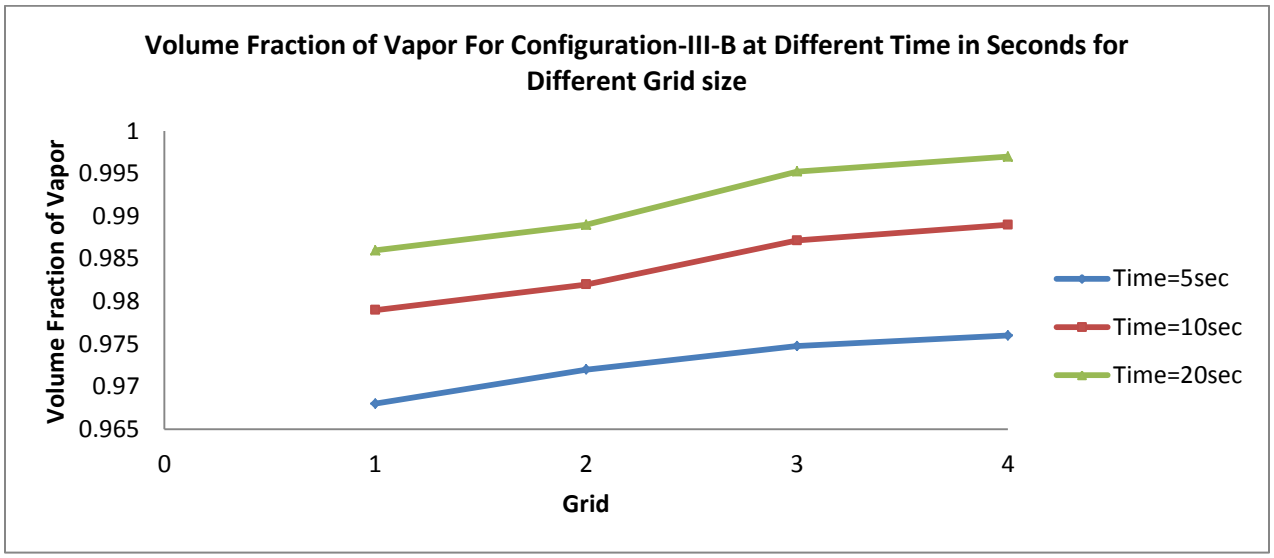

Figure C.26 Volume fraction of vapor at different grids size for Configuration-III-B

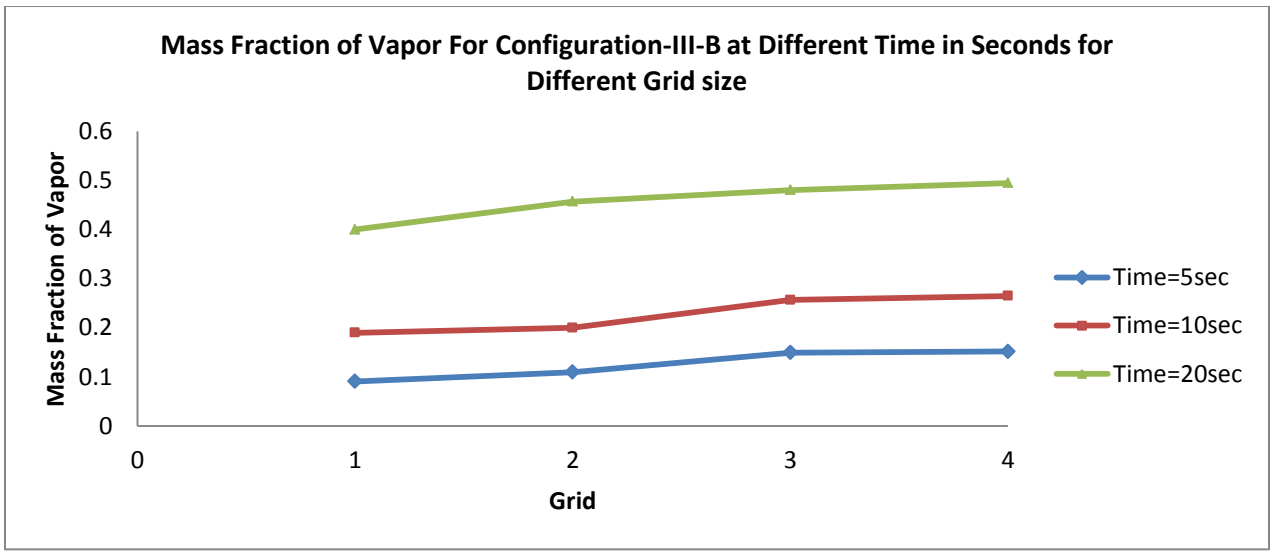

Figure C.27 Mass fraction of vapor at different grids size for Configuration-III-B

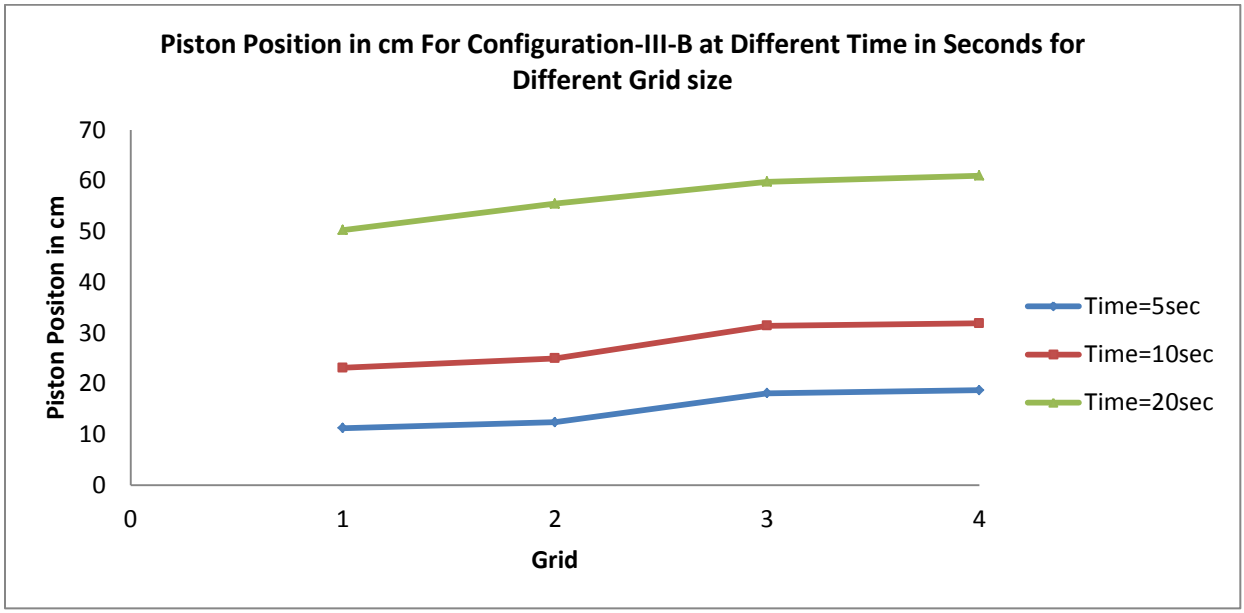

Figure C.28 Piston position at different grids size for Configuration-III-B

Table C.10 Time step values used for the time-step dependency test for Configuration-III-B

Case1	Case 2	Case 3	Case 4
0.01	0.005	0.0025	0.001

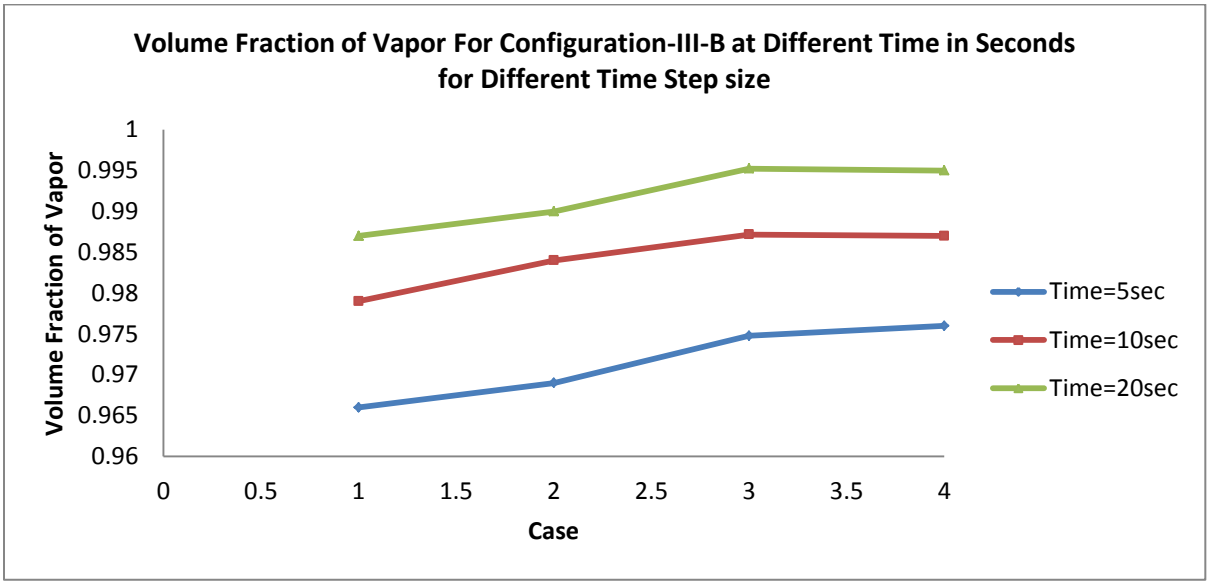

Figure C.29 Volume fraction of vapor at different time step size for Configuration-III-B

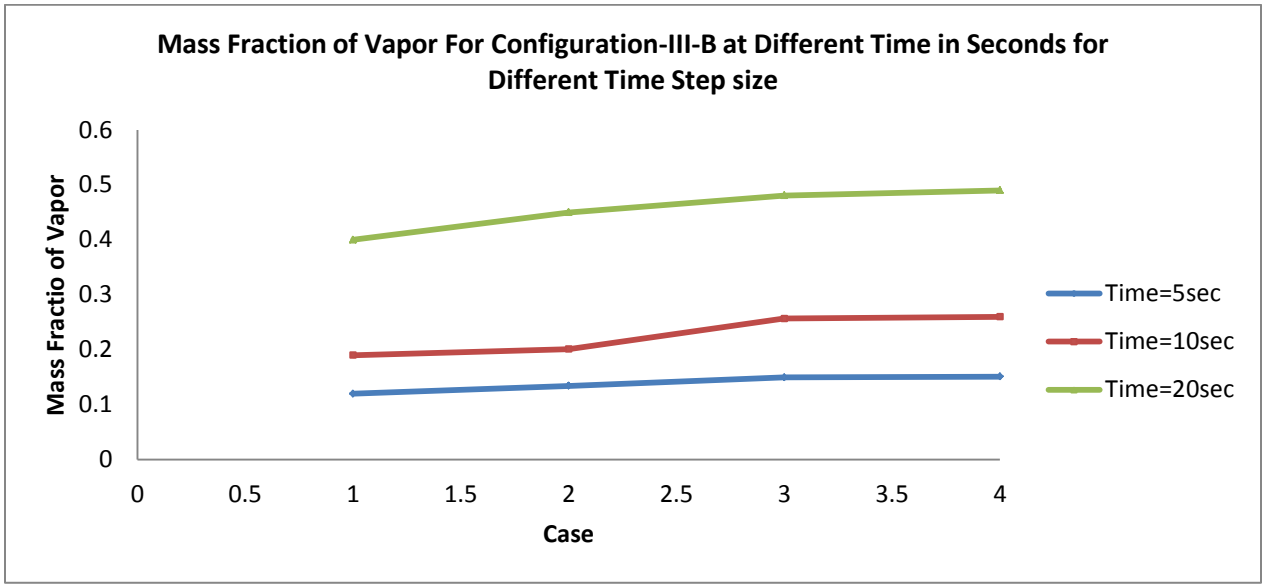

Figure C.30 Mass fraction of vapor at different time step size for Configuration-III-B

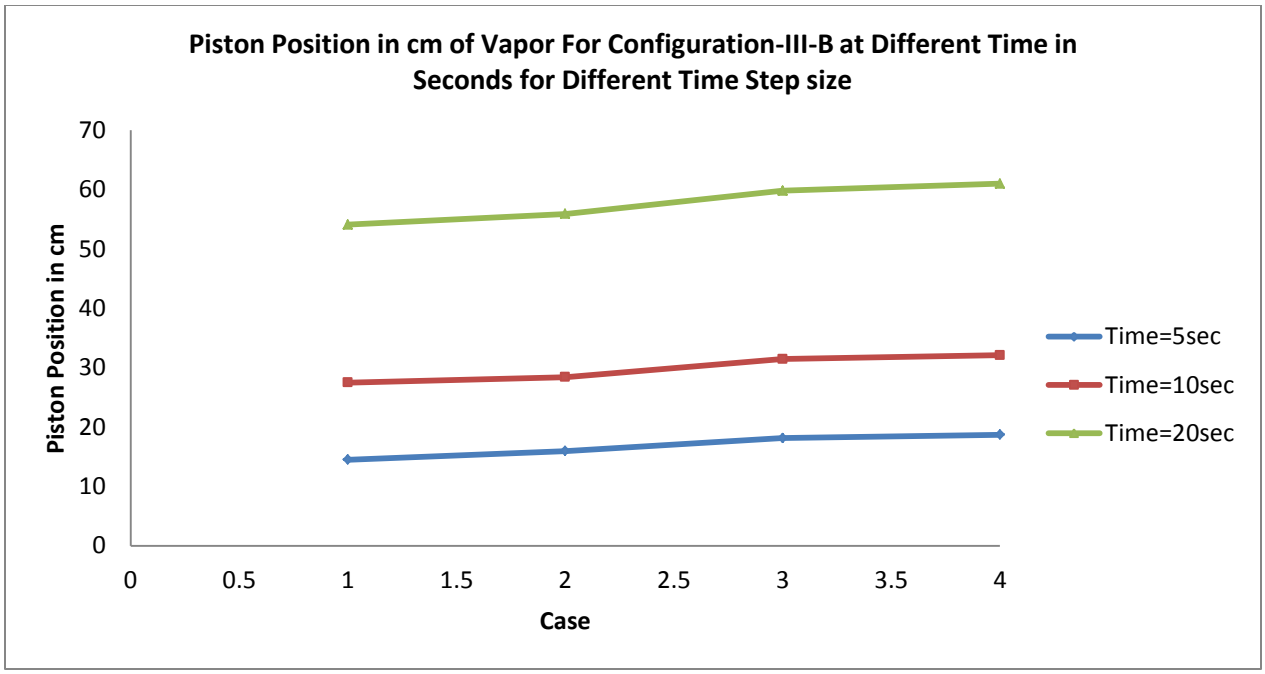

Figure C.31 Piston position at different time step size for Configuration-III-B

Mesh and time dependency of Configuration-IV-A

Table C.11 Grid sizes used in the mesh dependency test for Configuration-IV-A

	Grid 1	Grid 2	Grid 3	Grid 4
Element size in mm	**2**	**1.4**	**1**	**0.75**
Element initial counts	**4,210**	**7,420**	**13,550**	**24,434**

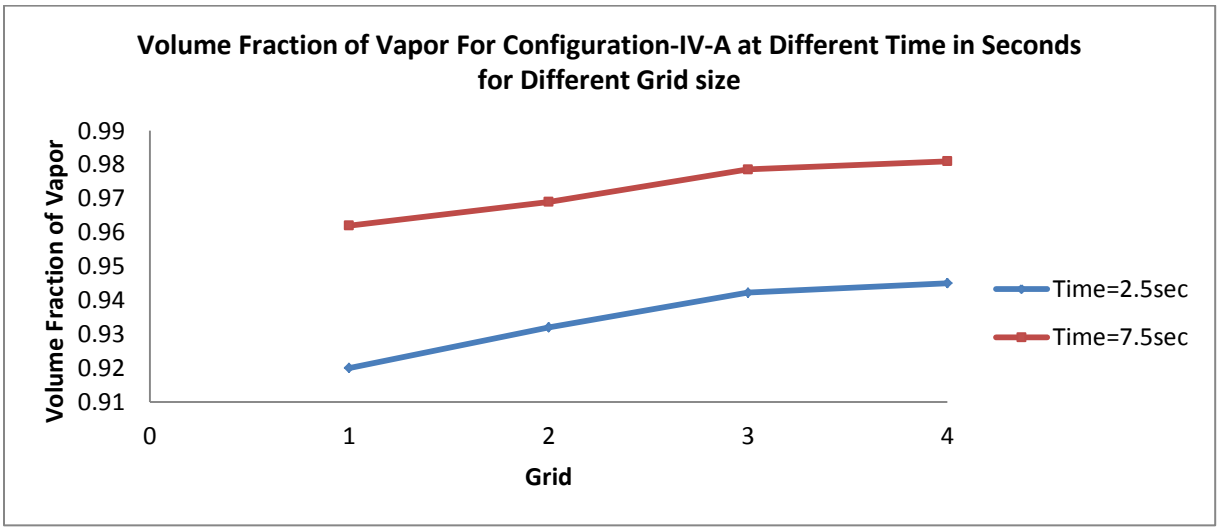

Figure C.32 Volume fraction of vapor at different grids size for Configuration-IV-A

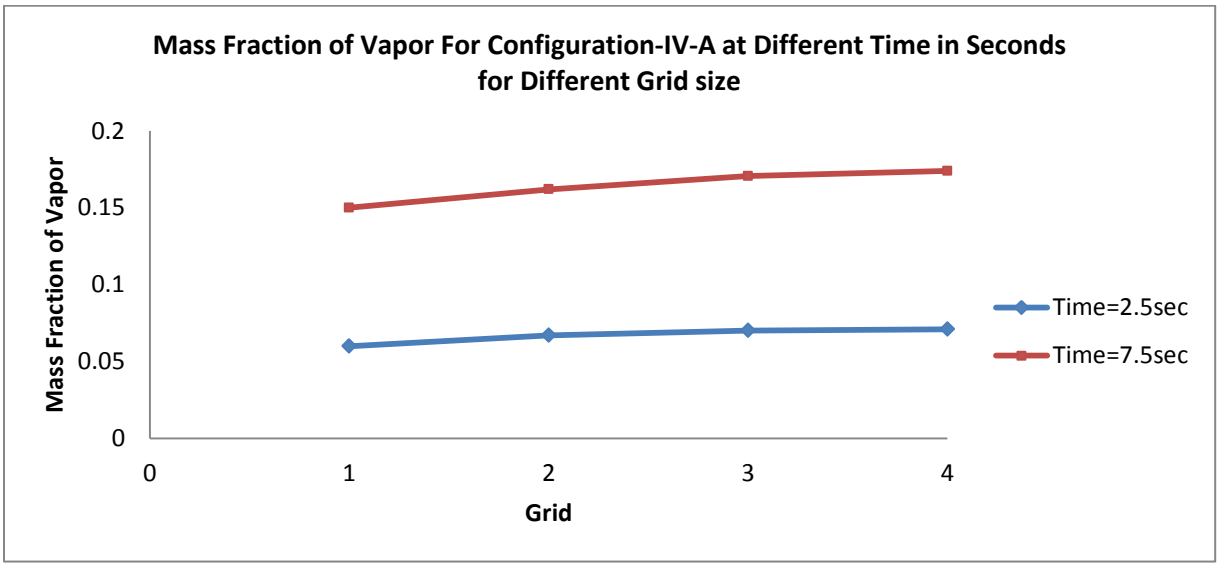

Figure C.33 Mass fraction of vapor at different grids size for Configuration-IV-A

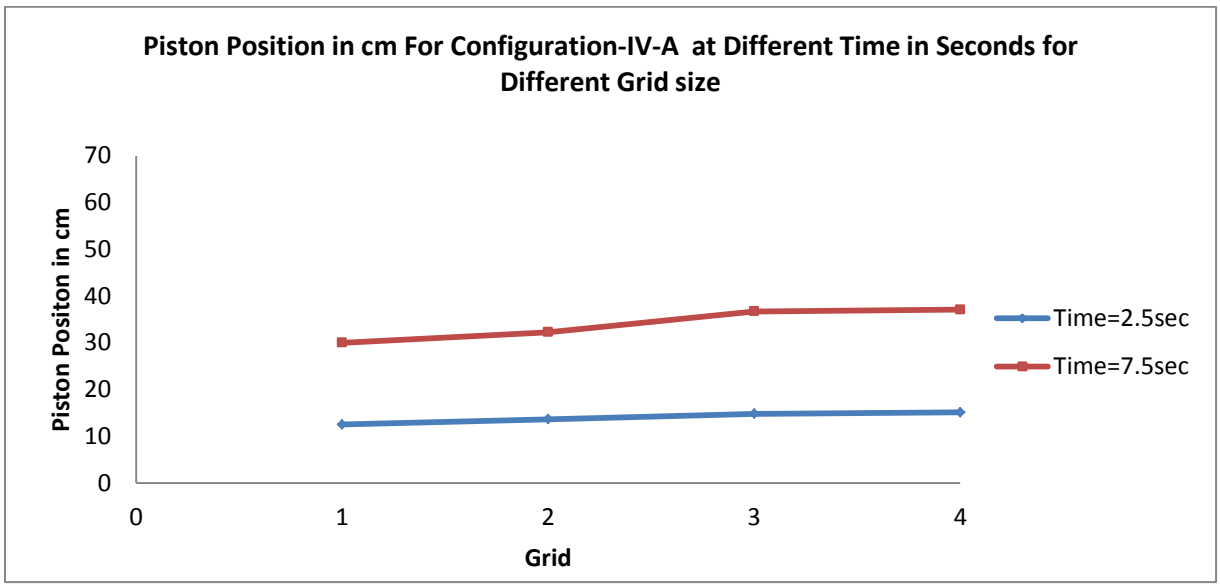

Figure C.34 Piston position at different grids size for Configuration-IV-A

Table C.12 Time step values used for the time-step dependency test for Configuration-IV-A

Case1	Case 2	Case 3	Case 4
0.01	0.005	0.0025	0.001

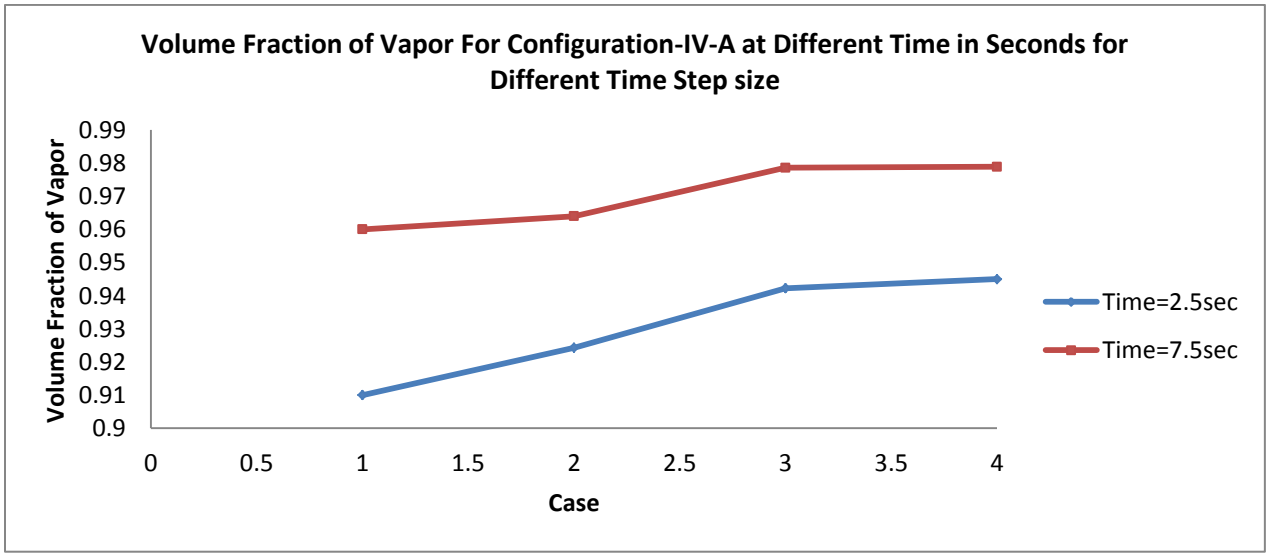

Figure C.35 Volume fraction of vapor at different time step size for Configuration-IV-A

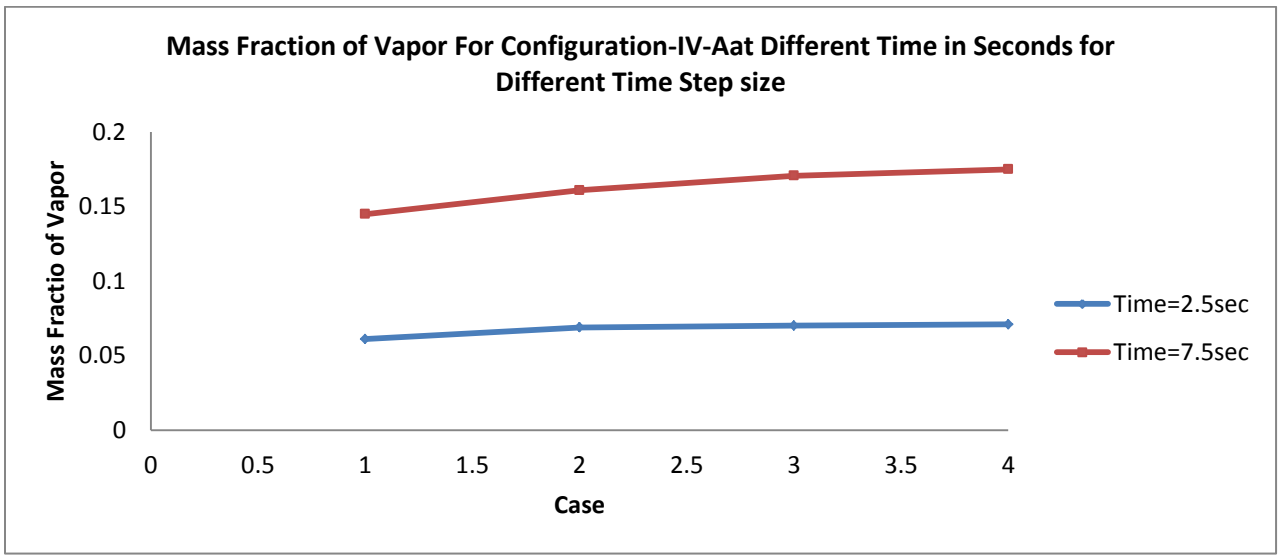

Figure C.36 Mass fraction of vapor at different time step size for Configuration-IV-A

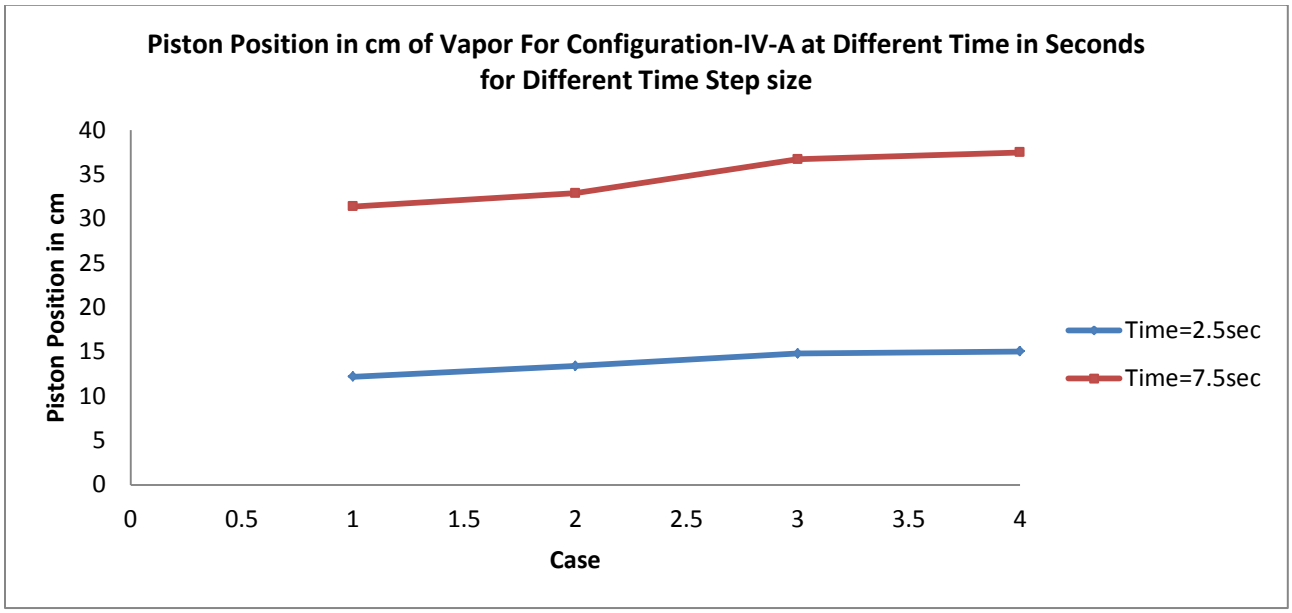

Figure C.37 Piston position at different time step size for Configuration-IV-A

Mesh and time dependency of Configuration-IV-B

Table C.13 Grid sizes used in the mesh dependency test for Configuration-IV-B

	Grid 1	Grid 2	Grid 3	Grid 4
Element size in mm	**2**	**1.4**	**1**	**0.75**
Element initial counts	**4,900**	**8,100**	**14,105**	**25,140**

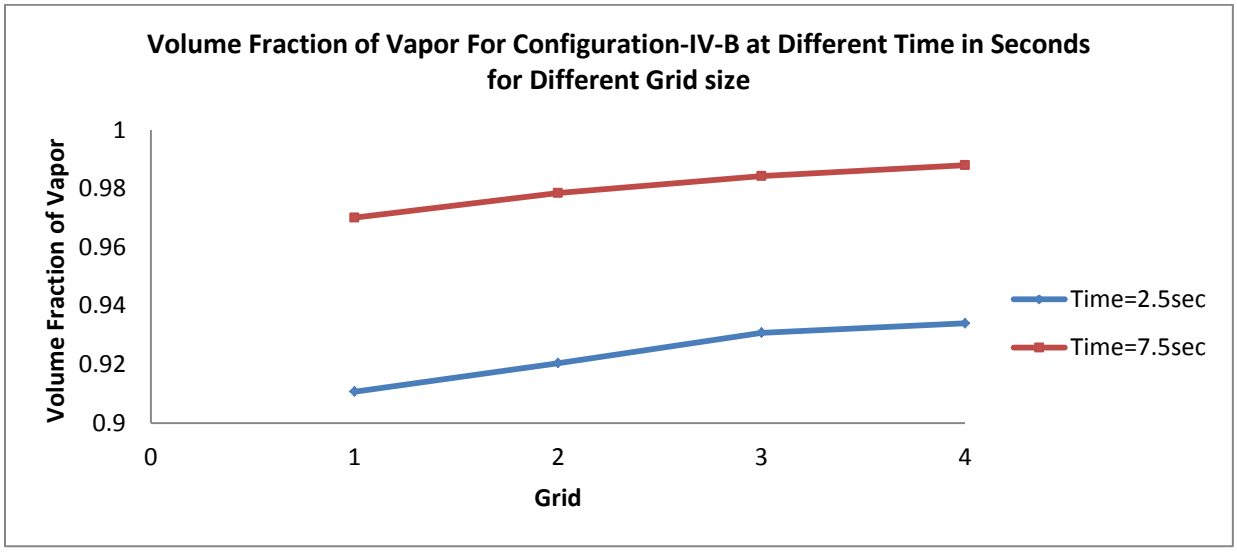

Figure C.38 Volume fraction of vapor at different grids size for Configuration-IV-B

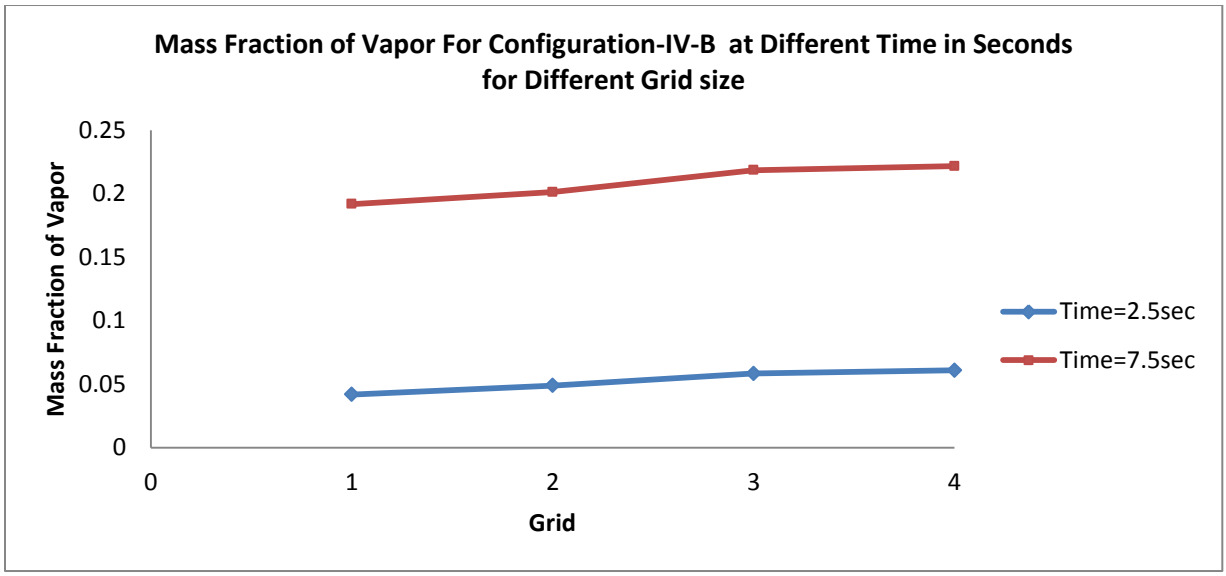

Figure C.39 Mass fraction of vapor at different grids size for Configuration-IV-B

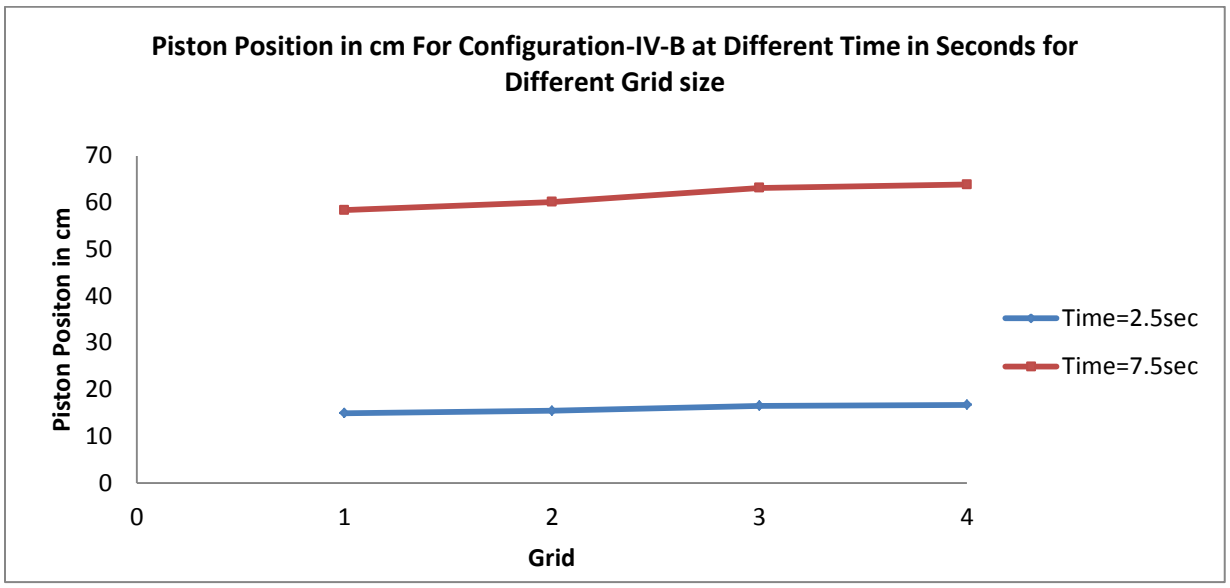

Figure C.40 Piston position at different grids size for Configuration-IV-B

Table C.14 Time step values used for the time-step dependency test for Configuration-IV-B

Case1	Case 2	Case 3	Case 4
0.01	0.005	0.0025	0.001

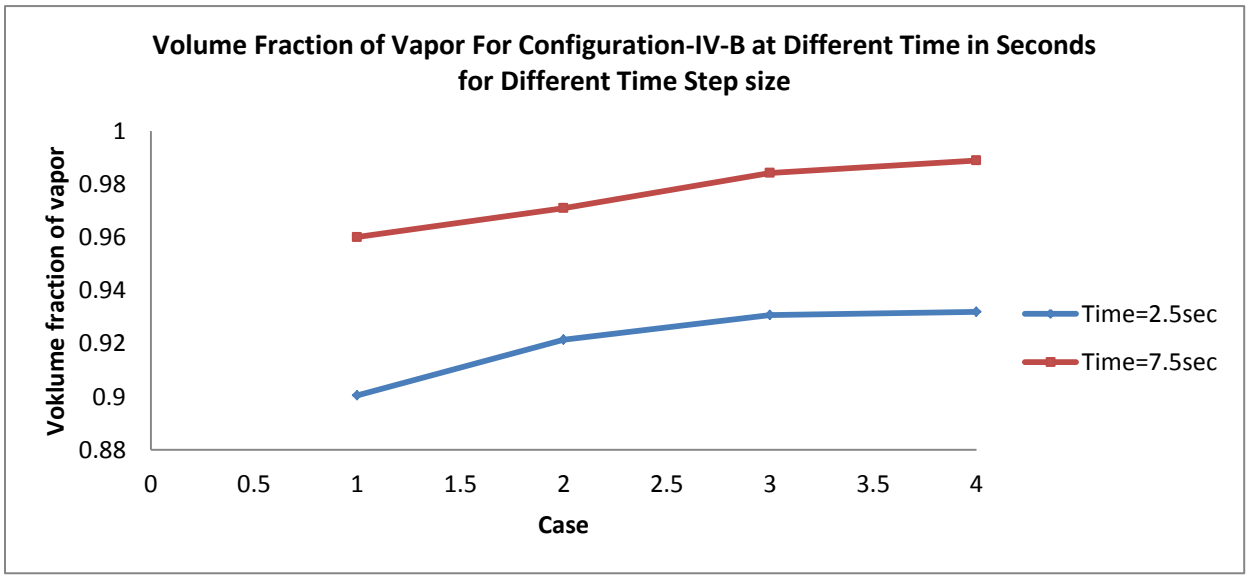

Figure C.41 Volume fraction of vapor at different time step size for Configuration-IV-B

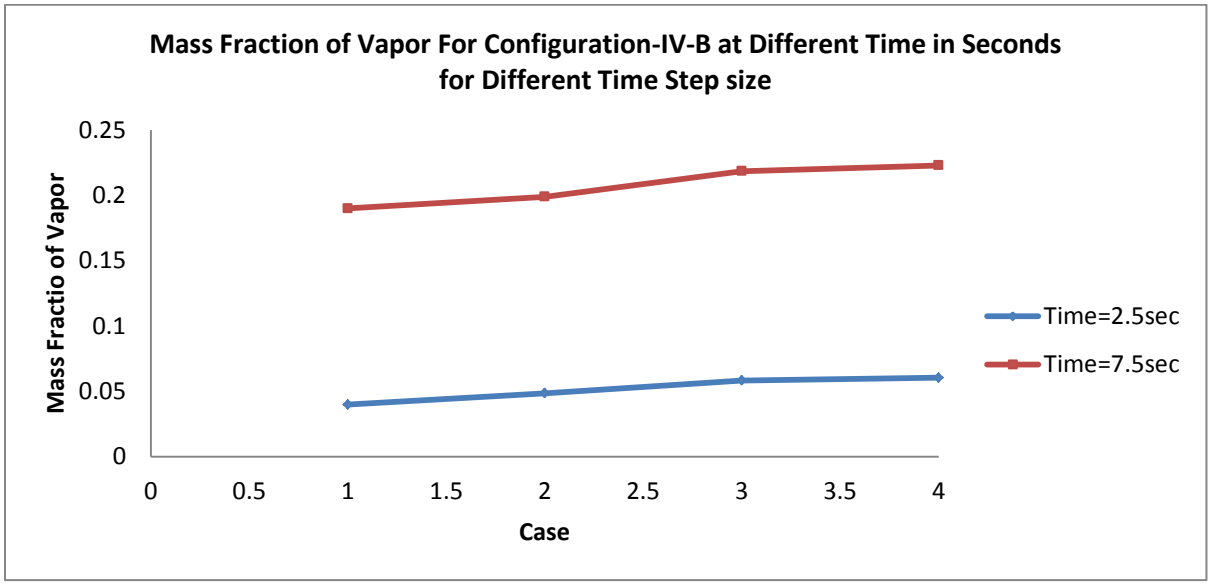

Figure C.42 Mass fraction of vapor at different time step size for Configuration-IV-B

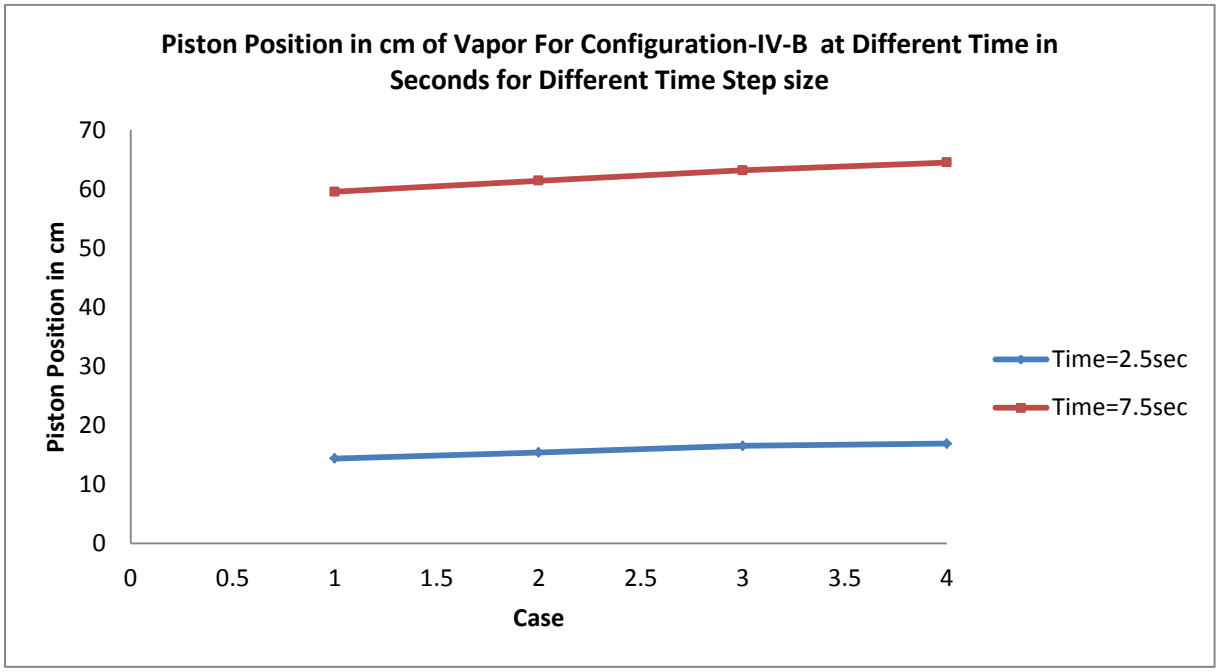

Figure C.43 Piston position at different time step size for Configuration-IV-B

Mesh and time dependency of Configuration-VI

Table C.15 Grid sizes used in the mesh dependency test for Configuration-VI

	Grid 1	Grid 2	Grid 3	Grid 4
Element size in mm	**2**	**1.4**	**1**	**0.75**
Element initial counts	**4,00**	**7,55**	**1,440**	**2,854**

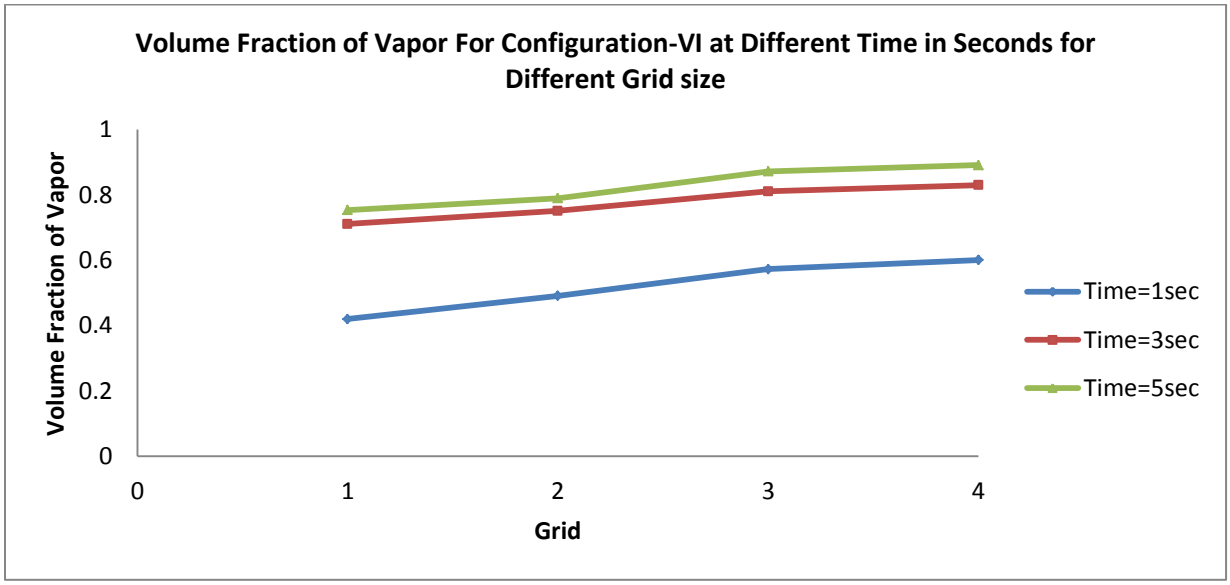

Figure C.44 Volume fraction of vapor at different grids size for Configuration-VI

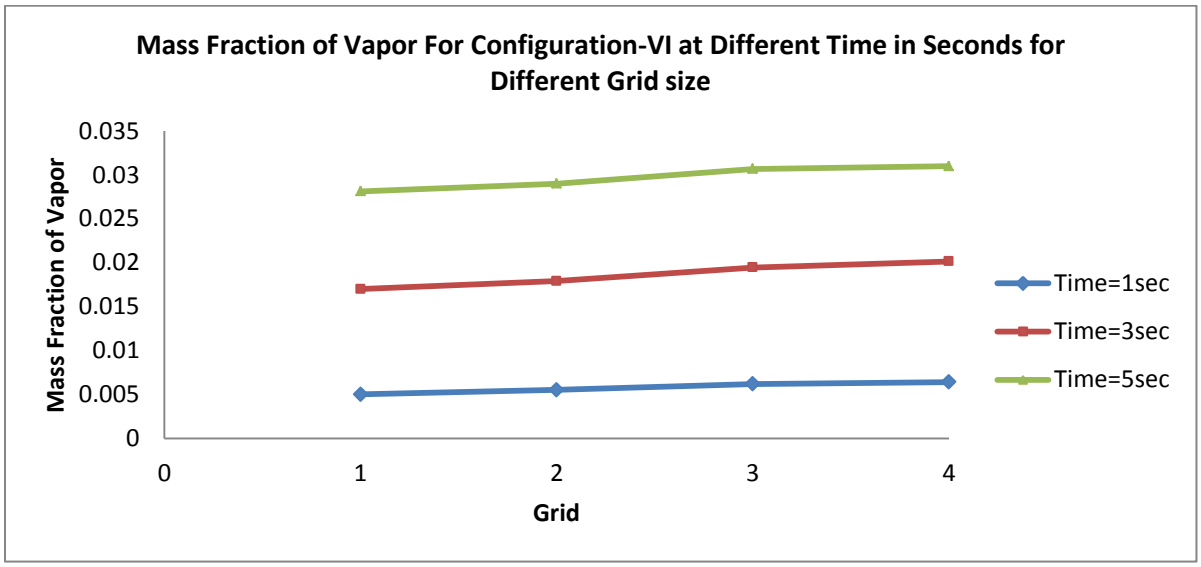

Figure C.45 Mass fraction of vapor at different grids size for Configuration-VI

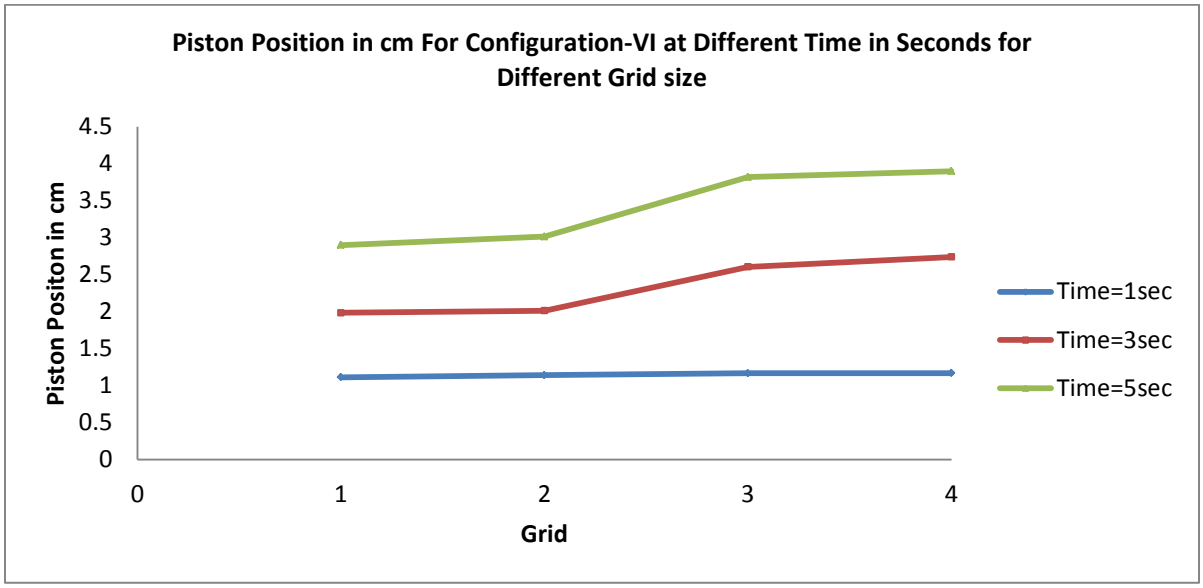

Figure C.46 Piston position at different grids size for Configuration-VI

Table C.16 Time step values used for the time-step dependency test for Configuration-VI

Case1	Case 2	Case 3	Case 4
0.01	0.005	0.0025	0.001

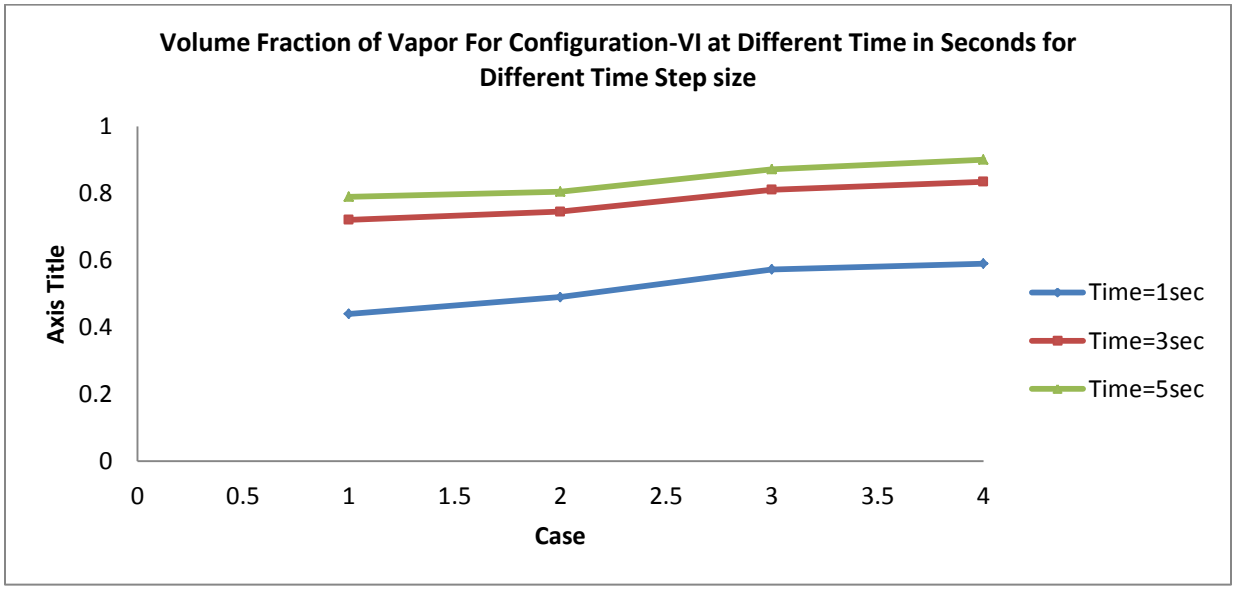

Figure C.47 Volume fraction of vapor at different time step size for Configuration-VI

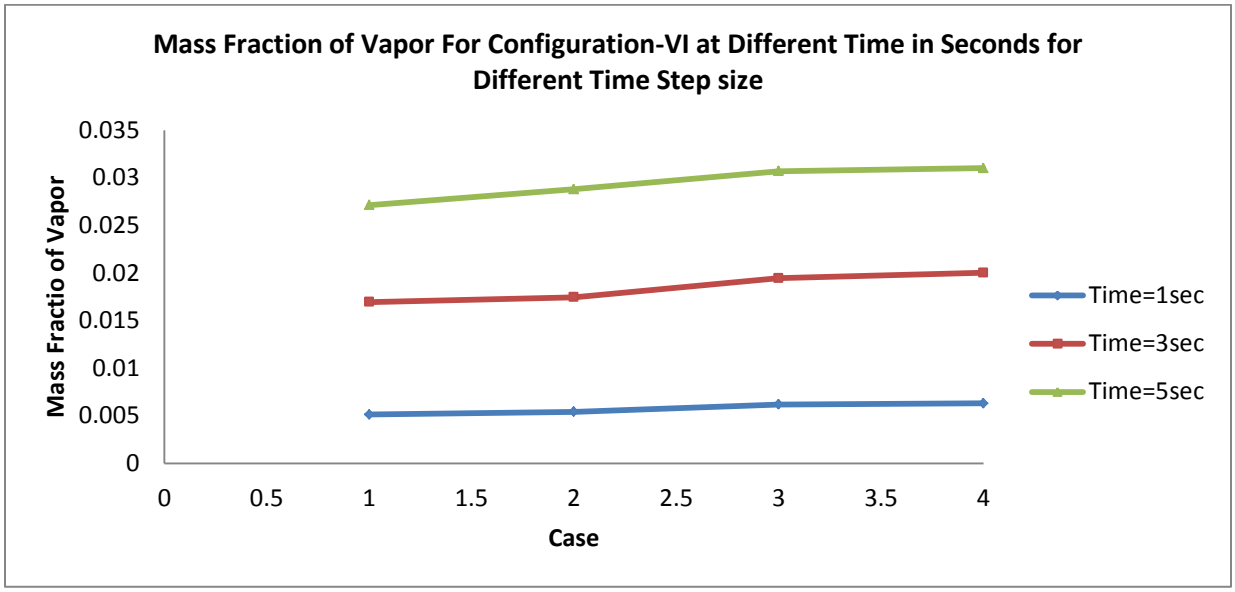

Figure C.48 Mass fraction of vapor at different time step size for Configuration-VI

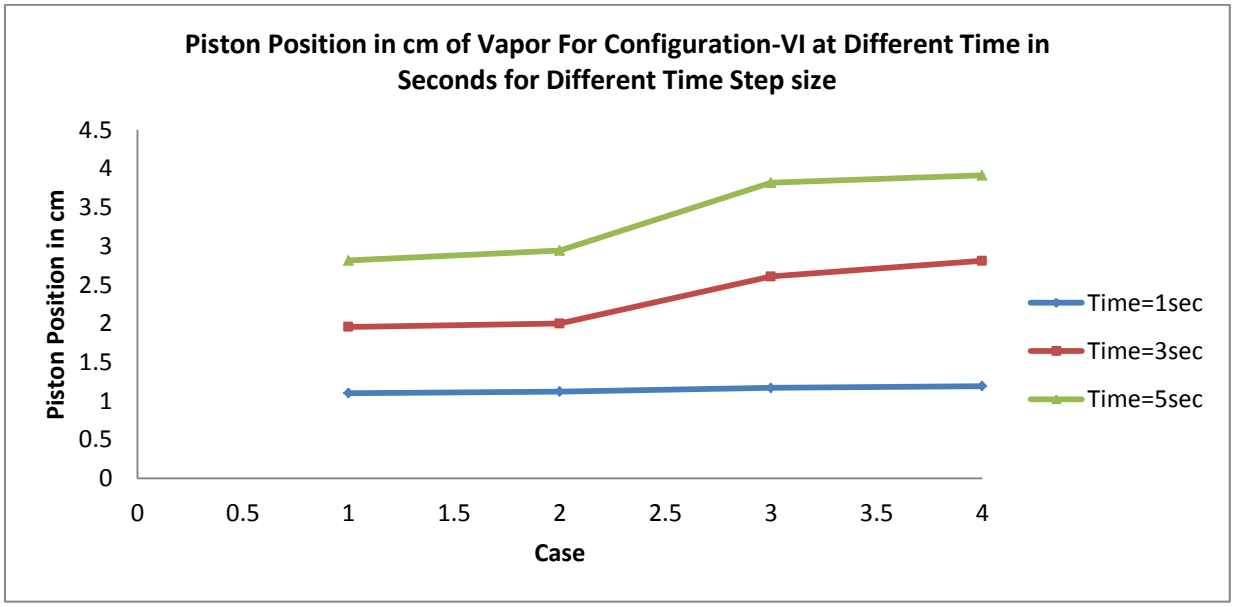

Figure C.49 Piston position at different time step size for Configuration-VI

Mesh and time dependency of Configuration-VII

Table C.17 Grid sizes used in the mesh dependency test for Configuration-VII

	Grid 1	Grid 2	Grid 3	Grid 4
Element size in mm	**2**	**1.4**	**1**	**0.75**
Element initial counts	**945**	**1,247**	**2,800**	**4,510**

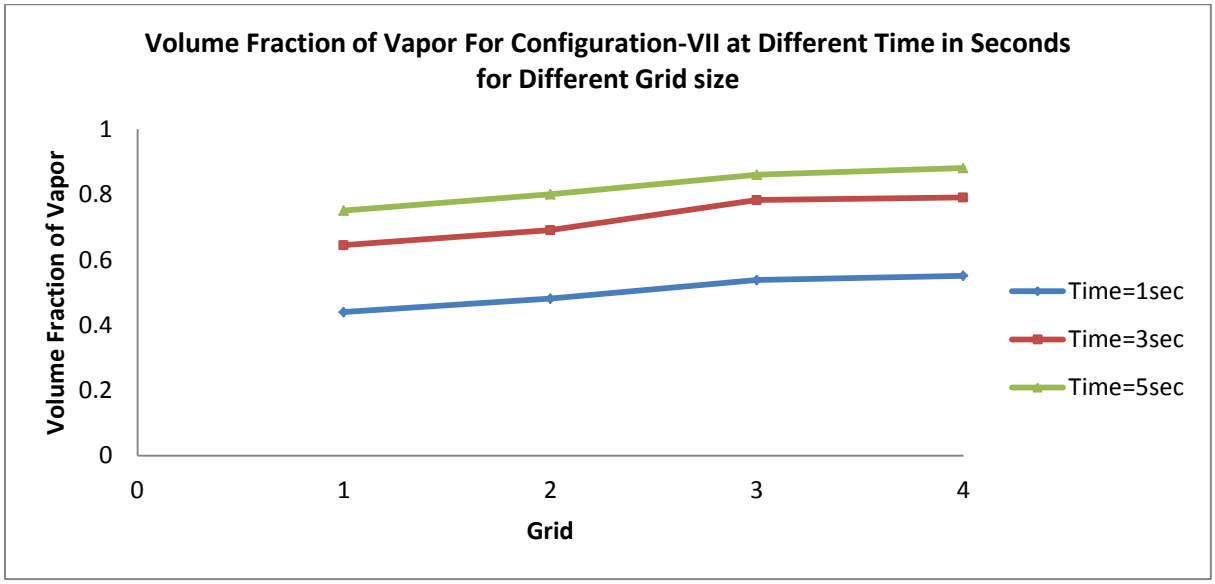

Figure C.50 Volume fraction of vapor at different grids size for Configuration-VII

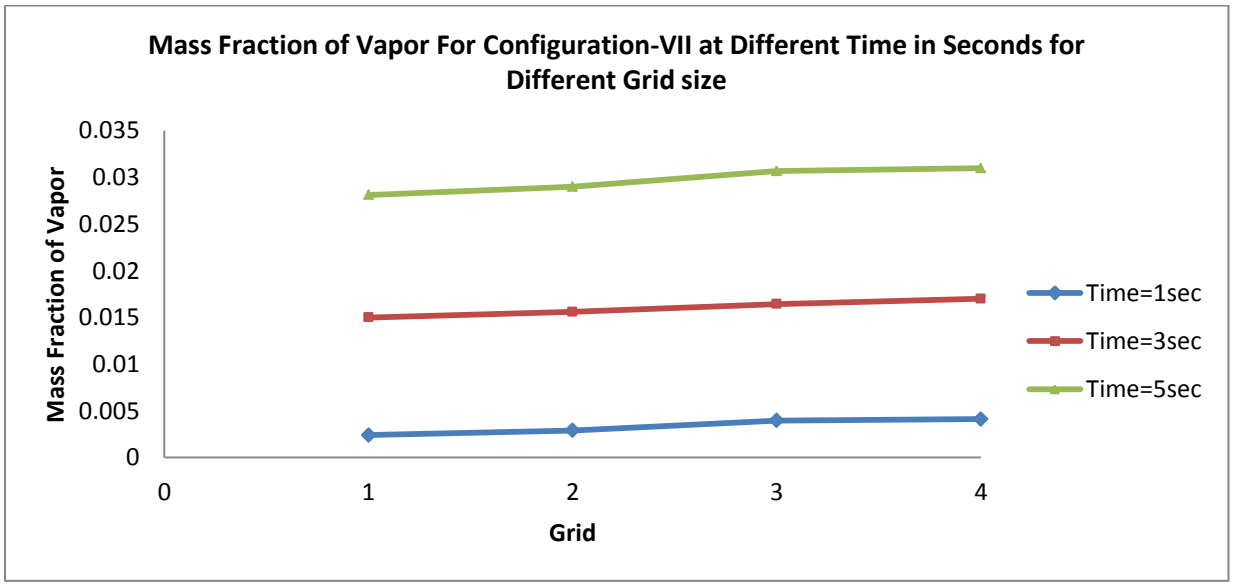

Figure C.51 Mass fraction of vapor at different grids size for Configuration-VII

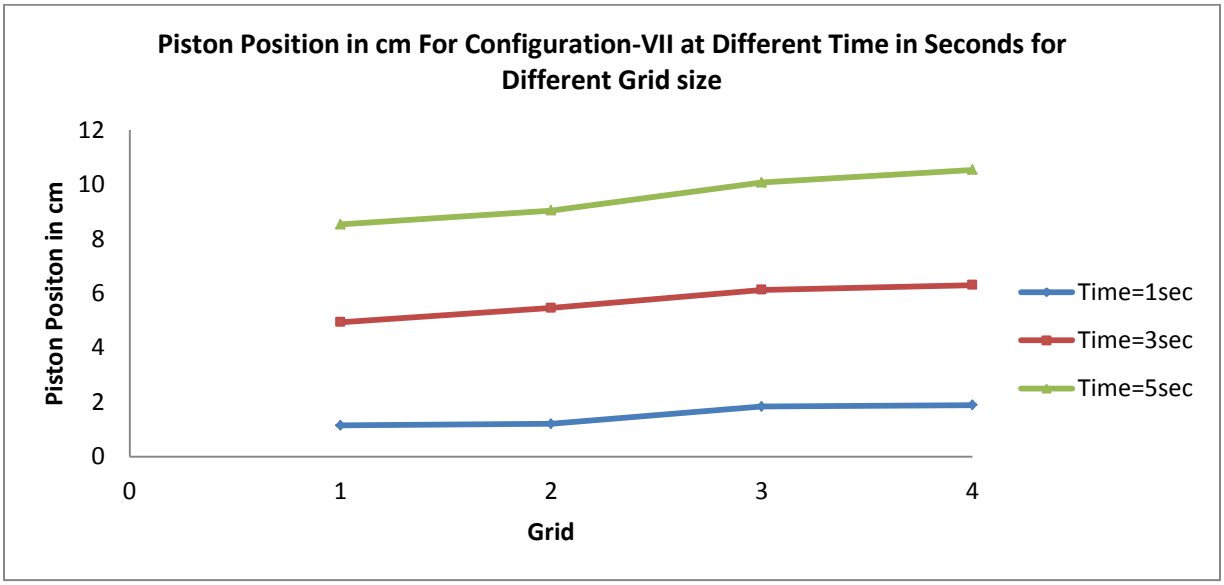

Figure C.52 Piston position of vapor at different grids size for Configuration-VII

Table C.18 Time step values used for the time-step dependency test for Configuration-VII

Case1	Case 2	Case 3	Case 4
0.01	0.005	0.0025	0.001

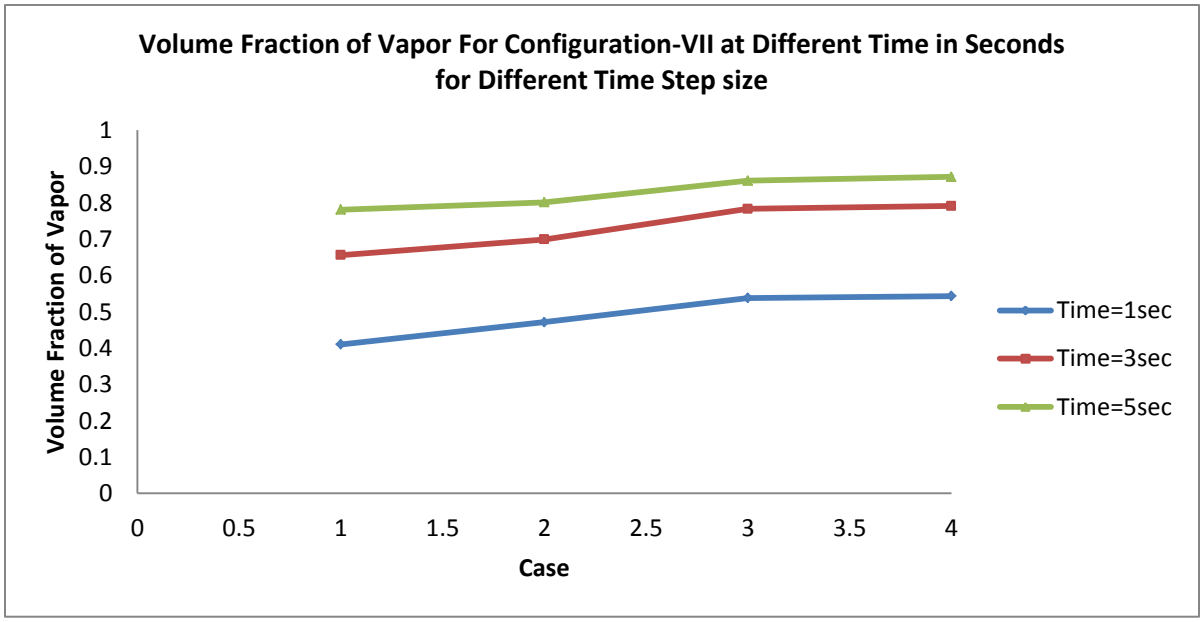

Figure C.53 Volume fraction of vapor at different time step size for Configuration-VII

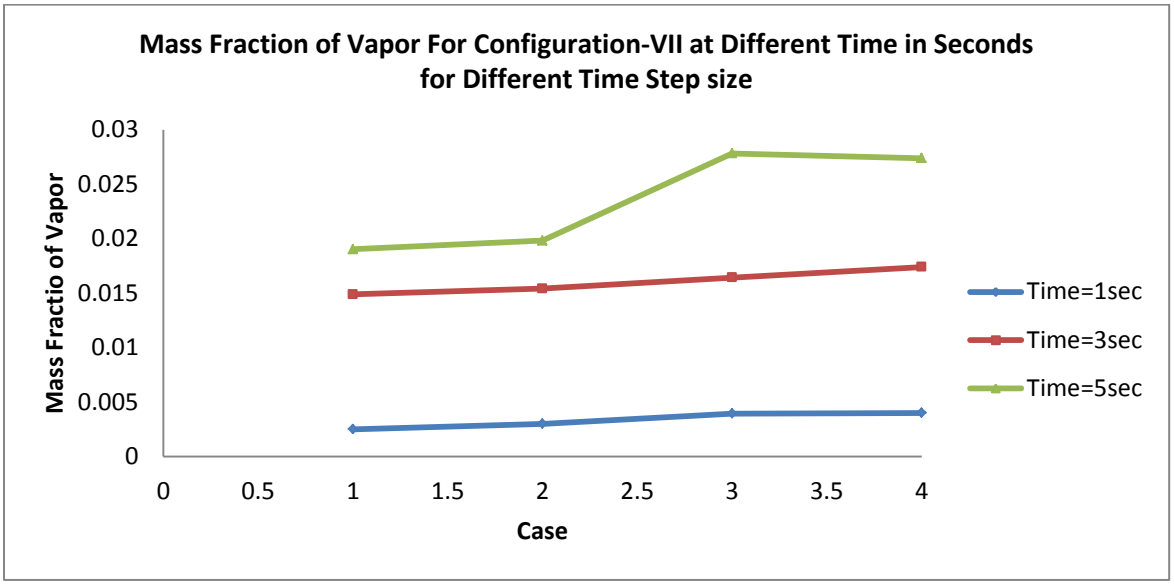

Figure C.54 Mass fraction of vapor at different time step size for Configuration-VII

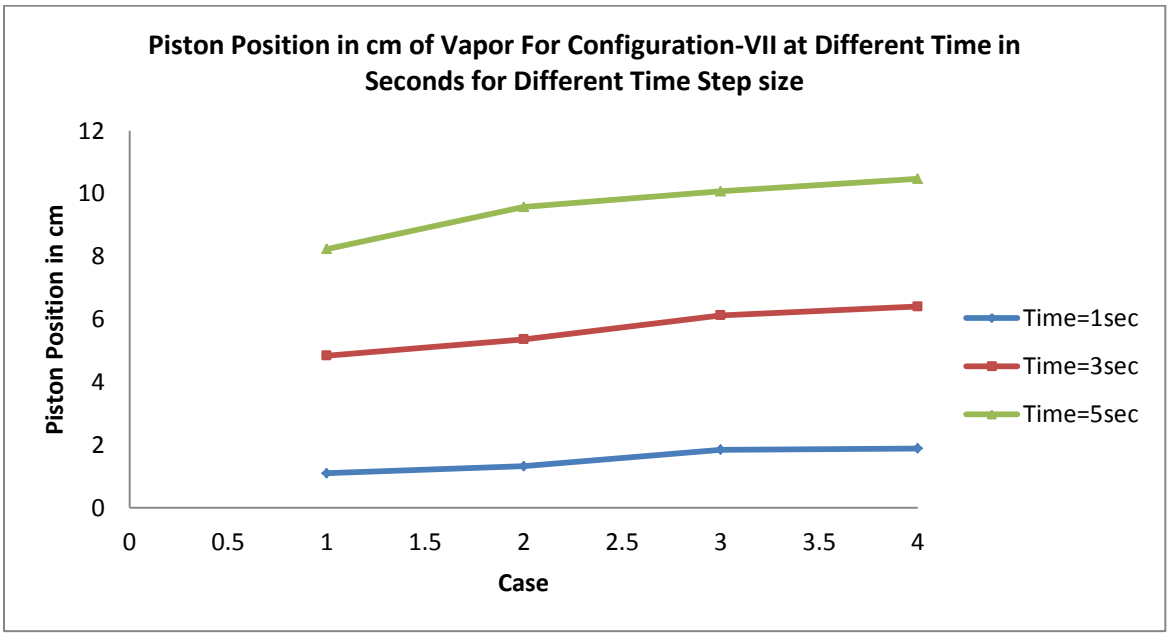

Figure C.55 Piston position at different time step size for Configuration-VII

Ghaleb R. A. Sater

ACADEMIC ACHIEVEMENTS

Masters of Engineering Science, Mechanical Engineering January 2013
Western University, London, ON

- Western Graduate Research Scholarship (WGRS) 2010-2012
- NSERC Research Scholarship 2010-2011
- Mitacs Research Scholarship 2011-2012

Bachelor of Engineering Science, Mechanical Engineering June 2010
Western University, London, ON

- Graduated with distinction; GPA: 3.7
- Dean's Honour list 2006, 2007, 2008, 2009

WORK EXPERIENCE

Intern Student October 2011 – December 2012
Mitacs-Accelearate Graduate Research Internship Program and Dyveraga Inc.-Waterloo

- Measured essentia parameters of Dyverga's novel energy system
- Presented analysis and results of research work at Western

Research Assistant January 2011 - December 2012
Mechanical Engineering Department-Western

- Investigated Dyverga's energy system using numerical modeling in Fluent 13
- Prepared a two phase numerical model with moving boundary
- Initiated a detailed parametric study on the proposed numerical model

Teacher Assistant January 2011 - December 2012
Mechanical Engineering Department-Western

- Prepared course related materials
- Proctored and marked exams

Research Assistant January 2010 - May 2010
Chemical and Biomedical Engineering Department- Western

- Determined mechanical properties of different nano-composite materials using a servo-hydraulic material testing system (MTS Bionix 858)
- Co-author of a research project presented at the Canadian Biomaterials Society Conference

ADDITIONAL INFORMATION

ASHRAE - Western and London, Ontario 2009 - 2011

- Member of American Society of Heating, Refrigeration and Air-Conditioning (ASHRAE) London
- Presented final design project during London's ASHRAE chapter conference
- Initiated with a group of engineers the ASHRAE club at Western

Skills

- Strong academic experience in mechanical engineering, Computational Fluid Dynamics (CFD)
- Expertise in using CFD package including Fluent 13, Design Modular, ANSYS mesh utility including and ICEM
- Strong experience in using design tools: HAP, AutoCAD/MEP, Solid Works
- Proficient in C, C++ and Matlab languages
- Solid communication, organization, and problem solving skills

Other Activities:

- Outdoor sports: mountain biking and hiking
- Basketball and Swimming
- World travel